THE DISEASE MECHANISMS OF SKELETAL DYSPLASIA CAUSED BY TWO AGGRECAN MUTATIONS

A thesis submitted to Newcastle University for
the degree of Doctor of Philosophy in the
Institute of Genetic Medicine

Beth Grace Gibson

October 2018

Skeletal dysplasias are a complex group of over 350 disorders of cartilage and bone with a combined incidence of 1/5000. Diagnosis is difficult and based on clinical and radiographic findings, with many cases having no known genetic cause. An allelic series of mutations has been identified in aggrecan that results in a broad phenotypic spectrum, including spondyloepimetaphyseal dysplasia (SEMD) and familial osteochondritis dissecans (OCD). Aggrecan, a large chondroitin sulfated proteoglycan, attracts ions and water molecules, allowing the cartilage to withstand the high mechanical load found in the skeletal joint. The SEMD (p.D2276N) and OCD (p.V2303M) causative mutations are found at highly conserved residues in the C-type lectin domain (CLD) which interacts with other extracellular matrix (ECM) molecules to provide stability.

PolyGene Transgenetics introduced mutations into the C57Bl/6 mouse line using homologous gene targeting. The resultant mice were assessed with radiography, morphometry and growth measurements. Histological techniques, electron microscopy, RNA-sequencing and SDS-PAGE Western blotting were used to analyse the underlying patho-molecular mechanisms.

The homozygous V2019M *Acan* (OCD) mouse exhibits mild disproportionate short stature, whereas the homozygous D1983N *Acan* (SEMD) mouse has severe disproportionate short stature with associated skeletal abnormalities, including mid-face hypoplasia. OCD and SEMD mice also exhibit intervertebral disc degeneration, which has not previously been reported in human patients. OCD and SEMD growth plate cartilage is disorganised, with reduced aggrecan in the extracellular matrix, increased apoptosis and mis-expression of other extracellular matrix proteins. The unfolded protein response is not upregulated in either OCD or SEMD cartilage, although SEMD chondrocytes exhibit mild cellular stress. Comparative transcriptomic analysis indicates that autophagic flux, vesicular transport and regulation of chondrocyte differentiation are altered between these two models.

The data presented in this thesis demonstrates that OCD and SEMD mice recapitulate the human short stature phenotypes and that altered matrix organisation may impair cellular differentiation, causing reduced bone growth. These mouse models could be used to further investigate the disease mechanisms of these two skeletal disorders.

DEDICATION

To my family, for their constant support and unconditional love.

ACKNOWLEDGEMENTS

Thank you to my supervisors Professor Michael Briggs and Dr Katarzyna Pirog for their advice and to all the members of the Briggs and Pirog labs (past and present) for their help and support during my PhD.

Thank you to Caroline Monaghan and the rest of the staff at the Functional Genomics Unit for looking after the mice.

Thank you to Dr Stephan Sonntag and Polygene Transgenetics for creating the knock-in aggrecan mouse lines and genotyping strategy.

Thank you to Dr Kath White and the staff of the Electron Microscopy Services for their patience, advice and sample preparation for the ultrastructural analysis.

Thanks to Mr Andrew Skelton of the Bioinformatic Support Unit for his practical help with RNA-sequencing analysis.

Thanks to Professor Danny Chan and Professor Kathy Cheah of Hong Kong University for their advice and encouragement during my placement. Thank you to Dr Wilson Chan and Dr Joyce Zhang for their advice and for acting as additional scorers for the intervertebral disc study. Many thanks to the staff and students of 3/F laboratory block, and in particular Dr Joyce Chan, Dr Mateusz Kudelko and Mrs Alice Lui, for making me feel so welcome during my placement at Hong Kong University.

Financial support from the SYBIL project (funded by the European Commission's Seventh Framework Programme for Research) and RUBICON network (funded by the European Union's Horizon 2020 research and innovation programme) is gratefully acknowledged.

TABLE OF CONTENTS

LIST OF FIGURES

LIST OF TABLES

INTRODUCTION

MATERIALS AND METHODS

RESULTS: VALIDATION AND PHENOTYPING OF MUTANT AGGRECAN MOUSE MODELS

RESULTS: QUALITATIVE TISSUE PATHOLOGY ANALYSIS OF THE SEMD AND OCD MOUSE MODELS

RESULTS: QUANTITATIVE TISSUE PATHOLOGY ANALYSIS OF THE SEMD AND OCD MOUSE MODELS

LIST OF FIGURES

LIST OF TABLES

Chapter 1. Introduction

1.1. Limb pattern development

The tetrapod limb (Figure 1A) is comprised of three compartments: the proximal stylopod which contains a single large bone such as the femur, the middle zeugopod with two bones and the distal autopod which forms the digits (Mariani and Martin 2003). Limb patterning begins when the limb bud is formed from mesenchymal cells covered with a layer of ectoderm (Figure 1B). Limb bud initiation and positioning is controlled by rostral and caudal HOX signalling. This signalling then affects the expression T-box transcription factors which determine the limb bud's ultimate fate, TBX4 promoting hindlimb identity and TBX5 the forelimb (Gibson-Brown, Agulnik et al. 1996). At the distal end of the limb bud is a thick ectodermal layer known as the apical ectodermal ridge (AER) which is primarily responsible for patterning the proximal-distal axis and maintaining the proliferative state which is required for limb growth (Mariani, Fernandez-Teran et al. 2017, Petit, Sears et al. 2017). Mesenchymal FGF10 expression is elicited by either TBX4 or TBX5, creating a positive regulatory feedback loop with ectodermal (AER) FGF8 expression. The zone of polarising activity (ZPA), a posterior area of mesodermal cells, controls the anterior-posterior axis by the secretion of the gradient morphogen sonic hedgehog (SHH). The dorso-ventral axis is patterned by the non-AER ectoderm under the regulation of WNT family member 7A. The presence and interaction of all three centres is required for the correct patterning of the limb and involves the specific coordination of many genes and their regulatory elements (Liu, Nakamura et al. 2003, Mariani, Fernandez-Teran et al. 2017, Parr and McMahon 1995, Petit, Sears et al. 2017). As an example, bone morphogenetic protein (BMP4) in the mesenchyme upregulates Gremlin1 (GREM1) forming a negative feedback loop which controls the area of the AER (Figure 1C). SHH becomes the main upregulator of GREM1 expression and a feedback loop forms between GREM1, BMP4, FGFs (AER) and SHH (ZPA) (Zuniga, Laurent et al. 2012). As the limb bud grows, the concentration of SHH near the GREM1 expression decreases and FGF inhibition of GREM1 occurs. This decreases downstream GREM1 signalling and halts the feedback loop.

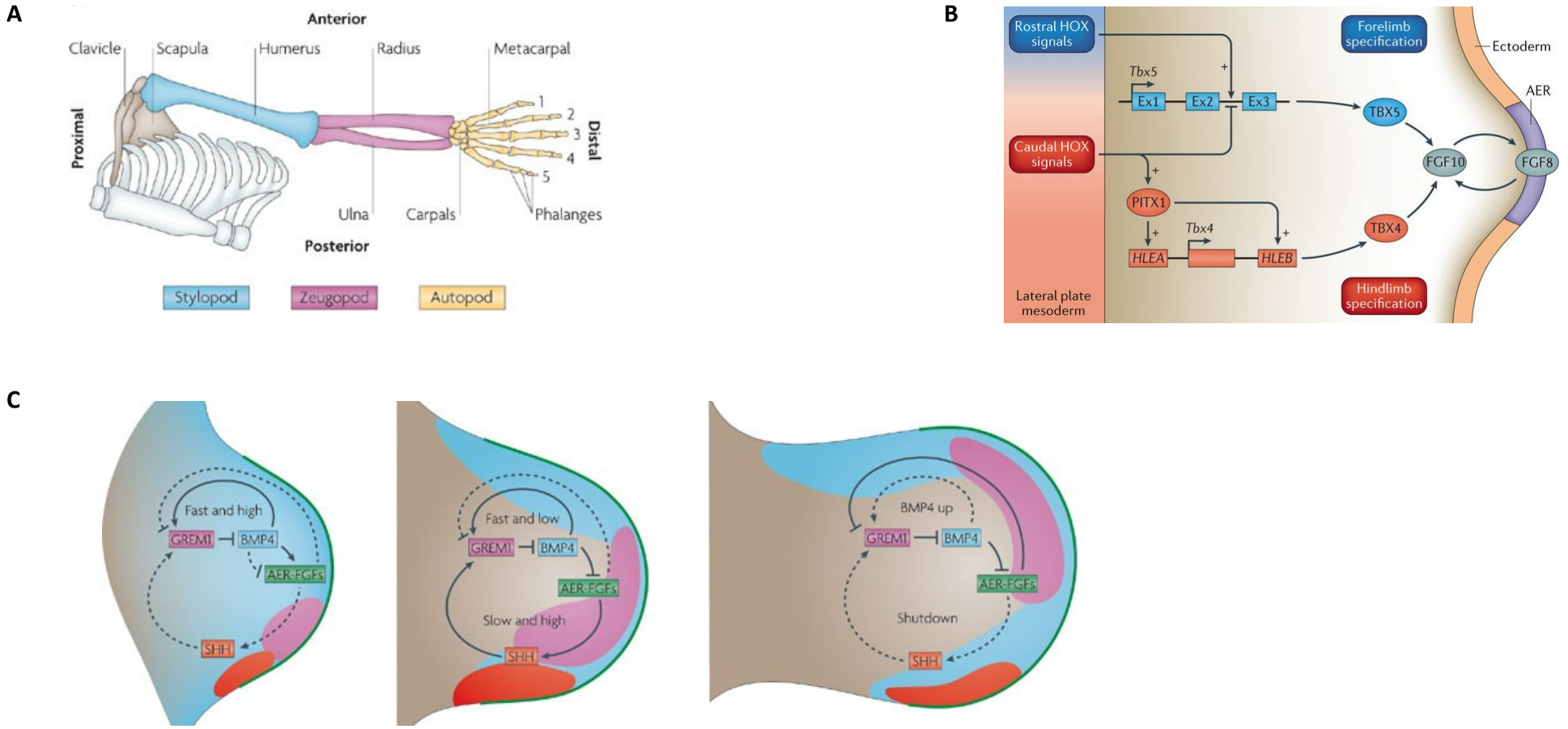

Figure 1 Patterning of the vertebrate limb

(A) The tetrapod limb is divided into three compartments and is described by posi onal axes. **(B)** Limb bud forma on is ini ated by HOX signalling, altering TBX gene expression and specifying final limb fate. **(C)** Limb development is controlled by the interplay of signalling feedback loops originating from the AER, ZPA and non-AER ectoderm. Key: ——— active loops ····· inactive loops GREM1 expression BMP4 expression FGF expression SHH expression. Figures taken from Petit, Sears et al 2017 and Zeller, Lopez-Rios et al 2009.

1.2. Bone development

The human musculoskeletal system is comprised of many different tissue types that work in synchrony to protect the internal organs and allow movement. The adult human skeleton is comprised of 206 bones which are connected to each other and the various muscles with ligaments and tendons respectively. The bones of the joint are covered by a layer of cartilage, which helps to prevent any damage to the bones that might be caused during movement. The development of the human skeleton occurs by two main processes: the formation of the long bones occurs through the process of endochondral ossification; the flat bones, such as those in the skull's cranial vault, develop by intramembranous ossification (Mackie, Ahmed et al. 2008, Karaplis 2008).

1.2.1. Endochondral ossification

Endochondral ossification relies upon formation of an initial cartilaginous template (Figure 2A). Mesenchymal stem cells condense and differentiate into cartilage cells or chondrocytes which begin to proliferate and secrete collagen, proteoglycan and glycoproteins to form an extracellular matrix. This matrix is arranged around the cells which sit in cavities called lacunae (Karaplis 2008). The chondrocytes in the centre of the condensation cease proliferation, enter hypertrophy (vastly increasing their cytoplasmic to nuclear ratio) and begin to secrete indian hedgehog (Figure 2B). As the cells mature in this hypertrophic zone they express collagen type X, matrix metalloproteinase 13 (MMP13) and vascular endothelial growth factor (VEGF) (Mackie, Ahmed et al. 2008). The perichondrial cells next to this region are induced to differentiate to osteoblasts and begin to secrete matrix to form a bone collar (Long, Chung et al. 2004). It was thought that the vast majority of the hypertrophic cells enter terminal differentiation and become apoptotic; however, more recent work has shown that these cells may also transdifferentiate into osteoblasts, with the exact proportion estimated as much as 60% (Ono, Ono et al. 2014, Yang, Tsang et al. 2014, Zhou, von der Mark et al. 2014). The expression of VEGF and several other factors causes blood vessels to invade and vascularise the tissue. Osteoprogenitor cells (chondroclasts) are attracted into the tissue and use the remaining matrix as a scaffold to begin bone formation (primary spongiosa). Osteoclasts degrade the cartilage ECM, which is then replaced by a characteristic bone matrix secreted by the osteoblasts. (Karaplis 2008) This forms the primary ossification

centre. As interstitial growth continues some of the proliferating chondrocytes assume a flattened discoid morphology, dividing perpendicular to the axis of growth and move over each other to form columns parallel to the axis of bone growth (Kronenberg 2003). As the skeleton develops, a secondary ossification site forms at the epiphysis of the long bone as the chondrocytes again cease proliferation and enter a hypertrophic state, initialising bone formation (Figure 2A). The secondary ossification centre is provided with nutrition by vessels known as the cartilage canals which originate from the perichondrium. These canals then recede during aging as they are gradually replaced by cartilage at their terminal ends in a process known as chondrification (Ytrehus, Ekman et al. 2004). The cells below the secondary ossification centre slow their rate of proliferation, forming a resting zone (Figure 2B). Chondrocytes in the resting zone are small, rounded and continue to secrete some extracellular matrix proteins (Mackie, Ahmed et al. 2008). The cells act as a reserve, storing lipids, glycogen and proteoglycan aggregates in preparation for future growth and increased matrix production. Above the secondary ossification centre (adjacent to the synovial cavity or joint space) a residual layer of cartilage forms the articular surface to protect the underlying bone from damage. This articular cartilage is also divided into zones with differences in cell morphology and ECM organisation (Figure 2C). The superficial zone is adjacent to the joint space with tightly packed flattened cells arranged parallel to the synovial cavity. This zone provides the remaining articular zones with a source of cartilage progenitors (Kozhemyakina, Zhang et al. 2015) and expresses a high level of the lubricating glycoprotein lubricin to facilitate joint movement (Jay and Waller, 2014). The intermediate zone forms approximately half of the total articular cartilage volume and consists of sparsely arranged rounded chondrocytes. Cells in the deep zone below this are organised in columns perpendicular to the joint. This region comprises about 30% of the cartilage and provides the greatest resistance to compression. The last zone, which resides between the deep zone and the underlying subchondral bone, is the calcified cartilage. A ‘tidemark’ separates the uncalcified and calcified tissue. Cells in this region are sparse and have entered a hypertrophic state (Sophia Fox, Bedi et al. 2009). The area of cartilage between the two ossification sites forms the epiphyseal growth plate (Mackie, Tatarczuch et al. 2011) and longitudinal bone growth continues at this site until maturity is reached and the primary and secondary ossification centres fuse (Kronenberg 2003). After this time periosteal appositional growth stills occurs, increasing bone diameter as mineralised tissue is added to the periosteal bone surface by

osteoblasts (Figure 2B). This acts in tandem with the action of osteoclasts which break down the older bone tissue around the medullary cavity to increase its size (Rauch 2004).

1.2.2. Regulatory signalling

Endochondral ossification is a highly complex process which involves many interacting regulatory cell signalling pathways (Figure 2B). The transcription factor SRY-related high-mobility group-box gene 9 (SOX9) has been implicated in the initial formation of cartilage condensations and has been shown to drive both condensation cell survival and their differentiation to chondrocytes. At later stages proliferating chondrocytes have the highest expression of SOX9, where it seems to increase proliferation, production of matrix and expression of other key signalling molecules such as SOX5, SOX6 and IHH (Akiyama, Chaboissier et al. 2002). Further to this, SOX9 also acts to suppress hypertrophy by inhibition of the transcription factor RUNX2 and the WNT signalling pathway (Zhou, Zheng et al. 2007, Topol, Chen et al. 2009). The cell signalling protein indian hedgehog (IHH) is expressed by pre-hypertrophic chondrocytes and is a key modulator of chondrocyte proliferation and differentiation and osteoblast differentiation. IHH binds to its receptor patched-1 (PTCH1) which is expressed in the proliferative zone and adjacent perichondrium. The binding of IHH and PTCH1 activates smoothened (SMO) which triggers a gene activation cascade. The classical IHH pathway involves the delay of hypertrophy through the upregulation of parathyroid hormone-related protein (PTHRP) in the early proliferative region. PTHRP binds to parathyroid hormone receptor 1 (PTH1R) which is expressed in the proliferative zone and highly expressed by chondrocytes undergoing hypertrophy, delaying terminal differentiation. However, IHH has also shown an ability to accelerate chondrocyte proliferation and maturation by signalling independently of PTHRP (Karp, Schipani et al. 2000) through the BMP and canonical WNT pathways (Mak, Kronenberg et al. 2008). The bone morphogenetic proteins (BMPs) or growth and differentiation factors (GDFs) have been implicated in condensation, chondrocyte proliferation, maturation and maintenance of articular cartilage (Bandyopadhyay, Tsuji et al. 2007, Nilsson, Parker et al. 2007, Salazar, Gamer et al. 2016). The BMPs are part of the TGFβ superfamily, signalling through cell surface serine-threonine kinase receptors (BMPR1/2) to phosphorylate the SMAD transcription factor proteins. These interacting proteins form a signalling gradient across the growth plate and articular cartilage,

with the highest BMP expression in the hypertrophic zone (decreasing towards the resting zone) and the superficial zone (decreasing towards the deep zone). However, the highest SMAD phosphorylation is found in the proliferative, pre-hypertrophic and superficial zones. This is thought to be due to increased expression of the BMP antagonists SMAD7 in the hypertrophic zone and GREM1 and SMAD7 in the intermediate and deep zones of the articular cartilage. BMP signalling is currently thought to act to promote chondrocyte maturation in the proliferative and pre-hypertrophic zones (by increasing IHH expression) and helps to maintain the articular cartilage surface (although the exact mechanism is so far unknown) (Seki and Hata 2004, Estrada, Wang et al. 2013, Garrison, Yue et al. 2017). In addition to this, double knockout mice for the BMPR1A and BMPR1B receptors exhibit markedly reduced cartilage condensations, matrix production and SOX5/6/9 expression indicating an important role for BMP signalling in early chondrogenesis (Grimsrud, Romano et al. 2001, Yoon, Ovchinnikov et al. 2005). The fibroblast growth factor (FGF) signalling pathway is antagonistic to the BMP pathway and is very complex, with 22 FGF and 4 FGF receptor genes implicated in endochondral ossification. The function and expression of many FGFs is unknown but the FGF receptors are expressed in distinct regions: FGFR1 by pre-hypertrophic, hypertrophic and perichondrial cells; FGFR2 in the perichondrium, periosteum and primary spongiosa; FGFR3 by proliferating chondrocytes. In postnatal development FGF signalling through FGFR3 appears to inhibit chondrocyte proliferation and differentiation, both through the Janus kinase–signal transducer and activator of transcription-1 (JAK-STAT1) pathway and inhibition of IHH expression (Sahni, Ambrosetti et al. 1999, Liu, Xu et al. 2002). However, in early development FGF/FGFR3 signalling has the opposite effect and is required for proper proliferation and initiation of hypertrophy. Thus far only the roles of FGF9 and 18 have been investigated, indicating substantial redundancy between the two ligands and complex interactions with signalling molecules such as SOX9, VEGF and RUNX2. This indicates that FGF signalling is biphasic according to the stage of development and has a role at every point of growth, from limb patterning to vascularisation (Liu, Lavine et al. 2007, Karuppaiah, Yu et al. 2016, Hung, Schoenwolf et al. 2016). In addition to those already discussed, chondrocyte hypertrophy appears to be regulated by a number of transcription factors, including Runt-related transcription factor 2 (RUNX2/CBFAI) myocyte enhancer factor 2c (MEF2C) and forkhead box (FOX) proteins. All three have been shown to increase expression of COL10A1 and RUNX2 is also able to directly transcribe other markers of hypertrophy, such as IHH and MMP13 (Yoshida, Yamamoto et al. 2004, Arnold, Kim et al.

2007, Hirata, Kugimiya et al. 2012, Yoshida, Hata et al. 2015). The study of regulatory signalling in long bone growth is very complex due to redundancy between ligands (as in the FGF pathway) cross interaction between pathways (the antagonistic interaction of BMP and FGF signalling) and multiphasic roles (FGFR3 initially increases proliferation but then acts to supress it during postnatal development). In addition to this, many other factors also appear to be involved. These factors include vitamin D, cytokines, glucocorticoids, WNTs, thyroid hormone and androgen. Recent research has even revealed cross talk between the FGF and IHH/PTHRP pathways with autophagy and its master regulator mTORC (Cinque, Forrester et al. 2015, Zhang, Bai et al. 2017) further illustrating how little is known about these complex signalling interactions.

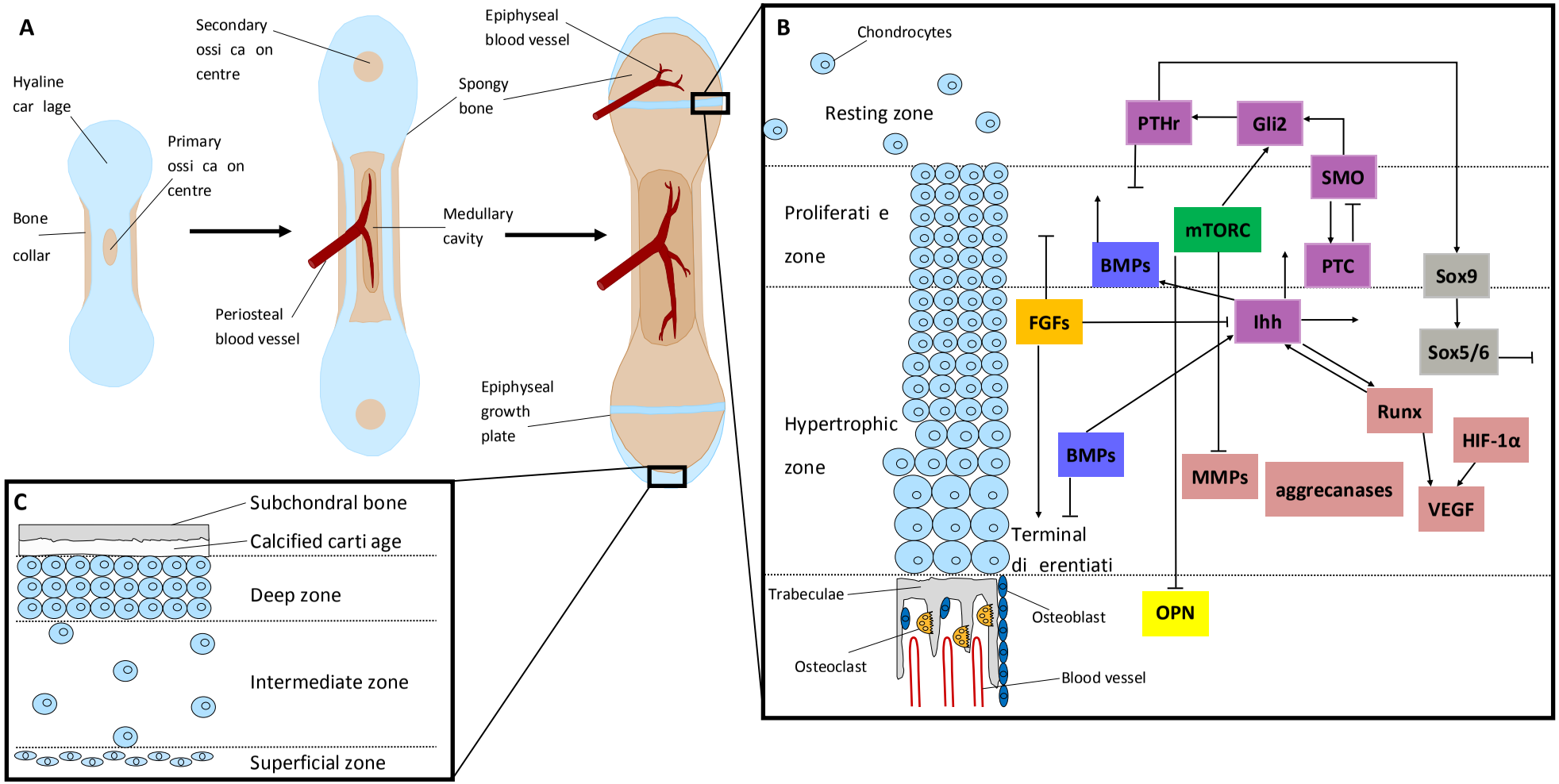

Figure 2 Structure and regulation of endochondral ossification

(A) Endochondral ossification **(B)** The epiphyseal growth plate and some of the signalling pathways that regulate it **(C)** Structure of articular cartlage. Schematic adapted from (Marieb and Hoehn 2006, Page-McCaw, Ewald et al. 2007). Key: ⊣ inhibition → activation

1.2.3. Intramembranous ossification and the development of the skull

The development of the skull is complex as although the facial bones and those in the cranial base are formed by endochondral ossification, those in the cranial vault develop by intramembranous ossification. In addition to this, the facial bones originate from the neural crest (Noden 1983) but the cranial vault or neurocranium has its origins in both the cranial neural crest and mesoderm (Jiang, Iseki et al. 2002). The neurocranium consists of five major bones or calvaria: two frontal, two parietal and a single occipital bone (Figure 3A). Intramembranous ossification does not involve the formation of a cartilaginous precursor as the mesenchymal stem cells differentiate straight into osteoprogenitor cells and then osteoblasts after the formation of condensations (Hall and Miyake 2000) (Figure 3C). These osteoblasts deposit collagens, proteoglycans and other extracellular matrix proteins to produce osteoid, a bone matrix formed predominantly of collagen type I (McKee and Cole 2012). Some of the osteoblasts then differentiate into osteocytes and the bone matrix mineralises. This forms a structure of bone spicules around primary ossification centres which expand with maturity. This immature woven bone is then slowly replaced by stronger mature lamellar bone. Where these cranial bone 'plates' meet (sagittal, metopic) or overlap (lambdoid, coronal) they are connected by a flexible fibrous tissue known as a suture (or fontanelle where there are more than two bone fronts) (Figure 3A-B). This flexible model allows both passage through the birth canal and expansion of the neurocranium during development, as the sutures function as sites of bone growth (Opperman 2000, Jin, Sim et al. 2016). Each bone growth site is comprised of osteogenic bone fronts, the fibromesenchymal suture, the underlying dura mater that surrounds the brain and the external periosteum (pericranium) above. The cells in the centres of the fibromesenchymal suture maintain an undifferentiated state throughout development as those adjacent to the two bone fronts gradually differentiate into bone cells as the skull expands. This continues until growth ceases and the sutures fuse (Beederman, Farina et al. 2014, Katsianou, Adamopoulos et al. 2016). The regulation of cranial growth and maintenance of suture patency involves the interplay between signals from the dura mater, osteogenic front and fibromesechymal suture. Investigation of the premature suture fusion disorder craniosynostosis has implicated a variety of transcription factors (such as MSX2) and signalling pathways, including the

canonical WNT, FGF and TGFβ/BMP pathways (Kim, Rice et al. 1998, Warren, Brunet et al. 2003).

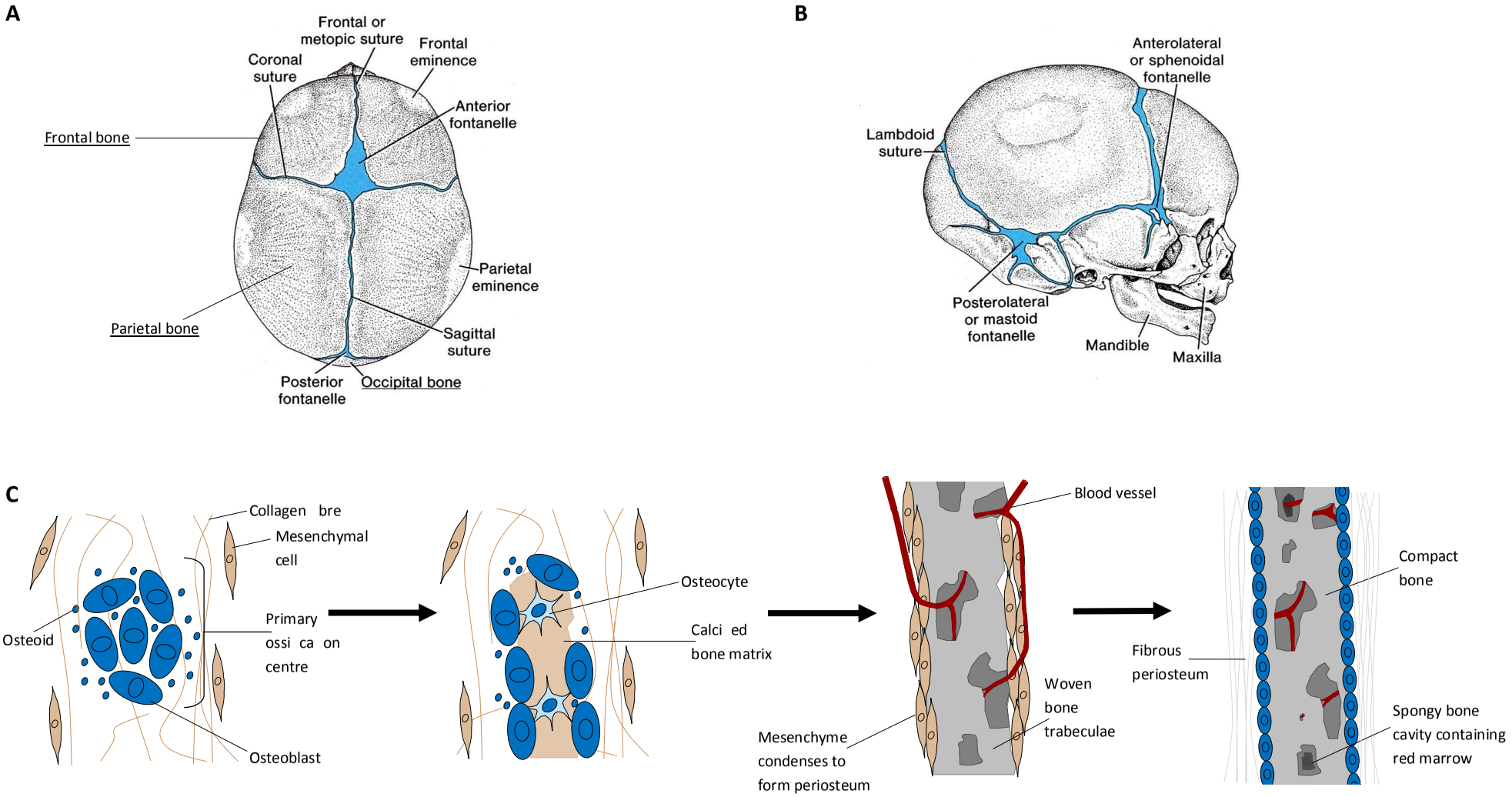

Figure 3 Intramembranous ossification and the skull

The flat bones and sutures of the human skull **(A)** superior view **(B)** sagittal view. **(C)** Schematic of intramembranous ossification. Adapted from Marieb and Hoehn 2006.

1.3. The vertebral column

The human vertebral column is comprises of 24 bony vertebral bodies and the sacrum, interspersed with intervertebral discs (IVD) (Figure 4D). The IVD provide the spine with both flexibility and shock absorption and are formed of the outer annulus fibrosus and inner nucleus pulposus (Ferguson 2008). The formation of the spinal skeleton is initiated during early embryonic development (week 4) as somitocoel and pre-sclerotome cells migrate to surround the notochord and neural tube, forming the perichordal tube or sclerotome (Figure 4A). The large vacuolated notochordal cells within this structure generate osmotic pressure against basement sheath of the notochord, providing structure and aiding in sclerotome elongation (Aszódi, Chan et al. 1998, Stemple 2005). The regulation of vertebral body and IVD formation involves the complex interaction of many signalling molecules secreted by both the notochord (NOG, SHH, FOXA1) and sclerotome (BMP, TGF-β, SOX9, PAX1) to ensure correct patterning and differentiation (Peters, Wilm et al. 1999, Pearson, Lemons et al. 2005, Baffi, Moran et al. 2006, Maier, Lo et al. 2013). Segmental patterning of the sclerotome occurs under the regulation of the HOX transcription factors as the mesenchymal sclerotome cells condense to form areas of variable cellular density (Pearson, Lemons et al. 2005, Rodrigues-Pinto, Richardson et al. 2014) (Figure 4B). High density segments form the putative annulus fibrosus (IVD) and expand to accommodate the notochord, which retracts from the low density segments that will form the vertebral bodies (McCann, Tamplin et al. 2012) (Figure 4C). The exact mechanism by which the notochord is removed from the putative vertebrae is not currently known but both Eph/ephrin and ROBO/SLIT signalling pathways have been implicated in its regulation (Lawson and Harfe 2015). Those cells which will form the vertebrae differentiate into chondrocytes to form a cartilaginous structure (Aszódi, Chan et al. 1998). The development of the vertebral bodies and adjacent cartilage endplates continues by endochondral ossification, driven by SHH and FGF signalling molecules secreted by the notochord (Chan, Au et al. 2014, Ashley, Enomoto-Iwamoto et al. 2016) and other regulatory molecules, including the transcription factor osterix (Chen, Feng et al. 2014). The remnants of the notochord then form the nucleus pulposus (NP). The NP contains a heterogeneous cell population which varies with age, disease and species. In newborn humans the nucleus pulposus consists of clustered large vacuolated notochordal-like cells which decrease in number during childhood as the proportion of smaller chondrocyte-like cells increases (Purmessur, Guterl et al. 2013, Chan, Au et al. 2014). This transition is thought

to occur through both differentiation of notochordal-like cells to a chondrogenic phenotype (regulated by a canonical Wnt-Shh feedback loop) and cellular migration from other tissues (McCann, Tamplin et al. 2012, Tanaka, Sakai et al. 2012, Chen, Feng et al. 2014). The exact function of each cell type is not currently known but notochordal-like cells have been shown to have a protective role against degeneration *in vitro,* suggesting that they play an important role in the maintenance and repair of the NP (Erwin, Islam et al. 2011, Chan, Au et al. 2014).

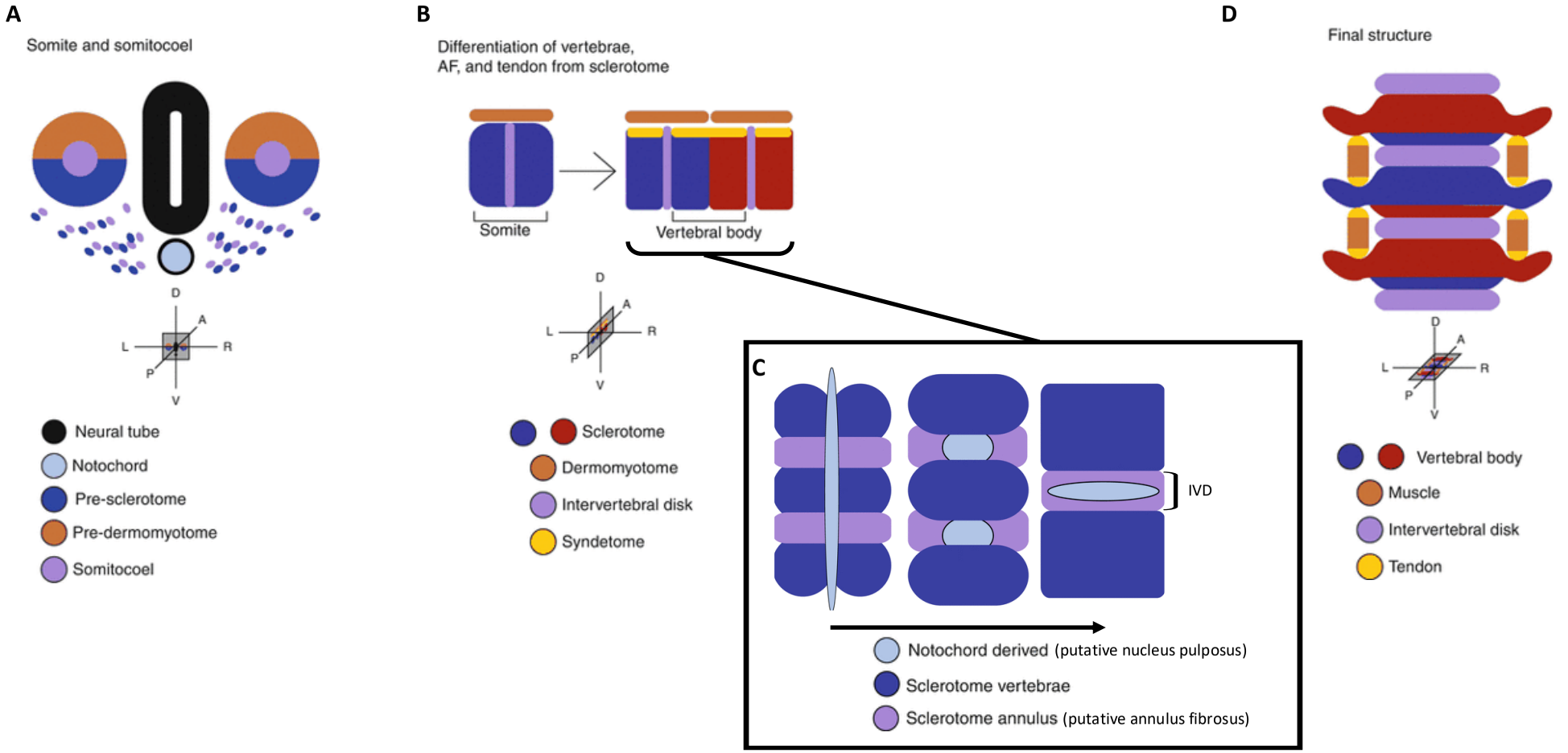

Figure 4 The development of the vertebral column

(A) Cells migrate to surround the notochord, forming the sclerotome. **(B)** The sclerotome cells condense into segments to form the intervertebral discs (IVD) and vertebral bodies. **(C)** The notochord retracts from the putative vertebral bodies into the annulus fibrosus (outer IVD) to form the nucleus pulposus (inner IVD). **(D)** The final structure of the vertebral column. Adapted from Cox, Serra et al. 2014.

1.4. Cartilage and the extracellular matrix

Cartilage is a dynamic tissue which is usually comprised of a single cell type (the chondrocyte) and a highly organised and complex extracellular matrix (ECM) (Figure 5A). This ECM is continuously remodelled throughout life and in response to injury and degenerative disease. ECM composition and organisation also differs between its tissue type (hyaline, elastic or fibrocartilage), location and indeed its location within that particular sub-type of cartilage (Onnerfjord, Khabut et al. 2012).

1.4.1. The articular surface and growth plate

Hyaline cartilage is a highly specialised translucent tissue found on the articular joint surface and in the epiphyseal growth plate. The chondrocytes within this tissue exist in a mostly avascular, hypoxic, aneural and alymphatic environment, using glycolysis for ATP production (Karaplis 2008). The cartilage ECM consists of networks of interacting molecules that provide structural support for the chondrocyte cells and 90% of the tissue's dry weight (Hardingham and Fosang 1992) (Figure 5). In addition to its important structural role it has also been shown to be involved in cell adhesion, migration, proliferation, differentiation, and survival, mostly through integrin-mediated cell-matrix signalling (Buckwalter and Mankin 1998, Toole 2001, Pulai, Del Carlo Jr et al. 2002, Schmidt and Friedl 2010, Gao, Liu et al. 2014). The two major structural components are collagen type II and the proteoglycan aggrecan; however, the ECM is comprised of many families of molecules, including collagens, proteoglycans and non-collagenous glycoproteins (Frantz, Stewart et al. 2010). The matrix composition of articular and growth plate hyaline cartilage varies depending on a number of factors, including zone and distance from the cell. The pericellular matrix encircles the chondrocyte forming a capsule. This matrix is mainly comprised of a collagen type VI microfibrillar network (Zelenski, Leddy et al. 2015) and is enriched in proteoglycan (perlecan, biglycan) (Kavanagh and Ashhurst 1999, Melrose, Roughley et al. 2007) collagen type IX (Parsons, Gilbert et al. 2011) hyaluronan (Knudson 1993) and glycoproteins such as matrilin 3 (Vincourt, Etienne et al. 2012). It is thought that the structure of this matrix capsule

influences cell response to stimuli, facilitates mechanotransduction and allows the modification of ECM molecules as they are secreted and move towards the interterritorial matrix. As an example, the pericellular matrix can affect cartilage metabolism by the incorporation of the catabolic matrilin 3 into the matrix where it then exerts an anabolic effect (Vincourt, Etienne et al. 2012, Wilusz, Sanchez-Adams et al. 2014). The thicker territorial matrix surrounds each chondron and is postulated to provide resistance to mechanical stress (Sophia Fox, Bedi et al. 2009). It contains a network of larger banded collagen fibrils comprised of collagen types II, IX and XI. As these collagen fibrils move into the interterritorial matrix, which lies between the chondrons, they enlarge and move parallel to the adjacent fibrils (Prein, Warmbold et al. 2016). Cartilage's main tensile strength and resistance to compression are provided by the combined action of these heterotopic collagen fibrils (which provide tensile strength) and proteoglycan aggregates (which provide resistance to compression) (Roughley and Mort 2014). These aggregates lie within the collagen network and are formed from the large proteoglycan aggrecan, cartilage link protein and the glycosaminoglycan hyaluronan. Aggrecan has a great number of attached sulfated chains which have a high fixed charge and become hydrated in proximity to the aqueous joint space environment, creating an osmotic pressure in the spaces between the collagen fibrils. When a mechanical force is applied through movement of the joint the water is displaced and the ECM compresses without any structural damage occurring. As the force abates, water is pulled back into the cartilage from the joint space and the cartilage re-swells. This mechanism is not only useful for resistance to mechanical load but is thought to aid with nutrition and waste removal (Roughley and Mort 2014). In the articular cartilage collagen fibril diameter and orientation differ depending on the distance from the joint space. In the superficial zone, directly adjacent to the joint surface, the thin collagen fibrils are parallel to the joint space and there is a low abundance of proteoglycan. In the intermediate zone below, fibril diameter and orientation are more varied and proteoglycan abundance is increased. The deep zone contains the greatest amount of proteoglycan and collagen fibrils are organised perpendicular to the joint surface (Sophia Fox, Bedi et al. 2009). Matrix composition also changes according to the zone of chondrocyte differentiation; for example, the collagens expressed by hypertrophic cells in the deep articular zone and the hypertrophic growth plate zone consist of 45% collagen type X (Shen 2005).

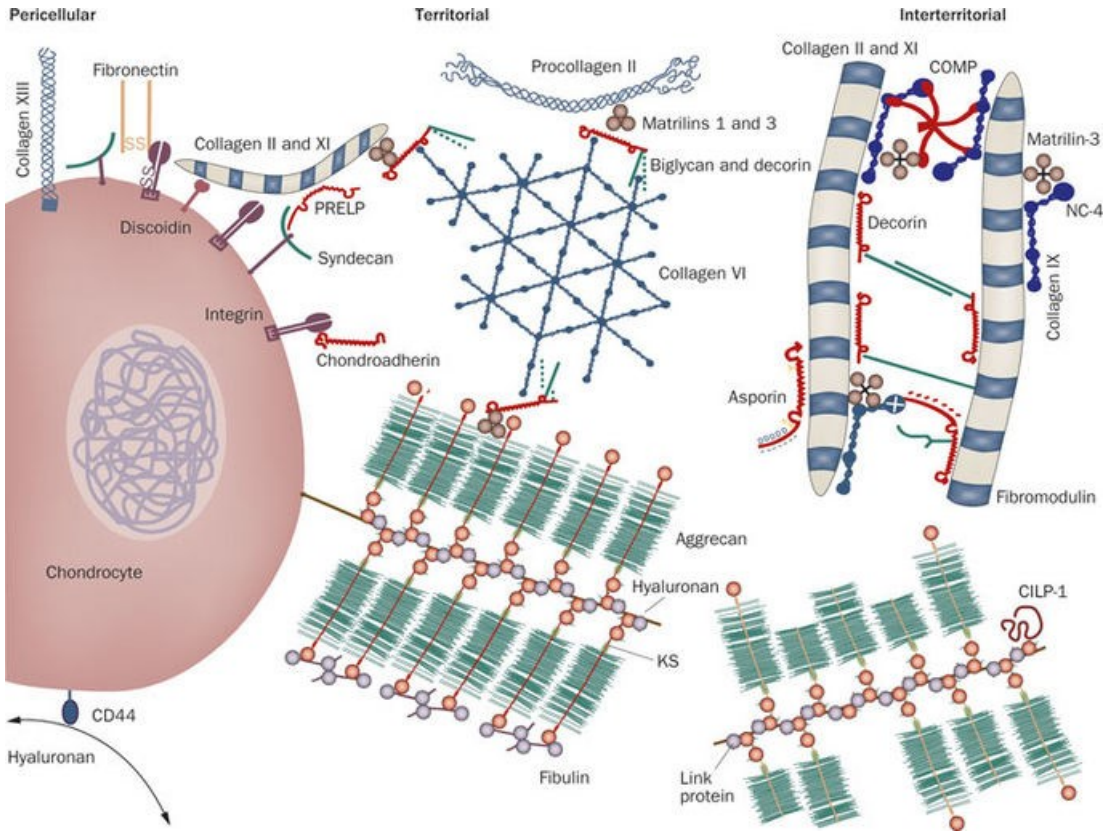

Figure 5 The hyaline cartilage extracellular matrix

The molecular components and interactions of the extracellular matrix (ECM) (Heinegard and Saxne 2011).

1.4.2. The intervertebral disc

The intervertebral disc (IVD) is a mostly avascular tissue comprised of three parts, each with a distinct cartilaginous matrix composition according to function, which will be discussed in brief. Each IVD is comprised of a central nucleus pulposus (NP) surrounded by a lamellar annulus fibrosus (AF) and bordered by two cartilage endplates which connect the IVD to the vertebral bodies (Chan, Au et al. 2014). The cartilage endplates are composed of hyaline cartilage rich in collagens type II and X and provide the IVD with both nutrition and waste removal through its nutrient supply channels (Rodrigues-Pinto, Richardson et al. 2014). The annulus fibrosus (AF) is formed from both fibrous and cartilaginous tissue (known as fibrocartilage) and contains collagen fibers interspersed with elastic fibers. This matrix composition allows fibrocartilage to resist tension and so it is also found in the tendon, ligament and meniscis. Interestingly, it also forms during the wound healing response to hyaline cartilage damage (Freemont and Hoyland 2006). This alteration in matrix composition can cause additional problems; for example, the replacement of the flexible cartilaginous nucleus pulposus with the more rigid fibrocartilage during disc degeneration can cause fissure formation. The outer annulus fibrosus (AF) is predominantly formed of parallel collagen type I fibers which are inserted through the endplates into the upper and lower vertebrae (Risbud and Shapiro 2011). These collagen fibers lie between the AF lamellae in the inter-lamellar matrix. This matrix is comprised of a proteoglycan-rich gel, elastic fibers, elongated fibroblast-like cells and a cross-bridge network which interconnects the lamellae (Tavakoli, Elliott Dawn et al. 2016). The inner AF encircles the NP and, although similar to the outer AF, is more cartilaginous in structure with rounded cells and an increased proportion of both proteoglycan and collagen type II fibers (Rodrigues-Pinto, Richardson et al. 2014). The nucleus pulposus (NP) has a hyaline cartilage-like structure and, much like hyaline cartilage, provides the IVD with resistance to compression and tensile strength through its collagen fibril network and proteoglycan aggregates. Unlike hyaline cartilage however the nucleus pulposus contains a heterogeneous cell population formed of large vacuolated notochordal-like cells and smaller chondrocyte-like cells (Chan, Au et al. 2014). The NP matrix is comprised of randomly organised collagen fibers, radial elastin fibers and an aggrecan-rich gel, which becomes less gelatinous with age due to proteoglycan loss (Massey, van Donkelaar et al.

2012). These changes in matrix composition and those due to age and disease state will be discussed in greater detail in the following section.

1.4.3. Collagens

The collagens are a group of ubiquitously expressed structural proteins of which 28 types have thus far been described. They are the most abundant proteins in the cartilage extracellular matrix, comprising ~60% of its dry weight (Eyre 2004). Each collagen molecule is formed of three polypeptide α chains organised into a triple helix. These proteins can either be homotrimeric (in which each α chain is identical) or, more commonly, heterotrimeric (where each chain may be encoded by an individual gene) (Bella and Hulmes 2017). The triple helix is created through hydrogen bond formation between Xaa-Yaa-Gly triple helix motifs in which Xaa and Yaa can be a number of different amino acids (most often proline and hydroxyproline). These motifs are known as the collagenous (COL) domains and they are interspersed with a number of non-collagenous (NC) domains, such as a thrombospondin domain (Shoulders and Raines 2009). The collagen protein family is large and can be divided into a number of categories. More recent research has illustrated the important roles of even minor low abundant collagens in the cartilage ECM; however, for the purposes of this thesis only a small number of the fibrillar, network, beaded filament and FACIT collagens will be discussed (Bella and Hulmes 2017, Luo, Sinkeviciute et al. 2017) (Table 1).

1.4.3.1. Fibril-forming/fibrillar collagens

The collagen fibrillary network provides cartilage with structure and allows it to resist both tensile and shear stress. Fibrillar collagens are secreted as procollagens and are characterised by a large COL1 domain, a short COL2 domain and a trimeric C-terminal NC1 domain. They can then be divided into three clades according to their N-terminal structure. Clade A collagens (types I, II and III) have an additional von Willebrand factor type C (VWC) domain. The COL2 and VWC domains are cleaved off during processing, leaving the COL1 domain surrounded by two telopeptides which allow for crosslinking during fibril formation

Collagen	Structure	Relevant tissue location	Function
Fibril-forming (clade A)			
I	Heterotrimer	Bone	Structure, resistance to mechanical force
II	Homotrimer	Artic lar and hyaline cartil ge	Structure, resistance to mechanical force
III	Homotrimer	Artic lar cartil ge	Structure, response to ti sue injury, collagen I brillogenesis
Fibril-forming (clade B)			
V	Heterotrimer	Artic lar cartil ge, bone	Fibril nucleati n
XI	Heterotrimer	Cartil ge	Fibril nucleati n, ECM organisati n
Fibril-forming (clade C)			
XXIV	Homotrimer	Bone	Collagen I brillogenesis in early development, bril diameter regulatio
XXVII	Homotrimer	Proliferati e cartil ge	Structure, pericellular ECM organisati n, bone mineralisati n
Network forming			
IV	Heterotrimer	Artic lar cartil ge	Chondrocyte phenotype and survival
VI	Heterotrimer	Cartil ge, invertebral disc	Mechanotransduc on, chondrocyte a achment
VIII	Homo/ heterotrimer	Perichondrium, periosteum, cartil ge, calvarium	Response to ti sue injury
X	Homotrimer	Hypertrophic and calcifying cartil ge	Hypertrophy and bone mineralisati n
FACIT			
IX	Heterotrimer	Cartil ge	Collagen brillogenesis, ECM organisati n
XII	Homotrimer	Perichondrium, bone	Mechanical proper es and organisati n of collagen I fi rils
XIV	Homotrimer	Artic lar cartil ge, invertebral disc	Collagen I brillogenesis in early development, di erentiati , mechanical stress
XVI	Homotrimer	Cartil ge	Di erenti tio , cell adhesion, proliferatio , focal adhesion
XX	Homotrimer	Sternal cartil ge	Possible cytokine receptor
XXII	Homotrimer	Artic lar cartil ge	Fibrillogenesis, cell adhesion, osteogenesis, mechanical stress
Transmembrane			
XIII	Homotrimer	Chondrocytes	Cell adhesion

Table 1 Collagens of the musculoskeletal ECM

(Bella and Hulmes 2017). Clade B is comprised of the minor fibril-forming collagens (types V and XI) which have an N-terminal thrombospondin domain. Their processing differs from clade A collagens as the N-terminal domains are only partially cleaved and the C-terminal propetide is removed. The resultant structure is thought to help in fibril diameter regulation (Bella and Hulmes 2017). Clade C collagens are structurally quite different from other fibrillar collagens and form thin, non-striated fibrils (Koch, Laub et al. 2003, Plumb, Dhir et al. 2007). They consist of a short interrupted COL1 domain and non-helical NC1 domain. The C-terminal region is removed during processing to mature collagen but the N-terminal region is retained (Bella and Hulmes 2017). Collagen type XXVII is expressed in the pericellular matrix of both proliferating chondrocytes, where it is thought to regulate ECM organisation and hypertrophic chondrocytes, where it is associated with bone mineralisation (Hjorten, Hansen et al. 2007, Plumb, Dhir et al. 2007, Plumb, Ferrara et al. 2011, Ricard-Blum 2011).

1.4.3.2. Fibril-associated collagens with interrupted triple helices (FACIT)

The FACIT collagens, as their name suggests, associate with the collagen fibril surface and have a number of interruptions in their triple helix domain. In addition to this, FACIT collagens also have great variation in the number of COL domains (2-10) an N-terminal thrombospondin domain and a diverse number of other NC domains (Ricard-Blum 2011). The main FACIT collagen in cartilage is the heterotrimeric collagen type IX which is predominantly expressed by proliferative chondrocytes and covalently links to collagen type II/XI fibrils via its NC-1 domain (Eyre, Pietka et al. 2004). Mutations in the genes encoding the three α(IX) chains (*COL9A1*, *COL9A2* and *COL9A3*) have been shown to cause multiple epiphyseal dysplasia (Paassilta, Lohiniva et al. 1999, Czarny-Ratajczak, Lohiniva et al. 2001, Jackson, Marcus-Soekarman et al. 2010).

1.4.3.3. Network-forming collagens

The network-forming collagens retain their C-terminal NC domains during processing (Khoshnoodi, Cartailler et al. 2006). The homotrimeric collagen type X is the predominant

collagen expressed in the hypertrophic zone, where it forms pericellular hexagonal networks and has an important role in endochondral ossification (Kwan, Cummings et al. 1991, Shen 2005). Collagen type X is also implicated in bone mineralisation through annexin V-mediated binding to mineral and alkaline phosphatase-containing matrix vesicles, which calcify the matrix (Kirsch and Pfaffle 1992). Mutations in the *COL10A1* gene cause Schmid metaphyseal chondrodysplasia (MCDS) (Chan, Weng et al. 1998) and Spondylometaphyseal dysplasia (SMD) (Ikegawa, Nishimura et al. 1998). Collagen type VI is a heterotrimeric beaded filament collagen which, unlike other collagens, is assembled into aggregates before secretion (Cescon, Gattazzo et al. 2015). It is able to interact with a number of ECM molecules including matrilins and small leucine-rich proteoglycans (SLRPs) (Wiberg, Klatt et al. 2003) and forms a microfibrillar network in the pericellular matrix. This network has roles in chondrocyte attachment to the matrix and mechanotransduction in response to osmotic stress (Marcelino and McDevitt 1995, Zelenski, Leddy et al. 2015). The importance of this is illustrated by the collagen VI null mouse which has joint degeneration, delayed bone age, altered osteoblast morphology, ostepenia and reduced mineralisation (Alexopoulos, Youn et al. 2009, Christensen, Coles et al. 2012, Izu, Ezura et al. 2012).

1.4.3.4. Collagen fibril structure

Collagen fibrils are heterotopic, composed of many different collagenous and non-collagenous molecules (Bruckner 2010). Collagen type II is the predominant fibrillar collagen in the cartilage extracellular matrix, making up 95% of the total collagen present and most of the collagen fibril superstructure (Figure 6). The remainder of the structure consists of collagen type XI microfibrils which nucleate assembly and regulate lateral fibril growth (Bruckner 2010). The ratio of collagen II and XI is therefore essential in order to assemble fibrils of the correct length and width. In immature cartilage this process is enhanced by the presence of collagen type IX which also provides the fibrils with a negatively charged surface (due to its attached dermatan sulfate chains) and stabilises the fibrillar network by binding to a number of non-collagenous ECM proteins, such as COMP via its NC4 (thrombospondin) domain (Blaschke, Eikenberry et al. 2000, Bruckner 2010, Acharya, Yik et al. 2014). The important role of collagen IX is further demonstrated by the null mouse which has altered

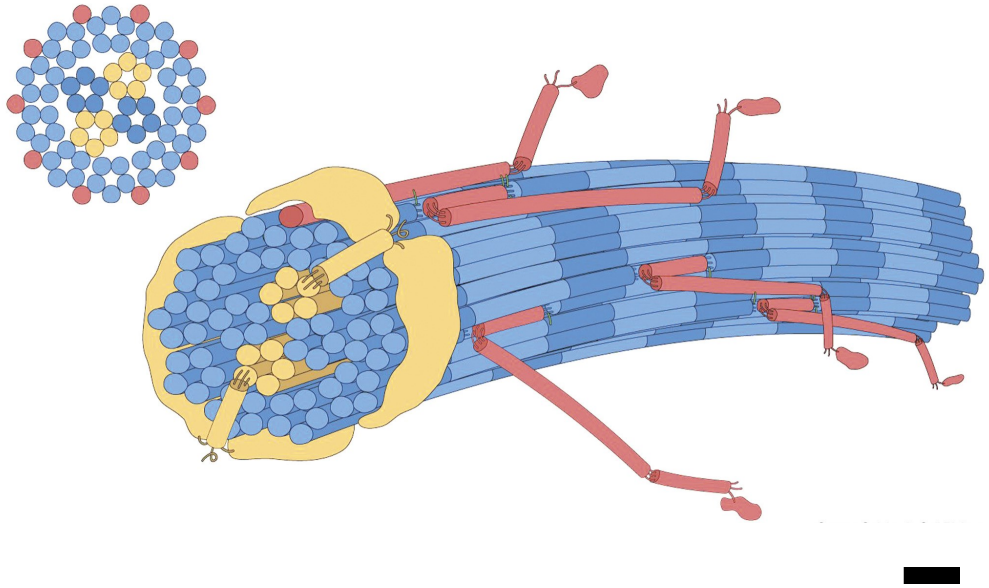

Figure 6 Collagen fibril structure

The main collagen fibrils of the extracellular matrix are predominantly comprised of collagen type II with attached collagen type XI microfibrils and collagen type IX.

Blue, type II collagen; Yellow, type XI collagen; Red, type IX collagen; scale bar = 4nm (Kadler, Hill et al. 2008).

chondrocyte morphology (Brachvogel, Zaucke et al. 2013). In addition to those collagens mentioned, fibril assembly can also be affected by non-collagenous proteins, including matrilins, perlecan and SRLPs (Svensson, Aszodi et al. 2002, Wiberg, Klatt et al. 2003, Douglas, Heinemann et al. 2006, Kvist, Johnson et al. 2006). This illustrates the complexity of collagen fibrillogenesis and the number of molecules required for correct organisation. As an example, tenascin X has been shown to not only regulate the rate of fibril assembly but fibril packing density (Mao, Taylor et al. 2002, Egging, van den Berkmortel et al. 2007). As skeletal development continues and the fibrils move further towards the territorial matrix the composition of fibrils alters with a decrease in collagen type IX abundance and an increase in the proportion of decorin (which is also dermatan sulfated). It is hypothesised that this assists in the fusion of immature fibrils to form the larger fibrils found in the interterritorial matrix (Bruckner 2010). Interestingly, during articular cartilage maturation the proportion of collagen type XI also decreases as it is slowly replaced by collagen type V. In addition to this, the abundance of collagen type III also increases in damaged areas of cartilage where it is cross-linked to the collagen II fibrils, providing additional structural support to a weakened collagen network (Wu, Weis et al. 2009, Wu, Weis et al. 2010).

1.4.4. Glycoproteins

The non-collagenous glycoproteins fulfil the role of adaptor proteins in the extracellular matrix (along with the small proteoglycans) and connect the fibrillar collagen network with the proteoglycan aggregates to stabilise the extracellular matrix (Zaucke 2016) (Table 2). Furthermore, they have also been implicated in collagen fibrillogenesis, cell-cell and cell-matrix interactions and growth factor binding (Svensson, Aszodi et al. 2002, Haudenschild, Hong et al. 2011). There are a great number of glycoproteins in the ECM (Zaucke 2016) including chondroadherin (Hessle, Stordalen et al. 2014) and von Willebrand factor A-domain-related protein (WARP) (Hansen, Allen et al. 2012).

Glycoprotein	Function
Thrombospondins	
TSP-1	Cell-cell and cell-matrix interactions, angiogenesis
TSP-2	Collagen fibrillogenesis, chondrocyte differentiation
TSP-3	Unknown
TSP-4	Cell-matrix interaction, articular chondrocyte phenotype
TSP-5/COMP	Collagen fibrillogenesis, growth factor binding
Matrilins	
Matrilin 1/CMP	Cell attachment, ECM organisation
Matrilin 3	ECM organisation, growth factor binding
Fibulins	
Fibulin 1	Cell adhesion
Fibulin 2	Integrin-mediated cell adhesion and migration
Fibulin 3	Chondrocyte differentiation
Proteoglycans	
Asporin	(See table 3)
PRELP	(See table 3)
Perlecan	(See table 3)
Other glycoproteins	
WARP	ECM organisation
Chondroadherin	Cell-cell and cell-matrix interactions
CILP	TGFβ-binding
Fibronectin	Cell-matrix interaction
Laminin	Chondrocyte phenotype and survival
Nidogen	Chondrocyte phenotype and survival
Tenascin C	Development, cartilage repair

Table 2 Glycoproteins of the musculoskeletal ECM

1.4.4.1. The Thrombospondins: Cartilage oligomeric matrix protein

The thrombospondin (TSP) family is a group of five matricellular proteins, of which TSP5 or cartilage oligomeric matrix protein (COMP) is the best characterised of those found in cartilage (Tan and Lawler 2009). It is a 552kDa glycoprotein (Oldberg, Antonsson et al. 1992) which exists as a homopentamer (Morgelin, Heinegard et al. 1992) and is expressed in several tissues including skeletal muscle, tendon, synovium, skin and ligament (DiCesare, Hauser et al. 1994, DiCesare, Morgelin et al. 1994, Di Cesare, Carlson et al. 1997). The exact function of COMP is not fully known; however, it is thought to act as a bridging molecule in the cartilage ECM, interacting with many ECM proteins including aggrecan, matrilin3, fibronectin and collagen type II and IX (Di Cesare, Chen et al. 2002, Mann, Ozbek et al. 2004, Chen, Herndon et al. 2007, Acharya, Yik et al. 2014). Further to this, it has also been implicated in collagen fibrillogenesis (Halasz, Kassner et al. 2007) cell attachment, growth factor binding and the complement system (Chen, Thomas et al. 2005, Tan, Duquette et al. 2009). The COMP gene is comprised of 19 exons encoding an N-terminal oligomerisation domain, 4 Type II (epidermal growth factor-like) repeats, 8 TSP Type III repeats and a C-terminal globular domain (Oldberg, Antonsson et al. 1992). Mutations in the C-terminal domain and Type III repeats have been shown to cause the skeletal dysplasias pseudoachondroplasia and multiple epiphyseal dysplasia (Briggs, Hoffman et al. 1995, Deere, Sanford et al. 1998, Jackson, Mittaz-Crettol et al. 2012, Briggs, Brock et al. 2014). The COMP null mouse has no skeletal phenotype, indicating that other members of the TSP family may compensate for its absence (Svensson, Aszodi et al. 2002). This finding strongly suggests that the disease pathology caused by COMP mutations is due to the effects of the mutant protein itself rather than a loss of protein (antimorphic or dominant-negative effect).

1.4.4.2. The Matrilins

The matrilins are a family of four oligomeric matrix proteins comprised of varying arrangements of von Willebrand factor-like (VWA) and EGF-like domains which form either trimers (MATN1/4) or tetramers (MATN2/3) through an oligomerisation domain. Matrilin 1 and 3 are also able to form both homo- and hetero-oligomers (Kleemann-Fischer, Kleemann

et al. 2001). The two predominant matrilins in cartilage are matrilin 1 and 3 (Klatt, Becker et al. 2011) although only matrilin 4 is present in the superficial layer of articular cartilage (Klatt, Paulsson et al. 2002). There is also some redundancy in function as the characterisation of single and double matrilin 1 and 3 null mice indicates that other matrilin family members may try to compensate for their loss in the cartilage ECM (Nicolae, Ko et al. 2007). Matrilins are thought to act as adaptor proteins within the matrix, connecting the aggrecan-hyaluronan aggregates with the collagen fibrillar network. Matrilins 1, 3 and 4 are able to form complexes with the small leucine-rich proteoglycans (SLRPs) biglycan and decorin, which then interact with collagen type VI microfibrils. The matrilins then bind to aggrecan or collagen type II fibrils, forming a matrilin-SLRP bridge between these large structures and the collagen type VI microfibrils (Wiberg, Klatt et al. 2003). Matrilin 3 is also able to bind a number of other proteins, including type IX collagen (Budde, Blumbach et al. 2005). In addition to this, the matrilins have a high binding affinity for another adaptor protein, COMP, which is also able to interact with aggrecan and collagens type II and IX (Thur, Rosenberg et al. 2001, Chen, Herndon et al. 2007, Otten, Hansen et al. 2010). Thus far, no causative mutations for skeletal disorders have been found in matrilin 1; however, a number of polymorphisms are associated with susceptibility to mandibular prognathism, osteoarthritis and idiopathic scoliosis in certain ethnic populations (Meulenbelt, Bijkerk et al. 1997, Strusberg, Sembaj et al. 2002, Jang, Park et al. 2010, Zhang, Zhao et al. 2014). This may be explained by recent research which highlighted a possible mechanotransduction role. Matrilin 1-null mice exhibited a reduced anabolic gene expression response to mechanical loading and had increased articular surface damage when subjected to the surgical destabilization of the medial meniscus (DMM) osteoarthritis model, indicating its protective role against mechanical stress (Chen, Cossman et al. 2016). Matrilin 3 polymorphisms are also associated with a predisposition to osteoarthritis (Min, Meulenbelt et al. 2006) and antimorphic missense mutations are implicated in a range of skeletal disorders, including spondyloepimetaphyseal dysplasia and multiple epiphyseal dysplasia (Chapman, Mortier et al. 2001, Borochowitz, Scheffer et al. 2004). In addition to the previously discussed functions, matrilin 3 is also thought to play an important role in cartilage homeostasis, chondrocyte proliferation and hypertrophy, due to its role in Sox9, TGF-β and BMP2 signalling and upregulation of osteoarthritis-associated genes for MMPs and pro-inflammatory cytokines such as MMP13 (Klatt, Klinger et al. 2009, Yang, Trehan et al. 2014, Zhang, Ji et al. 2015,

Muttigi, Han et al. 2016). Furthermore, the removal of either matrilin 1 or 3 from the pericellular matrix reduced the chondrocyte's response to mechanical loading, decreasing mechanically induced IHH signalling, proliferation and differentiation (Kanbe, Yang et al. 2007).

1.4.5. Proteoglycans and glycosaminoglycans

The proteoglycans form around 10% of the cartilage extracellular matrix and form aggregates which allow the tissue to resist compression and distribute mechanical load. Further to this, they also have roles in matrix assembly and innate immunity through their interaction with Toll-like receptors (TLRs) and the complement pathway (Orlowsky and Kraus 2015). Proteoglycans are comprised of a protein core and a mixture of attached glycosaminoglycan (GAG) chains, such as dermatan sulfate (DS) heparan sulfate (HS) keratin sulfate (KS) and the predominant chondroitin sulfate (CS) (Knudson and Knudson 2001). DS, HS and CS are all attached to the protein core by the serine residue in a serine-glycine motif via a tetrasaccharide linker whereas KS is either N or O-linked (to serine or threonine residues). The composition of these sulfate chains can have a great effect on proteoglycan function; for example, heparan sulfate is well-known to sequester growth factors (Vlodavsky, Bar-Shavit et al. 1991). The important GAG hyaluronan is unusual as, unlike the others mentioned, it is not attached to a protein core and is released by transmembrane hyaluronan synthases into the extracellular matrix (Aspberg 2016). Once in the ECM it interacts with a number of cell surface receptors such as CD44 and forms aggregates with large proteoglycans like aggrecan (Misra, Hascall et al. 2015). Proteoglycans are implicated in both chondrogenesis and post-natal skeletal development and this section will highlight a few of the most important (Table 3).

1.4.5.1. Small leucine-rich proteoglycans (SLRPs)

The small leucine-rich proteoglycans are regulators of extracellular matrix assembly due to their ability to binds collagens (Aspberg 2016) and include fibromodulin, epiphycan and chondroadherin (Iozzo and Schaefer 2015). They consist of a leucine-rich repeat (LLR) region,

Proteoglycan	Main GAG	Location	Function
Class I SLRPS			
Biglycan	CS	Extracellular	Bone mineralisatio , osteoblast di erentiati , infl mmati n, angiogenesis, collagen brillogenesis, cell growth
Decorin	DS		Cell growth, collagen brillogenesis, angiogenesis, autophagy, immunity, infl mmatio
Asporin			Bone mineralisatio , chondrogenesis, growth factor binding
Class II SLRPS			
Fibromodulin	KS	Extracellular	Possible growth factor sequestratio , collagen brillogenesis,
PRELP			Osteclast formati n, complement ac vati n, ECM organisati n
Keratocan			Osteogenesis, infl mmati n
Lumican	KS		Collagen fi rillogenesis, infl mmatio
Osteoadherin			Bone mineralisatio , osteoblast a achment
Class III SLRPS			
Epiphycan	DS/CS	Extracellular	Chondrogenesis, growth plate organisati n
Opti in			Angiogenesis
Osteoglycin			Collagen brillogenesis
Class IV SLRPS			
Chondroadherin		Extracellular	Collagen brillogenesis
Pericellular and basement membrane			
Perlecan	HS	Pericellular/ extracellular	Cell adhesion, cell death, endochondral bone formatio , growth factor regulatio , car lage biomechanics, angiogenesis, collagen
Modular (hyalectans/lecticans)			
Aggrecan	CS	Extracellular	Carti age development and homeostasis, growth factor seques-tratio , proliferatio , cell adhesion, cell-matrix interactio
Versican	CS		Growth factor sequestratio , cell adhesion, infl mmati n
Transmembrane			
Syndecan 1-4	HS	Cell surface	Morphogen regulatio , growth factor regulatio , angiogenesis
CSPG4	CS		Cell migratio , proliferatio , proteolyti ac vity, apoptosis
Betaglycan	CS/HS		Carti age development and homeostasis
GPI-anchored			
Glypican 1-6	HS	Cell surface	Morphogen regulatio , angiogenesis, car lage development
Intracellular			
Serglycin	Heparin	Intracellu-lar/cell sur-face	Cell adhesion, MMP expression, infl mmati n, growth factor regulatio

Table 3 Proteoglycans of the cartilage ECM

stabilised by N- and C-terminal cysteine bridges (Aspberg 2016). They are divided into five classes according to their structure and are either canonical (classes I-III, leucine-rich repeat cysteine capping (LRRCE) motif, long leucine-rich repeats) or non-canonical (classes IV-V, leucine-rich repeat C-terminal (LRRCT) motif). They can be further subdivided according to their attached sulfate chains: chondroitin (class III) dermatan (class I, III) keratan (class II, III) or none at all (class III-V) (Knudson and Knudson 2001). SLRPs are able to regulate collagen fibril diameter and polymerisation rate, binding to the fibrils by leucine-rich repeats as they form (Douglas, Heinemann et al. 2006). After this some SLRPs remain bound to the collagen fibrils, acting as a bridge with other molecules and protecting against fibril degradation. In addition to this, they are implicated in growth factor regulation, cell growth, inflammation, bone formation and innate immunity (Yamaguchi and Ruoslahti 1988, Merline, Moreth et al. 2011, Grafe, Yang et al. 2014, Iozzo and Schaefer 2015). The best characterised SLRP is the class I decorin which is mainly associated with collagen type I and II fibrillogenesis (Robinson, Sun et al. 2017). Indeed, decorin deficient mice are reported to have irregular collagen fibrils resulting in skin fragility (Danielson, Baribault et al. 1997). It is strongly expressed in growth plate cartilage and has been found to increase with age in the interterritorial matrix of articular cartilage (Del Santo, Marches et al. 2000). Decorin is able to bind to its ligands via both the protein core and its attached chondroitin and dermatan sulfate chains, which allows it to interaction with a vast number of ligands. Decorin is therefore able to affect several signalling pathways, ECM molecule processing and growth factor sequestration. As an example, it is able to affect cell proliferation via its ability to bind TGF-β (Gubbiotti, Vallet et al. 2016).

1.4.5.2. Hyalectans

The hyalectans or lecticans are a group of chondroitin sulfate proteoglycans which include versican and neurocan. The major lectican proteoglycan in the cartilage ECM is aggrecan which forms large aggregates with cartilage link protein and hyaluronan (Hardingham and Fosang 1992). Aggrecan (in conjunction with the other proteoglycans) provides the tissue with its resistance to compression as its large fixed negative charge attracts ions and water molecules, allowing the cartilage to withstand the high mechanical load in the skeletal joint (Aspberg 2012). This important proteoglycan will be discussed in greater detail in section 1.4.8. Versican is structurally very similar to aggrecan and is expressed as a number

of isoforms, depending on tissue and disease state (Iozzo and Schaefer 2015). It has a tightly regulated dynamic expression pattern suggestive of important roles in early limb patterning, joint morphogenesis and nerve patterning (Snow, Riccio et al. 2005). After early development, expression levels of versican decrease and it is mainly confined to the interterritorial matrix of growth plate and articular cartilage where it forms aggregates with link protein and hyaluronan (Matsumoto, Kamiya et al. 2006). Versican is also able to bind other ECM proteins, including tenascins, fibulins and a number of cell surface molecules. Such a variety of binding partners allows this diverse proteoglycan to be involved in processes such as proliferation, migration, adhesion, inflammation and cell phenotype (Wu, Pierre et al. 2005, Wight, Kang et al. 2014, Wight, Kinsella et al. 2014).

1.4.5.3. Pericellular and basement membrane proteoglycans

Proteoglycans in this category are either present in a basement membrane or anchored to the cell surface and most are heparan sulfated (Iozzo and Schaefer 2015). Perlecan is a non-hyaluronan binding heparan sulfate proteoglycan which is expressed in a wide variety of tissues. In cartilage it is mainly localised to the pericellular and inter-territorial matrix in the pre-hypertrophic and hypertrophic zones (SundarRaj, Fite et al. 1995) and is implicated in growth factor sequestration and cell-matrix interaction (Chang, Tseng et al. 2015). Perlecan null mice are embryonic lethal with a wide variety of phenotypic features in the heart, brain and cartilage, including growth plate disorganisation, reduced bone mineralisation and an altered collagen fibril network. This research suggests that perlecan is essential for growth plate organisation (Costell, Gustafsson et al. 1999). In humans, mutations that lead to a reduction in the amount of functional perlecan have been shown to cause lethal dyssegmental dysplasia, Silver-Handmaker type (DSSH) (Arikawa-Hirasawa, Wilcox et al. 2001) and Schwartz-Jampel syndrome (SJS) (Arikawa-Hirasawa, Le et al. 2002).

1.4.5.4. Transmembrane and GPI-anchored proteoglycans

The transmembrane and GPI-anchored proteoglycans are cell surface proteins and, apart from phosphacan and CSPG4, all are predominantly heparan sulfated (Iozzo and

Schaefer 2015). The glypicans are GPI-anchored proteoglycans with a range of functions, including hedgehog signalling regulation (Filmus and Capurro 2014). In the case of glypican 3 a loss of function mutation has been shown to alter hedgehog signalling and lead to Simpson–Golabi–Behmel syndrome, a condition with a broad phenotypic spectrum including craniofacial abnormalities (Filmus and Capurro 2014). Many of the transmembrane proteoglycans belong to the syndecan family, cell surface receptors with a vast array of ligands including growth factors, ECM proteins, cytokines and cell-cell adhesion receptors. This ability to bind such a wide variety of proteins and their capability for extracellular domain shedding means that syndecans are involved in angiogenesis, inflammation, ECM organisation and many other biological processes (Choi, Chung et al. 2011).

1.4.6. Aggrecan

The chondroitin sulphate proteoglycan aggrecan is also known as chondroitin sulfate proteoglycan core protein 1 (CSPG1) and is expressed in several tissues, including the brain (Kwok, Dick et al. 2011, Morawski, Bruckner et al. 2012). It is the founding member of the lectican protein family which includes versican, brevican and neurocan and is 2.5MDa in size (Ruoslahti 1996). It consists of a 250kDa protein core and approximately 100 chondroitin sulfate glycosaminoglycan and 30 keratan sulfate chains attached to a large domain between the 3 globular domains of the core (Wiedemann, Paulsson et al. 1984) (Figure 7). Aggrecan is the predominant proteoglycan of the extracellular matrix, has a short half-life of 3.4 years (in its uncleaved form) and is found in the pericellular, interterritorial and territorial matrix (Poole, Pidoux et al. 1982, Maroudas, Bayliss et al. 1998). It is involved in many biological processes essential for normal cartilage growth such as chondrocyte differentiation, proliferation and survival, growth factor binding and regulatory signalling (Lauing, Cortes et al. 2014). Its key role, however, is in its ability to form large sulfated aggregates with cartilage link protein and hyaluronan, allowing the cartilage to resist compression forces (Roughley and Mort 2014).

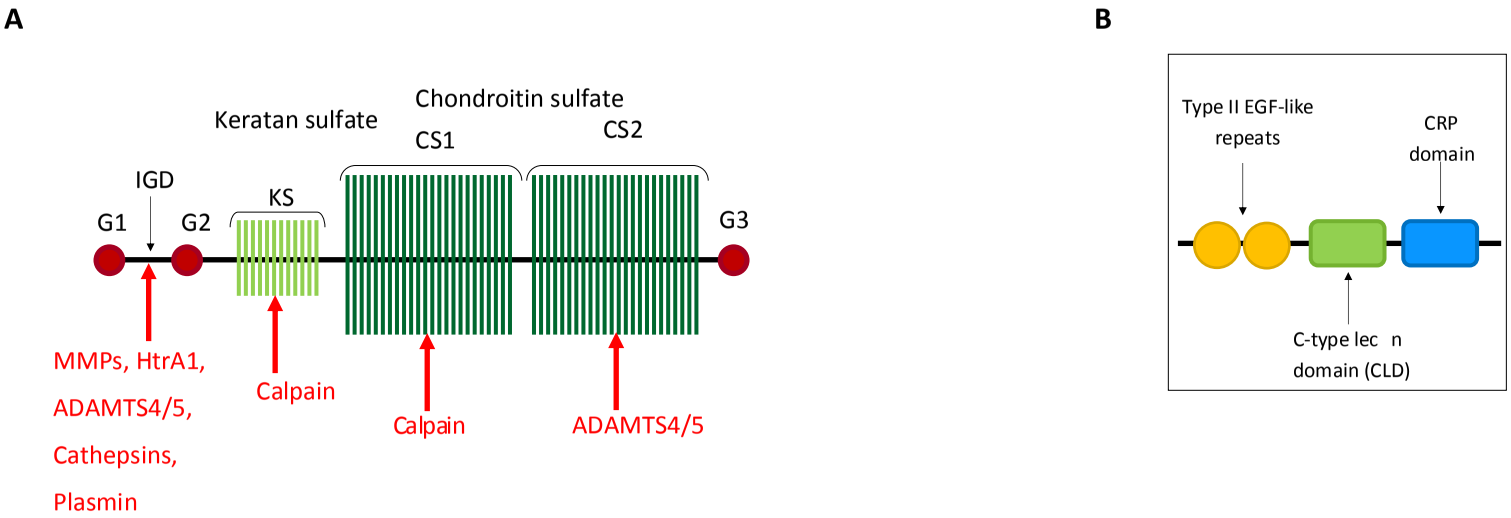

Figure 7 The structure of aggrecan

(A) The aggrecan protein is comprised of three globular (G) domains, an interglobular domain, a keratan sulfate-attachment region and two chondroitin sulfate-attachment domains. A selection of proteinases and their approximate proteolytic cleavage sites are depicted in red. **(B)** The G3 domain of aggrecan is composed of two Type II EGF-like repeats, a C-type lectin domain (CLD) and a complement regulatory protein (CRP) domain.

1.4.6.1. Gene structure and expression pattern

The human aggrecan (*ACAN*) gene is found on chromosome 15 and is comprised of 19 exons. Exon 1 is non-coding and exons 2 to 19 encode an N-terminal globular domain (G1) a second globular domain (G2) two interglobular domains and a C-terminal selectin-like globular domain (G3) (Figure 5C) which is subject to alternative splicing (Doege, Sasaki et al. 1991). Aggrecan is expressed in development after mesenchymal condensation and throughout the growth plate during post-natal growth. Chondrocytes in the resting zone express low levels of aggrecan which increases significantly as the cells proliferate and then decreases as they enter a mature hypertrophic state (Domowicz, Cortes et al. 2009).

1.4.6.2. Protein structure and function

The N-terminal G1 domain is encoded by exons 3-6 and consists of a 100 amino acid immunoglobulin-like repeat (A subdomain) and two cysteine-rich proteoglycan tandem repeats (B and B' subdomains) (Kiani, Chen et al. 2002). The interaction of these three disulphide-bonded subdomains allows the formation of proteoglycan aggregates through the binding of the G1 domain to hyaluronan and link protein. The protein sequences of the G1 domain and cartilage link protein are very homologous (Doege, Sasaki et al. 1987) and these large aggregates are arranged as a single hyaluronan filament bound to several aggrecan proteins. Both the B and B' subdomains are required to bind to hyaluronan and this non-covalent binding appears to be enhanced by the A subdomain (Watanabe, Cheung et al. 1997). The A subdomain also binds to link protein (Matsumoto, Shionyu et al. 2003) which then binds to hyaluronan, stabilising the aggregate (Roughley and Mort 2014). This aggregation does not occur immediately upon aggrecan's secretion but is delayed depending on G1 maturation (immature cartilage forms aggregates more readily) and abundance of link protein (Vincent 2000) possibly to allow aggrecan to move past the chondrocyte's HA coat and into the ECM before aggregation occurs (Roughley and Mort 2014). Furthermore, an inbalance in the ratio of aggrecan to link protein (by overexpression of either the G1 domain or link protein) has been shown to reduce cell adhesion (Cao, Zhang et al. 1998). The presence of an immunoglobulin-like repeat (A subdomain) in the G1 also suggests that this

domain may have a role in cell attachment and survival, as the majority of proteins with similar immunoglobulin hypervariable regions are important for cell recognition and adhesion (Kiani, Chen et al. 2002).

The interglobular domain (IGD) is coded by exon 7 and resides between the G1 and G2 domains (Valhmu, Palmer et al. 1995). It has an important role in aggrecan turnover as it contains a large number of proteinase cleavage sites (Figure 5C). The G2 domain is coded by exons 8-10 and is unique in the lectican protein family as it is only found in aggrecan. It consists of two proteoglycan tandem repeats, similar to those in the G1 domain, but is not able to bind to hyaluronan or link protein (Fosang and Hardingham 1989, Valhmu, Palmer et al. 1995). Little is known about this domain's function but it is highly conserved and has been shown to inhibit protein secretion, suggesting it is likely to play an important role, possibly in protein quality control (Kiani, Lee et al. 2001, Aspberg 2012).

The G2 domain is then followed by GAG-attachment regions, a keratan sulfate (KS)-rich domain and two chondroitin sulfate domains (CS1 and CS2) (Wiedemann, Paulsson et al. 1984, Doege, Sasaki et al. 1991) which are coded by exons 11-12. The KS-rich domain is comprised of proline-serine sequences within repeats of six amino acids. These serine residues can attach to O-linked oligosaccharides which act as the keratan sulfate linkage regions. KS chains have been shown to interact with collagen fibrils and appear to have a protective role in OA pathogenesis. However, the number of KS repeats varies quite considerably between species (rat aggrecan has no keratan sulfate chains) and so keratan sulfation, although useful, is perhaps not essential for basic aggrecan function (Lohmander, Yoshihara et al. 1996, Guerassimov, Zhang et al. 1999, Hedlund, Hedbom et al. 1999). Both the CS1 and CS2 domains consist of amino acid repeats containing serine-glycine sequences which can attach to chondroitin-6- and chondroitin-4-sulfate (Roughley and Mort 2014). These three regions are functionally very important as it is the addition of GAG chains that provides aggrecan with its large anionic charge (Valhmu, Palmer et al. 1995). The importance of these sulfate chains in the growth plate is also illustrated by a number of skeletal dysplasia disorders and animal models with defects in chondroitin sulfate synthesis or sulfation (Faiyaz ul Haque, King et al. 1998). Consistency in the number of chondroitin sulfate chains is not, however, required for relatively normal aggrecan function as the number of these amino acid repeats (and so chondroitin sulfate chains) varies within a population (between 13 and 33).

Interestingly, this variable number tandem repeat (VNTR) is only found in humans (Doege, Coulter et al. 1997).

The large C-terminal G3 domain is encoded by the remaining 13-19 exons of the aggrecan gene. It consists of two Type II (epidermal growth factor-like) repeats (Baldwin, Reginato et al. 1989) a C-type lectin domain (CLD) and a complement regulatory protein domain (CRP) (Doege, Sasaki et al. 1987) (Figure 7B). The CLD domain is constitutively expressed but the remaining domains are modulated with alternative splicing (Baldwin, Reginato et al. 1989, Doege, Sasaki et al. 1991, Fulop, Walcz et al. 1993, Grover and Roughley 1993, Bonaventure, Kadhom et al. 1994, Fulop, Cs-Szabo et al. 1996) which is thought to modify binding interactions with other ECM molecules (Day, Olin et al. 2004). This also varies between species as most animals (except humans) do not express the EGF1 subdomain (Fülöp, Cs-Szabó et al. 1996). The CLD domain of the lectican protein family interacts in a calcium-dependent manner with extracellular matrix molecules that contain EGF repeats, such as fibrillins (Isogai, Aspberg et al. 2002) fibulins (Aspberg, Adam et al. 1999, Olin, Morgelin et al. 2001) and tenascins (Aspberg, Miura et al. 1997, Rauch, Clement et al. 1997). The role of the other domains is currently unclear but the entire G3 domain has been implicated in aggrecan secretion (Kiani, Lee et al. 2001) cell adhesion (Miura, Aspberg et al. 1999) proliferation (Zhang, Cao et al. 1998) and organisation of the proteoglycan aggregates within the matrix (Olin, Morgelin et al. 2001, Lundell, Olin et al. 2004). The G3 domain has also shown binding affinity with a number of proteins, including connective tissue growth factor (CCN2) (Aoyama, Hattori et al. 2009).

1.4.6.3. Folding, post-translation modification and trafficking

The aggrecan core protein undergoes post-translational modification. After synthesis of the initial polypeptide, N-linked mannose-rich oligosaccharides are added co-translationally in the rough endoplasmic reticulum. The importance of this modification is illustrated by a number of animals models with defects in aggrecan N-linked glycosylation (Aspberg 2012). Quality assured protein folding within the endoplasmic reticulum (ER) is regulated by a range of molecular chaperones. Although the exact mechanism is not known, a number of chaperones have been suggested including binding immunoglobulin protein (BIP) proline disulfide isomerase (due to aggrecan's numerous disulfide bonds) heat shock

protein 25 (HSP25) (as it can bind the G3 domain) HSP70, calnexin and calreticulin (due to the N-linked oligosaccharides) (Zheng, Luo et al. 1998, Luo, Guo et al. 2000, Chen, Wang et al. 2001). After folding, in order to begin the addition of chondroitin sulfate chains, xylosylation occurs in the late endoplasmic reticulum compartment and cis Golgi (Vertel 1995). As the modified aggrecan core protein transitions through the cis and medial Golgi, glycosyltransferases add sugars in a sequential manner. These linkage chains are then extended and sulfated to form chondroitin sulfate chains. O-linked oligosaccharides are also added during O-linked glycosylation in the late Golgi with some extended and sulfated to form keratan sulfate chains (Luo, Gao et al. 2000, Kiani, Chen et al. 2002). As the cartilage matures several changes in sulfation occur. The length of chondroitin sulfate chains decreases from ~66 at birth to ~14 repeats in adulthood. Furthermore, the composition of the attached monosaccharides alters, increasing the proportion of 6-O-sulfation compared to 4-O-sulfation over time (Plaas, Wong-Palms et al. 1997). As this occurs, the keratan sulfate chains increase in length with increased sulfation of the galactose residues (Santer, White et al. 1982). The composition of the attached sulfated chains is variable and may be altered in a disease state (Heinegard 2009).

1.4.6.4. Degradation and turnover

Aggrecan turnover occurs as part of general cartilage homeostasis at different rates depending on its position in the matrix, as the turnover rate is much higher in the pericullar and territorial matrix compared to the interterritorial (Mok, Masuda et al. 1994). This aggrecan degradation leads to an accumulation of aggrecan fragments over time (Dudhia, Davidson et al. 1996). Interestingly, despite the apparent importance of the G3 domain and its conservation between species, its abundance decreases with age, relative to the other aggrecan domains. This was shown to be independent of normal aggrecan turnover and possibly due to proteolytic degradation (Dudhia, Davidson et al. 1996). This raises interesting questions about the function of the G3 domain in the ECM and disease, especially as the G3 cleavage product has a 6-fold longer half-life than the uncleaved aggrecan molecule (Maroudas, Bayliss et al. 1998) and the CLD subdomain is able to activate both the classical and alternate complement pathways, implicating aggrecan in joint inflammation (Melin Fürst, Mörgelin et al. 2013). The aggrecan aggregate can undergo degradation by a number of methods, including proteolytic cleavage and non-enzymic glycation and the aggrecan core

protein contains several proteolytic cleavage sites (Figure 7A). These sites are subject to various enzymes including serine proteases (HtrA1, plasmin) aspartic proteinases (Cathepsin K, D and B) and cysteine proteases (calpain) (Fosang, Neame et al. 1992, Sandy and Verscharen 2001, Troeberg and Nagase 2012). It is thought that the proteolytic cleavage of aggrecan can exert both a protective and a pathogenic effect. Cleavage mediated by the matrix metalloproteinases (MMPs) appears to be involved (but not essential) in cartilage homeostasis and protects against arthritic changes. In contrast, the a disintegrin and metalloproteinase with thrombospondin motifs (ADAMTS) aggrecanases (ADAMTS 4 and 5) are associated with increased GAG loss, decreased aggrecan functionality (and so cartilage destruction) in degenerative diseases such as osteoarthritis (Clements, Price et al. 2003, Little, Meeker et al. 2005, Sandy 2006, Boeuf, Graf et al. 2012). GAG loss may also occur due to non-enzymic glycation which increases with age, modifying lysine residues in the G1 domain, altering hyaluronan binding and either preventing or reducing aggregation (Verzijl, DeGroot et al. 2001, Roughley and Mort 2014).

1.5. Aggrecan-related skeletal dysplasias

The skeletal dysplasias are a complex group of 481 (Chen, Jiang et al. 2016) disorders of cartilage and bone with a combined incidence of 1 in 5000 (Geister and Camper 2015). The diagnosis of these disorders is based on clinical and radiographic findings and precise classification is often difficult. As discussed previously in this chapter, mutations in several extracellular matrix proteins have been implicated as the genetic cause of these conditions; however, in many cases no causative mutation is found. Genome wide associations studies (GWAS) have shown that aggrecan gene sinle` ncleotide` polymorphisms affect adult height (Weedon, Lango et al. 2008) and there are a number of skeletal animal models with mutations in aggrecan (Watanabe, Nakata et al. 1997, Primorac, Johnson et al. 1999). In recent years aggrecan has therefore become a novel and promising target with causative mutations identified in cases of spondyloepiphyseal dysplasia Kimberley type (SEDK) (Gleghorn, Ramesar et al. 2005, Sentchordi-Montané, Aza-Carmona et al. 2018) various idiopathic short stature conditions, familial osteochondritis dissecans (Stattin, Wiklund et al. 2010) and spondyloepimetaphyseal dysplasia (SEMD) aggrecan type (Tompson, Merriman et al. 2009). In recognition of this, aggrecan skeletal disorders are now beginning to be classified together as a separate group forming a spectrum from mild idiopathic short stature to the severe SEMD (Warman, Cormier-Daire et al. 2011). Although little is known about the possible disease mechanisms involved, several of the reported patients with idiopathic short stature responded to growth hormone treatment (Gkourogianni, Andrew et al. 2017, van der Steen, Pfundt et al. 2017, Crippa, Giangiobbe et al. 2018). This treatment increased the height of the probands compared to their affected family members; however, there was no reported effect on any skeletal abnormality or the accelerated degenerative disease associated with these disorders and so there is clear scope for further phenotype drug amelioration. Thus far, 47 pathogenic mutations have been reported in 48 families (Dateki 2017, Hu, Gui et al. 2017, van der Steen, Pfundt et al. 2017, Crippa, Giangiobbe et al. 2018) (Figure 8, Appendix A). All of the mutations are inherited in an autosomal dominant manner, except the recessive causative SEMD mutation (Tompson, Merriman et al. 2009) and only five were *de novo* mutations (Tatsi, Gkourogianni et al. 2017). The mutations have been found throughout the *ACAN* gene in every domain and the vast majority cause premature truncation of the protein due to novel stop codons, nonsense mutations, deletions, insertions or duplications. 13 are nonsense mutations, 18 missense mutations, 10 cause frameshifts, 1 a reciprocal chromosomal translocation and 2

affect splicing and are predicted to cause the skipping of either exon 2 or 10 (Nilsson, Guo et al. 2014, Sentchordi-Montané, Aza-Carmona et al. 2018). All patients within the disease spectrum exhibited short stature but most appeared to be within the normal range for weight and length at birth (Gkourogianni, Andrew et al. 2017). During childhood and puberty, the majority of the probands displayed a normal or accelerated bone maturation (Dateki, Nakatomi et al. 2017, Gkourogianni, Andrew et al. 2017, Tatsi, Gkourogianni et al. 2017, van der Steen, Pfundt et al. 2017) coupled with premature growth cessation (Gkourogianni, Andrew et al. 2017) although delayed bone maturation has been reported (Tatsi, Gkourogianni et al. 2017, Sentchordi-Montané, Aza-Carmona et al. 2018). There does not appear to be any difference between the average height of patients with missense mutations and those with mutations that led to premature truncation of the aggrecan protein (Gkourogianni, Andrew et al. 2017). Interestingly, however, all of the cases associated with osteochondritis dissecans (OCD) had causative missense mutations in the C-type lectin domain of the G3 globular domain (Figure 8) (Nilsson, Guo et al. 2014, Aspberg personal communication 2017, Gkourogianni, Andrew et al. 2017, van der Steen, Pfundt et al. 2017). Many conditions were associated with a range of other skeletal abnormalities such as brachydactyly (Gkourogianni, Andrew et al. 2017) short thumbs (Gkourogianni, Andrew et al. 2017, van der Steen, Pfundt et al. 2017) and broad toes (van der Steen, Pfundt et al. 2017) although two families were reported with short stature and no bone abnormalities (Hu, Gui et al. 2017). Further to this, patients also exhibited dysmorphic facial features such as mid-face hypoplasia (Gkourogianni, Andrew et al. 2017, Tatsi, Gkourogianni et al. 2017, van der Steen, Pfundt et al. 2017) frontal bossing (Gkourogianni, Andrew et al. 2017) or posterially rotated ears (Gkourogianni, Andrew et al. 2017, van der Steen, Pfundt et al. 2017). There was often vertebral involvement including lumbar lordosis (van der Steen, Pfundt et al. 2017) scoliosis, flattened vertebral bodies (Gleghorn, Ramesar et al. 2005) and invertebral disc degeneration (Dateki, Nakatomi et al. 2017, Gkourogianni, Andrew et al. 2017). Furthermore, as is often the case with skeletal dysplasias, 22 of the mutations also presented with early-onset osteoarthritis or joint pain (Gleghorn, Ramesar et al. 2005, Stattin, Tegner et al. 2008, Gkourogianni, Andrew et al. 2017, Tatsi, Gkourogianni et al. 2017, van der Steen, Pfundt et al. 2017, Sentchordi-Montané, Aza-Carmona et al. 2018) although joint degeneration was not associated with mutations in a particular aggrecan domain. This shows a clear phenotypic spectrum for aggrecan disorders from mild disproportionate short stature to the severe short stature and skeletal abnormalities of SEMD. Furthemore, single nucleotide polymorphisms in

the aggrecan gene are associated with lumbar intervertebral disc degeneration without short stature and osteoarthritis (Perera, Dissanayake et al. 2017) illustrating the importance of aggrecan in both common and rare conditions.

A

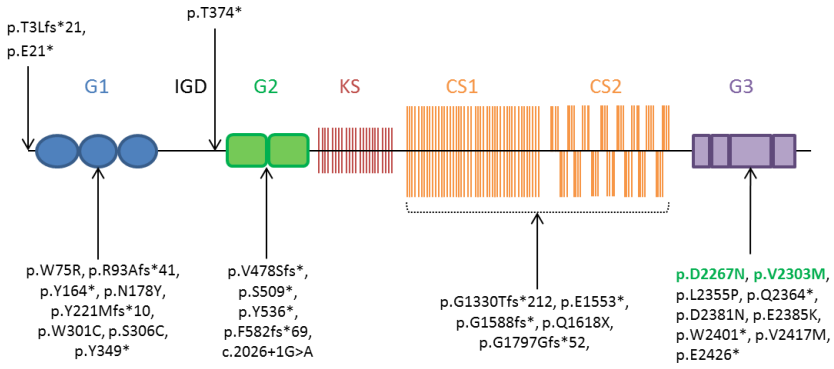

B

c.DNA	Variant	Exon	Domain	Bone age	Phenotype	
c.7249G>A	p.V2417M	16	G3	No data	Familial OCD with short stature and early-onset OA	Gkourogianni, Andrew et al 2017, Stattin, Wiklund et al 2010
c.7141G > A	p.D2381N	15	G3	No data	SEMD	Tompson, Merriman et al 2009
c.3986dupC	p.G1330fs*212	12	CS	No data	SEDK with early-onset OA	Gleghorn, Ramesar et al 2005
n/a	p.C2348S	14	G3	No data	Familial OCD with short stature and early-onset OA	Aspberg, personal communication, 2017
c.7064T>C	p.L2355P	14	G3	Advanced, premature growth cessation	Familial OCD with short stature, early-onset OA, brachydactyly, short thumbs	Gkourogianni, Andrew et al 2017, Nilsson, Guo et al 2014
c.7090C>T	p.Q2364*	14	G3	Slightly advanced	Familial OCD with short stature, early-onset OA, broad toes, short thumbs, midface hypoplasia, prognathism, lumbar lordosis	van der Steen, Pfundt et al 2017
n/a	p.L2379P	15	G3	No data	Familial OCD with short stature and early-onset OA	Aspberg, personal communication, 2017

Figure 8 The aggrecanopathies

(A) A schematic of the aggrecan protein and a selection of pathogenic protein changes which lead to skeletal dysplasia. Those changes which form the focus of this thesis are highlighted in green. **(B)** A summary table of skeletal disorders with causative mutations in aggrecan. An expanded table may be found in Appendix A.

1.5.1. Dominant familial osteochondritis dissecans (fOCD)

Osteochondrosis can refer to a number of cartilage and bone disorders found in both humans and animals. It can occur in the vertebral column (Scheuermann's disease) several of the articular joints (Legg-Calve-Perthes, Panner's disease, Frieberg's disease, Kohler's disease) and in non-articular cartilage (Osgood-Schlatter disease, Sever's disease) (McCoy, Toth et al. 2013). It is defined by the formation of lesions in the cartilage which, in the final clinical stage (osteochondritis *dissecans*) leads to the separation of cartilage and subchondral bone from the cartilage surface. Osteochondritis *latens* and *manifesta* lesions (which form before the closure of the epiphyseal growth plate) can eventually undergo ossification and resolve (Figure 9C). Those lesions which remain or develop after growth cessation are structurally weak and lead to the formation of clefts through the articular cartilage (osteochondritis *dissecans*). The cartilage and bone tissue above this fissure can then dissociate from the surface and form a loose body which requires surgical removal in order to reduce the accompanying joint pain and stiffness. The formation of clefts then usually leads to the development of osteoarthritis (McCoy, Toth et al. 2013). Osteochondrosis is a particularly common problem in horses and pigs and extensive research has been conducted on the disorder's progression in these commercially valuable animals. This research is additionally important as the condition only presents in humans during the last stage (osteochondritis *dissecans*) when the symptoms are most obvious and the lesions are already formed, providing little information on the initial cause. The resultant data from both animal and human studies has indicated that the condition is multifactorial and is associated with genetic predisposition, the male gender, repetitive micro-trauma (such as sports injuries) major trauma and local ischemic necrosis in the growth plate (Takahara, Ogino et al. 1999, Tóth, Nissi et al. 2015). GWAS studies of both animals and humans have implicated ECM proteins, vesicular transport, posttranslational modification and cellular differentiation, including the PTH/PTHRP and WNT signalling pathways which are vital for proper growth plate differentiation (Bates, Jacobs et al. 2014). Further to this, analysis of cartilage biopsies from patients with normal stature showed abnormal mineralisation, mislocalisation of matrix proteins and abnormally wide type II collagen heterofibrils. Type I, II, VI and X collagens and aggrecan appeared to be partially co-accumulated within the ER and there were a number of budding vesicles containing ECM material present. In addition to this, the chondrocytes contained vacuoles, inclusion bodies, irregular hyperchromatic nuclei and

several filopodia (Skagen, Horn et al. 2011). This indicates that chondrocyte differentiation, matrix organisation and protein secretion are perturbed in late-stage osteochondrosis, whether as a secondary effect or as a potential cause of the disorder. Osteochondritis dissecans has been reported in a number of short stature patients with dominant causative missense mutations in the C-type lectin domain of the G3 globular domain of aggrecan (Nilsson, Guo et al. 2014, Aspberg personal communication 2017, Gkourogianni, Andrew et al. 2017, van der Steen, Pfundt et al. 2017). This phenotype was initially reported in several generations of a large Swedish family with mild disproportionate short stature and early-onset osteoarthritis (Stattin, Tegner et al. 2008, Stattin, Wiklund et al. 2010) (Figure 9A). All the patients displayed short stature which appeared to be responsive to growth hormone treatment. Characteristic osteochondritis *dissecans* lesions were observed in the hip, knee and/or elbow (depending on the patient) although lesions were most often found on the medial femoral condyle (Figure 9B). The age of symptom onset resulting from these lesions was variable but tended to occur in late childhood or adolescence. Inheritance was fully penetrant but some family members exhibited additional skeletal abnormalities such as brachydactyly, *tibia vara* or scoliosis. The dominant causative missense mutation (c.6907G>A) causes an amino acid change (p.V2303M) in the C-type lectin domain of the G3 domain. The V2303 residue is highly conserved between species and is found in a beta strand of the ligand-interaction site of the aggrecan CLD, buried in the hydrophobic core of the protein (Lundell, Olin et al. 2004). Computational modelling indicates that the p.V2303M mutation causes a conformational change in the aggrecan CLD (Stattin, Wiklund et al. 2010). Mass spectrometry analysis of patient articular cartilage obtained from knee arthroplasty indicated that the wild type and mutant aggrecan protein were equally secreted into the matrix and glycosaminoglycan sulfation appeared to be unaffected. An *in vitro* study of different splice variants of the recombinant mutant G3 domain of aggrecan in mammalian cells indicated that the p.V2303M *ACAN* mutation disrupted interaction with other extracellular matrix proteins. The mutant G3 domain showed a loss or reduced affinity for the aggrecan ligands fibulin 1, fibulin 2 and tenascin R, suggesting that the mutation may exert an antimorphic effect (Stattin, Wiklund et al. 2010). A further *in vitro* study investigated chondrocyte differentiation in mesenchymal stromal cells (MSCs) and induced pluripotent stem cells (iPSCs) generated from patients with the p.V2303M *ACAN* mutation. Data from both methods indicated that the mutant aggrecan was retained within the endoplasmic reticulum (ER) with little staining in the

interterritorial matrix. Analysis of MSC pellets indicated aggrecan was downregulated by 50% but link protein was upregulated. Furthermore, there was an increase in the expression of the SLRPs asporin, osteoadherin, fibromodulin, decorin, PRELP, lumican, bigylcan and mimecan and the lectican proteoglycans versican and perlecan. In addition to this, collagen VI and XI and the glycoproteins matrilin 3, COMP, fibronectin and tenascin-C were also upregulated. Interestingly, CILP2 was found in the heterozygous mutant ECM but not in that of the control. Immunostaining and transmission electron microscopy (but not mass spectral analysis) indicated a decrease in type II collagen and fibrillar material, suggesting that type II collagen may have been removed during processing and so was not properly bound within the ECM. GAG content decreased in patient cultures overtime, potentially due to either degradation, synthesis inhibition or delayed differentiation. iPSC pellets were comprised of densely packed cells, suggesting a delay in differentiation or a decreased amount of matrix. Overall this *in vitro* data suggests that the p.V2303M *ACAN* mutation disrupts ECM interactions and impedes aggrecan secretion, contrary to mass spectral analysis of late-stage lesions obtained from patient knee arthroplasty (Xu, Stattin et al. 2016).

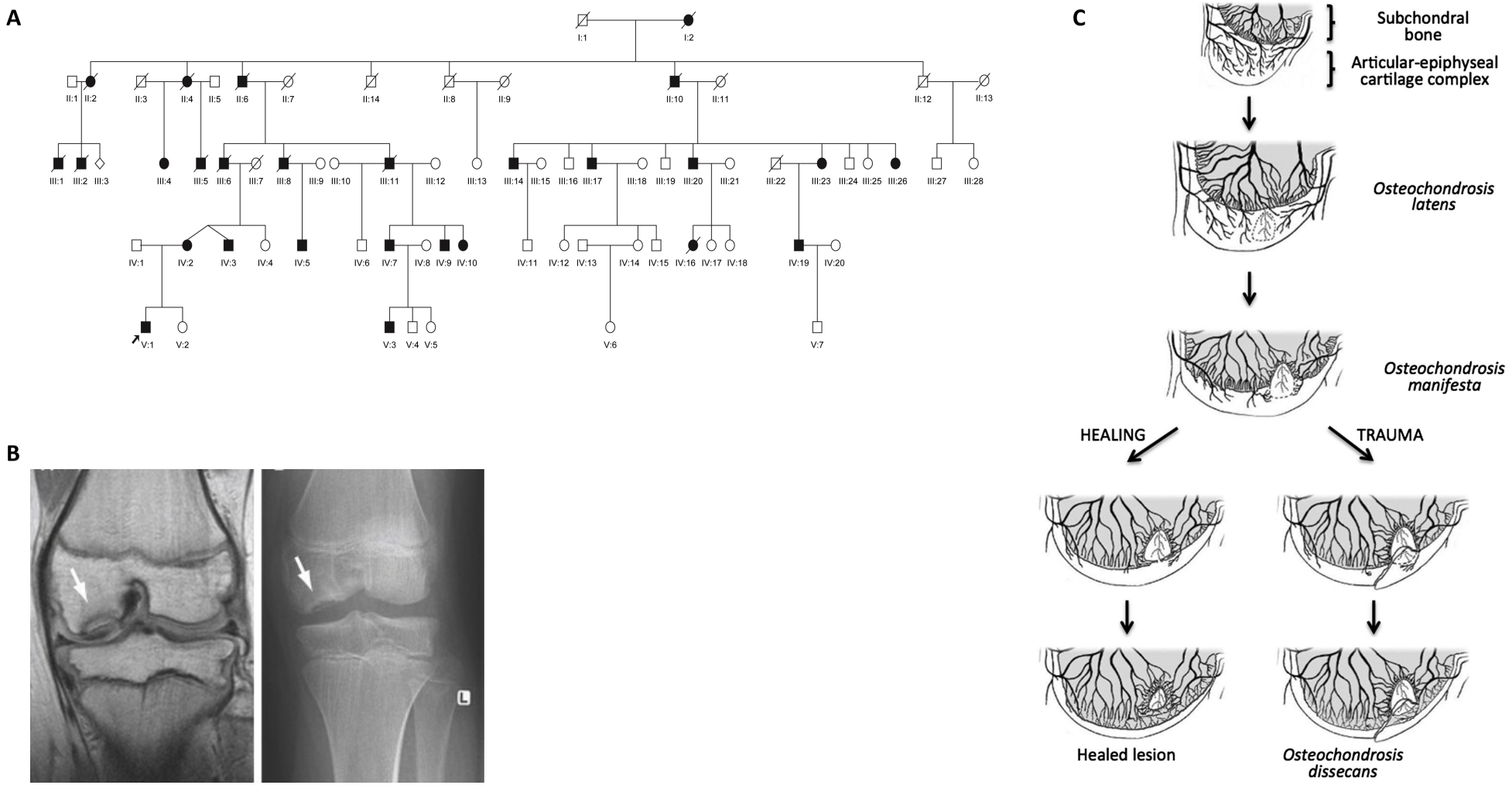

Figure 7 Familial osteochondritis dissecans (OCD)

(A) Familial OCD is a dominantly-inherited disorder (Stattin, Tegner et al 2008). **(B)** MRI (left) and radiographic (right) images showing a lesion (arrows) in the ar cular cartilage and underlying subchondral bone (Stattin, Wiklund et al 2010). **(C)** A schematic showing the formation of early lesions and either subsequent healing or progression to OCD (McCoy, Toth et al 2013).

1.5.2. Spondyloepimetaphyseal dysplasia (SEMD) aggrecan type

The spondyloepimetaphyseal dysplasias (SEMD) are a group of heterogenous bone and cartilage disorders characterised by involvement of the vertebral bodies, epiphyses and metaphyses. There are X-linked, autosomal recessive and autosomal dominant (Grosch, Gruner et al. 2013) forms with causative mutations in genes such as *COL2A1* (Tysoe, Saunders et al. 2003) *MATN3* (Borochowitz, Scheffer et al. 2004) and *MMP13* (Kennedy, Inada et al. 2005). A clinical study reported SEMD in three patients from a single potentially consanguineous family (Figure 10) (Tompson, Merriman et al. 2009). Sequencing data revealed homozygosity for a c.6799G<A missense mutation in *ACAN* which causes an amino acid change (D2267N) in the C-type lectin domain of the G3 globular domain. This is unlike all the other aggrecan mutations reported thus far which are all inherited in an autosomal dominant manner. The homozygous phenotype was characterised by extreme short stature (66-71cm) and a range of bone abnormalities such as accessory carpal ossification centres, irregular epiphyses and widened metaphyses. As reported with many other aggrecanopathies, there were a number of craniofacial irregularities observed, including severe mid-face hypoplasia and relative mandibular prognathism. This indicates the possible involvement of both intramembranous and endochondral ossification. Thus far, the three patients have not complained of any joint pain or shown any signs of osteoarthritis. The D2276 residue is highly conserved between species and is one of five residues required for the coordination of a calcium ion. This calcium ion (in conjunction with two others in the CLD) is an important part of the CLD calcium coordinating loops which mediates calcium-dependent ligand binding with ECM molecules such as tenascin R. *In vitro* analysis of two different variants of the recombinant mutant G3 domain of aggrecan (with and without the EGF repeats) in mammalian cells indicated that the p.D2267N ACAN mutation alters cation-dependent binding with tenascin C but does not affect secretion of the G3 domain (Tompson, Merriman et al. 2009). In addition to the potential disruption caused to ligand binding by the D2267N *ACAN* mutation, the mutation also introduces a novel N-linked glycosylation recognition site, causing the mutant G3 domain to migrate more slowly. This was confirmed by N-glycanase treatment which then allowed the mutant G3 domain to migrate at a similar rate to the wildtype G3 domain (Tompson, Merriman et al. 2009). It has been suggested that this glycan substitution may also hinder ligand interaction (Aspberg 2012); however, little is known

about the effect of the p.D2267N ACAN mutation on the interactions between aggrecan and other ECM molecules.

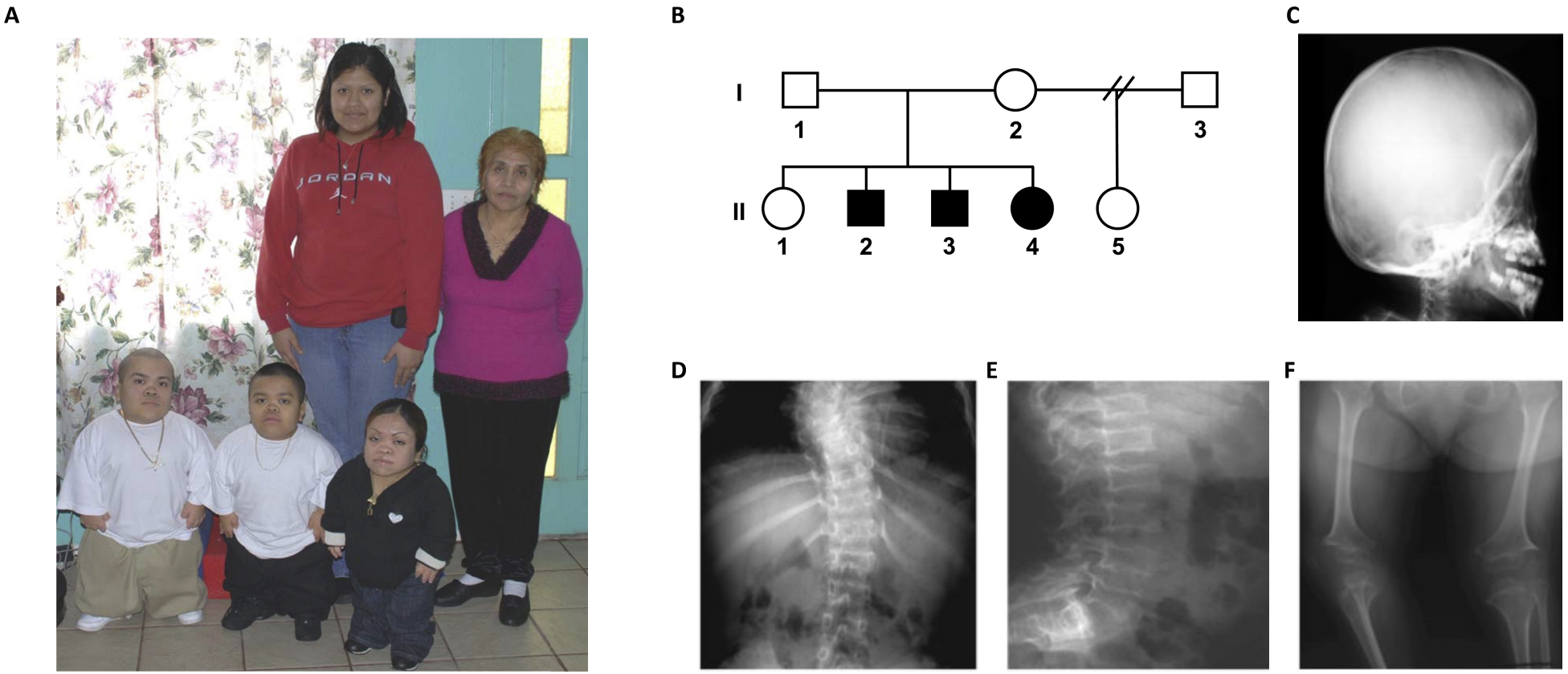

Figure 10 Spondyloepimetaphyseal dysplasia (SEMD) aggrecan type

(A) The three probands and two family members (back row) II1 and I2 (front row) II2, II3 and II4 **(B)** SEMD is inherited in a recessive manner. The homozygous probands exhibited **(A)** extreme short stature **(C)** mid-face hypoplasia **(D)** thoracic scoliosis **(E)** lumbar lordosis **(F)** widened metaphyses and irregular epiphyses (Tompson, Merriman et al 2009).

1.6. Disease mechanisms of the skeletal dysplasias

Although little is known about the possible mechanisms involved in the disease progression of the aggrecanopathies, many studies have been conducted in animal models of other skeletal dysplasias. This research has identified several pathways which have not been fully investigated in the aggrecanopathies and could be implicated in the disorders caused by antimorphic aggrecan mutations.

1.6.1. The classical pathway: ER stress and the unfolded protein response (UPR)

Previous studies of skeletal dysplasia have demonstrated that cells expressing these mutations in ECM molecules, such as COMP and collagen type X, produce misfolded protein. This disrupts protein folding and trafficking and impairs secretion of mutant protein from the rough endoplasmic reticulum (ER) (Pirog-Garcia, Meadows et al. 2007, Mullan, Mularczyk et al. 2017). The resultant misfolded protein accumulation causes the ER cisternae to enlarge and may activate the unfolded protein response (UPR). The UPR is thought to be the main pathway used by the cell to reduce stress caused by protein retention (Figure 11Aii). It attempts to reduce the protein accumulation by downregulating translation and re-folding or degrading the misfolded protein. Eventually prolonged UPR activation causes upregulation of apoptosis pathways leading to increased cell death. BIP is often used as a marker for endoplasmic reticulum stress as it is bound to the ER stress sensors Inositol-requiring kinase 1 (IRE1) (PKR)-like endoplasmic reticulum kinase (PERK) and activating transcription factor 6 (ATF6) during their inactive state. During upregulation of the UPR pathway, BIP dissociates from these sensors and acts as a protein chaperone and potentially anti-apoptotic factor (Lee 2005). BIP dissociation causes cleavage of ATF6 in the Golgi (Figure 11Aii). The cleaved ATF6 then moves to the nucleus where it upregulates the transcription of ER chaperones (Lee 2005). Chaperones assist in the folding and processing of secreted proteins and so are often upregulated in response to the presence of misfolded proteins. Protein re-folding is also assisted by protein disulfide isomerases (PDIs) which catalyse the formation and breakage of disulfide bonds between cysteine residues as proteins fold. The dissociation of BIP causes IRE1 to autophosphorylate and catalyse the alternative splicing of *Xbp1* (Figure 11Aii). The

spliced XBP1 then acts as a transcription factor, upregulating other UPR genes including those associated with endoplasmic reticulum-associated protein degradation (ERAD) thus reducing the total protein accumulation (Calfon, Zeng et al. 2002, Hiramatsu, Messah et al. 2014). The last aim of the UPR occurs via the phosphorylation of EIF2A by PERK (Figure 11Aii). This causes attenuation of translation, reducing the amount of accumulated protein burden on the ER (Harding, Zhang et al. 1999).

1.6.2. Other possible disease mechanisms

Although the UPR is thought to be the main response to protein accumulation in the ER several other associated pathways have been reported (Figure 11) including possible roles for oxidative stress and integrin and nuclear factor-κB (NFκB) signalling (Pahl and Baeuerle 1995, Pirog-Garcia, Meadows et al. 2007, Suleman, Gualeni et al. 2012, Posey, Coustry et al. 2015). The ER overload response (EOR) also occurs in response to mutant protein accumulation in the ER but acts independently of the UPR (Figure 11Ai). This protein accumulation appears to cause a release of calcium from the ER and the production of reactive oxygen intermediates (ROS) which then induce apotosis and NFκB (Pahl and Baeuerle 1997, Ekeowa, Freeke et al. 2010). This calcium release has also been shown to indirectly upregulate both apoptosis and macroautophagy. The upregulation of macroautophagy is also associated with the UPR and acts as a protective mechanism by degrading misfolded protein aggregates (Ishida, Yamamoto et al. 2009) (Figure 11A). During macroautophagy, cytoplasm is sequestered by an isolation membrane through the recruitment of ATG proteins (Figure 11B). The isolation membrane precursor can originate from a variety of sources, including mitochondrial, plasma and nuclear membranes, although most evidence points to the endoplasmic reticulum as the main source (Nascimbeni, Giordano et al. 2017, Sakoh-Nakatogawa, Kirisako et al. 2015). The membrane then elongates to form a double-membraned autophagosome. This autophagosome subsequently fuses with an endosome and then a lysosome, degrading the inner membrane and cytoplasmic contents through the action of lysosomal enzymes (Sakoh-Nakatogawa, Kirisako et al. 2015). Research has also shown that modulation of this pathway can elicit a pathogenic response; for example, the Sumf1 knock-out mouse exhibits a short stature phenotype partially caused by increased cell death due to impaired autophagy (Settembre, Fraldi et al. 2008).

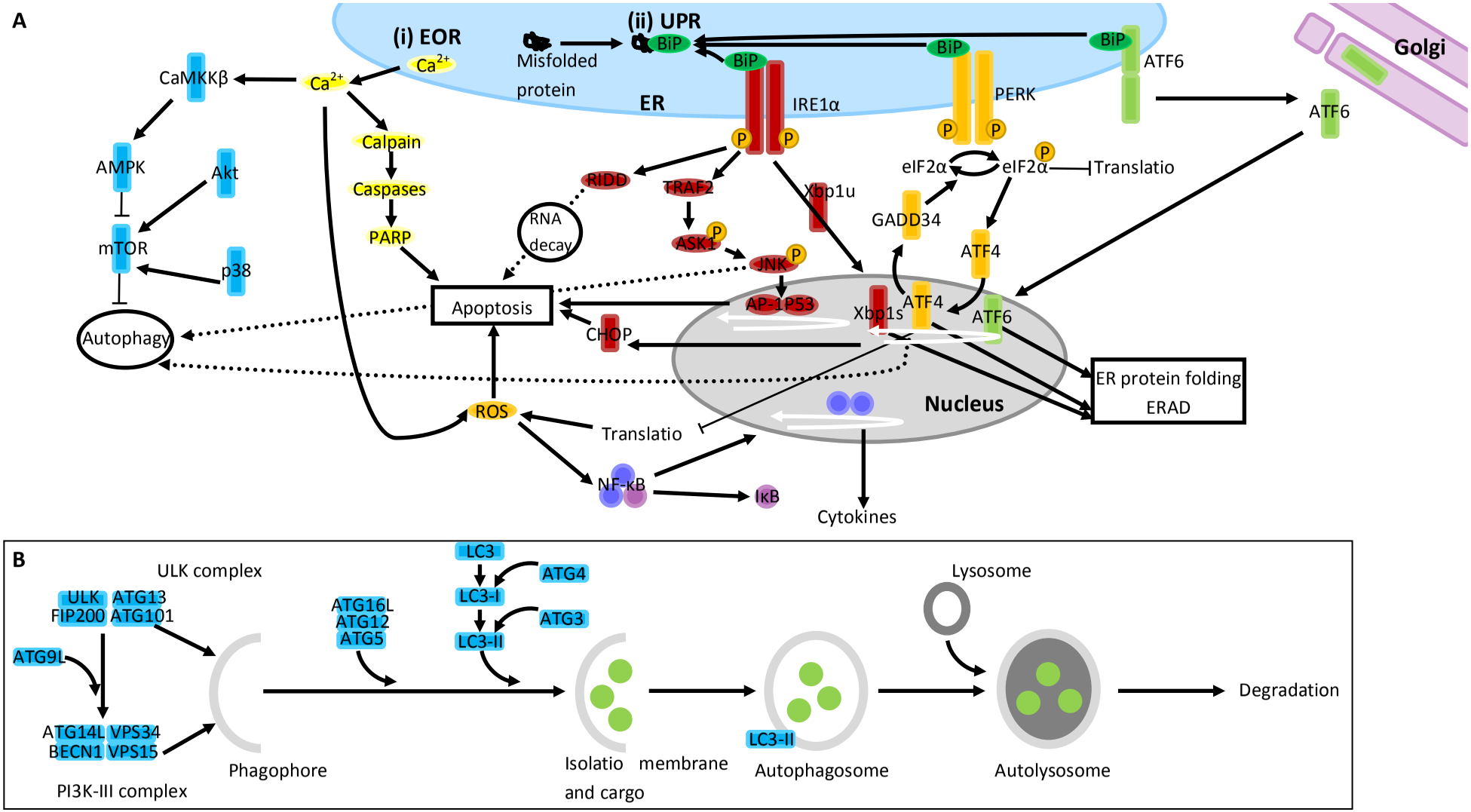

Figure 11 Known disease mechanisms of the skeletal dysplasias.

(A) The unfolded protein response (**UPR**) and the ER overload response (**EOR**) **(B)** The canonical macroautophagy pathway. Schematic adapted from (Wang and Kaufman et al 2014, Hassan, Selimovic et al 2015, Hasnain, Lourie et al, 2012). Key: ⊣ inhibition → activation white arrow = gene transcription

1.7. Aggrecan model systems

There are a number of naturally occurring aggrecan mutations in animals which have allowed for the *in vivo* study of aggrecan's role in cartilage development and homeostasis. Unfortunately this research has had its limitations for a variety of reasons, for example, variable penetrance of the mutation (Dexter Bulldog dwarfism) (Cavanagh, Tammen et al. 2007). Furthermore, due to the important role of aggrecan, several of these mutations lead to embryonic or perinatal homozygous lethality (nanomelia chick and cmd/cmd-bc mouse). In addition to this, all of the existing animal models are caused by functionally null mutant aggrecan alleles due to haploinsufficiency (through nonsense-mediated mRNA decay) or the production of truncated proteins (Cavanagh, Tammen et al. 2007). This occurs through deletions (cmd, cmd-bc) premature termination codons (nanomelia, Dexter BD1) or novel initiation codons (Dexter BD2). Therefore, although this work has been extremely useful it may be of limited relevance to the study of human aggrecan disorders which are caused by possibly antimorphic missense mutations (Gleghorn, Ramesar et al. 2005, Tompson, Merriman et al. 2009).

1.7.1. Nanomelia chicken

The autosomal recessive nanomelia mutation (G4553T) introduces a premature stop codon in exon 10 which codes for the CS2 domain (Li, Schwartz et al. 1993, Primorac, Stover et al. 1994). This causes a truncated aggrecan precursor to be produced which is not secreted from the ER and is thought to be degraded in the cytoplasm (Li, Schwartz et al. 1993, Vertel, Walters et al. 1993, Primorac, Johnson et al. 1999). The mutation causes a chondrodysplasia phenotype and embryonic lethality (Landauer 1965) with defects in both endochondral and intramembranous ossification (Wong, Lawton et al. 1992) (Figure 12A). The affected chicken embryos have a range of skeletal abnormalities including an abnormal mandible and maxilla (forming a parrot-like beak) micromelia and a large, brachycephalic head (Landauer 1965). The growth plate is very disorganised with a small hypertrophic zone and both increased proliferation and apoptosis in the proliferative and hypertrophic zones. The IHH, FGF and BMP chondrocyte differentiation signalling pathways are altered, with overlap of pre-hypertrophic and hypertrophic markers and premature expression of osteopontin, a marker of mineralisation.

This suggests that hypertrophy and ossification are accelerated in this aggrecan null model and indicates that aggrecan is vital for correct chondrocyte differentiation (Domowicz, Cortes et al. 2009).

1.7.2. Cartilage matrix deficiency (cmd) and cmd-bc mouse

The spontaneous C57BL/6 Cmd mutation is a 7bp deletion in exon 5 (which codes for the G1 domain) and causes both heterozygous and homozygous phenotypes. As with the nanomelic chick, a truncated aggrecan precursor is produced and aggrecan mRNA levels are reduced to 81% (Watanabe, Kimata et al. 1994). Homozygosity for the mutation causes perinatal lethality due to respiratory failure caused by abnormal tracheal cartilage. Homozygous neonates have disproportionate short stature with a short snout and tail, protruding tongue and cleft palate (Figure 12B). The disorganised growth plate lacks zonation and has a reduced number of hypertrophic chondrocytes (Kobayakawa 1985, Wai, Ng et al. 1998). In addition to this the expression pattern of other ECM proteins, such as link protein, syndecan 3, and collagen types IX, X and XI, was shown to be abnormal (Wai, Ng et al. 1998). Mice heterozygous for the cmd mutation have proportionate short stature and age-associated spinal disc degeneration (Rittenhouse, Dunn et al. 1978, Watanabe, Kimata et al. 1994, Watanabe, Nakata et al. 1997). The affected mice develop cervical lordosis and thoraco-lumbar kyphosis, causing spine misalignment, disc herniation and spastic paralysis of the hind limbs. This causes a decrease in movement and the mice die within 19 months through starvation. As with the homozygous mouse, heterozygous mice have a disorganised growth plate and transcript levels of aggrecan are reduced to 41% (Watanabe, Nakata et al. 1997). The cmd-bc mutation spontaneously arose on the BALB/c GaBc background and is thought to be caused by a non-homologous recombination event. It is autosomal recessive and is a large deletion which results in the loss of exons 2-18. Homozygous mice are phenotypically very similar to the cmd model with disproportionately short limbs and snout, enlarged abdomen, protruding tongue and cleft palate (Krueger, Kurima et al. 1999). A phenotype rescue study performed in C57BL/6 cmd-bc embryos showed that mutant mice had disorganised growth plates with areas of hypocellularity, reduced ECM and lack of zonation. Further to this, apoptosis was increased, proliferation decreased and IHH, SOX9 and FGF chondrocyte differentiation signalling pathways altered. The transgenic expression of chick aggrecan was able to restore the growth plate zonation, cell morphology and expression patterns of these

vital signalling factors. It also increased proliferation and reduced apoptosis. This again suggests that the presence of aggrecan in the epiphyseal growth plate is essential for the regulation of chondrocyte survival and differentiation (Lauing, Cortes et al. 2014).

1.7.3. Dexter Bulldog dwarfism

Dexter Bulldog dwarfism is one of the oldest described naturally-occurring animal models and was first reported in the 18th century (Cavanagh, Tammen et al. 2007). Initially thought to only be found in Dexter cattle, it has more recently been reported in miniature Highland cattle (Catalina Cabrera, McNabb et al. 2016). Thus far, two causative mutations have been reported with variable penetrance and both heterozygous and homozygous phenotypes (Cavanagh, Tammen et al. 2007) (Figure 12D). Heterozygous cows have disproportionate short stature with rhizomelia, mild irregular vertebral bodies and posterior vertebral wedging. Transcript levels of the mutant aggrecan are decreased to 8% due to nonsense-mediated decay (Harper, Latter et al. 1998, Cavanagh, Tammen et al. 2007). Homozygosity of the mutant alleles causes embryonic lethality, resulting in mid to late term spontaneous abortion. Stillborn calves exhibit extreme short-limbed dwarfism, a large abdominal hernia, and a range of skeletal abnormalities such as marked vertebral platyspondyly, shortened vertebral column, extreme rib shortening and micromelia. The disproportionally large head has many craniofacial abnormalities including relative prognathism, midfacial retraction and cleft palate. The bulldog dwarfism 1 mutation (BD1, 2266_2267insGGCA) is a 4bp insertion in exon 11 which codes for the GAG-attachment region. This results in a frameshift, introduction of a premature stop codon and the loss of part of the GAG attachment region and the G3 domain. The BD2 mutation (-198C>T) is much rarer and is a transition in exon 1 which introduces a novel ATG start codon and consequently a large frameshift. The putative mutant protein arising from this mutation therefore does not resemble normal aggrecan (Harper, Latter et al. 1998, Cavanagh, Tammen et al. 2007).

1.7.4. A1946V Acan mouse

A large scale N-ethyl-N-nitrosourea (ENU)-based mutagenesis screen was conductedto identify novel disease genes in laboratory mice (C57BL/6J and C3H.Pde6b+ cross). Mice homozygous for the A1946V *Acan* missense mutation in the C-type lectin domain had bone deposits in multiple joints by 18 months of age (Figure 12E). Further to this, by 12 months of age the mice exhibited metabolic obesity. Adipocytes in white adipose tissue were enlarged and showed inflammatory infiltration. Adipocytes in brown adipose tissue, on the other hand, exhibited reduced fat accumulation (Potter, Bowl et al. 2016).

1.7.5. Cartilage Calcification Insufficient (CCI) rat

The CCI rat exhibits disproportionate short-stature with a short vertebral column, tail and skull length (Figure 12F). The unknown causative mutation spontaneously arose in a Jcl-derived Sprague-Dawley colony and is thought from progeny phenotype analysis to be inherited in an autosomal recessive manner. The resting and proliferative zones are wide and disorganised with a poorly formed secondary ossification centre, indicating that endochondral ossification is delayed. The randomly organised bone spicules are enlarged and the cranial base synchondrosis abnormal. Additional research revealed an abnormal expression pattern for aggrecan in both the growth plate and articular cartilage, with a suggestion that aggrecan synthesis was affected (Takeuchi, Nagayama et al. 2015, Tanaka, Watanabe et al. 2015). Analysis of this model has not so far elucidated the causative mutation or a potential disease mechanism but a mutation in the *Acan* gene has not yet been ruled out.

1.7.6. Models associated with abnormal post-translational sulfation

In addition to models caused by mutations in the aggrecan gene itself, there are a number of models resulting from defects in proteins involved with aggrecan's post-

translational modification. As an example, the brachymorphic mouse has a short stature phenotype resulting from decreased levels of 3'-phosphoadenosine 5'-phosphosulfate (PAPS) synthase and so undersulfation of proteoglycan (Pennypacker, Kimata et al. 1981) (Figure 12C). Furthermore, the chondroitin 4-sulfotransferase 1 (C4st1) gene trap mouse displays disproportionate short stature due to abnormal chondroitin 4-O-sulfation (Kluppel, Wight et al. 2005) (Figure 12G) illustrating the importance of correct post-translational modification of aggrecan.

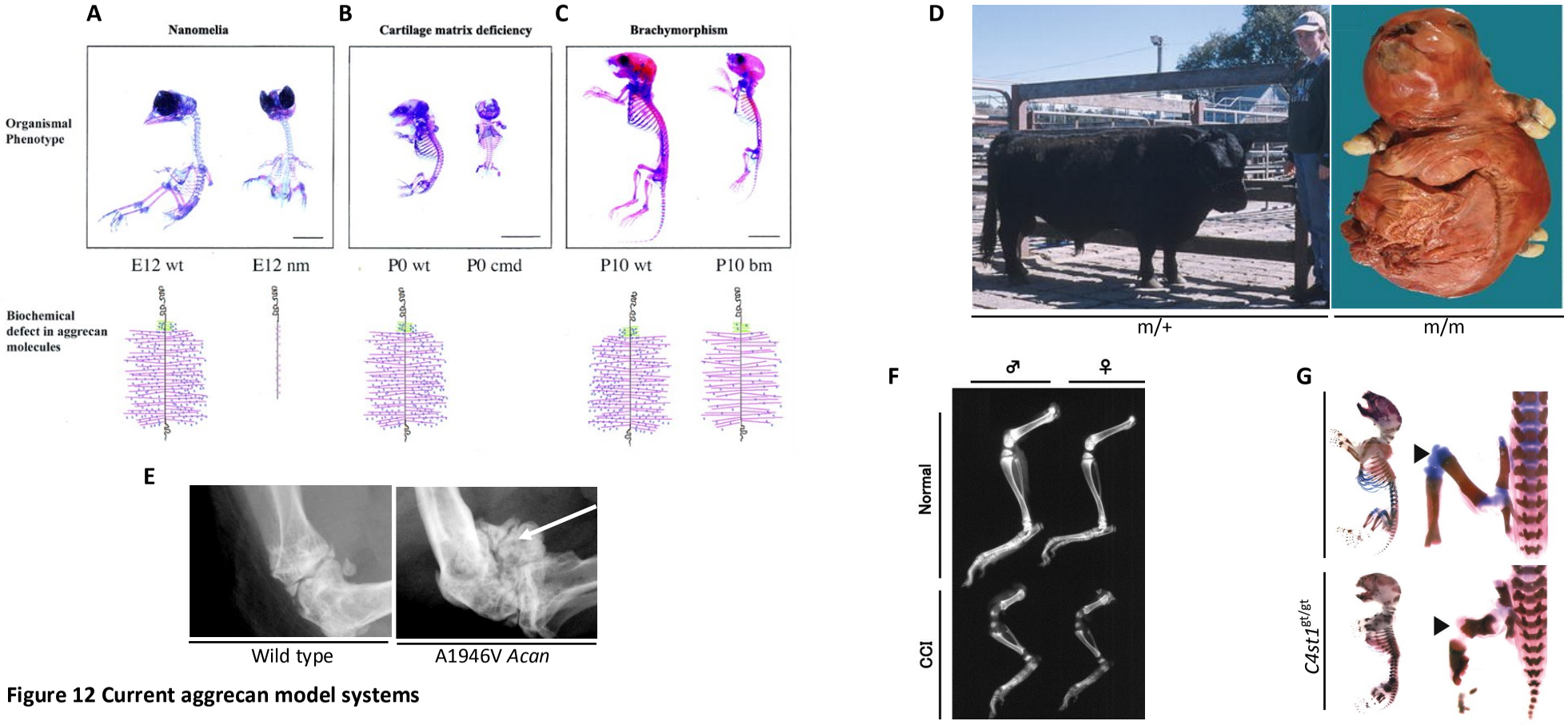

Figure 12 Current aggrecan model systems

(A) The nanomelic chick expresses a truncated aggrecan precursor and displays a short stature embryonic lethal phenotype. **(B)** The murine cmd mutation is homozygous lethal. Neonates express a truncated aggrecan precursor and exhibit short stature. (**C)** The brachymorphic mouse exhibits a short stature phenotype due to reduced aggrecan sulfation (Schwartz and Domowicz 2002, scale bars = 10mm). **(D)** Dexter cattle display a heterozygous short stature phenotype and homozygous lethality (Cavanagh, Tammen et al 2007). **(E)** The A1946V *Acan* mouse exhibits late-onset joint deterioration and bony deposits (white arrow) (Potter, Bowl et al 2016). **(F)** The CCI rat exhibits disproportionate short stature due to an unknown aggrecan sulfation defect (Tanaka, Watanabe et al 2015). **(G)** The *C4st1* gene trap mouse has a short stature phenotype due to abnormal chondroitin sulfation (Kluppel, Wight et al 2005).

Key: m/+ (heterozygous for the mutation) m/m (homozygous for the mutation)

1.8. Project Aims

In recent years, several patients have been reported with disproportionate short stature caused by mutations in the proteoglycan aggrecan. Preliminary research has indicated that although many of these disorders are due to haploinsufficiency, several of the mutations are likely to exert an antimorphic effect. The phenotypes of all but one of the aggrecan animal models currently available (cmd, nanomelia) are also due to haploinsufficiency. The remaining model (A1946V *Acan* mouse) is not a disease causing mutation found in humans. To this end, two mouse models were generated for two skeletal disorders: OCD (dominant V2303M *ACAN* mutation) and SEMD (recessive D2267N *ACAN* mutation). These mutations are only a few base pairs apart and are both found in the CLD of the G3 domain, but are phenotypically very different. The aims of this project were therefore:

- To analyse the phenotypes of two knock-in mouse models with disease causing mutations in the major proteoglycan aggrecan.

- To assess and compare the pathomolecular mechanisms of spondyloepimetaphyseal dysplasia aggrecan type and familial osteochondritis dissecans with analysis of cartilaginous tissues.

- Further elucidate the disease mechanisms of these disorders with transcriptomic analysis and pathway validation.

Chapter 2. Materials and Methods

All steps were performed at room temperature unless specified otherwise.

2.1 Materials

All chemicals and solvents were obtained from Sigma Aldrich unless otherwise stated.

Antibody suppliers are detailed in Appendix B.

Primers were synthesised by Eurofins Scientific Ltd.

Restriction enzymes were obtained from New England Biolabs.

Image J was obtained from www.imagej.net (Schneider, Rasband et al. 2012).

Adobe Photoshop CS3 and Graphpad Prism software were obtained on licence from Adobe Systems and Graphpad Software respectively.

LICOR image studio lite software and REVERT total protein stain were obtained from LI-COR Biosciences.

Bovine serum albumin, dithiothreitol (DTT) DNAse I, ethidium bromide, fetal bovine serum, glycerol, isopropanol, non-essential amino acids, Novex 3-8% tris-acetate precast gradient gels, Novex 4-12% Bis-Tris precast gradient gels, NuPAGE MES SDS Running Buffer, paraffin wax, Pierce BCA protein assay kit, penicillin-streptomycin and sodium dodecyl sulfate were obtained from ThermoFisher Scientific.

Acetic acid, coverslips, Dulbecco's modified eagle medium/nutrient mixture (DMEM) F-12, ethanol, hydrochloric acid, methanol, sterile phosphate-buffered saline (PBS) Superfrost Plus slides, tissue culture plates and xylene were obtained from VWR International.

ImmEdge hydrophobic barrier pen, normal rabbit serum, normal goat serum, Nuclear Fast Red and VectaMount permanent mounting medium were obtained from Vector Laboratories.

Dead End Fluorimetric TUNEL system, ethylenediaminetetraacetic acid (EDTA) and ReliaPREP RNA tissue miniprep system were obtained from Promega.

Cell proliferation labelling reagent bromodeoxyuridine (BrdU) was obtained from GE Healthcare.

Donkey serum and Precision plus protein standards were obtained from Bio-Rad Laboratories.

Fluoroshield mounting medium with DAPI and Picro-Sirius Red kit were obtained from Abcam.

25% E.M. grade glutaraldehyde and epoxy embedding resin kit were obtained from TAAB Laboratory Equipment Ltd.

Non-skirted PCR 96 well plates were obtained from Cell projects.

BioMix red was obtained from Bioline Reagents.

Qiagen DNA extraction kit was obtained from Qiagen Ltd.

Agarose was obtained from Melford Laboratories Ltd.

2% aqueous uranyl acetate and lead citrate were obtained from Leica UK Ltd

Osmium tetroxide and pioloform were obtained from Agar Scientific.

RNA 6000 nano kit was obtained from Agilent Technologies.

Epoxomicin was obtained from Merck Milllipore.

Nitrocellulose membranes were obtained from Scientific Laboratory Supplies Ltd.

2.2 Reagents and solutions

All solutions referenced in the methods section are described in Appendix C.

Primer sequences are detailed in Appendix D.

Information on the antibodies and their dilutions can be found in Appendix B.

2.3 Generation of mutant mice

The generation of mutant mice was performed by Polygene Transgenetics in Switzerland. The D2267N and V2303M aggrecan mutations were introduced into the C57BL/6N inbred mouse line using gene targeting. The mouse aggrecan protein is very similar to the human aggrecan protein. Human aggrecan is encoded by 19 exons found on chromosome 15. The mouse aggrecan gene contains 18 exons and is found on murine chromosome 7. This change from the 19 exons of human *ACAN* to 18 exons in the mouse *Acan* is because murine exon 13 (encoding 1 of the Type II EGF-like repeats) is a pseudoexon. The murine ortholog for the human aspartic acid (D) residue in position 2267 is D1983 on exon 14 (Figure 13A). The murine ortholog for the human valine 2303 residue is V2019 on exon 15 (Figure 13B). As the two mutations are located in the adjacent exons, Polygene generated targeting vectors with the same homology regions. The final targeting vectors were identical apart from the D1983N and V2019M point mutations. The bacterial artificial chromosome BAC RP23-390O18 has an insert length of 188 kb and contains exons 2-17 of mouse *Acan* (but not exon 1 or the promoter region) was used to generate the targeting construct. The identity of the BAC was confirmed by polymerase chain reaction (PCR) to amplify a fragment of *Acan* intron 14 (the neomycin cassette insertion site) using primer pair P12 and P13 (appendix D). PCR was used to generate the short (containing exons 13-14) and long (containing exons 15-17) arms of homology (confirmed by sequencing). The PCR products were cloned into PolyGene vector 0008.4a which contained an FRT-flanked neomycin resistance cassette. Restriction sites were added to the 5' (*Not*I) and 3' (*Bam*HI) ends of the short arm of homology to insert it into the vector upstream of the neomycin cassette, which was placed in intron 14 of the *Acan* gene (Figure 14A). A *Bsi*WI restriction site was created to facilitate site directed mutagenesis. Restriction sites were added to the 5' (*Sbf*I) and 3' (*Xho*I) ends of the long arm of homology to allow insertion into the vector downstream of the neomycin cassette (Figure 14B). This vector (SY01.2, Figure 14C) was then used as the basis for the following targeting strategies.

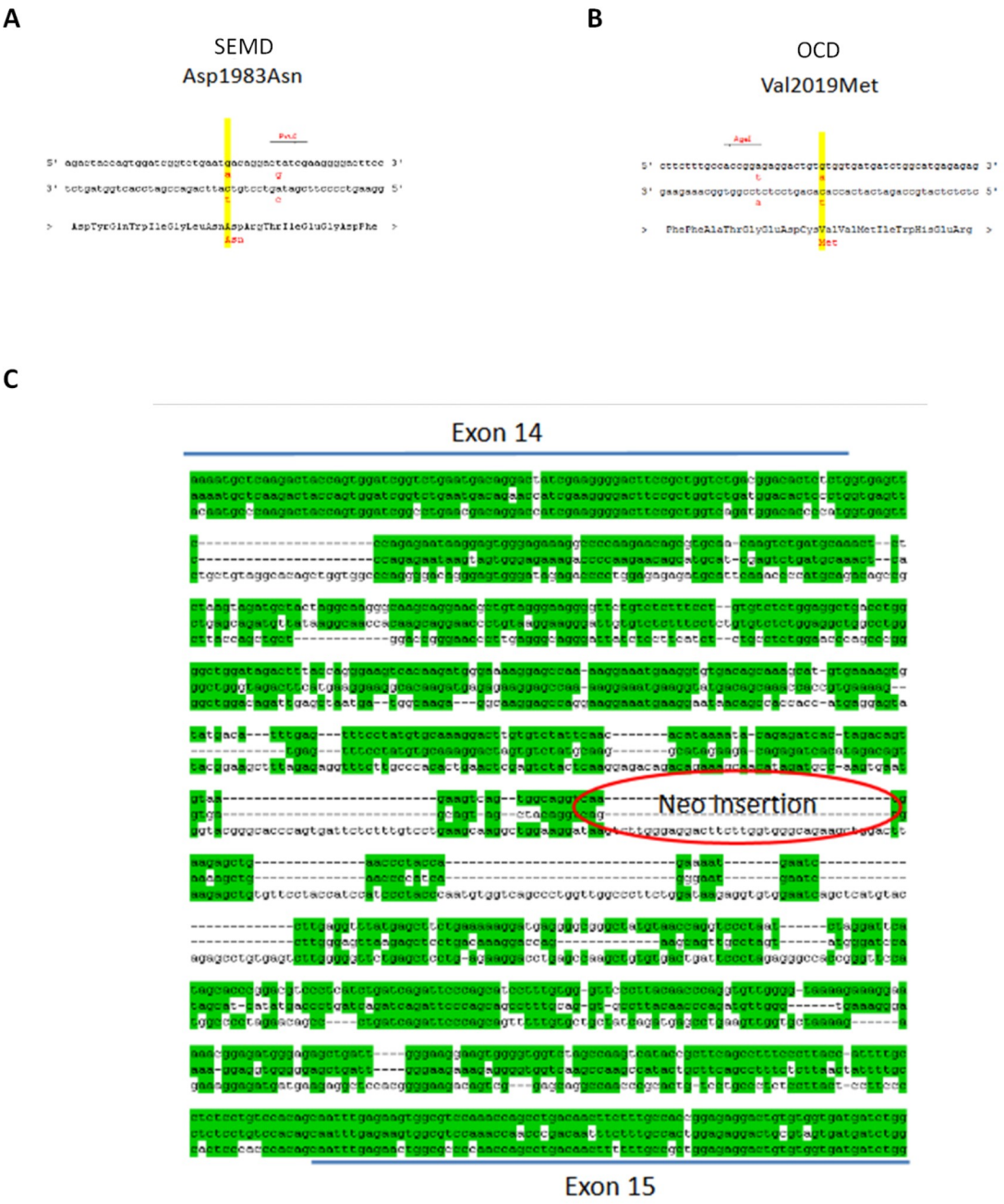

Figure 13 The genetargeting strategy for the generation of the OCD and SEMD mice.

(A) The murine D1983N (SEMD) amino acid change is caused by a G5947A mutation (yellow) in exon 14. A silent T5955G mutation was introduced to generate a *Pvu*I restriction site. **(B)** The murine V2019M (OCD) amino acid change is caused by a G6055A mutation (yellow) in exon 15. A silent A6045T mutation was introduced to generate a *Age*I restriction site. **(C)** Comparison of the genomic regions from mouse (top) rat (middle) and human (bottom) showed no conserved sequences at the insertion site for the neomycin cassette. All diagrams kindly provided by Polygene Transgenetics.

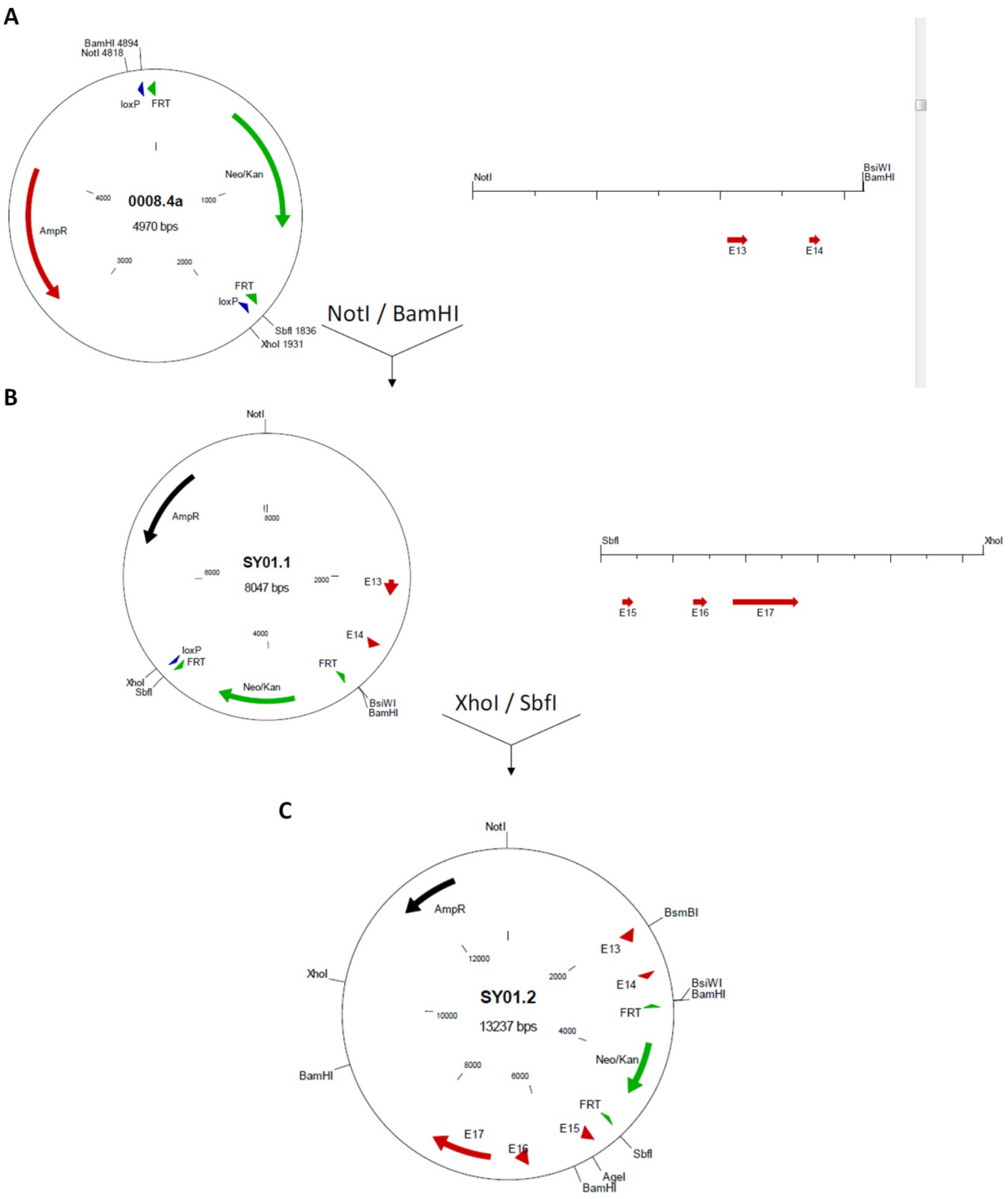

Figure 14 Generation of the initial targeting vector.

(A) The short arm of homology was cloned into PolyGene vector 0008.4a using the restriction enzymes *Not*I and *Bam*HI. **(B)** The long arm of homology was cloned into PolyGene vector 0008.4a using the restriction enzymes *Xho*I and *Sbf*I. **(C)** The initial targeting vector used for the generation of the SEMD and OCD mice. All diagrams kindly provided by Polygene Transgenetics.

Key: ➡ FRT– flanked neomycin resistance cassette

2.3.1 SEMD (D1983N Acan) gene targeting strategy

The D1983N mutation (G5947A) and an additional silent mutation to introduce a *Pvu*I restriction site (T5955G) were introduced into the vector upstream of the neomycin cassette using the restriction enzymes *Bsm*BI and *Bsi*WI (Figure 15A). The *Pvu*I restriction site was created to facilitate confirmation of the presence of the D1983N point mutation by restriction digestion with the *Pvu*I enzyme. The restriction enzyme *Sna*BI was then used to collapse the vector (SY01.3 CV) by removing the sequence between the two restriction sites to produce the final targeting vector (SY01.4 TV) (Figure 15B-C). The vector sequence was confirmed by Sanger sequencing of exonic regions and by restriction digestion with *Xma*I, *Nco*I, *Sph*I, *Bgl*II, *Bsp*HI, *Pvu*I (Figure 15C). The vector was linearised with the restriction enzyme *Sna*BI (Figure 15C).

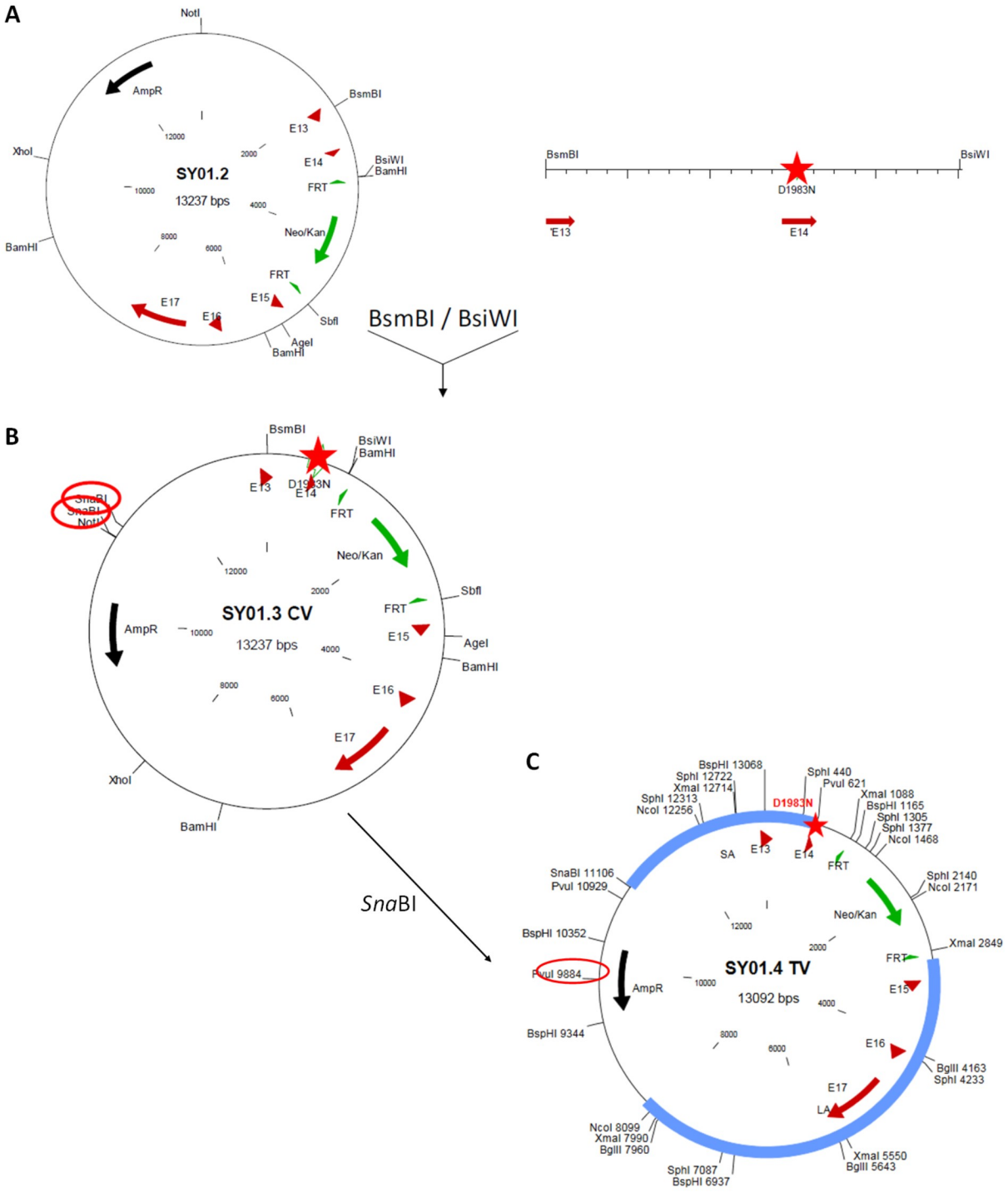

Figure 15 The genetargeting strategy for the generation of the SEMD mice.

(A) The D1983N mutation (G5947A) and a silent T5955G mutation to introduce to generate a *Pvu*I restriction site were introduced into the SY01.2 vector using the restriction enzymes *Bsm*BI and *Bsi*WI. **(B)** The sequence between the two *Sna*BI restriction sites was removed using the restriction enzyme *Sna*BI. **(C)** The final targeting vector for the generation of the SEMD mouse. The restriction enzymes marked were used for confirmation of the vector sequence. The restriction enzyme *Sna*BI (highlighted in red) was used for vector linearisation. All diagrams kindly provided by Polygene Transgenetics.

Key: ★ point mutation ➡ FRT– flanked neomycin resistance cassette ▬ long/short arm of homology

2.3.2 OCD (V2019M Acan) gene targeting strategy

The V2019M mutation (G6055A) and an additional silent mutation to introduce an *Age*I restriction site (A6045T) were introduced into the vector (SY01.2) downstream of the neomycin cassette using the restriction enzymes *Sbf*I and *Age*I (Figure 16A). The *Age*I restriction site was created to facilitate confirmation of the presence of the V2303M point mutation (by restriction digestion with the *Age*I enzyme). The restriction enzyme *Sna*BI was then used to collapse the vector (D115.4a CV) by removing the sequence between the two restriction sites to produce the final targeting vector (D115.5 TV) (Figure 16B-C). The vector sequence was confirmed by Sanger sequencing of exonic regions and by restriction digestion with *Xma*I, *Nco*I, *Sph*I, *Bgl*II and *Bsp*HI (Figure 16C). The vector was then linearised by restriction digestion with *Not*I (Figure 16C).

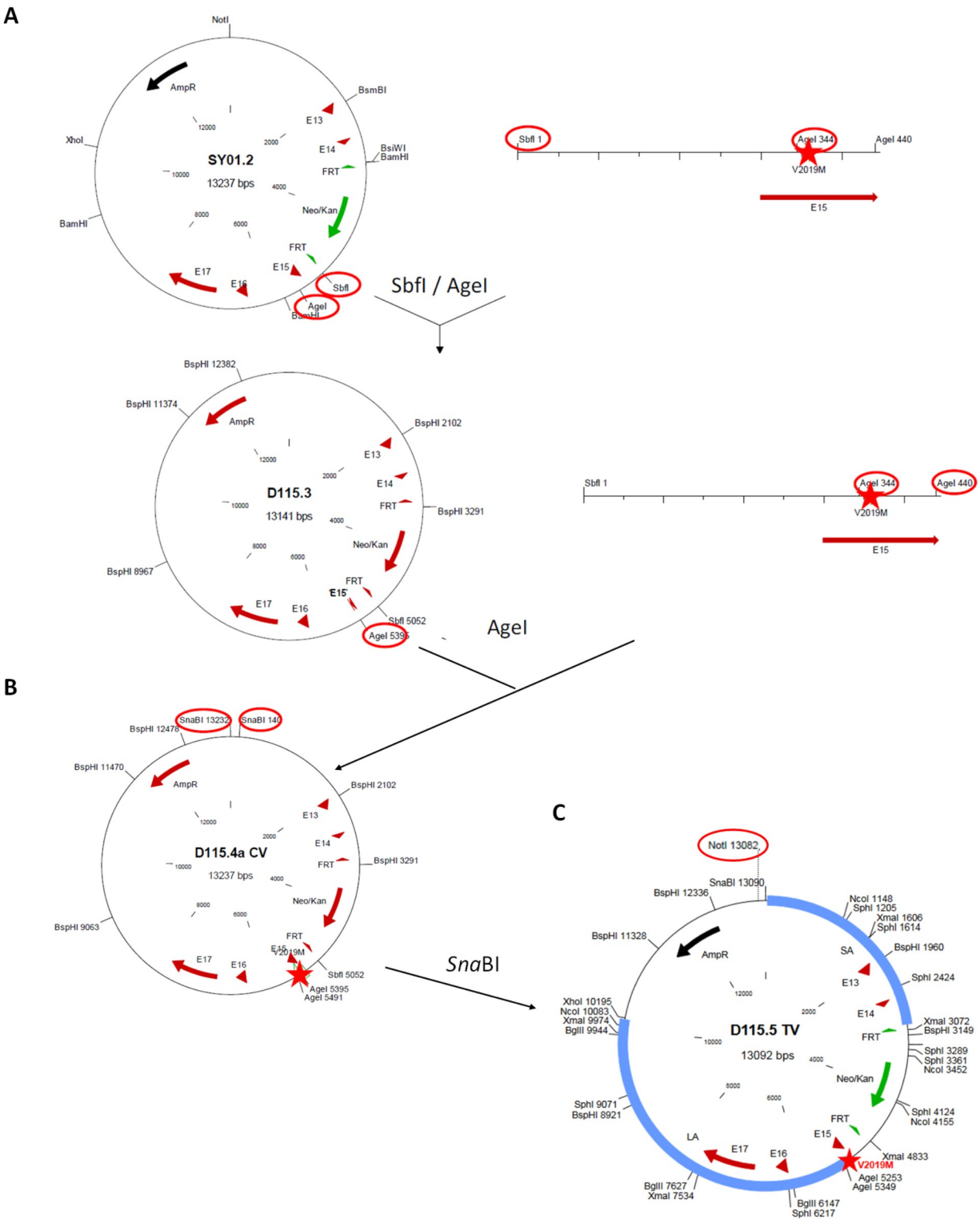

Figure 16 The genetargeting strategy for the generation of the OCD mice.

(A) The V2019M mutation (G6055A) and a silent mutation to introduce an *Age*I restriction site (A6045T) were introduced into the SY01.2 vector using the restriction enzymes *Sbf*I and *Age*I. **(B)** The sequence between the two *Sna*BI restriction sites was removed using the restriction enzymes *Sna*BI. **(C)** The final targeting vector for the generation of the OCD mouse. The restriction enzymes marked were used for confirmation of the vector sequence. The restriction enzyme *Not*I (highlighted in red) was used for vector linearisation. All diagrams kindly provided by Polygene Transgenetics.

Key: ★ point mutation ➡ FRT– flanked neomycin resistance cassette ▬ long/short arm of homology

2.3.3 Screening of the ES cells

The linearised targeting vectors were electroporated into 2.3 x 10^7 C57BL/6N-derived embryonic stem (ES) cells. The ES cells were then screened for the presence of either the OCD or SEMD targeting vectors as follows. The stably-transfected cells were selected for eight days with 0.3 mg/ml Geneticin and screened by polymerase chain reaction (PCR) using primer pair D115.2 (which bound outside the short arm of homology) and 5182LRPCR (which bound to the neomycin cassette) (Figure 17A). The positive clones were expanded and tested for homologous recombination on both homology arms by long-range PCR using the primer pair SY01.14 (which bound upstream of the long arm of homology) and LRPCRneo1 (which bound to the neomycin cassette) (Figure 17A) followed by restriction digestion with *Age*I and *Bam*HI. The restriction digestion of the PCR fragment with *Age*I was also used to test for the presence of the V2019M mutation as an *Age*I restriction digest site had been introduced into the vector with the mutation (Figure 17A). Semi-quantitative PCR (using primer pair D115.2 and 5182LRPCR) and restriction digestion with *Pvu*I were used to test for the presence of the D1983N mutation as a *Pvu*I restriction digest site had been introduced into the vector with the mutation (Figure 17A).

2.3.4 Blastocyst injection and implantation

The screened C57BL/6N clones were then injected into blastocysts from grey C57BL/6 mice and the surviving blastocysts implanted into CD-1 pseudopregnant foster mice. The offspring were assessed and the 100% chimeric mice (with 100% black coats) were mated to C57BL/6N based grey Flp-deleter mice. Flp-deleter mice express the site-specific recombinase FLP1 gene driven by the phosphoglycerate kinase 1 (*Pgk1*) promotor. Germline transmission was assessed based on coat colour (as black is dominant over grey) and offspring with black coats were screened by PCR (using primer pair SY01.P12 and SY01.P13) (Figure 17B-C) for Flp-mediated deletion of the FRT-flanked neomycin resistance cassette. The neomycin resistance cassette had been required as a positive drug marker during the antibiotic selection of ES cells, however it was removed to prevent any off-target effects such as disrupted expression of

nearby genes. Semi-quantitative PCR (using primer pair D115.3 and D115.4) and restriction digestion with *Age*I was used to test for germline transmission of the V2019M mutation (Figure 17). Semi-quantitative PCR (using primer pair SY01.15 and SY01.16) and restriction digestion with *Pvu*I was used to test for germline transmission of the D1983N mutation (Figure 17). Semi-quantitative PCR was used to screen for the presence of the FLP1-transgene (primer pair SD24 and SD25) (Figure 17).

2.4 Establishment of the OCD and SEMD mouse lines

Mice heterozygous for either 1) the SEMD (D1983N *Acan*) mutation or 2) the OCD (V2019M *Acan*) mutation (after Flp-mediated removal of the neomycin resistance cassette) and positive for the FLP1 transgene were transported to our facility for further breeding.

2.4.1 Tissue and genomic DNA extraction

An ear notcher was used to obtain ear tissue and allow identification of mice after 3 weeks of age. Tail or skin tissue was obtained post-mortem from pups under 3 weeks of age. Genomic DNA was then isolated from tissue according to the following hotshot protocol: 75 µl of cell lysis buffer was added to each tissue sample and incubated for 30 minutes at 95°C, followed by 10 minutes at 4°C; 75 µl of neutralising buffer was added and the samples vortexed to homogenise.

2.4.2 Semi-quantitative polymerase chain reaction (PCR)

This standard protocol was used for all subsequent PCR. The reactions were performed in thin-walled PCR plates with the following reagents per reaction: 7.4 µl ddH_2O, 10 µl of 2x Biomix red, 0.8 µl of 10nm forward oligonucleotide primer, 0.8 µl of 10nm reverse oligonucleotide primer. The master mix was briefly pipette mixed and 19 µl was added to each well. 1 µl of genomic DNA was then added per well. Genomic DNA extracted from a FLP1-

positive colony founder mouse heterozygous for the targeted mutant *Acan* amplicon (previously genotyped by Polygene Transgenetics) was used as a positive control and 1 µl of distilled water was used as a template-negative control. The samples were placed in a Labnet Multigene Optimax thermocycler with the appropriate cycling protocol (Appendix D). The DNA fragments were separated with horizontal gel electrophoresis.

2.4.2.1 Flp-mediated removal of the neomycin cassette

Semi-quantitative PCR with the primers P12 and P13 was used to check that Flp-mediated removal of the neomycin cassette from the targeted *Acan* allele had occurred. This PCR protocol was also used for the routine genotyping of mice from the OCD and SEMD mouse colonies. The expected size of the wild type amplicon was 434 bp and the expected size of the targeted mutant *Acan* amplicon (with only one FRT site remaining) was 545 bp (Figure 17).

2.4.2.2 Removal of the FLP transgene

The FLP1 transgene had been used during the generation of the knock-in mice to remove the neomycin cassette from the targeted *Acan* allele. Semi-quantitative PCR with the primers SD24 and SD25 was used to identify mice positive for the FLP1 transgene (with an expected amplicon of 500bp). Mice which were negative for the FLP1 transgene were then selected for breeding.

2.4.2.3 Confirming the presence of the point mutation

In order to confirm presence of either 1) the SEMD (D1983N *Acan*) mutation or 2) the OCD (V2019M *Acan*) mutation, semi-quantitative PCR was used in combination with restriction digestion with either the 1) *Pvu*I or 2) *Age*I restriction enzymes (as restriction digest sites were introduced with the mutations of interest). PCR using DNA extracted from mice heterozygous or homozygous for the SEMD mutant *Acan* allele was performed with the

primers SY01.15 and SY01.16 (Figure 17B). The expected amplicon was 617bp. Semi-quantitative PCR using DNA extracted from mice heterozygous or homozygous for the OCD mutant *Acan* allele was performed with the primers D115.3 and D115.4 (Figure 17C). The expected amplicon was 662bp.

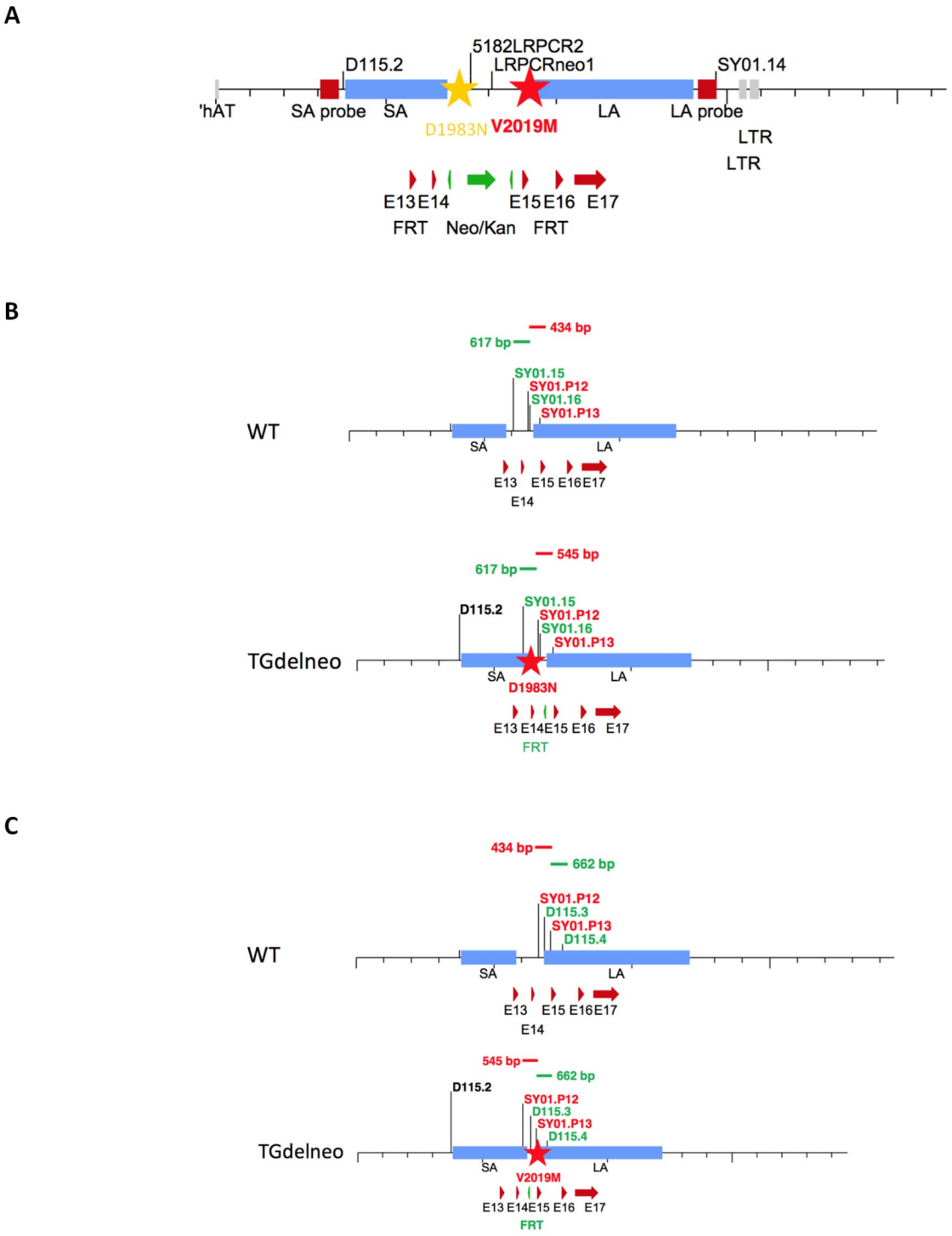

Figure 17 The PCR screening strategy.

(A) The targeted *Acan* locus. Primers D115.2 and 5182LRPCR2 were used for PCR screening of the recombined ES cells. Primers SY01.14 and LRPCRneo1 were used for long range PCR. **(B-C)** Screening of offspring after the mating of **(B)** SEMD or **(C)** OCD chimeras and Flp-deleter mice. The wild type *Acan* allele and the targeted allele after deletion of the neomycin cassette (Tgdelneo) are shown. Primers used for genotyping are indicated with PCR fragments in the corresponding colour. All diagrams kindly provided by Polygene Transgenetics.

Key: ★ ★ point mutation → FRT– flanked neomycin resistance ▬ cassette long/ short arm of homology

2.4.2.4 DNA extraction

A Qiagen DNA extraction kit was used to obtain DNA from the agarose gel according to the manufacturer's protocol. Briefly, the PCR products were separated using horizontal gel electrophoresis on a 1.5% agarose (w/v) gel at 30V for 30 minutes. The DNA bands were cut from the gel under UV light using a clean scalpel and weighed. 3 µl of QG buffer per mg of gel was added. The samples were incubated at 50°C for 10 minutes with vortexing every 2 minutes until the gel slice had dissolved. 1 µl of isopropanol per mg of gel was added in order to precipitate the DNA. The solution was then applied to a spin column and centrifuged at 13, 000 x g for 1 minute to bind the DNA to the column membrane. The flow-through was discarded and 500 µl QG buffer was applied to remove remaining agarose. The column was centrifuged at 13, 000 x g for 1 minute and the flow-through discarded. The column was washed with 750 µl PE buffer and centrifuged at 13, 000 x g for 1 minute to remove residual buffer. The column was placed into a clean Eppendorf and the DNA eluted in 30 µl of distilled water. The resultant DNA was then digested with the appropriate restriction enzymes.

2.4.2.5 Restriction digestion

The DNA fragments originally extracted from mice heterozygous or homozygous for either the 1) SEMD or 2) OCD mutant *Acan* allele were digested with the restriction enzyme 1) *Pvu*I or 2) *Age*I, respectively. A reaction mastermix was made with the following reagents: 14 µl of distilled water, 5 µl of 10x NEBuffer3.1, 1 µl of 10U/µl restriction enzyme and 30 µl of DNA. The reactions were then incubated at 37°C overnight. The DNA fragments were separated with horizontal gel electrophoresis. The expected size of the undigested SEMD DNA fragment was 617 bp. The expected size of the digested DNA fragments (those containing the SEMD D1983N mutation) was 349 bp and 268 bp. The expected size of the undigested OCD DNA fragment was 662 bp. The expected sizes of the mutant digested DNA fragments (those containing the OCD V2019M mutation) were 314, 252 and 96 bp. The expected sizes of the wild type digested DNA fragments (those not containing the V2019M mutation) were 410 and 252 bp.

2.4.3 Animal husbandry

Heterozygote mutant crosses were established to enable preliminary phenotypic comparison of littermates of all three genotypes (heterozygous mutant, homozygous mutant and wild type). This minimised the effect of environmental factors such as quality and abundance of milk provided by the female in each breeding pair during the pre-weaning phase of development. Defined crosses which produced offspring of a single genotype ((wild type or homozygous for the OCD (V2019M) allele)) were established for the collection of tissue and cells for culture *in vitro* and to reduce animal usage in line with the 3Rs principal of animal research (Flecknell 2002). Unfortunately, it was difficult to establish a defined cross for mice homozygous for the SEMD (D1983N) allele due to the high mortality rate during the first few days after birth. Breeding trios consisting of a homozygous mutant male, a homozygous mutant female and a heterozygous mutant female were more successful and pups born from each female survived to seven days of age. Pups were selected based on their visual appearance (relative size and craniofacial features) and the genotype confirmed by PCR analysis of DNA extracted from a tail tissue or skin biopsy. All mice were checked for teeth overgrowth upon weaning due to the high incidence of malocclusion in the C57BL/6 background strain. In addition to this, skeletal dysplasias can affect tooth formation (Dressler, Meyer-Marcotty et al. 2010, Low, Ansari et al. 2017) and so mice were monitored for tooth abnormalities throughout life. Mice with malocclusion had their teeth clipped every week and were provided with hydrated diet pellets to reduce the impact of dietary differences on weight and skeletal growth phenotype.

2.4.4 Generation of genotype ratios

The number of pups of each genotype per 100 pups born was counted from a minimum of five independent breeding pairs. The frequency of each genotype was then analysed statistically with a Chi-square test.

2.5 Phenotype analysis

Wild type mice and mice heterozygous and homozygous for the mutant *Acan* alleles were included in the preliminary phenotype analysis.

2.5.1 Generation of growth curves

Male and female adult mice were weighed at 3, 6 and 9 weeks of age in order to measure the rate of growth. The difference in the average mass of each genotype was statistically analysed with a Student's t-test.

2.5.2 Radiographical analysis

A Faxitron MX-20 digital X-ray machine was used to capture dorsal and lateral radiographs of mice at 1, 3, 6 and 9 weeks of age. Bone length measurements were obtained by analysing the original DICOM files using ImageJ (Schneider, Rasband et al. 2012) measurement tools in order to assess the length of the mandible, maxilla, tibia, femur, skull, pelvis (illium and ischium), the intercanthal distance (ICD) and the angle between the illium and the tuberosity of the ischium (Figure16A-B). The difference in the average bone length of each genotype was statistically analysed with a Student's t-test. The dorsal angle of spine curvature was measured with an adapted version of the Diab method in order to assess scoliosis (Figure16A). This method was chosen as other more widely used techniques, such as the Cobb and Ferguson methods, rely on manual identification of the end vertebrae (Diab, Sevastik et al. 1995). The difference in the average dorsal angle of each genotype was statistically analysed with a Student's t-test. The Grubbs' test function in Graphpad Prism was used to detect significant outliers within the data set for each genotype.

2.5.3 Histological and morphometric analysis of skeletal preparations

Neonatal skeletal preparations were generated to assess the number and organisation of early skeletal components. Newborn mice were culled by overdose of isoflurane anaesthetic and placed in tap water for 24 hours at 4°C. Each pup was scalded in 65-70°C tap water for 30 seconds and the skin and viscera removed. Preparations were placed into a 6 well tissue culture plate and fixed in 95% ethanol for 3 to 5 days. The pups were then stained with Alcian Blue (Appendix C) for 24 hours, rinsed twice with 95% ethanol and incubated in 95%ethanol for 48 hours. The preparations were cleared in 1% (w/v) potassium hydroxide for 6 hours, stained with Alizarin Red (Appendix C) for 3 hours and cleared in 2% (w/v) potassium hydroxide for 48 hours. The pups were then incubated in 80:20 2% KOH:glycerol for 24 hours followed by incubation in 60:40 2% KOH:glycerol for 24 hours and 40:60 2% KOH:glycerol for 24 hours. Each preparation was then stored in 20:80 2% KOH:glycerol. Images of the neonatal skeletal preparations were taken using a Zeiss Stemi SV6 dissecting microscope. Bone measurements were obtained by analysing the original ZVI files with ImageJ measurement tools to assess the length of the femoral and tibial bones (Figure 18C). The difference in the average bone length of each genotype was statistically analysed with a Student's t-test.

2.5.4 Histological and morphometric analysis of skull preparations

Alizarin Red and Alcian Blue were used to stain the calcified bone and proteoglycans in the cartilage respectively in order to analyse the ossification patterns and the size and shape of the skull bones. Mice were culled by an appropriate Schedule 1 method. Skulls were dissected from male mice at 3 weeks of age, the skulls skinned and loose soft tissue and eyes removed. The skulls were then fixed in 4% paraformaldehyde for 48 hours at 4°C and incubated in Alcian blue for 24 hours. Samples were then post-fixed in 95% ethanol for 48 hours and incubated in 1% potassium hydroxide to remove the remaining soft tissue, changing the solution every few days. Once the majority of soft tissues were removed, the skulls were incubated in Alizarin red for 24 hours. The samples were incubated in 1% potassium hydroxide to remove the remaining soft tissue, changing the solution every few days, until all the soft tissue was removed. The mandible was removed by severing the

attached ligaments in order to allow the skull to lie flat for imaging. Skulls were imaged with a Zeiss Stemi SV6 dissecting microscope. Bone measurements were obtained by analysing the original ZVI files with ImageJ measurement tools to assess the length and width of the nasal, parietal and frontal bones (Figure 18D, protocol modified from Kawakami and Yamamura 2008). The difference in the average bone length or width of each genotype was statistically analysed with a Student's t-test.

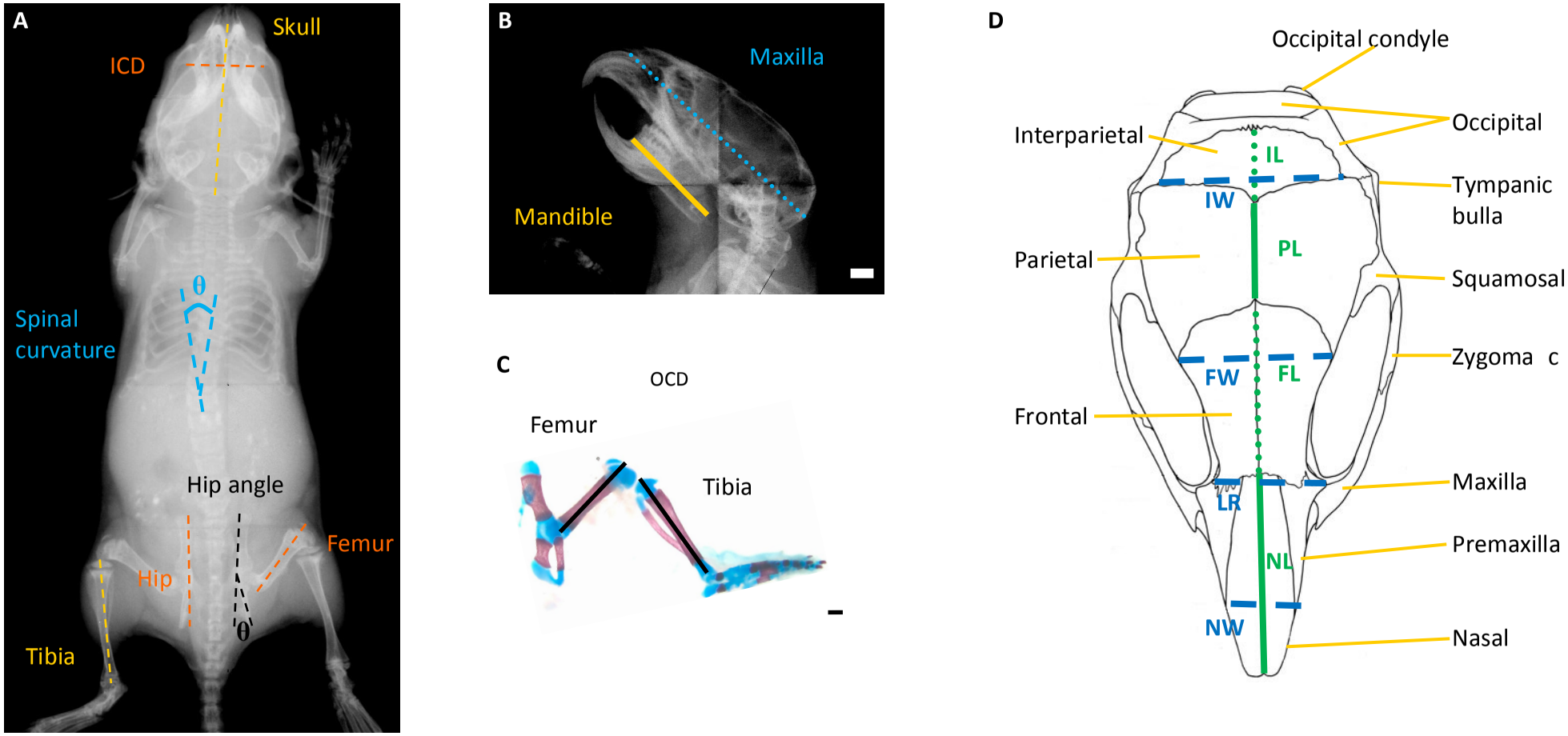

Figure 18 Bone morphometric analysis.

(A) Bone length measurements, the angle of the hip between the ilium and the tuberosity of the ischium and the angle of spinal curvature were measured using dorsal radiographs, scale bar = 2mm. **(B)** The length of the maxilla and mandible were measured using lateral radiographs, scale bar = 2mm. **(C)** Neonatal bone lengths were measured from histological prepara ons, scale bar = 50µm. **(D)** Skull bone parameters (Modifi d from Cook, 1965). Key: NW (nasal bone width) LR (distance between the antero-lateral corners of the frontal bone) FW (frontal bone width) IW (interparietal bone width) NL (nasal bone length) FL (sagi al frontal bone length) PL (sagi al parietal bone length) IL (interparietal bone length).

2.6 Histological analysis

All staining was performed manually, except toluidine blue and haematoxylin and eosin staining which was performed using a Linistat linear automated stainer. Images of all tissue sections were taken using a Zeiss Axioplan or Z2 Axioimager microscope.

2.6.1 Tissue dissection and preparation

Mice were culled by an appropriate Schedule 1 method. Tissues were dissected and fixed in 95% ethanol and 5% acetic acid (immunohistochemistry) or 4% paraformaldehyde (histology) for 48 hours at 4°C. Skeletal samples were decalcified for 14 days in 20% ethylenediaminetetraacetic acid (EDTA, pH 7.4) and washed under running tap water for an hour to remove any residual EDTA. The samples were placed in a Thermo Scientific Spin Tissue Processor to infiltrate with paraffin before embedding (Appendix E). The tissue samples were embedded in paraffin wax and sectioned on a sagittal (joint samples) or frontal (IVD samples) plane in 6μm thick sections with a Thermo Scientific Automatic Rotary microtome. The slides were air-dried, heated to 64°C to increase tissue adherence to the slide and then air dried again.

2.6.2 Haematoxylin and Eosin staining

Harris' modified Haematoxylin and Eosin Y were used to investigate cell morphology and the structure of the growth plate, articular surface and intervertebral disc (IVD). A linistat linear automated stainer was used (Appendix F). The joint areas were matched by morphological assessment of 5 slides per animal. Slides were dewaxed with two 5 minute washes of xylene. The tissue sections were then rehydrated with decreasing concentrations of ethanol and one wash of water. The slides were incubated in filtered Harris' modified haematoxylin and rinsed with alkaline tap water. Differentiation was achieved by washing in 1% acid alcohol. The tissue was then rinsed with water, counterstained with filtered Eosin Y and rinsed with water to remove the excess stain. The tissue sections were dehydrated with

increasing concentrations of ethanol and then cleared with two 5 minute washes of xylene. The slides were then mounted using Vectamount mounting media and 22 x 55 mm coverslips and dried overnight.

This method stains the cell nuclei blue, cytoplasm pink and the surrounding cartilage matrix a light purple/pink.

2.6.3 Quantification of the growth plate

A Zeiss Z2 Axioimager microscope was used to take tiled images of the entire tibial growth plate which were then stitched together for analysis. At least one section from each of the three regions of the joint compartment was selected (3-5 mice per genotype). ImageJ measurement tools were used to measure the total growth plate height, the height of each zone (resting, proliferative and hypertrophic) (Figure 19A) and the mineralised area of the secondary ossification centre (Figure 19B). Height measurements were taken as an average of three measurements of the central section of the growth plate (avoiding the perichondrium). The difference in the average height or area of each genotype was statistically analysed with a Student's t-test.

2.6.4 Quantification of the thoracic vertebral column

A Zeiss Axioplan microscope was used to take overlapping images of the vertebral column and the Photoshop photomerge function was used to produce a reconstruction of the entire thoracic spine. ImageJ measurement tools were used to measure the height and width of each vertebral body, the height of the mid-region in each intervertebral disc and the height and width of the nucleus pulposus (Figure 1C). Measurements were taken as an average of five vertebral bodies or discs per mouse. The difference in the average of each parameter was statistically analysed with a Student's t-test (4-5 mice per genotype).

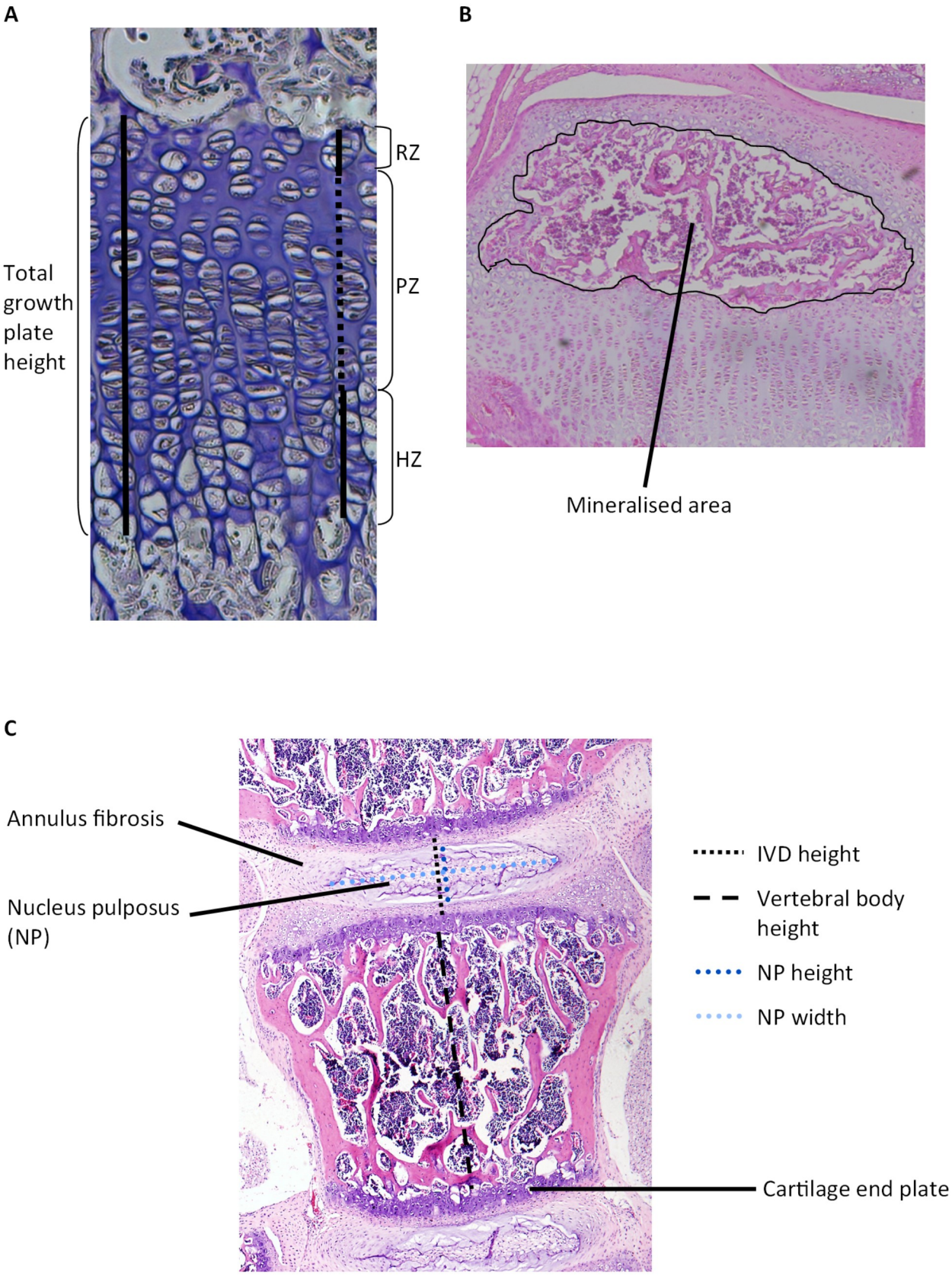

Figure 19 Quantification of the cartilage growth plate and the thoracic spine.

(A) Measurement of the total growth plate height and the height of each individual zone. **(B)** Measurement of the mineralised area of the secondary ossification centre. **(C)** Measurement of the vertebral body and the intervertebral disc (IVD).

Key: RZ (resting zone) PZ (proliferation zone) HZ (hypertrophic zone)

2.6.5 Scoring for intervertebral disc degeneration

Intervertebral discs (IVD) were assessed for degenerative changes by one new and two experienced scorers using an established histo-morphometric technique (Tam, Chan et al. 2018). The individual components of the IVD (annulus fibrosis, nucleus pulposus) were scored for morphological features associated with either normal disc structure or degenerative changes. Normal disc morphology was scored with a value of 0 and degenerative features scored according to severity. Morphological features associated with degeneration included the formation of fissures or clefts, loss of boundary between the annulus fibrosis and nucleus pulposus and cell loss within the nucleus pulposus. The average score was calculated for each disc component (maximum score of 6) the annulus fibrosis- nucleus pulposus boundary (maximum score of 2) and the entire IVD (maximum score of 14). The difference in the average of each score was statistically analysed with a Student's t-test (3-5 mice per genotype).

2.6.6 Toluidine Blue staining

The histological stain Toluidine Blue was used to look at the relative abundance of proteoglycans and glycosaminoglycans. A linistat linear automated stainer was used (Appendix F). Each slide was dewaxed with two 5 minute washes of xylene. The tissue sections were then rehydrated with decreasing concentrations of ethanol and one wash of distilled water. The slides were incubated in Toluidine Blue (Appendix C) and rinsed with one wash of distilled water. The tissue was counterstained with Nuclear Fast Red and rinsed with two washes of distilled water to remove the excess stain. The tissue sections were then dehydrated with increasing concentrations of ethanol and cleared with two 5 minute washes of xylene. The slides were then mounted using Vectamount mounting media and 22 x55mm coverslips and dried overnight.

This method stains the cytoplasm blue and the cell nuclei and surrounding cartilage matrix purple.

2.6.7 Picro-Sirius Red staining

An Abcam Picro-Sirius Red kit was used to look at the relative abundance, orientation and diameter of collagen fibrils by exploiting the bifringence of collagen under polarised light. The manufacturer's protocol was used as follows. Each slide was dewaxed with two 5 minute washes of xylene. The tissue sections were then rehydrated with decreasing concentrations of ethanol and two washes of distilled water. The slides were incubated in Picro-Sirius Red for one hour and rinsed with two changes of 0.5% acetic acid. The slides were shaken vigorously to remove excess water, dehydrated with 3 changes of 100% ethanol and cleared with two 5 minute washes of xylene. The slides were then mounted using Vectamount mounting media and 22 x55mm coverslips and dried overnight. Images of tissue sections were taken using a Leica DM2700 microscope under polarised light.

When observed under polarised light this method stains larger collagen fibers orange/red and thinner fibres green.

2.6.8 Von Kossa staining

Von Kossa staining was performed on calcified tissue in order to assess calcium and calcium salt deposition as a marker of bone mineralisation. Each slide was dewaxed with two 5 minute washes of xylene and rehydrated with decreasing concentrations of ethanol and two washes of distilled water. Tissue sections were incubated for 20 minutes in 1% (w/v) Silver Nitrate under ultra violet (UV) light. The sections were rinsed with distilled water, incubated in 1% (w/v) sodium thiosulphate for 5 minutes to remove unreacted silver and washed again with distilled water. Slides were counterstained with Nuclear Fast Red and dehydrated with 1 change each of 90% and 100% ethanol. Slides were cleared with two 5 minute washes of xylene and mounted using Vectamount mounting media and 22 x55mm coverslips before drying overnight.

This method stains calcium and calcium salts brown/black.

2.6.9 Tartrate-resistant acid phosphatase (TRAP) staining

A Sigma Aldrich acid phosphatase kit was used to assess the abundance of the osteoclast marker tartrate-resistant acid phosphatase and the manufacturer's protocol was followed with a few modifications. In summary, each slide was dewaxed with two 5 minute washes of xylene and rehydrated with decreasing concentrations of ethanol and two washes of distilled water. The sections were incubated in pre-warmed (37^{o}C) TRAP staining solution for 1 hour protected from light then rinsed in distilled water for 5 minutes and counterstained with Fast Green solution. The tissue sections were then rinsed thoroughly and dehydrated in 95% and 100% ethanol. Slides were cleared with two 5 minute washes of xylene and mounted using Vectamount mounting media and 22 x55mm coverslips before drying overnight.

This method stains cells containing tartrate acid-resistant phosphatase red/purple.

2.6.10 Safranin O staining

Safranin O was used to assess relative proteoglycan loss in the articular cartilage. The growth plate was used as an internal control between individuals of the same genotype. Each slide was dewaxed with two 5 minute washes of xylene and rehydrated with decreasing concentrations of ethanol. The nuclei were stained with Weigert's iron hematoxylin for 10 minutes and excess staining solution removed by washing under running tap water for 10 minutes. The slides were counterstained with 0.05% fast green for 5 minutes and briefly decolourised with 1% acetic acid for 10–15 seconds. Tissue sections were stained with 0.25% safranin O solution for 5 minutes and dehydrated with 2 changes of 95% ethanol and 100% ethanol for 2 minutes. Slides were then cleared with two 5 minute washes of xylene and mounted using Vectamount mounting media and 22 x55mm coverslips before drying overnight.

This method stains cell nuclei black, cytoplasm grey/green and the proteoglycan in the cartilage matrix red.

2.6.11 Immunofluorescent analysis

Primary antibodies used for the analysis of tibial tissue were against aggrecan, COMP, matrilin 3, collagen type IX, collagen type X, collagen type II, LC3 and IHH (Appendix B). Each slide was dewaxed with two 5 minute washes of xylene. The tissue sections were then rehydrated with decreasing concentrations of ethanol and two washes of distilled water. The tissue sections were washed with two 3 minute washes of phosphate-buffered saline (PBS). An ImmEdge hydrophobic barrier pen was used to mark around the sections in order to reduce the volume of reagents required. All incubations after this point were performed with the slides in a humidified chamber in the dark. Tissue sections were incubated with bovine hyaluronidase (0.2% in 1x PBS) for 30 minutes (for antigen retrieval) and then rinsed with three 2 minute PBS washes. Further antigen retrieval was performed with incubation in 10 µg/ml proteinase K for 5 minutes, followed by three 2 minute PBS washes. Sections were then incubated for one hour with 1% bovine serum albumin (BSA), 0.6% serum and 0.3% Triton X-100 in 1x PBS. The tissue sections were then incubated with primary antibody (in 1% BSA, 0.3% Triton X-100, 1x PBS) overnight at 4°C. Slides were rinsed with two 5 minute washes of 1% BSA in PBS and incubated with a fluorescent AlexaFluor secondary antibody (1% BSA, 0.6% serum, 1x PBS) for one hour at room temperature. The tissue sections were rinsed with three 5 minute washes of PBS. The slides were then mounted using Fluoroshield mounting media (with DAPI to counterstain the cell nuclei) and 22 x55mm coverslips and dried overnight in the dark.

2.6.12 Bromodeoxyuridine labelling and detection

The thymidine analog 5-bromo-2-deoxyuridine (BrdU) was used to analyse chondrocyte proliferation. 3 week old mice were injected subcutaneously with 0.1ml of BrdU reagent per 10g of mouse mass. The mice were left for 130 minutes to allow the BrdU to incorporate into the DNA during S-phase and then culled. The legs were dissected out and the tissue processed as per the protocol for immunohistological analysis. Each slide was dewaxed with two 5 minute washes of xylene. The tissue sections were then rehydrated with decreasing concentrations of ethanol and two washes of distilled water before three 5 minute washes of phosphate-buffered saline (PBS). The DNA in the tissue sections was denatured by a 15 minute incubation in 4M hydrochloric acid. The acid was then neutralised by incubation in 0.1M

borate buffer for 5 minutes, followed by three 2 minute washes of PBS. An ImmEdge hydrophobic barrier pen was used to mark around the sections in order to reduce the volume of reagents required. All incubations after this point were performed with the slides in a humidified chamber in the dark. Tissue sections were blocked with 4% donkey serum in 1x PBS for 20 minutes to prevent non-specific binding. The tissue sections were incubated with primary antibody (1% BSA in 1x PBS) for one hour and then rinsed with two 5 minute washes of PBS. The slides were then incubated with an Alexafluor fluorescent secondary antibody for 1 hour and then rinsed with two 5 minute washes of PBS. The slides were mounted with Fluoroshield DAPI mounting medium (to counter-stain the nuclei) and 22 x55mm coverslips and dried overnight in the dark. A Zeiss Z2 Axioimager microscope was used to take images of the entire tibial growth plate which were then stitched together for analysis in ImageJ using the cell counter (Schneider, Rasband et al. 2012) and the Watershed plug-in (Soille and Vincent 1990). The number of fluorescent cells was counted as a percentage of the total number of DAPI stained cells in the proliferative zone. The percentage of fluorescent proliferating cells in a mutant growth plate was then compared with that of a wild type mouse and statistically analysed with a Student's t-test.

2.6.13 Terminal deoxynucleotidyl transferase dUTP nick end labelling (TUNEL)

The Dead End Fluorimetric TUNEL system was used to assess apoptosis. The manufacturer's protocol was followed with some modifications as follows. Each slide was dewaxed with two 5 minute washes of xylene. The tissue sections were then rehydrated with decreasing concentrations of ethanol, a five minute wash of 0.85% sodium chloride and a five minute wash of PBS. The tissue sections were then post-fixed with a 15 minute incubation in 4% paraformaldehyde. The tissue sections were then rinsed with two 5 minute washes of PBS and boiled in citric buffer for 12 minutes to allow antigen retrieval. The slides were then rinsed in PBS for five minutes, post-fixed in 4% paraformaldehyde for five minutes and washed with PBS for five minutes. An ImmEdge hydrophobic barrier pen was used to mark around the sections in order to reduce the volume of reagents required. All incubations after this point were performed with the slides in a humidified chamber in the dark. In order to produce a positive control one slide was treated with DNase I in order to fragment the DNA. The slide

was incubated firstly in DNase I buffer for five minutes, then DNase I (in DNase buffer) for ten minutes and rinsed with three washes of dH_2O. All of the slides were incubated for 5 minutes with equilibration buffer. The TdT master mix was then added and the slides incubated at 37C for 1 hour. The slides were incubated in SSC buffer for 15 minutes to stop the reaction and then washed with three 5 minute washes of PBS. The slides were then mounted in Fluoroshield (with DAPI to counterstain the nuclei) and 22 x 55mm coverslips and dried overnight. A Zeiss Z2 Axioimager microscope was used to take images of the entire tibial growth plate which were then stitched together for analysis in ImageJ using the cell counter and watershed plug-in. The number of cells with fluorescein-12-dUTP- labeled DNA in each zone was counted as a percentage of the total number of DAPI stained cells in each zone. The percentage of fluorescent cells per zone in a mutant growth plate was then compared with that of a wild type mouse and statistically analysed with a Student's t-test.

2.6.14 Transmission electron microscopy

The structure of the cartilage extracellular matrix was analysed with transmission electron microscopy. Mice were culled by neck dislocation at 7 days of age. The cartilage was dissected and cut into 1mm by 2mm pieces of tissue. The tissue was fixed in 2% glutaraldehyde in sodium cacodylate buffer at 4°C for 14 days. The following protocol was then performed by staff at Newcastle University Electron Microscopy Research Services. The samples were post-fixed with 1% osmium tetroxide to preserve the lipid content and add contrast to the tissue. The tissue was dehydrated with increasing concentrations of acetone, impregnated with increasing concentrations of resin in acetone and embedded in resin at 60°C for 24 hours. 0.5µm survey sections were cut and stained with 1% toluidine blue in 1% borax to visualise the growth plate. 70nm sections were then cut with a diamond knife on either an RMC MT-XL or Leica EM UC7 ultramicrotome. The sections were stretched with chloroform to prevent compression and mounted in pioloform-filmed copper grids. The tissue was then stained with 2% aqueous uranyl acetate and lead citrate. The tissue was analysed with a Philips CM100 Compustage (FEI) Transmission Electron Microscope and an AMT CCD camera (Deben). It is important to note that the fixation methods used here do not preserve the proteoglycan content of the cartilage (Hunziker, Lippuner et al. 2014). The Photoshop photomerge function was used to produce a growth plate reconstruction.

2.7 Transcriptome analysis

2.7.1 Cartilage tissue extraction

Mice were culled by neck dislocation at 5 days of age. Each leg was skinned, the femur severed 5mm above the knee and the tibia cut at the ankle. The muscle and fibrous tissues were removed if possible and the remaining tissue incubated in 250µl collagenase at 37°C for 50 minutes. The tissue was then placed in warm phosphate-buffered saline (PBS) and dissected under a Leica MZ 12.5 stereomicroscope to remove any remaining muscle and fibrous tissue. A clean scalpel was then used to separate the cartilage from the bone by a single cut at the bone-cartilage interface. The cartilage was snap-frozen in liquid nitrogen and stored at -80°C until required for RNA isolation.

2.7.2 Total RNA extraction

Total RNA was isolated from the cartilage tissue using the Promega ReliaPREP RNA tissue miniprep system. The manufacturer's protocol was used as follows. A Sartorius Mikro-dismembranator S tissue homogeniser was used to disrupt the frozen cartilage's tissue structure in flash frozen lysis buffer. The tissue was then allowed to thaw directly into the tissue lysis buffer in order to protect the integrity of the RNA and release the RNA into solution free of associated protein. The DNA was then sheared with pipetting and the sample diluted with an equal volume of RNA dilution buffer, vortexed and incubated for 1 minute. The sample was centrifuged for 3 minutes at 10, 000 x g to pellet insoluble cell debris and the cleared lysate transferred to a clean eppendorf. The RNA was precipitated with the addition of 340µl isopropanol and applied to the minicolumn. The column was centrifuged for 1 minute at 13, 000 x g to bind the RNA to the membrane and incubated with RNase-free DNase I in order to remove any genomic DNA. The column was then washed several times to remove any other contaminants. The RNA was eluted with Nuclease-Free Water and assessed with an Agilent 2100 Bioanalyser for quantity and quality. Samples with an RNA integrity number (RIN) of 7 or above were used for downstream transcriptome analysis (Appendix H).

2.7.3 Next-generation sequencing and bioinformatic transcriptome analysis

Next-generation RNA sequencing (RNA-seq) was performed in order to analyse the mutant transcriptome and identify possible disease mechanisms. In-house RNA-sequencing for differential gene expression analysis was performed by Newcastle University Genomics Core Facility using an Illumine NextSeq 500 sequencer. 220 ng of DNAse-treated total RNA was used per sample. Total RNA was pooled from two mice per sample and three samples (from three different litters) were sequenced per genotype to allow downstream statistical analysis. 15-23,000,000 reads were obtained per sample. In-house transcriptome analysis was performed by the Newcastle University Bioinformatics Support Unit. The MultiQC (FastQC) tool was used for quality control. Alignment free quantification and counting were both used for mapping and quantification. Kallisto 0.43.0 was used for alignment free quantification. Alignment was finished with a STAR 1-Pass protocol and the features counted with HTSeq-Count. Principal component analysis (PCA) was applied to normalised data (Appendix H). Differential gene expression modelling was performed with DESeq2. Further pathway enrichment analysis was then performed by myself using the database for annotation, visualisation and integrated discovery (DAVID) functional annotation tool to identify GO terms (Huang da, Sherman et al. 2009). REVIGO was then applied to cluster redundant GO terms (Supek, Bošnjak et al. 2011)

2.8 Tissue culture

All tissue culture was performed in Class II tissue hood. All tissue cultures were incubated at 37°C and 5% CO_2 in a humidified atmosphere. Cartilage explants and cells were grown in maintenance media (Appendix C). L-ascorbic acid 2-phosphate sesquimagnesium salt was used to enhance the chondrocytes' collagen type II production at both a transcription and post-transcriptional level. Further to this, chondrocytes are stereo-selective for the L-forms and ascorbic acid is unstable at 37°C (88-98% disappear within 24 hours) and so fresh media was added every 24 hours (Anderson, McLean et al. 1991, McNulty, Vail et al. 2005).

2.8.1 Chondrocyte extraction

Mice were culled by neck dislocation at 7 days of age. The mice were dissected, the rib cages isolated and placed in warm PBS. The tissue was then dissected under a Leica MZ 12.5 stereomicroscope to remove any remaining soft tissue. A clean scalpel was used to separate the cartilage from the bone by a single cut at the bone-cartilage interface. The pieces of cartilage were incubated in 3 mg/ml collagenase for 45 minutes at 37°C and 5% CO_2 in a humidified atmosphere. The tissue samples were agitated with a 25 ml pipette to assist in the removal of soft tissue and the translucent cartilage transferred to a clean 6 well tissue culture plate. The cartilage was incubated in 0.5 mg/ml collagenase overnight at 37°C and 5% CO_2 in a humidified atmosphere to digest the extracellular matrix around the chondrocytes. 25 ml of maintenance media was added to dilute the collagenase and decrease the rate of digestion. The cell suspension was agitated through decreasing sizes of pipettes to disperse cell aggregates and filtered through a 48 µm cell strainer. The cell suspension was centrifuged for 10 minutes at 400 x g. The media was removed and the cell pellet washed with PBS and resuspended in 1 ml of maintenance media per animal. 5 µl of Trypan blue, which selectively stains dead cells, was added to 15 µl of cell suspension in order to assess cell viability. The suspension was pipetted into a FastRead 102 disposable haemocytometer and visualised under a Nikon Eclipse TS100 microscope. The number of live cells (those not stained dark blue) was counted in four squares and the total number of viable cells extracted was calculated according to the following calculation:

$$\text{counts/ml} = \text{total counts} \times 10^4 \times \text{sample dilution}$$

The chondrocytes were seeded in a 6 well plate at a density of 25×10^3 cells/cm^2.

2.8.2 Drug treatment

None of the drugs used were sterilised as they were all dissolved in 100% tissue-culture standard DMSO which has exhibited anti-microbial activity (Howard, William et al. 1969).

2.8.2.1 Autophagy inhibition

Drug treatment was performed in cartilage explants. Briefly, mice were culled by neck dislocation at 7 days of age. Each leg was skinned, the femur severed 5mm above the knee and the tibia cut at the ankle. The tissue was then placed in warm PBS and dissected under a Leica MZ 12.5 stereomicroscope to remove any remaining muscle and fibrous tissue. A clean scalpel was then used to separate the cartilage from the bone by a single cut at the bone-cartilage interface. The cartilage explants were incubated overnight in maintenance media and then washed with PBS twice before transfer to a clean 24 well plate. To inhibit the autophagy pathway the end-stage autophagy inhibitor chloroquine was used. Chloroquine prevents the fusion of the lysosome with the autophagasome leading to the accumulation of the autophagic vesicles. Cartilage explants were incubated in maintenance media supplemented with 250μM chloroquine for 0, 1, 3 and 6 hours. After chloroquine treatment the cartilage tissue was rinsed twice in PBS and centrifuged at 800 x g for 5 minutes to remove any residual media. The cartilage was then snap-frozen and stored at -80°C until required for protein extraction.

2.8.2.2 Carbamazepine

Carbamazepine (CBZ) has been shown to reduce intracellular protein retention and endoplasmic reticulum stress in a mouse model of Schmid metaphyseal chondrodysplasia (MSDS) by stimulating the mTORC-independent autophagy and proteasomal protein degradation pathways (Mullan, Mularczyk et al. 2017). It was not possible to use an *in vivo* drug treatment protocol as mice homozygous for the OCD and SEMD mutations were below the minimum weight threshold (10 kg) for subcutaneous drug pellet implantation (using the pellets available). Tissue explants were therefore used as an alternative in order to assess tissue pathology and bone length. Mice were culled by neck dislocation at 7 days of age and the entire leg dissected out and skinned. Explants were incubated for two weeks in maintenance media supplemented with 200μM CBZ. After CBZ treatment the cartilage tissue was rinsed in dH2O, x-rayed to facilitate bone length measurements and processed for downstream histology.

2.9 Immunoblotting

2.9.1 Sequential protein extraction

Mice were culled by an appropriate Schedule 1 method at three weeks of age. Two femoral heads were dissected per mouse and three mice were used per genotype. Samples were snap-frozen in liquid nitrogen and stored at -80°C until required for use. The femoral heads were cut into small pieces with a scalpel, transferred to a pre-weighed clean eppendorf and weighed. All buffers were pre-chilled to 4°C before use. The appropriate amount of Buffer I (Appendix C) per weight was added and samples rotated at 4°C for six hours. The samples were then centrifuged for 5 minutes at 13, 000 x g and 4°C. The supernatant was removed in 100 µl aliquots and stored at -20°C. The pellet was resuspended in an appropriate amount of Buffer II per weight, vortexed vigorously and rotated at 4°C overnight. The samples were then centrifuged for 5 minutes at 13, 000 x g and 4°C. The supernatant was removed in 100 µl aliquots and stored at -20°C. The pellet was resuspended in an appropriate amount of Buffer III per weight, vortexed vigorously and rotated at 4°C for six hours. The samples were then centrifuged for 5 minutes at 13, 000 x g and 4°C. The supernatant was removed in 100µl aliquots and stored at -20°C. All protein samples were ethanol precipitated. Briefly, 1.4ml 95% ethanol was added to each supernatant aliquot, mixed with gentle agitation (without vortexing) and incubated overnight at 4°C. The samples were then centrifuged for 15 minutes at 13, 000 x g and 4°C and the supernatant removed with a syringe. 1 ml of wash solution (Appendix C) was added and the sample vortexed to dissociate the pellet before incubation for one hour. The samples were centrifuged for 15 minutes at 13, 000 x g and 4°C and the supernatant removed with a syringe. The samples were briefly centrifuged and the remaining wash solution removed with a syringe. The pellets were air dried, resuspended in 20µl dH2O. 5 µl 5x SDS-PAGE loading buffer (Appendix C) and 1 µl 1M dithiothreitol (DTT) (if under reducing conditions) were added and the samples incubated for 10 minutes at 95°C before analysis by Western Blotting.

2.9.2 Total protein extraction and quantification: tissue

A Sartorius Mikro-dismembrator S tissue homogeniser was used to disrupt the flash frozen cartilage. The vessel and ball bearing were pre-cooled in liquid nitrogen. The frozen cartilage tissue was then added to the vessels with 100µl flash frozen PBS and homogenised for 1 minute at a shaking frequency of 1500 rpm. The tissue was allowed to thaw directly into the PBS and stored at -20°C. A Pierce BCA protein assay was used to quantify the extracted protein and the manufacturer's protocol was performed as follows. Bovine serum albumin (BSA) was diluted in the same diluent as the samples to produce a range of protein standards (Appendix G). 25 µl of the samples and protein standards were pipetted into a 96 well plate in duplicate. The BCA working reagent was prepared by adding 1 part of BCA reagent B to 50 parts of BCA reagent A. 200 µl of working reagent was added to each well and vortexed for 30 seconds. The plate was then incubated for 30 minutes at 37°C and allowed to cool to room temperature. A Thermoscientific Varioskan Lux plate reader was used to measure the absorbance at 562 nm wavelength. The average absorbance of protein standard I (the blank) was subtracted from the average absorbance of the standards and the samples. A standard curve was plotted of the average blank-corrected absorbance of the standards against the BSA standard concentrations (µg/ml). Polynomial regression was performed to produce a polynomial trendline. The coefficient of multiple determination was required to be above 0.99 to ensure that the standard curve was a good fit to the data points. The resultant equation was used to determine the protein concentration of each sample.

2.9.3 Total protein extraction and quantification: cells

The cell culture media was removed, centrifuged at 800 x g for 4 minutes to pellet any cell debris and then stored at -20°C. The cells were washed twice with pre-warmed PBS and incubated on ice with 1 ml radioimmunoprecipitation assay (RIPA) buffer (Appendix C) for 15 minutes to lyse the cells. A cell scraper and pipette were then used to remove the cells and the cell suspension was centrifuged at 13, 000 x g for 10 minutes at 4°C to pellet the cell debris. A Thermoscientific nanodrop 1000 spectrophotometer was used to quantify the protein extracted in the supernatant by measuring the absorbance of the sample at 280nm. Equal

volumes of media (100 µl) were concentrated to 20 µl using a Thermo Scientific Savant DNA 120 speedvac concentrator. 15-25 µg cell lysate or 20 µl of media was added to 5 µl 5x sample buffer and 1 µl 1M DTT (to reduce disulfide bonds). Distilled water was then added to a total volume of 25 µl. The samples were denatured at 95°C for 10 minutes.

2.9.4 SDS-PAGE

Sodium dodecyl sulfate polyacrylamide gel electrophoresis (SDS-PAGE) was used to separate the extracted proteins according to their size (Blancher and Jones 2001). Novex 4-12% Bis-Tris precast gradient gels were used and the electrophoresis was performed in MES buffer. 5 µl of pre-stained molecular weight marker or 25 µl of sample were loaded per well, with 5 µl of sample buffer added to empty wells to avoid lane distortion. The gel was run at 200V for 60 minutes. The proteins were then transferred to a nitrocellulose membrane with the appropriate pore size (0.45µm or 0.2µm depending on protein size) to enable detection with antibodies. A Novex transfer module was assembled (Figure 20). Each of the components was soaked in 1x transfer buffer and protein transfer was performed in 1x transfer buffer at 30V for 60 minutes. The membrane was incubated in REVERT total protein stain for 5-10 minutes with agitation in order to check equal protein loading and visualised with a LICOR Oyssey CLx (Appendix G). The membrane was blocked with blocking buffer (Appendix C) for 1 hour with agitation. Primary antibodies were diluted as appropriate (Appendix D) in blocking buffer and the membrane incubated overnight at 4°C with agitation. The membrane was washed with six 5 minute PBS-T (Appendix C) washes and a secondary antibody diluted in PBS-T applied. The membrane was incubated for 1 hour with agitation and then washed with three 5 minute PBS-T washes. The membrane was then placed in the LICOR Oyssey CLx for antibody detection. Densitometry was performed with LICOR image studio lite software according to the Novus biological loading control handbook (The Novus biologicals loading control handbook. Available at: https:// images.novusbio.com/design/BR_loadingcontrolsguide_101416.pdf (Accessed 21 July 2018).

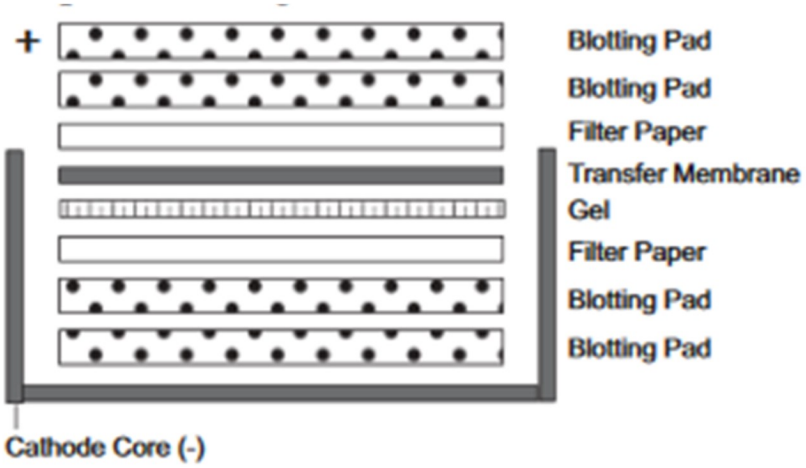

Figure 20 Schematic of Novex transfer module assembly

This schematic was taken from the Novex manual.

Chapter 3. Validation and Phenotyping of Mutant Aggrecan Mouse Models

3.1. Establishment of the V2019M *Acan* and D1983N *Acan* knock-in mouse colonies

The OCD and SEMD mouse models were generated by Polygene Transgenetics in Switzerland. The mouse colony founders (heterozygous for the FLP transgene and heterozygous for either 1) the OCD-causative V2019M *Acan* allele or 2) the SEMD-causative D1983N *Acan* allele) were then transferred to Newcastle University. The genotypes of these founder mice were validated by restriction digestion and PCR to ensure that the initial genotyping data provided by Polygene Transgenetics was correct. The DNA constructs, genotyping strategy and primers were designed and previously used by Polygene.

3.1.1. Validation of the SEMD mouse colony by screening for the D1983N Acan mutation

Founder mice were initially screened for the presence of the D1983N *Acan* mutation. *Pvu*I restriction sites had previously been introduced with the D1983N *Acan* mutation during generation of the D1983N *Acan* knock-in mouse. These *Pvu*I restriction sites enabled selective restriction digestion of the mutant allele but not the wild type allele. DNA was extracted from an ear biopsy and PCR was performed with primers P15 and P16 to amplify the region around the mutation producing an amplicon of 617bp (Figure 21). The PCR product was separated by horizontal gel electrophoresis and the 617bp DNA amplicon extracted from the agarose gel. This DNA was then digested with the *Pvu*I restriction enzyme. Digestion of the wild type allele had no effect, whereas digestion of the mutant fragment produced two fragments of 349bp and 268bp respectively. The heterozygous founder mice therefore presented with three DNA fragments: a 617bp wild type amplicon and the additional 349bp and 268bp fragments from the mutant allele (Figure 21C).

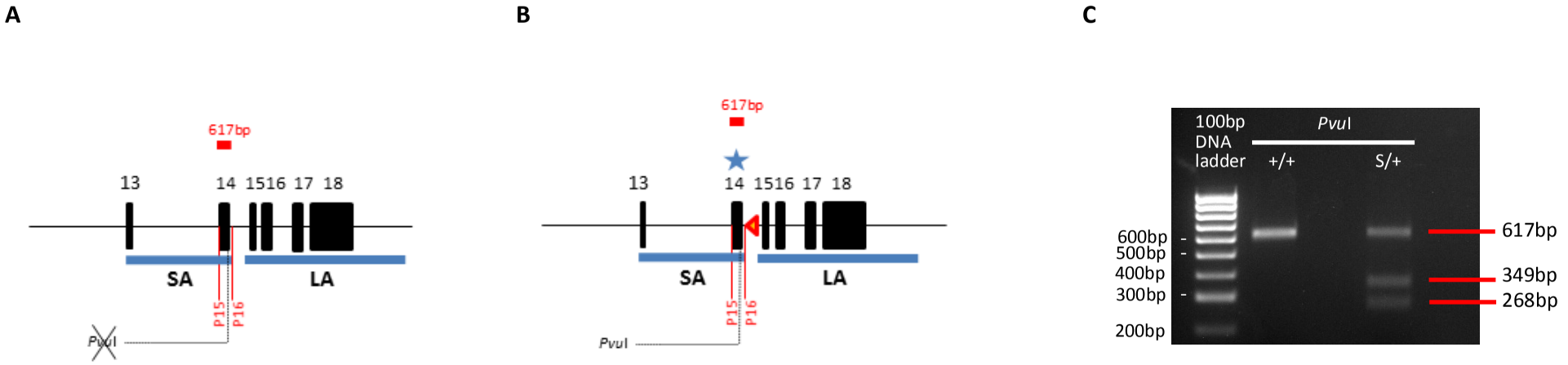

Figure 21 Validation of the SEMD mouse colony.

(A) Schema c of the WT *Acan* allele. **(B)** Schema c of the SEMD (D1983N *Acan*) allele. **(C)** Ini al amplifi ati n of the genomic region around the D1983N *Acan* muta on (using primers P15-16) produced an amplicon of 617bp. *Pvu*I restric on diges on of the mutant amplicon produced two fragments (349bp and 268bp).

Key: +/+ (wild type) S/+ (heterozygous for the muta on) ★ D1983N muta on ◀ FRT site for FLP-mediated removal of neomycin casse e SA (short arm of homology) LA (long arm of homology)

3.1.2 Validation of the OCD mouse colony by screening for the V2019M Acan mutation

Founder mice were initially screened for the presence of the V2019M *Acan* mutation. *Age*I restriction sites had previously been introduced with the V2019M *Acan* mutation during generation of the V2019M *Acan* knock-in mouse. Firstly, DNA was extracted from an ear biopsy and PCR was performed using the primers P3 and P4 to amplify the region around the mutation, producing an amplicon of 662bp (Figure 22). The PCR product was separated by horizontal gel electrophoresis and the 662bp DNA amplicon extracted from the agarose gel. This DNA was then digested with the *Age*I restriction enzyme. Digestion of the wild type fragment produced two fragments of 410bp and 252bp whereas digestion of the mutant fragment produced three fragments of 314bp, 252bp and 96bp. The heterozygous founder mice therefore presented with five DNA fragments: two wild type amplicons (410bp and 252bp) and three fragments from the mutant allele (314bp, 252bp and 96bp) (Figure 22C).

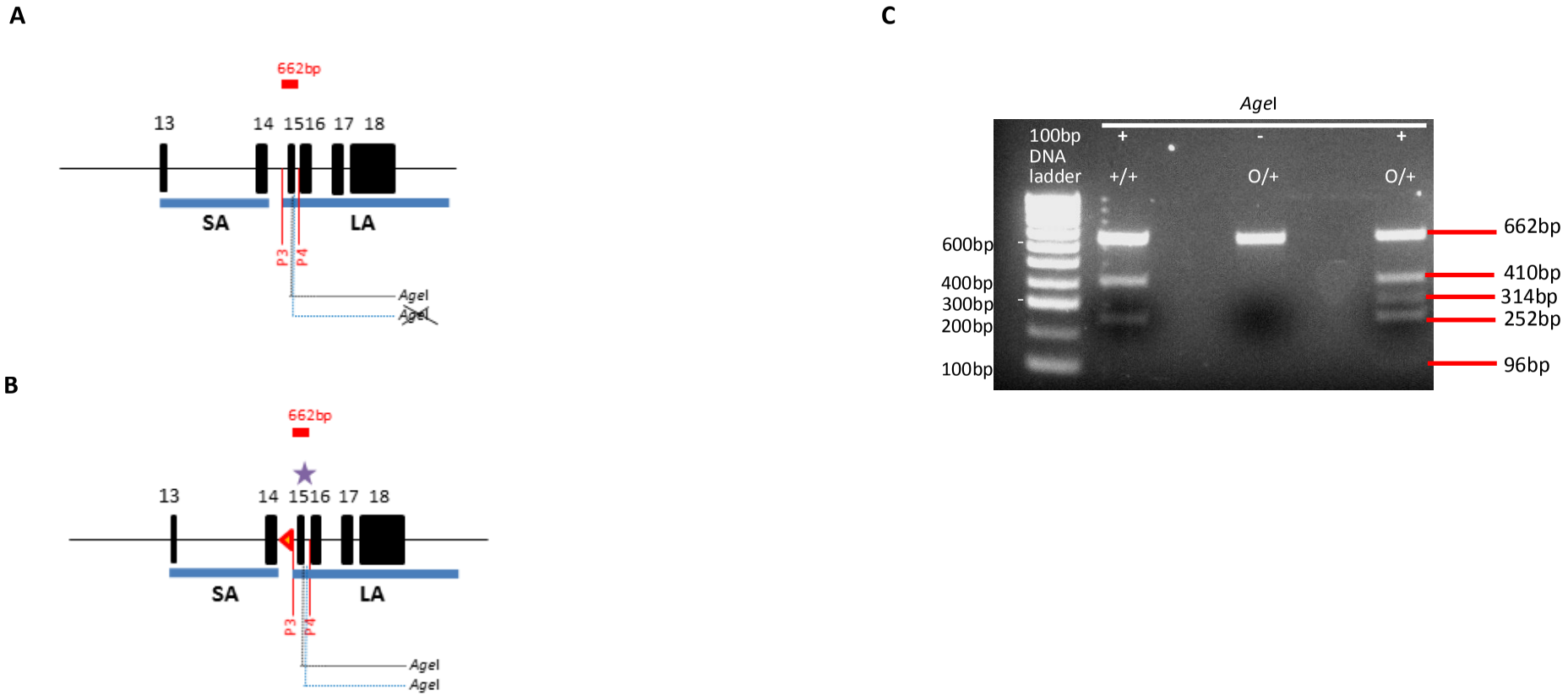

Figure 22 Validation of the OCD mouse colony.

(A) Schema c of the WT *Acan* allele. **(B)** Schema c of the OCD (V2019M *Acan*) allele. **(C)** Initi l amplifi ati n of the genomic region around the V2019M *Acan* muta on (using primers P3-4) produced an amplicon of 662bp. *Age*I restricti n diges on of the mutant amplicon produced three fragments (314bp, 252bp, 96bp). Diges on of the wild type fragment produced two fragments (410bp, 252bp).

Key: +/+ (wild type) O/+ (heterozygous for the muta on) ★ V2019M muta on ◀ FRT site for FLP-mediated removal of neomycin cassette SA (short arm of homology) LA (long arm of homology)

3.1.3 Genotyping of the OCD and SEMD colonies by screening for the targeted Acan allele

Once the founder mice had been validated for the presence of the relevant *Acan* mutation, routine genotyping was performed by screening mice in the OCD and SEMD colonies for the presence of the targeted *Acan* allele after deletion of the neomycin cassette. PCR was performed using the primers P12 and P13 to amplify the relevant region in the aggrecan gene. The wild type *Acan* allele produced an amplicon of 434bp whereas the mutant targeted allele (containing the remaining FRT site introduced with the gene targeting vector) produced a larger 545bp amplicon (Figure 23A-D). This PCR-based genotyping strategy was routinely used to distinguish mice heterozygous or homozygous for the mutation from their wild type littermates.

3.1.4 Establishment of the OCD and SEMD colonies by removal of the FLP transgene

The validated founder mice were bred at 6 weeks of age and the resultant pups (F1 generation) were genotyped using PCR in order to select FLP-negative individuals for further breeding (F2 generation). The FLP transgene had previously been used in the deletion of the neomycin cassette from the targeted allele but was no longer required and so was selectively removed to avoid any off-target effects. PCR was performed to amplify the FLP transgene, producing an amplicon of 500bp (Figure 23E). Those mice whose DNA was negative for the FLP transgene were then selected for further breeding once they had reached sexual maturity at 6 weeks of age.

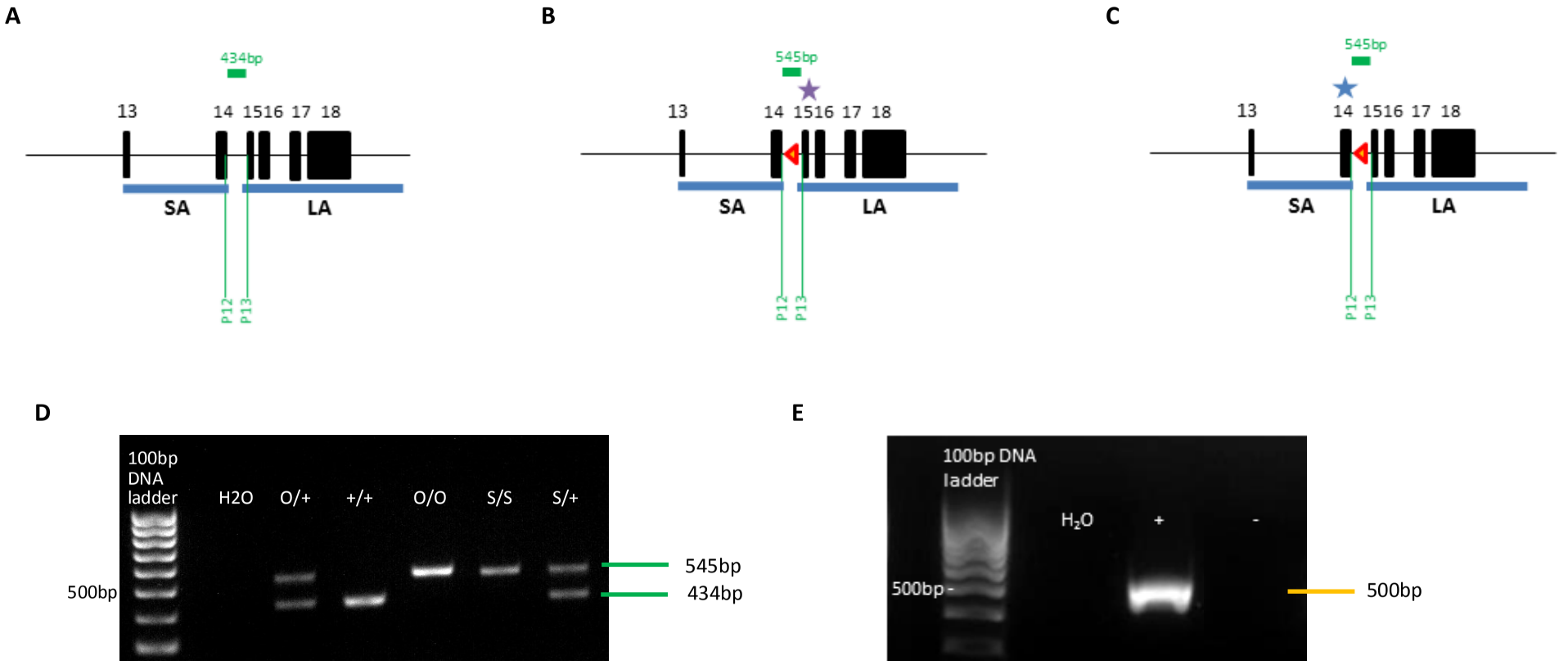

Figure 23 Genotyping of the OCD and SEMD mouse colonies.

(A) Schema c of the WT *Acan* allele. **(B)** Schema c of the OCD (V2019M *Acan*) allele. **(C)** Schema c of the SEMD (D1983N *Acan*) allele. **(D)** Genotyping PCR (using primers P12-13) for the targeted allele aft r FLP-mediated dele on of the neomycin casse e. The wild type allele produced an amplicon of 434bp and the V2019M *Acan* or D1983N *Acan* allele an amplicon of 545bp. **(E)** Genotyping PCR for the FLP transgene (500bp).

Key: +/+ (wild type) O/+ (heterozygous for the OCD muta on) O/O (homozygous for the OCD muta on) S/+ (heterozygous for the SEMD muta on) S/S (homozygous for the SEMD muta on) ★ D1983N muta on ★ V2019M muta on ◀ FRT site for FLP-mediated removal of neomycin casse e SA (short arm of homology) LA (long arm of homology)

3.1.5 Genotype ratio analysis of the SEMD mouse colony

Following genotyping the ratio of pups weaned with each genotype (wild type, heterozygous mutant, homozygous mutant) was analysed to assess the effect of the D1983N *Acan* mutation on pre-weaning lethality. Statistical analysis indicated Mendelian distribution of genotypes (p=0.2) and that heterozygous crosses produced normal sized litters (p=0.3). Crosses with a homozygous male and a heterozygous female also produced normal sized litters (p=0.8) (Figure 24A). These data indicated that the D1983N *Acan* mutation had no effect on pre-weaning mortality. Analysis of litter sizes produced by homozygous crosses was not performed due to high post-natal infanticide. Furthermore, in cages containing homozygous crosses with an additional heterozygous female, it was not always possible to confirm whether the pups used were the offspring of the homozygous or heterozygous female.

3.1.6 Genotype ratio analysis of the OCD mouse colony

The ratio of pups with each genotype (wild type, heterozygous mutant, homozygous mutant) was analysed to assess the effect of the V2019M *Acan* mutation on pre-weaning lethality. Statistical analysis indicated Mendelian distribution of genotypes (p=0.9) and that both heterozygous (p=0.2) and homozygous (p=0.7) crosses produced normal sized litters (Figure 24B). This data indicated that the V2019M *Acan* mutation had no effect on pre-weaning mortality.

A

Genotype	+/+	S/+	S/S
Expected number of pups	25	50	25
Observed number	29	55	16

Average litter size (S/+ x S/+)	**5.3± 1.9**
Average litter size (S/+ x S/S)	**6.3 ± 1.0**
Average litter size (+/+ x +/+)	**6.1 ± 1.6**

B

Genotype	+/+	O/+	O/O
Expected number of pups	25	50	25
Observed number	26	53	24

Average litter size (O/+ x O/+)	**7.1 ± 2.6**
Average litter size (O/O x O/O)	**6.5 ± 2.6**
Average litter size (+/+ x +/+)	**6.1 ± 1.6**

Figure 24 Genotype ratio of the OCD and SEMD mouse colonies

(A) Genotyping of 3 week old mice from the SEMD mouse colony showed Mendelian distribu on (p=0.2, total number of li ers = 19). Normal li er sizes were produced by heterozygous SEMD (p=0.3) and homozygous (male) heterozygous (female) SEMD crosses (p=0.8) . **(B)** Genotyping of 3 week old mice from the OCD mouse colony showed Mendelian distribu on (p=0.9, total number of li ers = 14). Normal li er sizes were produced by heterozygous OCD (p=0.2) and homozygous OCD (p=0.7) crosses.

Key: +/+ (wild type) S/+ (heterozygous for the SEMD mutation) S/S (homozygous for the SEMD mutation) O/+ (heterozygous for the OCD mutation) O/O (homozygous for the OCD mutation) Chi-square test (genotype ratio) Two-tailed T-test (litter sizes).

3.2 Phenotypic analysis of the SEMD mouse model

In order to assess the potential of the D1983N *Acan* knock-in mouse as a model for spondyloepimetaphyseal dysplasia (SEMD) aggrecan type, a range of phenotyping techniques were used. The morphology and skeletal development of the mice was assessed at birth and at key stages of their adult life, including 1) weaning at 3 weeks, 2) sexual maturity at 6 weeks and 3) cessation of bone growth at 9 weeks of age. SEMD aggrecan type is a recessive disorder; however, three family members who were heterozygous for the equivalant human D2267N *ACAN* mutation were reported to have mild proportionate short stature (Tompson, Merriman et al. 2009). Both homozygous and heterozygous mutant mice were therefore included in the phenotyping stage of this study to help resolve this question. The rate of growth was measured by weighing the mice over a 6 week time period to assess whether early growth cessation had occurred before 9 weeks of age. Skeletal morphology and the phenotypic onset of this bone disorder was assessed at birth by preparing skeletal preparations, using histological dyes which preferentially stain the cartilage and bone. This allowed the visualisation of the skeletal components, such as the ossification centres and quantitative measurement of the bone lengths. This assessed whether pre-natal development was affected by the disorder. The skeletal morphology and maturation of adult mice was assessed both radiographically and histologically. Patients with SEMD aggrecan type present with severe short stature and a broad range of skeletal defects (Tompson, Merriman et al. 2009). It was therefore decided that short stature, spine curvature, brachydactyly and mid-face hypoplasia would be assessed in the mutant mice compared to wild type littermates.

3.2.1 Morphological analysis of newborn SEMD mice

At birth heterozygous and homozygous mutant mice were not overtly visually different in size or appearance from their wild type littermates. Neonatal skeletal preparations were prepared and stained with Alcian Blue (which preferentially dyes proteoglycan, a major component of the cartilage growth plate) and Alizarin Red (which preferentially stains calcified bone). There was no major visible difference in the arrangement of skeletal components of mice heterozygous or homozygous for the mutation compared to those of wild type littermates (Figure 25A-B, D). The total lengths of the femur and tibia bones were measured at birth. There was no statistical difference in the average femoral bone length of either homozygous or heterozygous mutant mice compared to wild type littermates. However, the average length of the tibia in homozygous mutant mice was reduced to 87.5% of wild type bone length (Figure 25C). This suggests that although the SEMD mutation does not severely affect pre-natal skeletal developmental patterning, bone growth is reduced and therefore the phenotypic onset of SEMD likely occurs before birth.

3.2.2 Postnatal growth of SEMD mice

Mice were weighed at 3, 6 and 9 weeks of age in order to assess the growth rate of heterozygous and homozygous mutant mice relative to wild type littermates. At 3 weeks of age both male and female mice homozygous for the mutation were visibly smaller and by 9 weeks were 32.2% and 30.1% lighter than wild type littermates respectively (Figure 26). There was no statistical difference between the mass of heterozygous mutant mice and that of their wild type littermates (Figure 26).

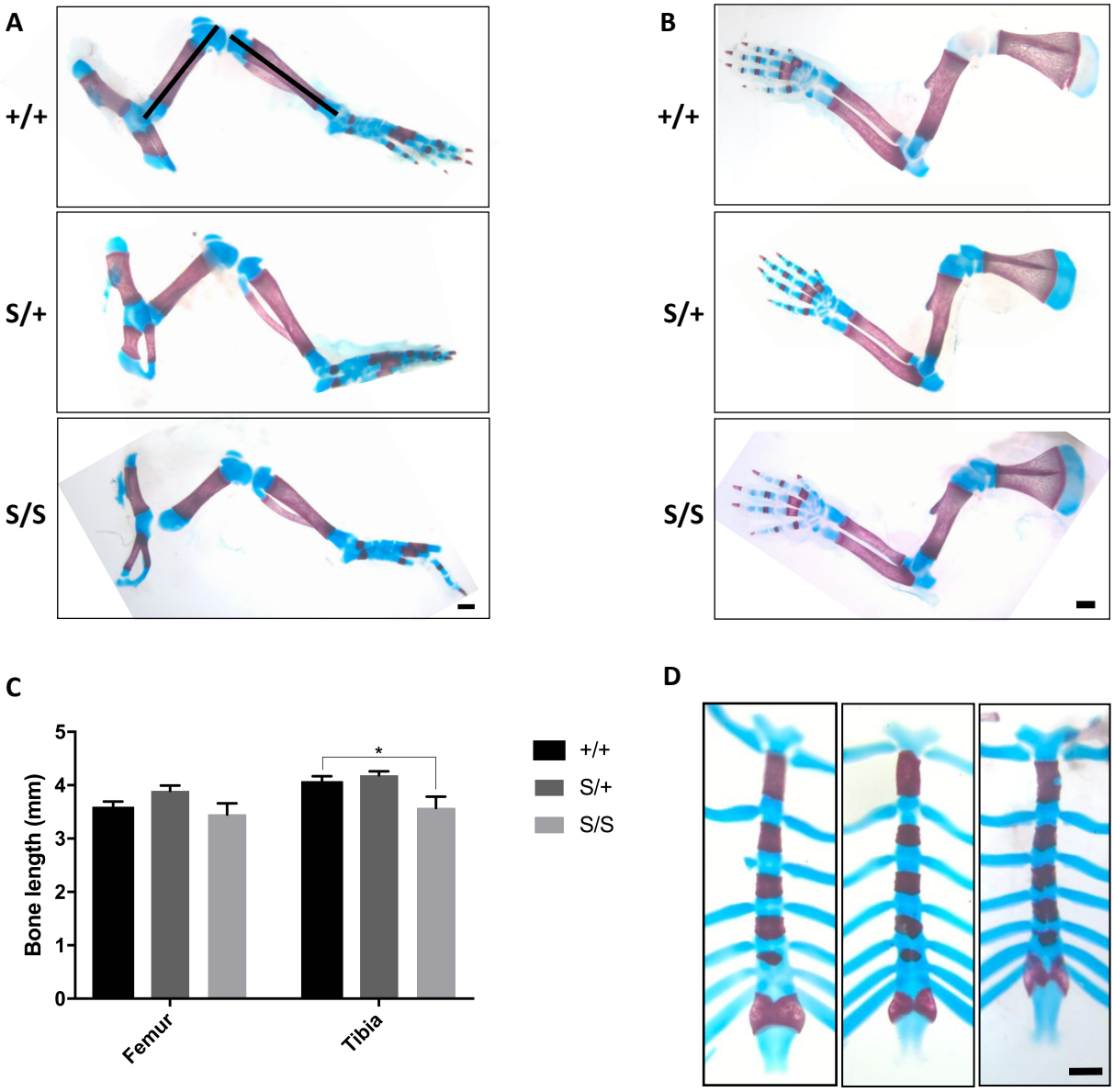

E

	+/+	S/+	S/S
Femur (mm) ± SEM	3.60±0.09	3.89±0.10	3.45±0.21
Tibia (mm) ± SEM	4.08±0.09	4.19±0.07	**3.57±0.21***

Figure 25 Morphology of SEMD mice at birth.

Skeletal preparations stained with Alizarin Red (to visualise calcified bone) and Alcian Blue (to visualise the cartilage). Pups either heterozygous or homozygous for the muta on were morphologically indistinguishable from wild type littermates. **(A)** Hind limb **(B)** Fore limb **(D)** Sternum **(C)** Tibia and femur bone lengths were measured in mice of all 3 genotypes (black lines). There was no statistical difference in the average femur length but the average tibia length of homozygous mice was reduced, reaching 87.5% of wild type bone length. **(E)** Numeric data used for the generation of graph A.

Key: +/+ (wild type) S/+ (heterozygous for the muta on) S/S (homozygous for the mutation) SEM (standard error of the mean) *p>0.05, Two tailed T-test, scale bars = 50µm, n≥3.

A

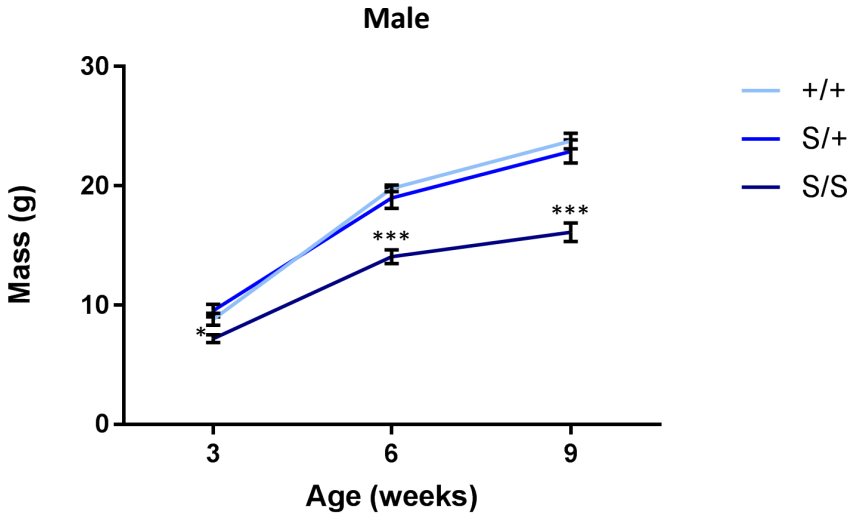

B

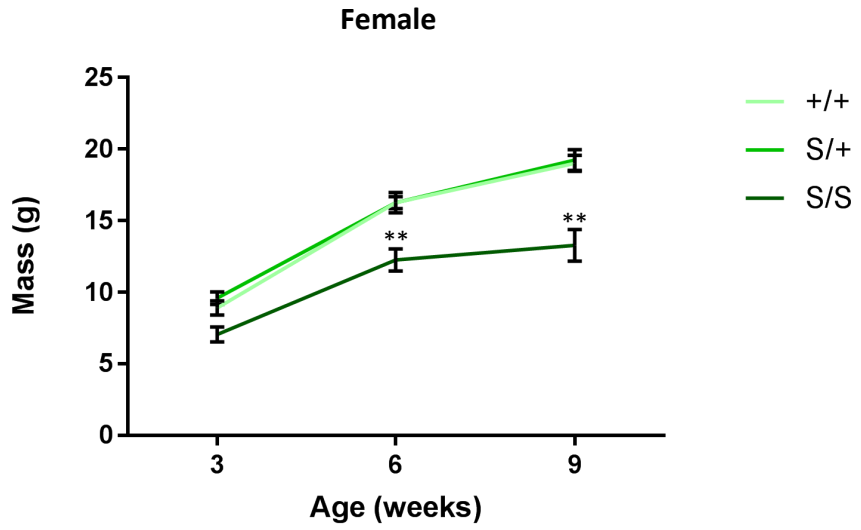

C

		Male			Female		
Age (weeks)		+/+	S/+	S/S	+/+	S/+	S/S
Mass (g) ±SEM	3	8.81±0.51	9.53±0.52	**7.18±0.33 ***	8.91±0.49	9.59±0.44	7.05±0.52
	6	19.79±0.27	19.00±0.89	**14.06±0.57 *****	16.26±0.71	16.27±0.42	**12.25±0.78 ****
	9	23.77±0.65	22.89±0.98	**16.11±0.78 *****	19.01±0.56	19.25±0.74	**13.28±1.12 ****

Figure 26 Growth rates of SEMD mice.

The body mass of mice of all 3 genotypes (wild type, heterozygous mutant and homozygous mutant) was measured at 3, 6 and 9 weeks of age. Male and female mice homozygous for the muta on had reduced body mass, reaching 67.8% **(A)** and 69.9% **(B)** of wild type body mass respectivel by 9 weeks. **(C)** Numeric data used for the genera on of graphs A and B.

Key: +/+ (wild type) S/+ (heterozygous for the muta on) S/S (homozygous for the muta on) SEM (standard error of the mean) *p>0.05, **p>0.01, ***p>0.001, Two tailed T-test, n≥3.

3.2.3 Radiographic and morphological analysis of developing SEMD mice

Mice were x-rayed in the dorsal plane and the length and angle of the appropriate bones were then measured (Figure 27). As the phenotype did not appear to be influenced by gender only data from male animals has been shown, but data from females is presented in Appendix I.

3.2.3.1 Long bones and the pelvic girdle

Mice homozygous for the SEMD mutation exhibited a number of bone abnormalities, including a bell-shaped rib cage, brachydactyly and irregular epiphyses, all consistent with the human SEMD phenotype (Figure 27) (Tompson, Merriman et al. 2009). At 3 weeks of age the average femoral, tibial and pelvic bone length measurements of male (and female) mice homozygous for the mutation were already significantly reduced compared to those of wild type littermates (Figure 28). By 9 weeks male (and female) mice homozygous for the mutation were exhibiting a severe short stature phenotype; for example, the average femur and tibia lengths of male mice homozygous for the mutation were 27.4% and 24.6% shorter that that of wild type littermates. Similarly, the combined length of the pelvic girdle bones (ilium and ischium) was reduced by 22.5% compared to wild type bones (Figure 28). There was no statistical difference between the bone lengths of mice heterozygous for the mutation and those of wild type littermates at 3 weeks of age. However, by 6 weeks of age mice had significantly reduced femoral and tibial bone lengths compared to those of wild type littermates. By 9 weeks heterozygote mice displayed a short stature phenotype; for example, the average femur and tibia lengths of male mice heterozygous for the mutation were 8.2% and 8.3% shorter than that of wild type littermates. Similarly, the combined length of the pelvic girdle bones (ilium and ischium) was reduced by 5.5% compared to wild type bone lengths (Figure 28). There was a 4-fold increase in the average angle between the illium and the tuberosity of the ischium in 9 week old male mice homozygous for the mutation compared with that of wild type littermates (Figure 29) suggesting a hip dysplasia. Interestingly, heterozygote mice did not exhibit hip dysplasia (Figure 29).

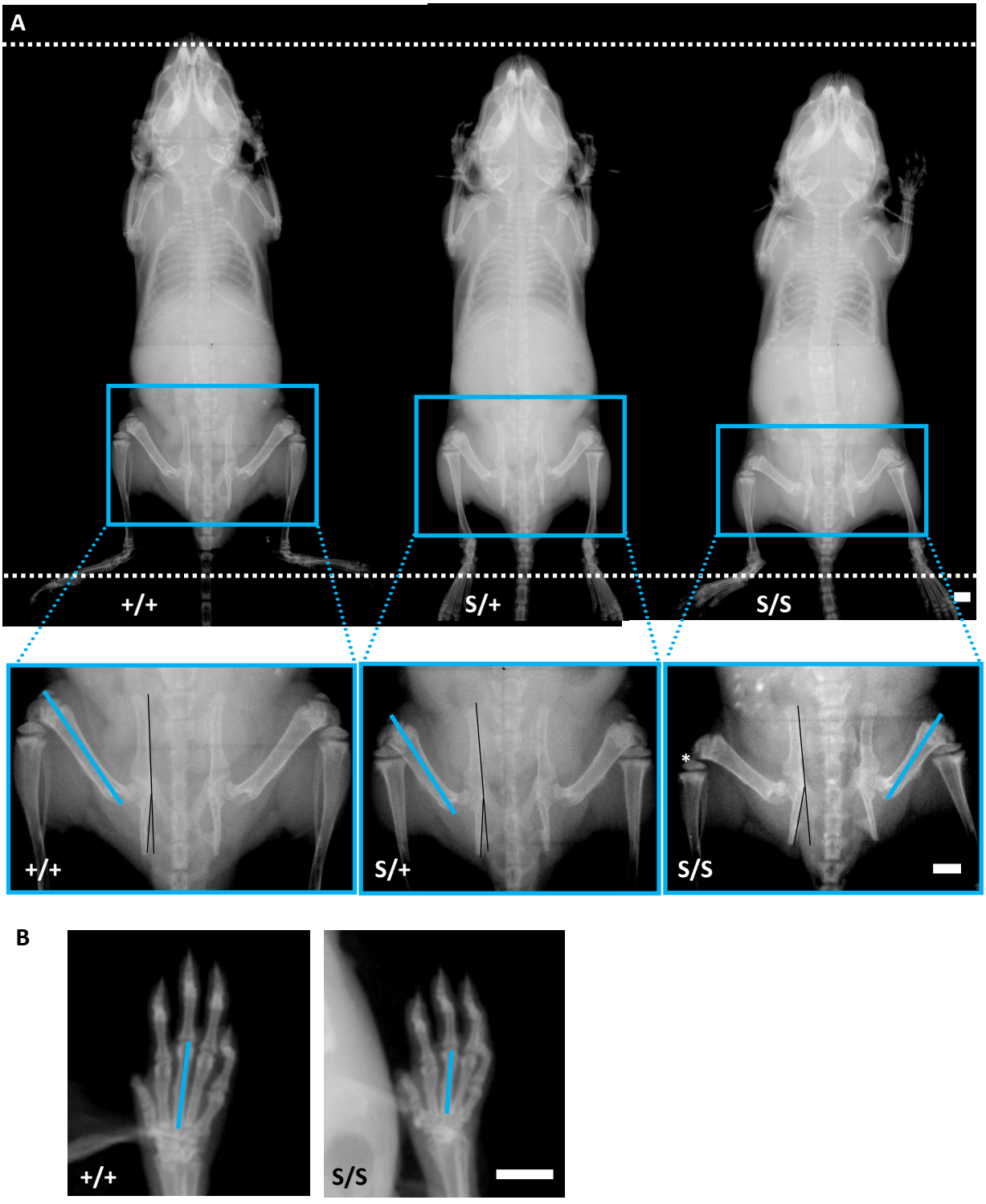

Figure 27 Radiographic analysis of SEMD mice.

(A) Representative X-ray imaging of 3 week old male mice (dorsal view). Mice homozygous for the mutation displayed irregular epiphyses (white star) hip dysplasia (black lines) bell-shaped rib cage, disproportionately short limbs (blue line) and brachydactyly. Mice heterozygous for the mutation exhibited disproportionately short limbs (blue line) but no other skeletal abnormalities **(B)** Representative X-ray imaging of 9 week old male mice (dorsal view). Homozygous mice exhibited brachydactyly.

Key: +/+ (wild type) S/+ (heterozygous for the mutation) S/S (homozygous for the mutation) n≥4, scale bars = 2mm

A

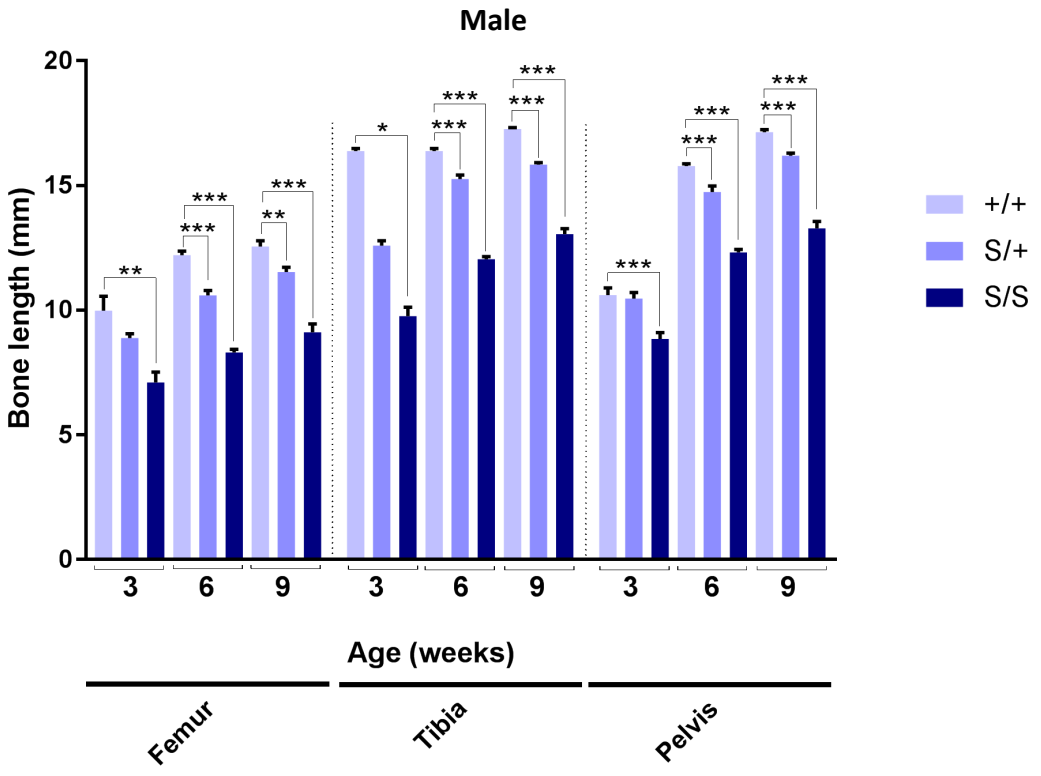

B

Age (weeks)		+/+	S/+	S/S
Femur (mm) ± SEM	3	9.99 ± 0.57	8.88 ± 0.18	**7.10 ± 0.42 ****
	6	12.21 ± 0.16	**10.60 ± 0.19 *****	**8.30 ± 0.13 *****
	9	12.56 ± 0.23	**11.53 ± 0.20 ****	**9.12 ± 0.33 *****
Tibia (mm) ± SEM	3	16.38 ± 0.10	12.60 ± 0.19	**9.76 ± 0.37 ***
	6	16.38 ± 0.10	**15.26 ± 0.16 *****	**12.05 ± 0.11 *****
	9	17.27 ± 0.06	**15.83 ± 0.08 *****	**13.05 ± 0.23 *****
Pelvis (mm) ± SEM	3	10.60 ± 0.29	10.47 ± 0.24	**8.85 ± 0.26 *****
	6	15.77 ± 0.10	**14.74 ± 0.24 *****	**12.32 ± 0.12 *****
	9	17.14 ± 0.11	**16.20 ± 0.10 *****	**13.28 ± 0.29 *****

Figure 28 Morphometric analysis of male SEMD mice.

Tibia and femur and pelvic (illium and ischium) bone lengths were measured at 3, 6 and 9 weeks of age in male mice of all 3 genotypes. **(A)** The average femur, tibia and pelvis lengths of mice homozygous for the mutation was reduced, reaching 72.6%, 75.6% and 77.5% of wild type bone lengths respectively by 9 weeks. The average femur, tibia and pelvis lengths of mice heterozygous for the mutation was reduced to 91.8%, 91.7% and 94.5% of wild type bone lengths respectively by 9 weeks. **(B)** Numeric data used for the generation of graph A.

Key: +/+ (wild type) S/+ (heterozygous for the muta on) S/S (homozygous for the muta on) SEM (standard error of the mean) *p>0.05, **p>0.01, ***p>0.001, Two tailed T-test, n≥3.

A

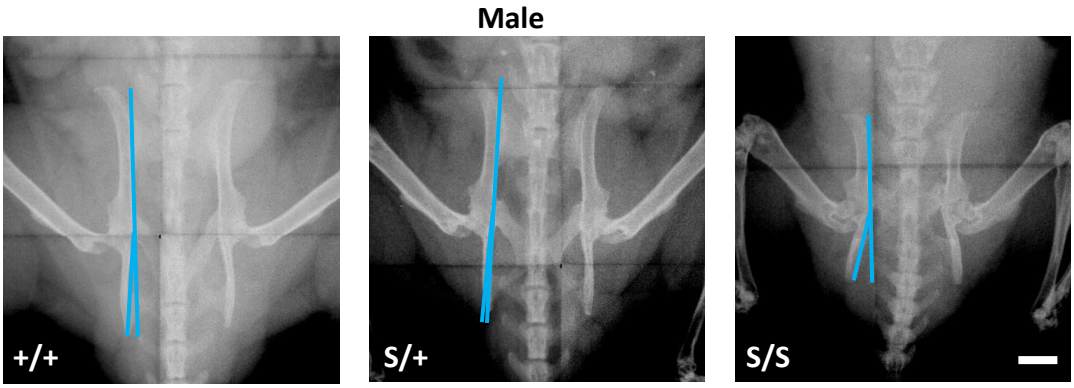

B

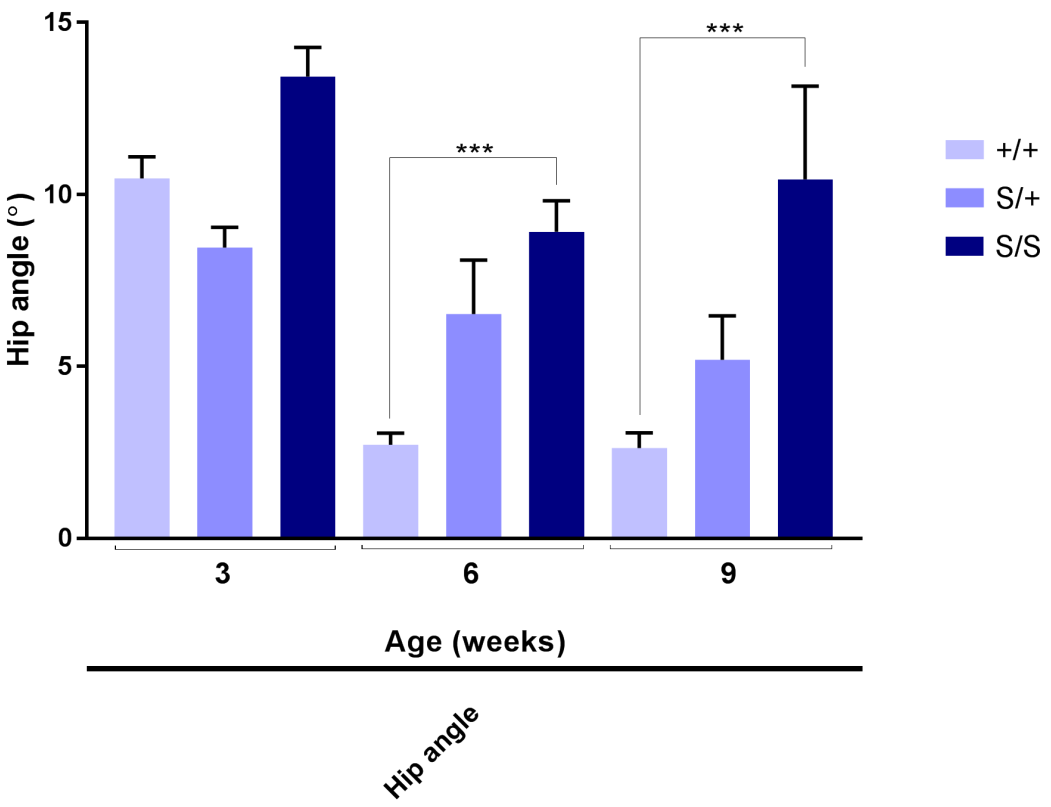

C

Age (weeks)		+/+	S/+	S/S
Hip angle (°) ± SEM	3	10.47±0.63	8.46±0.59	13.43±0.84
	6	2.72±0.34	6.53±1.56	**8.92±0.90 *****
	9	2.63±0.44	5.19±1.28	**10.44±2.71 *****

Figure 29 Hip dysplasia in male SEMD mice.

The angle of the hip was measured at 3, 6 and 9 weeks of age in male mice of all 3 genotypes. **(A)** Representative X-ray imaging of 9 week old male mice (dorsal view). **(B)** There was a 4-fold increase in the average hip angle of mice homozygous for the mutation compared with that of wild type littermates. **(C)** Numeric data used for the generation of graph B.

Key: +/+ (wild type) S/+ (heterozygous for the muta on) S/S (homozygous for the muta on) SEM (standard error of the mean) ***p>0.001, Two tailed T-test, scale bars = 2mm, n≥3.

3.2.3.2 Skull

There was no statistical difference in the average inner canthal distance between the homozygous mutant and wild type mice of either gender at 3, 6 and 9 weeks of age. However, the length of the skull was already reduced at 3 weeks of age and by 9 weeks was decreased by 16.9% in female and 20.6% in male mice compared to wild type bone lengths (Figure 30). In order to further investigate the skull morphology and development, skulls were dissected from newborn pups and male mice at 3 weeks of age. Newborn pups were not separated by gender as the previous radiographic and morphometric analysis indicated that both male and female mice had comparable features. All skull preparations were stained with Alcian Blue and Alizarin Red in order to determine the proportion of cartilage relative to the calcified bone during early and adult development. There were no overt differences in the appearance of ossification centre formation or proportion of cartilage relative to the calcified bone between the skulls of homozygous mutant mice and wild type mice (Figure 31A). However, at 3 weeks of age the length of the nasal bone and the distance between the antero-lateral corners of the frontal bones were significantly reduced in mice homozygous for the mutation when compared to wild type littermates (Figure 31C). There was no statistical difference in the inner canthal distance between heterozygous mutant and wild type mice at 3, 6 and 9 weeks of age. There was a small (4%), but statistically significant, decrease in skull length at 6 weeks of age, whereas the 0.5% decrease at 9 weeks of age was not statistically significant, suggesting that the effect of the single mutant allele on skull development was minimal (Figure 30). In addition to the pathological changes in skull parameters it was noted that 84.62% of the homozygous mice exhibited malocclusion by 3 weeks of age (Figure 32A,D). This represents a 1839-fold increase in the incidence of teeth overgrowth, as the recorded occurrence in the background strain of this model (C57BL/6) is only 0.046% (Garcia-Arocena). In contrast, wild type and heterozygous mutant littermates did not display any malocclusion. Rodent teeth grow continuously throughout life and the length of teeth is limited by tooth grinding. Malocclusion therefore often occurs when there is misalignment of the jaw, altering the bite of the animal and preventing efficient tooth grinding (Dontas, Tsolakis et al. 2010). SEMD patients display relative mandibular prognathism (Tompson, Merriman et al. 2009) and so mice were x-rayed in the lateral plane in order to assess the position and size of the mandible relative to the rest of the skull (Figure 32A). Unfortunately, due to the resolution of the radiographic images available, it was not possible to measure the maxilla. The size of the

mandible was therefore expressed as a percentage of the total skull length. At 3 weeks of age male homozygous mutant mice exhibited a 5.08% increase in mandible length relative to skull length (Figure 32A-C). This indicates that the SEMD mouse model displays the relative mandibular prognathism observed clinically in the SEMD patients, leading to a change in jaw alignment and so likely causing an increased incidence of malocclusion in these animals.

A

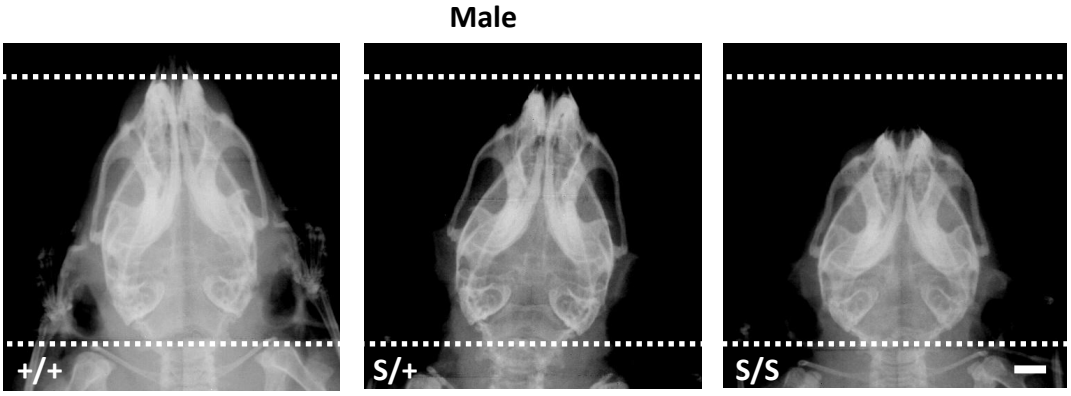

B

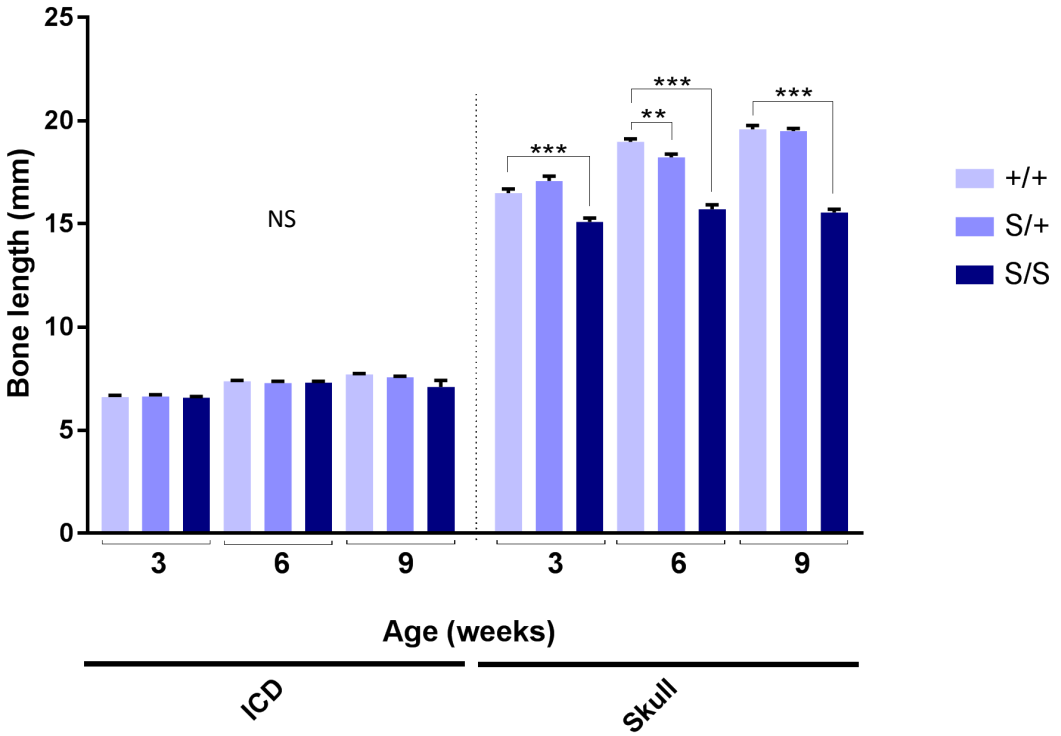

C

Age (weeks)		+/+	S/+	S/S
ICD (mm) ± SEM	3	6.60±0.08	6.64±0.08	6.57±0.07
	6	7.37±0.04	7.28±0.09	7.31±0.06
	9	7.71±0.04	7.57±0.05	7.09±0.32
Skull (mm) ± SEM	3	16.49±0.20	17.08±0.24	**15.09±0.18** ***
	6	18.97±0.15	**18.22±0.16** **	**15.71±0.22** ***
	9	19.59±0.18	19.50±0.13	**15.55±0.16** ***

Figure 30 Morphometric analysis of the skull in male SEMD mice.

ICD (inner canthal distance) and skull length were measured at 3, 6 and 9 weeks of age in male mice of all 3 genotypes. **(A)** Representative X-ray imaging of 9 week old male mice (dorsal view). **(B)** There was no difference in ICD but the average skull length of homozygous mice was reduced to 79.4% of wild type bone length by 9 weeks. **(C)** Numeric data used for the generation of graph B.

Key: +/+ (wild type) S/+ (heterozygous for the mutation) S/S (homozygous for the mutation) SEM (standard error of the mean) **p>0.01, ***p>0.001, Two tailed T-test, scale bars = 2mm

A

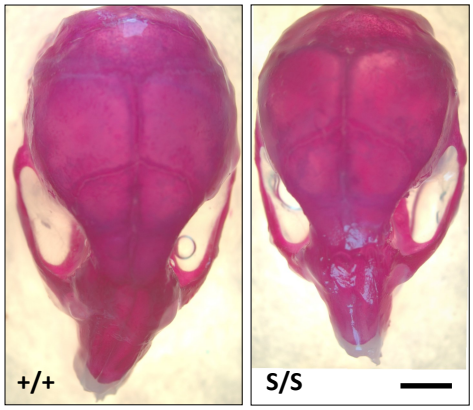

B

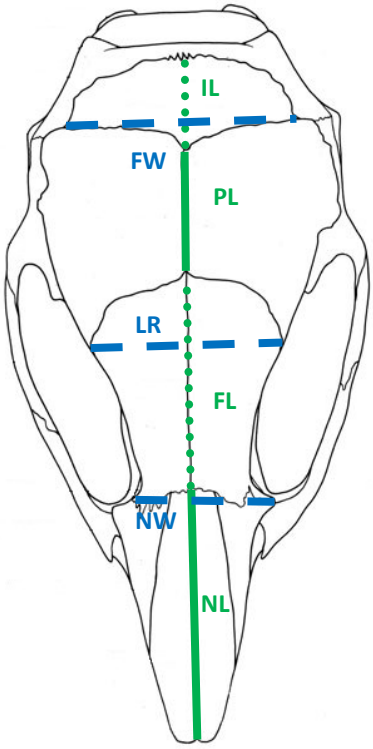

C

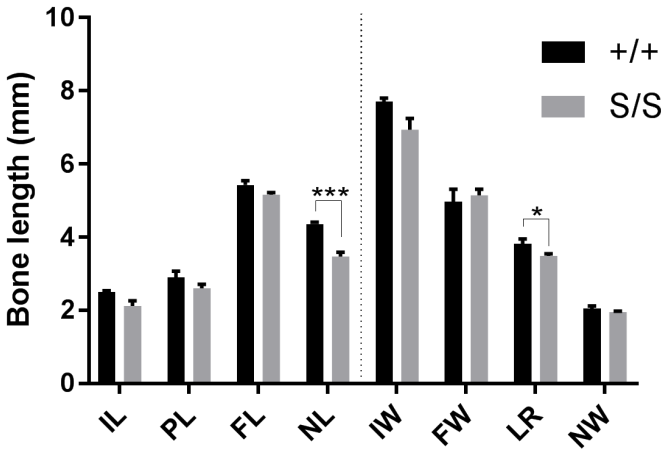

D

Genotype	+/+	S/S
interparietal bone length (IL) ± SEM	2.49±0.05	2.12±0.14
sagittal length of parietal bone (PL) ± SEM	2.90±0.17	2.60±0.11
frontal bone length (FL) ± SEM	5.43±0.12	5.16±0.06
nasal bone (NL) ± SEM	4.36±0.05	**3.47±0.12 *** **
interparietal bone width (IW) ± SEM	7.71±0.01	6.94±0.31
frontal bone width (FW) ± SEM	4.97±0.34	5.15±0.17
anterolateral distance of frontal bone (LR) ± SEM	3.82±0.14	**3.49±0.06 ***
nasal bone width (NW) ± SEM	2.05±0.07	1.95±0.03

Figure 31 Morphometric analysis of the cranial vault in SEMD mice.

(A) Skulls stained with Alizarin Red (to visualise calcified bone) and Alcian Blue (to visualise the cartilage). Skull parameters **(B)** were measured at 3 weeks of age in both homozygous mutant and wild type male mice. **(C)** Graph showing skull measurements with standard error of the mean. The average nasal bone length was reduced by 20.4% and the distance between the anterolateral corners of the frontal bone reduced by 8.6% in mice homozygous for the mutation compared with that of wild type mice. **(D)** Numeric data used for the generation of graph B.

Key: +/+ (wild type) S/S (homozygous for the mutation) SEM (standard error of the mean) *p>0.05, ***p>0.001, Two tailed T-test, n≥4.

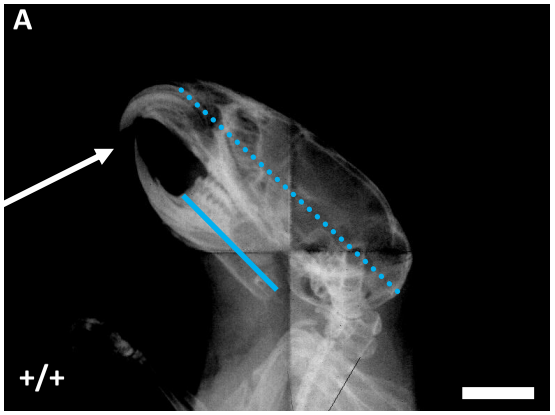

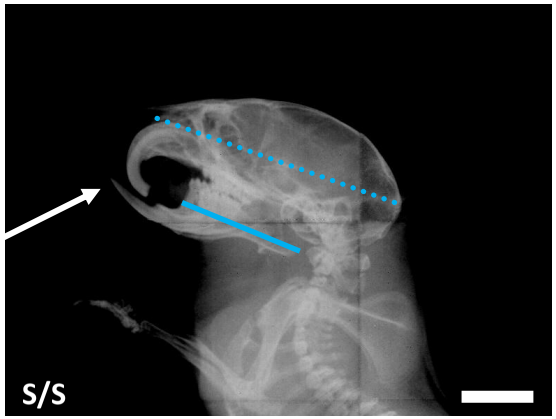

B

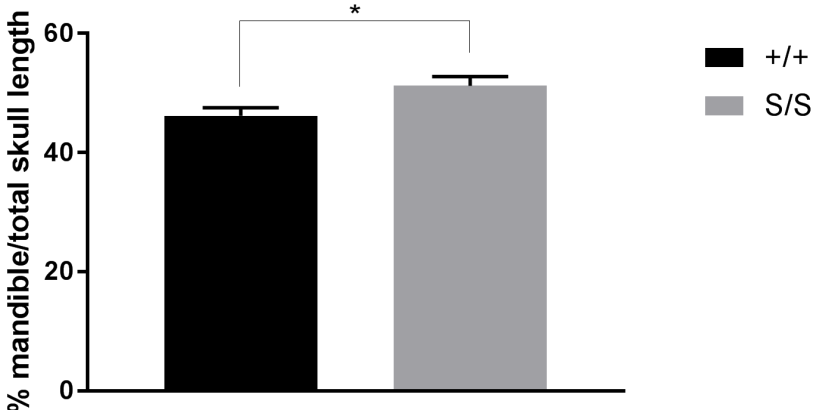

C

	+/+	S/S
% mandible/total skull length	46.16 ± 1.37	**51.24 ± 1.52** *

D

		C57BL/6 background	+/+	S/+	S/S
% incidence of malocclusion	Female		0	0	**88.89*** **
	Male		0	0	**75.00*** **
	Total	0.046	0	0	**84.62*** **

Figure 32 Relative prognathism and increased malocclusion in SEMD mice.

(A) Representative X-ray imaging of 9 week old male mice (lateral view). Homozygous mutant mice exhibited relative prognathism and malocclusion (white arrow) compared to wild type controls. **(B)** Graph showing relative prognathism quantitatively expressed as the length of the mandible (blue line) relative to the skull length (dotted blue line). Male mice homozygous for the muta on displayed a 5.08% increase in mandible length relative to the total skull length. **(C)** Numeric data used for the genera on of graph C. **(D)** Due to this change in jaw alignment, homozygous mutant mice displayed a total 1839-fold increase in malocclusion compared to that observed in the wild type C57BL/6 background strain.

Key: +/+ (wild type) S/+ (heterozygous for the muta on) S/S (homozygous for the muta on) *p>0.05, ***p>0.001, Two tailed T-test (relative prognathism) Chi-square test (malocclusion) scale bar = 5mm, n≥5.

3.2.3.3 Spine

SEMD patients exhibit mild thoracic scoliosis, cervical-vertebral clefts and lumbar lordosis (Tompson, Merriman et al. 2009). Heterozygous mutant mice were not assessed in this spinal study as their overall skeletal phenotype was relatively mild and the three heterozygous (carrier) members of the SEMD family did not exhibit any spinal malformations (Tompson, Merriman et al. 2009). Wild type mice did not exhibit abnormal spine curvature (Diab angle≥12); however, at 3 weeks of age 33.33% of homozygous mutant male mice exhibited mild thoracic scoliosis, with the incidence increasing to 57.14% with skeletal maturity at 9 weeks of age (Figure 33). At 9 weeks of age there was a two-fold increase in the angle of spinal curvature of the homozygous mutant mice, who displayed visible scoliosis compared to their wild type littermates. There was no statistical difference between the angle of spinal curvature in homozygous mice that presented without scoliosis and wild type mice. The angle of scoliosis was not significantly different between mice that presented with scoliosis at 3 and 9 weeks of age, indicating that although the incidence of scoliosis increases with age, there is not a further increase in severity during adult development (Figure 33).

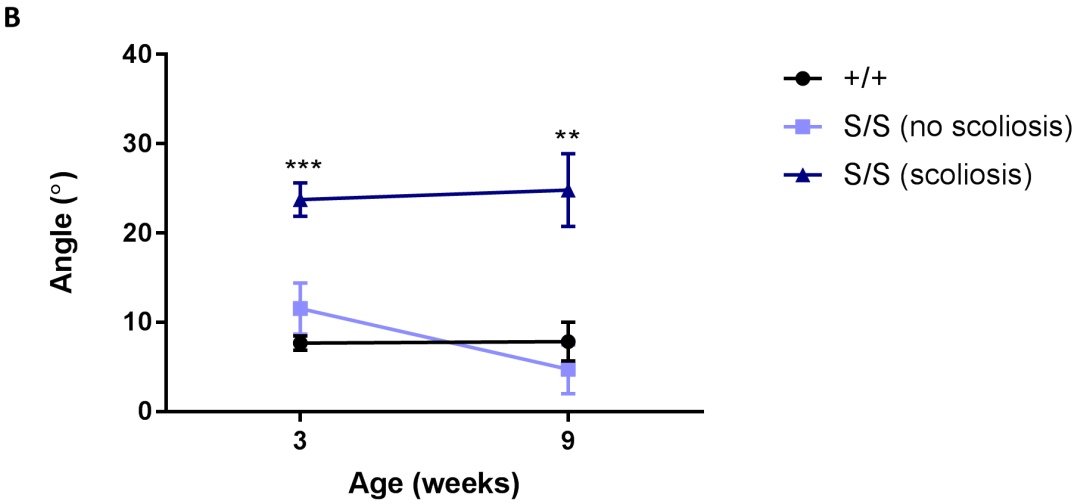

C

Age (weeks)		+/+ (no scoliosis)	+/+ (scoliosis)	S/S (no scoliosis)	S/S (scoliosis)
% mice	3	100	0	66.67	33.33
	9	100	0	42.86	57.14
Angle (°) ± SEM	3	7.70 ± 0.81		11.54 ± 2.88	**23.74 ± 1.87 *** **
	9	7.85 ± 2.17		4.74 ± 2.73	**24.80 ± 4.07 ** **

Figure 33 Severity of scoliosis in male SEMD mice.

(A) 57.14% of homozygous mice exhibited mild scoliosis by 9 weeks of age. The severity of the spine curvature was quantified by m easuring the Diab angle(θ). **(B)** Mice who displayed visible spine curvature had a two-fold increase in the average Diab angle. **(C)** Numeric data used for the generation of graph B. Key: +/+ (wild type) S/S (homozygous for the muta on) **p>0.01, ***p>0.001, Two tailed T-test, SEM (standard error of the mean) scale bar = 5mm, n≥5.

3.3 Phenotypic analysis of the OCD mouse model

In order to assess the potential of the V2019M *Acan* knock-in mouse as a model for dominant familial osteochondritis dissecans (OCD) a range of phenotyping techniques were used. The morphology and skeletal development of the mice was assessed at birth and at key stages of their adult life, including 1) weaning at 3 weeks, 2) sexual maturity at 6 weeks and 3) cessation of bone growth at 9 weeks of age. Familial osteochondritis dissecans (OCD) is a dominantly inherited disorder and only heterozygous patients have been reported (Stattin, Tegner et al. 2008, Stattin, Wiklund et al. 2010). Both homozygous and heterozygous mutant mice were therefore included in the initial phenotyping stage of this study. The rate of postnatal growth was measured by weighing the mice over a 6 week time period to determine whether early growth cessation had occurred before 9 weeks of age. Skeletal morphology and the phenotypic onset of this bone disorder was assessed at birth by preparing skeletal preparations of neonates and applying histological dyes which preferentially stain the cartilage and bone. This allowed the visualisation of the skeletal components, such as the ossification centres, and quantitative measurement of the bone lengths. The skeletal morphology of adult mice was assessed both radiographically and histologically. The radiographic strategy was based on established skeletal mouse phenotyping techniques (Suleman, Gualeni et al. 2012) protocols established in the literature for the assessment of mouse models predicted to have similar phenotypic features and the clinical findings of heterozygous patients carrying the equivalent human mutation (V2303M *ACAN*) (Stattin, 2010). Patients with dominant fOCD are characterised by mild disproportionate short stature and the formation of osteochondrotic lesions in the knee, patella, hip or elbow which can lead to the development of early-onset osteoarthritis. Some affected family members were also found to have a variety of heterogenous bone abnormalities, such as scoliosis and low invertebral discs in the thoracic- and lumbar-spine. It was decided to prioritise the study of only a few of these bone abnormalities, focusing on the short stature and spine curvature phenotype (Stattin, Tegner et al. 2008, Stattin, Wiklund et al. 2010).

3.3.1 Morphological analysis of newborn OCD mice

At birth, homozygous mutant mice were not visually different in size or appearance from their wild type littermates. Heterozygous mutant mice were not studied due to the very mild nature of the adult skeletal phenotype (section 3.3.2). Neonatal skeletal preparations were prepared and stained with Alcian Blue (which preferentially dyes proteoglycan, a major component of the cartilage growth plate) and Alizarin Red (which preferentially stains calcified bone). There was no major visible difference in the number and organisation of the skeletal components of homozygous mutant mice compared to those of wild type littermates and all ossification centres were present (Figure 34A-B and D). Further to this, the total lengths of the femur and tibia bones were measured. There was no statistical difference in the average femoral or tibial bone lengths of homozygous mutant mice compared to wild type littermates (Figure 34C). This indicates that the OCD mutation does not severely affect pre-natal skeletal developmental patterning or growth and so the phenotypic onset of OCD occurs during post-natal development.

3.3.2 Postnatal growth of OCD mice.

Mice were weighed at 3, 6 and 9 weeks in order to assess the growth of heterozygous and homozygous mutant mice relative to that of their wild type littermates. At 3 weeks of age there was no statistical difference between the mass of mice homozygous for the mutation and their wild type littermates. However, by 6 weeks of age the male mice homozygous for the mutation were 7.5% lighter, suggesting that their rate of growth had slowed, and by 9 weeks were 16.2% lighter than wild type littermates. The female mice homozygous for the mutation were not statistically lighter at 6 weeks of age, but by 9 weeks the average mass was reduced by 10.5% compared to that of wild type littermates (Figure 35). There was no statistical difference between the mass of heterozygous mutant mice and that of their wild type littermates (Figure 35).

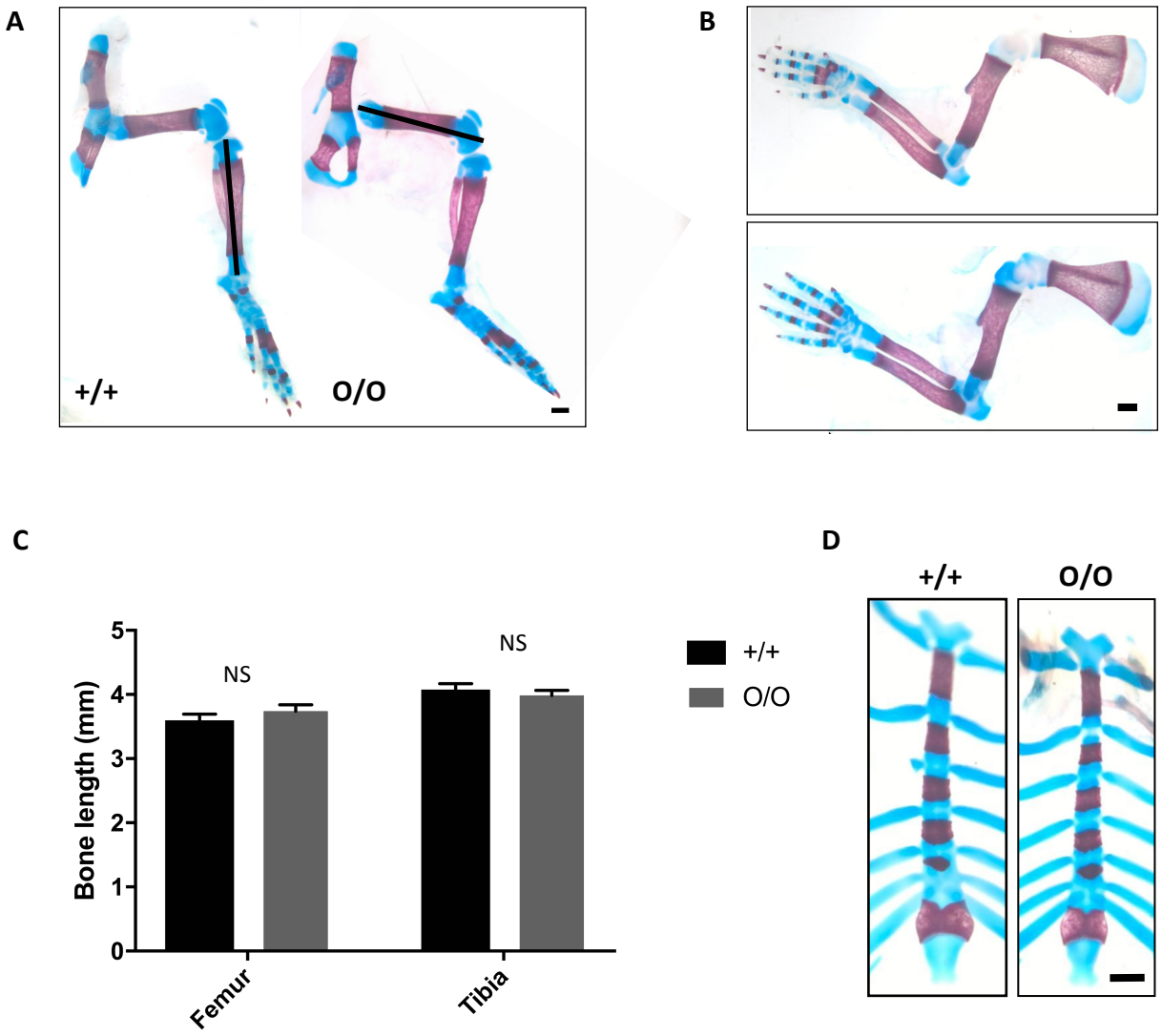

E

	+/+	O/O
Femur (mm) ± SEM	3.60±0.09	3.74±0.10
Tibia (mm) ± SEM	4.08±0.09	3.99±0.08

Figure 34 Morphology of OCD mice at birth.

Skeletal preparations stained with Alizarin Red (to visualise calcified bone) and Alcian Blue (to visualise the cartilage). Pups homozygous for the mutation were morphologically indis- nguishable from wild type li ermates. **(A)** Hind limb **(B)** Fore limb **(D)** Sternum **(C)** Tibia and femur bone lengths (black line) were measured in mice of all 3 genotypes. There was no statistical difference in the average length of the femur and tibia bones in homozygous mice compared to those of wild type littermates. **(E)** Numeric data used for the generation of graph C.

Key: +/+ (wild type) O/O (homozygous for the mutation) SEM (standard error of the mean) NS (not significa t) Two tailed T-test, scale bars = 50µm, n≥3.

A

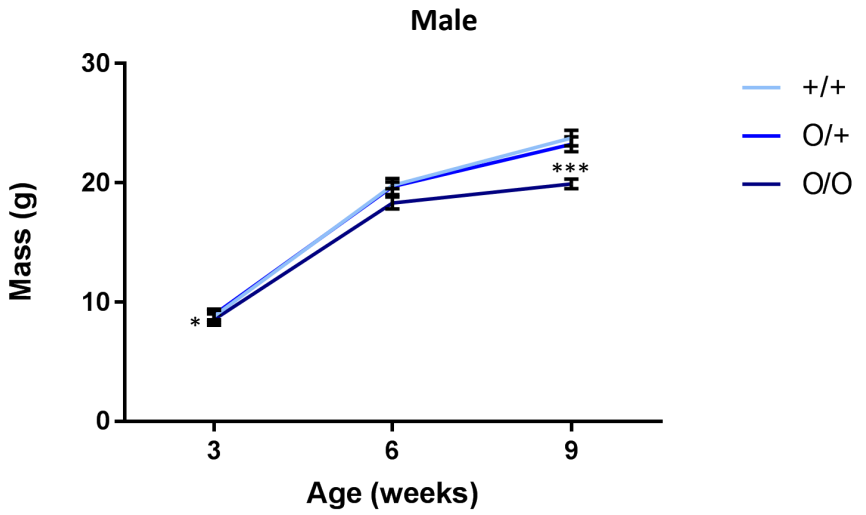

B

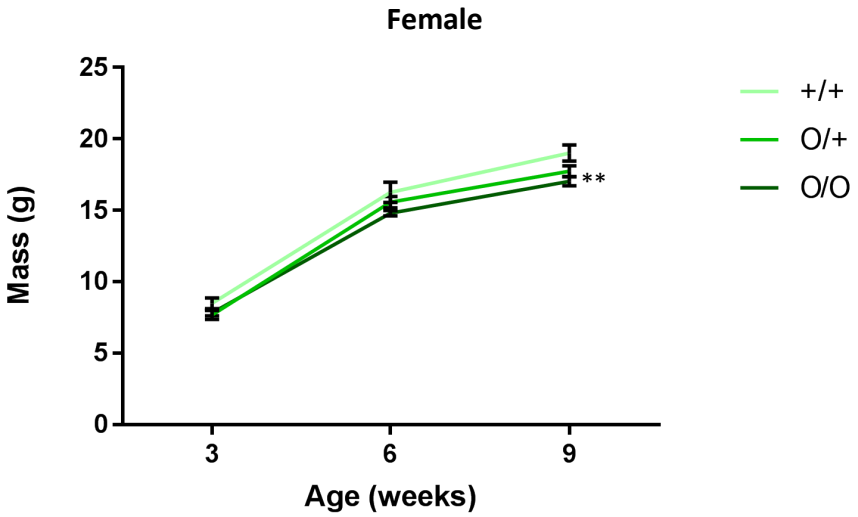

C

		Male			Female		
Age (weeks)		+/+	O/+	O/O	+/+	O/+	O/O
Mass (g) ±SEM	3	8.81±0.51	8.98±0.46	8.53±0.47	8.48±0.38	7.68±0.31	7.83±0.22
	6	19.79±0.27	19.70±0.69	**18.32±0.51 ***	16.26±0.71	15.58±0.40	14.79±0.20
	9	23.77±0.65	23.24±0.64	**19.92±0.40 *****	19.01±0.56	17.73±0.39	**17.02±0.32 ****

Figure 35 Growth rates of OCD mice.

The body mass of mice of all 3 genotypes (wild type, heterozygous mutant and homozygous mutant) was measured at 3, 6 and 9 weeks of age. Male and female mice homozygous for the mutation had reduced body mass, reaching 83.8% **(A)** and 89.5% **(B)** of wild type body mass respectively by 9 weeks. **(C)** Numeric data used for the generation of graphs A and B.

Key: +/+ (wild type) O/+ (heterozygous for the muta on) O/O (homozygous for the mutaon) SEM (standard error of the mean). **p>0.01, Two tailed T-test, n≥10.

3.3.3 Radiographic and morphological analysis of developing OCD mice

Radiographs were taken of the mice in the dorsal plane in order to measure the length and angle of the appropriate bones (Figure 36). As the phenotype did not appear to be affected by gender, only data from male animals has been shown and all data from females is presented in Appendix I. Mice heterozygous for the mutation were analysed in order to assess whether there was a milder intermediate phenotype.

3.3.3.1 Long bones and the pelvic girdle

At 3 weeks of age the average femoral and tibial length bone measurements of female mice homozygous for the mutation were already statistically reduced compared to those of wild type littermates (Appendix I). By 9 weeks both male and female mice homozygous for the mutation were exhibiting mild disproportionate short stature; for example, the average femur and tibia lengths of male mice homozygous for the mutation were 10% and 8.5% shorter that that of wild type littermates (Figure 37). Similarly the combined length of the pelvic girdle bones (ilium and ischium) was reduced by 7.3% compared to wild type bone lengths (Figure 37). There was a clear trend of reduced average tibial, femoral and pelvic bone length measurements, in both male and female heterozygote mice compared to those of wild type littermates; however, there was only one statistically significant difference (Figure 37). This indicates that any putative skeletal phenotype is very mild. There was no difference in the angle between the illium and the tuberosity of the ischium (and therefore no suggestion of hip dysplasia) in mice either homozygous or heterozygous for the mutation and wild type controls (Figure 38).

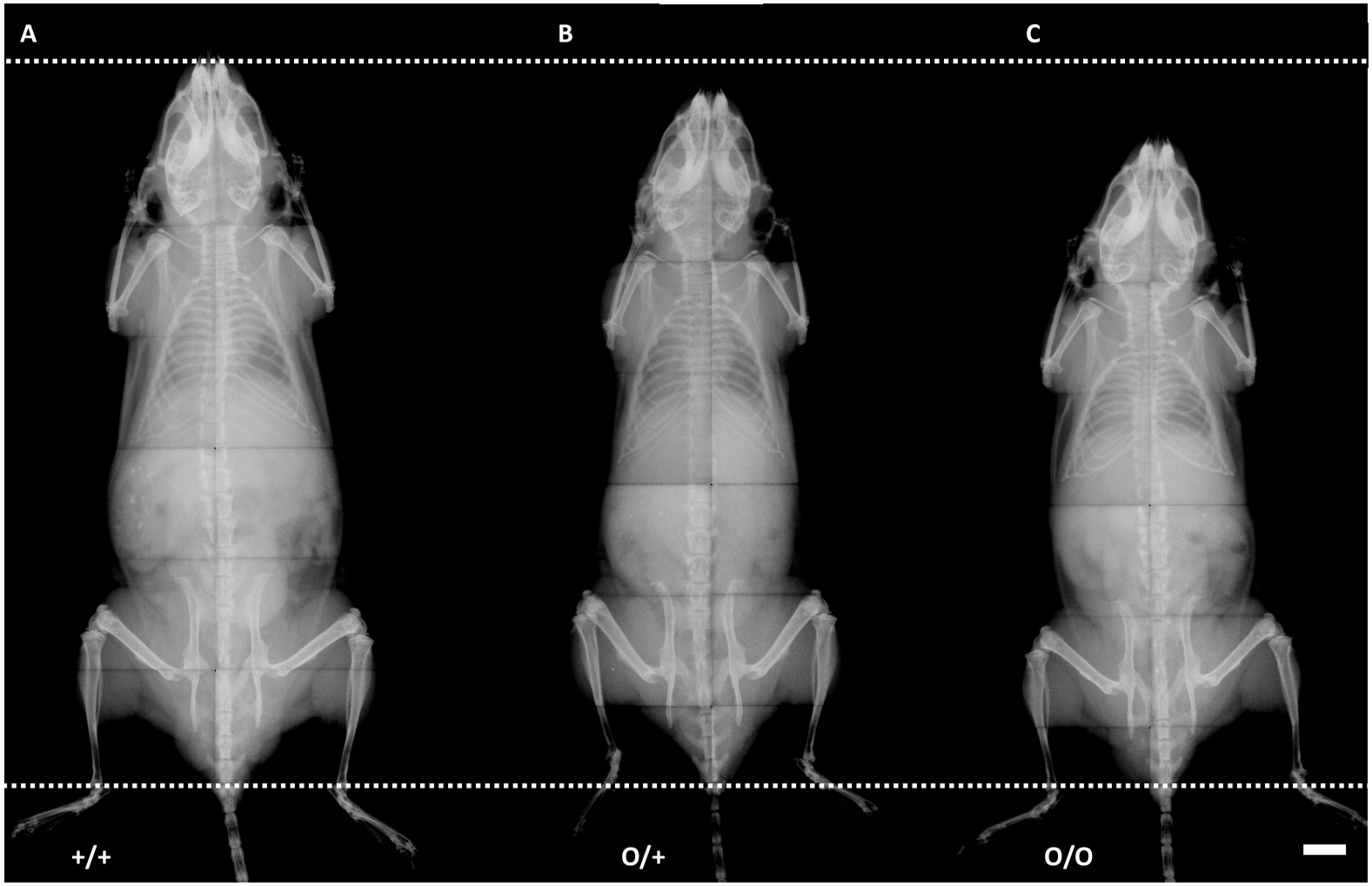

Figure 36 Radiographic analysis of OCD mice.

(A-C) Representative X-ray imaging of 9 week old male mice (dorsal view). Mice homozygous or heterozygous for the mutation displayed disproportionate short stature but no further visible bone abnormalities **(B-C)** when compared with wild type littermates. Key: +/+ (wild type) O/+ (heterozygous for the muta on) O/O (homozygous for the mutation) scale bars = 5mm, n≥10.

A

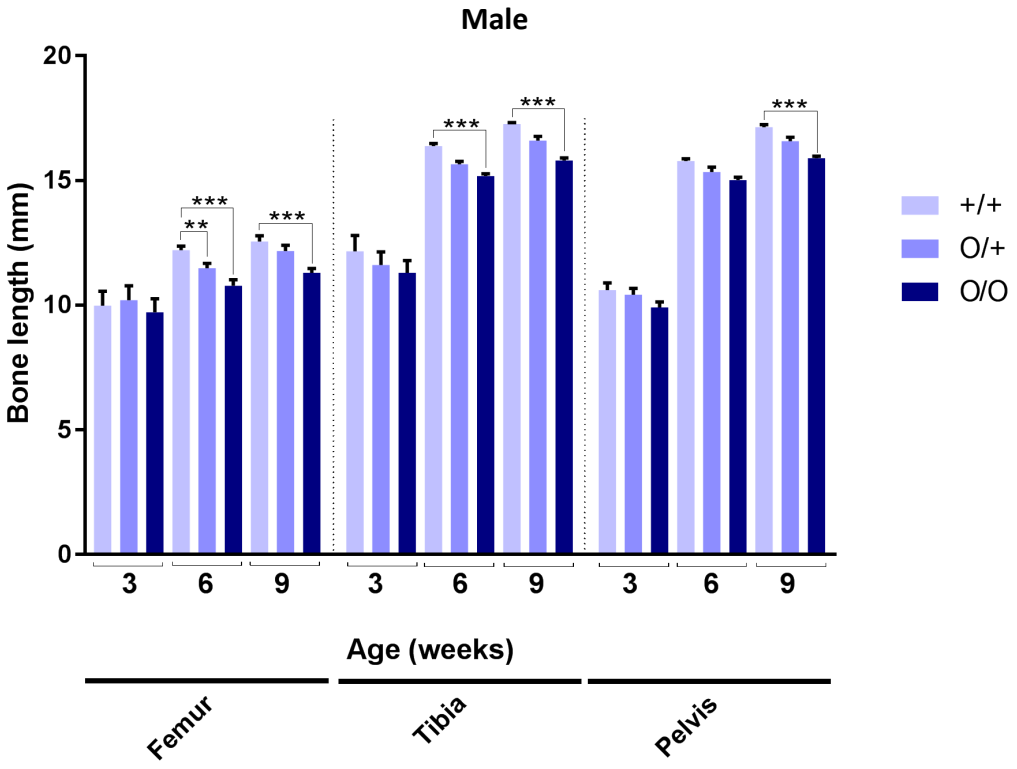

B

Age (weeks)		+/+	O/+	O/O
Femur (mm) ± SEM	3	9.99 ± 0.57	10.20± 0.58	9.72± 0.54
	6	12.21 ± 0.16	**11.48± 0.19** **	**10.78± 0.24** ***
	9	12.56 ± 0.23	12.18± 0.23	**11.30± 0.17** ***
Tibia (mm) ± SEM	3	12.17 ± 0.63	11.61± 0.53	11.30± 0.49
	6	16.38 ± 0.10	15.65± 0.12	**15.17± 0.10** ***
	9	17.27 ± 0.06	16.60± 0.17	**15.80± 0.10** ***
Pelvis (mm) ± SEM	3	10.60 ± 0.29	10.42 ± 0.26	9.91 ± 0.21
	6	15.77 ± 0.10	15.34 ± 0.20	15.02 ± 0.12
	9	17.14 ± 0.11	16.57 ± 0.17	**15.89 ± 0.09** ***

Figure 37 Morphometric analysis of male OCD mice.

Tibia, femur and pelvic (illium and ischium) bone lengths were measured at 3, 6 and 9 weeks of age in male mice of all 3 genotypes. **(A)** The average femur, tibia and pelvis lengths of mice homozygous for the mutation was reduced, reaching 90.0%, 91.5% and 92.7% of wild type bone lengths respectively by 9 weeks. The average femur length of mice heterozygous for the mutation was reduced to 88.3% of wild type femur length at 6 weeks but there was no statistical difference at 9 weeks. **(B)** Numeric data used for the generation of graph A.

Key: +/+ (wild type) O/+ (heterozygous for the muta on) O/O (homozygous for the mutation) SEM (standard error of the mean) **p>0.01, ***p>0.001, Two tailed T-test, n≥10.

A

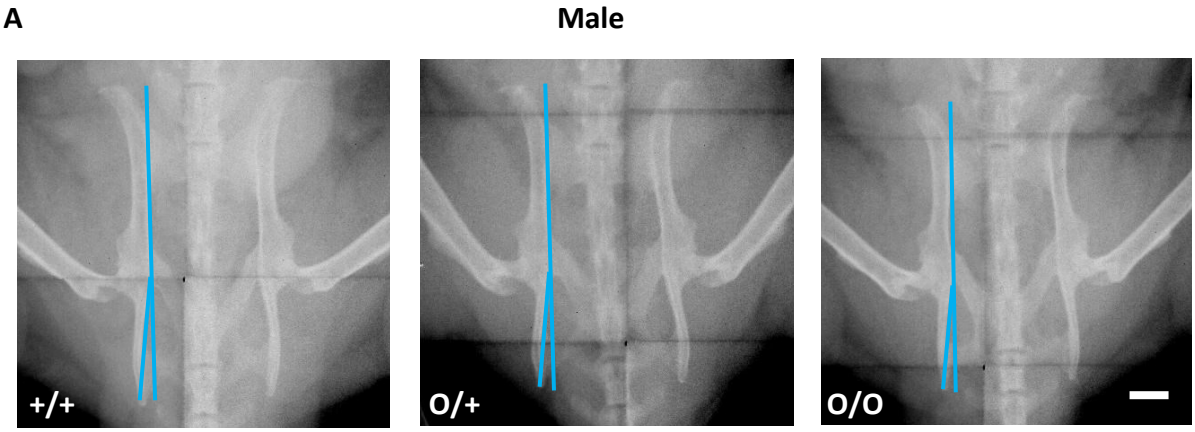

B

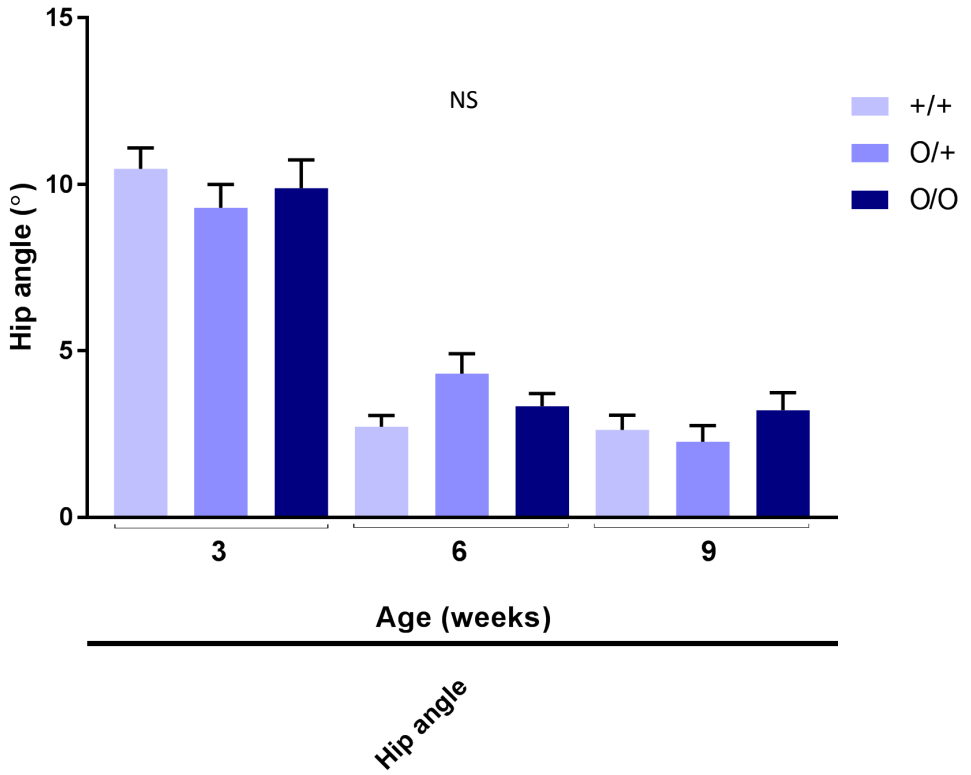

C

Age (weeks)		+/+	O/+	O/O
Hip angle (°) ± SEM	3	10.47±0.63	9.30±0.69	9.89±0.84
	6	2.72±0.34	4.32±0.59	3.34±0.38
	9	2.63±0.44	2.27±0.48	3.22±0.53

Figure 38 Hip dysplasia in male OCD mice.

The angle of the hip was measured at 3, 6 and 9 weeks of age in male mice of all 3 genotypes. **(A)** Representative X-ray imaging of 9 week old male mice (dorsal view). **(B)** There was no statistical difference in the average hip angle of mice either heterozygous or homozygous for the mutation compared with that of wild type littermates. **(C)** Numeric data used for the generation of graph B.

Key: +/+ (wild type) O/+ (heterozygous for the mutation) O/O (homozygous for the muta-on) NS (non-significant) SEM (standard error of the mean) Two tailed T-test, scale bars = 2mm, n≥10.

3.3.3.2 Skull

There was no statistical difference in the inner canthal distance or skull length between either the heterozygous or homozygous mutant and wild type mice at 3, 6 and 9 weeks of age (Figure 39) indicating that the V2019M *Acan* mutation has no overt effect on skull development or intramembranous ossification.

3.3.3.3 Spine

OCD patients exhibit a variety of heterogenous spine abnormalities such as scoliosis and low invertebral discs in the thoracic- and lumbar-spine (Stattin, Tegner et al. 2008, Stattin, Wiklund et al. 2010). In order to assess spine curvature, mice were sacrificed by terminal injection in order to avoid the spinal distortion that can occur with schedule one methods involving inhalation. Male mice were x-rayed in both the dorsal and lateral planes. Homozygous mutant mice did not display any signs of scoliosis up to 9 weeks of age (data not shown) and no further research was conducted.

A

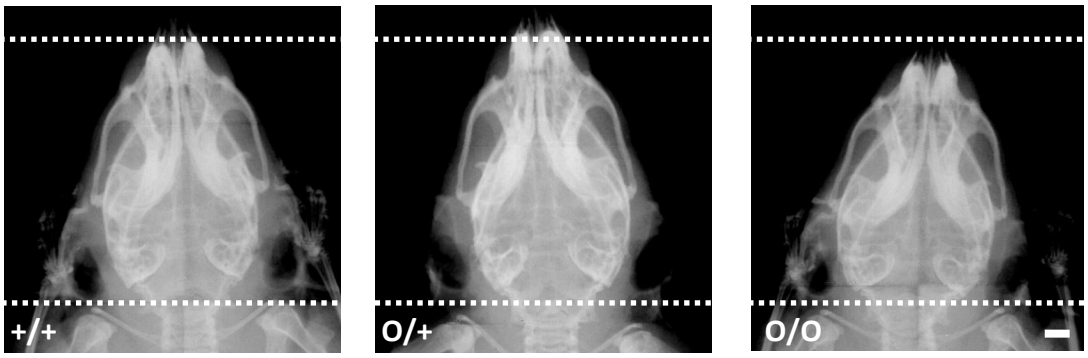

B

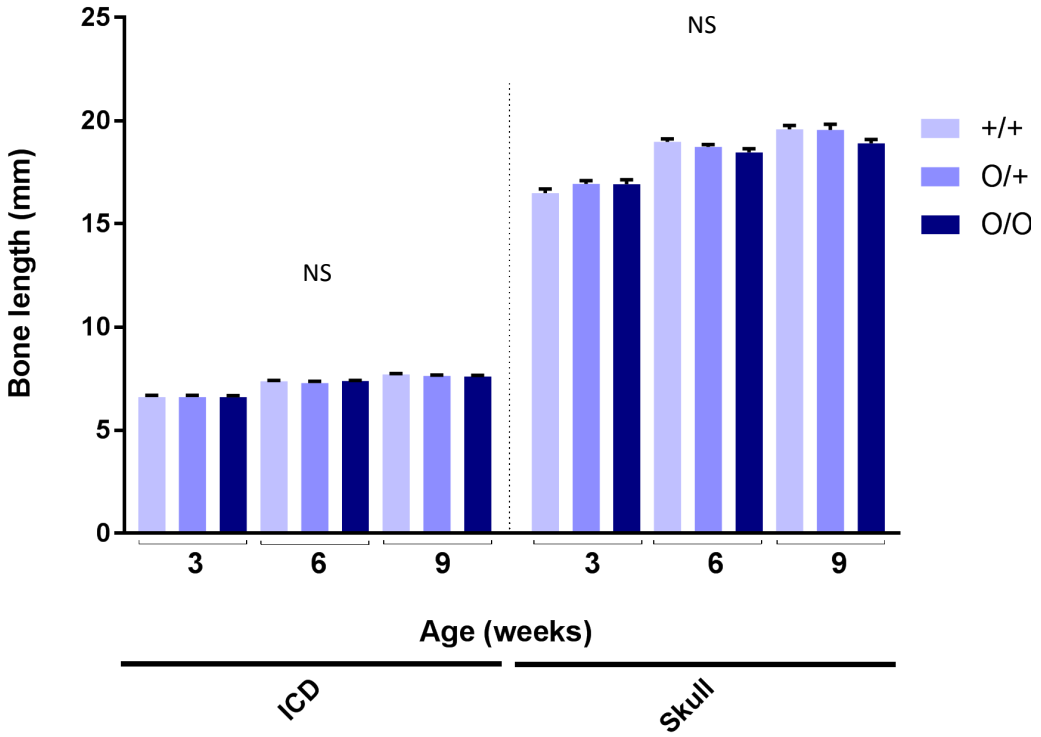

C

Age (weeks)		+/+	O/+	O/O
ICD (mm) ± SEM	3	6.60±0.08	6.60±0.09	6.60±0.07
	6	7.37±0.04	7.28±0.09	7.38±0.03
	9	7.71±0.04	7.63±0.04	7.61±0.05
Skull (mm) ± SEM	3	16.49±0.20	16.93±0.17	16.92±0.22
	6	18.97±0.15	18.73±0.11	18.48±0.17
	9	19.59±0.18	19.55±0.28	18.91±0.18

Figure 39 Morphometric analysis of the skull in male OCD mice.

ICD (inner canthal distance) and skull length were measured at 3, 6 and 9 weeks of age in male mice of all 3 genotypes. **(A)** Representative X-ray imaging of 9 week old male mice (dorsal view). **(B)** There was no difference in ICD or skull length between male littermates of all 3 genotypes. **(C)** Numeric data used for the generation of graph B.

Key: +/+ (wild type) O/+ (heterozygous for the mutation) O/O (homozygous for the mutation) SEM (standard error of the mean) NS (not significant) Two tailed T-test, scale bars = 2mm, n≥10.

3.4 Summary

The aim of this chapter was to validate and describe the skeletal phenotype of two knock-in mouse models of skeletal dysplasia with causative mutations in the C-type lectin domain of aggrecan. Morphometric and histological techniques were used to analyse the relative growth rates and skeletal development of mice homozygous or heterozygous for either the SEMD mutation (D1983N *Acan*) or fOCD mutation (V2019M *Acan*) relative to their wild type littermates. Once this radiographic and morphometric analysis of mutant mice was complete it demonstrated that both male and female mice replicated the human phenotype of the relevant skeletal disorder. All subsequent studies of adult skeletal development were therefore only conducted on mutant male mice since any phenotypic effect could be reasonably extrapolated to mutant female mice. This strategy increased the number of females available for the breeding programme and reduced the number of mice required in line with the principle of the 3Rs (Flecknel 2002). The initial establishment of both the SEMD and OCD mouse colonies was successful. PCR and restriction digestion was used to confirm the presence of germline transmission of the relevant *Acan* mutation in the founder mice provided by Polygene Transgenetics. PCR was also used to verify the presence of the targeted aggrecan allele after deletion of the neomycin cassette (previously used for antibiotic selection of C57Bl/6-derived embryonic stem (ES) cells used during the gene-targeting process). The use of selective breeding removed the FLP transgene (used to remove the neomycin resistance cassette during the generation of the two knock-in mice) within the F1 generation as assessed by PCR analysis. All mutant mice used for the subsequent phenotypic analysis were therefore validated as FLP-negative, with germline transmission of the relevant *Acan* mutation and deletion of the neomycin cassette. Initial phenotyping of the homozygous D1983N *Acan* knock-in mouse confirmed that it replicates the human SEMD aggrecan type phenotype. The D1983N *Acan* mutation had no effect on pre-natal skeletal developmental patterning as the arrangement of skeletal components in homozygous mutant (SEMD) mice was no different from that of their wild type littermates at birth. However, the average bones length of newborn SEMD mice were reduced compared to wild type controls, suggesting that onset of the short stature skeletal phenotype occurs during pre-natal development. Mice homozygous for the SEMD mutation displayed a reduced growth rate during post-natal development and by 9 weeks of age exhibited severe disproportionate short stature. SEMD mice also displayed a number of bone abnormalities which had been reported in the patient

clinical data, including bell-shaped rib cage, hip dysplasia, mild scoliosis, irregular epiphyses and brachydactyly. In addition to this, the morphology of the skull was altered, indicating mid-face hypoplasia and relative mandibular prognathism (all characteristic of the human SEMD phenotype). The distance between the antero-lateral corners of the frontal bone was also slightly reduced, showing a decrease in the size of the cranial vault. Although the bones that form the cranial base and caudal cranial vault ossify via endochondral ossification, the craniofacial and rostral cranial vault bones are formed by intramembranous ossification (Percival and Richtsmeier 2013). These data suggest that both intramembranous and endochondral ossification are perturbed in the SEMD mouse model. Mice who were heterozygous for the SEMD mutation did not display a reduced growth rate but exhibited a mild disproportionate short stature phenotype by 9 weeks of age. In contrast to the mice homozygous for the mutation, heterozygous mice did not exhibit any additional skeletal abnormalities such as hip dysplasia or brachydactyly. This is in line with patient clinical data in which it was reported that the heterozygous parents and half-sister of the proband appeared to have reduced proportionate short stature but no other bone abnormalities. It is worth noting, however, that the only family member with two wild type aggrecan alleles was thought to be above average height for the indigenous Mexican population and the region from which the family had originated (Krakow, personal communication, 2017). Initial phenotyping of homozygous V2019M *Acan* knock-in mice confirmed that they replicated the human familial OCD disproportionate short stature phenotype. The V2019M *Acan* mutation had no overt effect on pre-natal skeletal developmental patterning or growth. At three weeks of age female OCD mice were already exhibiting mild disproportionate short stature and by 9 weeks of age both male and female mice had a disproportionate short stature phenotype. OCD mice did not display a hip dysplasia often seen in mouse models of skeletal dysplasia disorders and radiographic analysis did not reveal any of the heterogenous skeletal abnormalities recorded in the patients' clinical data (such as scoliosis) apart from the mild short stature phenotype. Unfortunately, due to the resolution of the radiographic images obtained it was not possible to definitively say whether the other noted abnormalities (such as platyspondyly or osteochondrotic lesions) were present. Further to this, mice heterozygous for the V2019M *Acan* mutation appeared to exhibit an extremely mild intermediate skeletal phenotype. There was a clear non-statistical trend in the morphometric data indicating a decrease in pelvic, tibial and femoral bone lengths compared to those of the wild type mice.

In conclusion, morphometric analysis of both the SEMD and OCD mouse models accurately replicates the skeletal phenotypes reported in patients with these very different skeletal disorders. These mouse models formed a phenotypic disease spectrum from the very severe SEMD to the milder OCD and were promising models for the study of these conditions (Figure 40). Subsequent to this phenotypic study, analysis of the resultant tissue pathology was conducted.

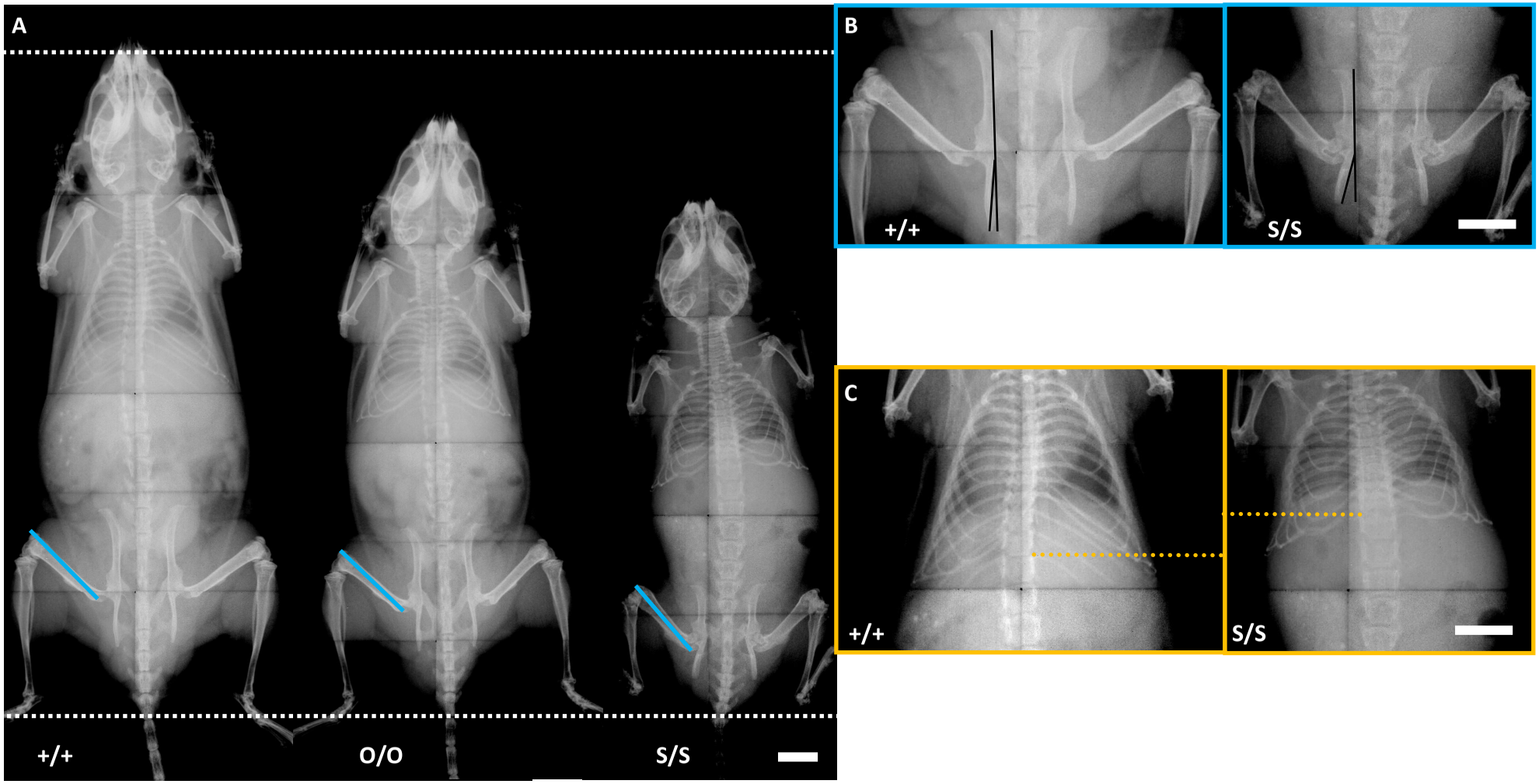

Figure 40 Radiographic comparison of the OCD and SEMD mouse models.

(A) Representa ve X-ray imaging of 9 week old male mice (dorsal view). Both the OCD and SEMD mouse models exhibit dispropor onate short stature (blue lines). The SEMD mouse model is phenotypically more severe and has a number of skeletal abnormali es including **(B)** hip dysplasia (black lines) and **(C)** a shortened bell-shaped rib cage. n≥4, scale bars = 2mm.

Chapter 4. Qualitative Tissue Pathology Analysis of the SEMD and OCD Mouse Models

The morphometric and radiographic analysis performed in Chapter 3 indicated that the homozygous D1983N *Acan* knock-in mice replicated the severe disproportionate short stature phenotype of the recessive human skeletal disorder spondyloepimetaphyseal dysplasia (SEMD) aggrecan type (Tompson, Merriman et al. 2009). Thus far, no analysis of patient tissue has been performed due to the rarity of SEMD aggrecan type in the population and because the three known patients have not undergone surgical intervention. *In vitro* studies of a recombinant aggrecan G3 domain demonstrated that the secretion of aggrecan is unaffected by the human D2267N mutation. The mutation is, however, predicted to affect the interaction of aggrecan with other extracellular matrix proteins and surface-plasmon-resonance studies showed that the D2267N *ACAN* G3 domain had altered binding with tenascin C (Tompson, Merriman et al. 2009). The homozygous V2019M *Acan* knock-in mouse also appeared to replicate the moderate disproportionate short stature phenotype of dominant familial OCD (Stattin, Wiklund et al. 2010). Familial osteochondritis dissecans is more common in the population than SEMD, with five causative mutations reported so far (Aspberg, personal communication, Gkourogianni, Andrew et al. 2017, van der Steen, Pfundt et al. 2017); however, little is known about the downstream effects exerted by these mutations. Due to the formation of osteochondrotic lesions and the resultant early-onset osteoarthritis, OCD patients often undergo arthroplasty to remove loose bodies from the joint space. Mass spectral analysis of arthro-plasty samples suggested that the V2303M *ACAN* mutation did not affect secretion or glycosaminoglycan sulfation (Stattin, Wiklund et al. 2010). *In vitro* analysis of patient MSC and iPSC pellet cultures indicated mutant aggrecan was retained within the ER with very little secretion into the inter-territorial matrix (Xu, Stattin et al. 2016). These two studies and an *in vitro* model system expressing recombinant mutant G3 domain in mammalian cells also suggested there was altered matrix composition and reduced binding with other extracellular matrix proteins (Stattin, Wiklund et al. 2010, Xu, Stattin et al. 2016). In addition to this, the C-type lectin domain of aggrecan is involved in both secretion of the aggrecan core protein and the binding of aggrecan to other ECM molecules (Day, Olin et al. 2004). The investigation of the tissue pathology for the OCD and SEMD mouse models was therefore performed as a broad analysis of the growth plate structure, mutant aggrecan secretion and the localisation of key extracellular matrix proteins. Wild type C57/BL6 mice and heterozygous and homozygous mutant mice were included in the initial histological analysis of tissue pathology. Tissue analysis was performed on mice at birth, 3 weeks, 9 weeks, 6 months and 9 months of age to reflect the onset and progression of the disorders.

4.1. Histological analysis of growth plate structure

Haematoxylin and Eosin staining was used to assess the structure of the tibial growth plate and cell morphology in male mice either heterozygous or homozygous for the OCD or SEMD mutations and their wild type littermates. Toluidine Blue staining was used to investigate the relative abundance of proteoglycans in the growth plate. Chondrocytes in the wild type growth plate were arranged into three distinct zones (resting, proliferating and hypertrophic) and proliferating chondrocytes were arranged in columns parallel to the direction of growth.

4.1.1. The SEMD mouse model

The organisation of tibial growth plates from mice homozygous or heterozygous for the SEMD mutation was comparable to those from wild type littermates although the growth plates of mice homozygous for the mutation appeared visually smaller (n=2) (Figure 41A). At birth there was no visible difference in toluidine blue staining intensity (and therefore proteoglycan abundance) in growth plates from wild type and mutant mice (Figure 41B). At three weeks of age there was a 23.7% reduction in the growth plate height of mice homozygous for the SEMD mutation compared to wild controls (Figure 42A-B). Further to this, the relative proportion of zones within the growth plate was abnormal, with a 16.0% decrease in the proliferative zone and an 11.8% proportional increase in the hypertrophic zone in SEMD growth plates compared to wild type controls (Figure 42C). The formation of the secondary ossification centre in the wild type murine tibial growth plate occurs after 7-10 days of age. At three weeks of age the secondary ossification centre is well-formed with a pronounced mineralized area. In growth plates from mice homozygous for the SEMD mutation there was a 49.9% reduction in the mineralised area of the secondary ossification centre (Figure 42A and D) suggesting that the formation of the secondary centre was delayed.

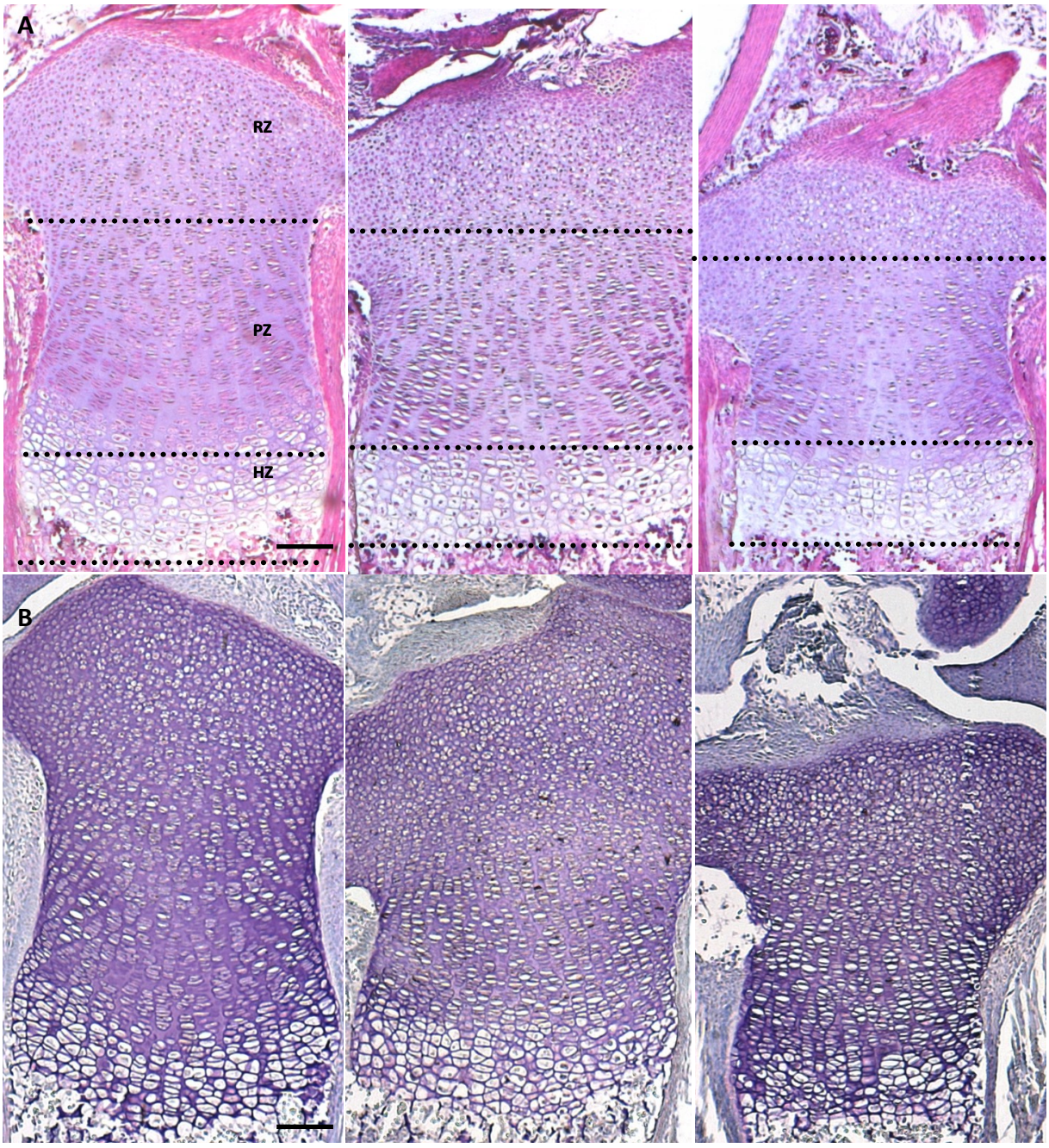

Figure 41 Tibial growth plate structure in newborn SEMD mice.

(A) H&E and **(B)** toluidine blue staining of sec ons from heterozygous and homozygous mice and wild type controls. There were no visible di erences in growth plate structure and all zones were present. Further to this, there were no visible di erences in toluidine blue staining intensity observed.

Key: +/+ (wild type) S/+ (heterozygous mutant) S/S (homozygous mutant) RZ (resti g zone) PZ (prolifera ve zone) HZ (hypertrophic zone) n≥2 (except S/+) scale bar = 20µm.

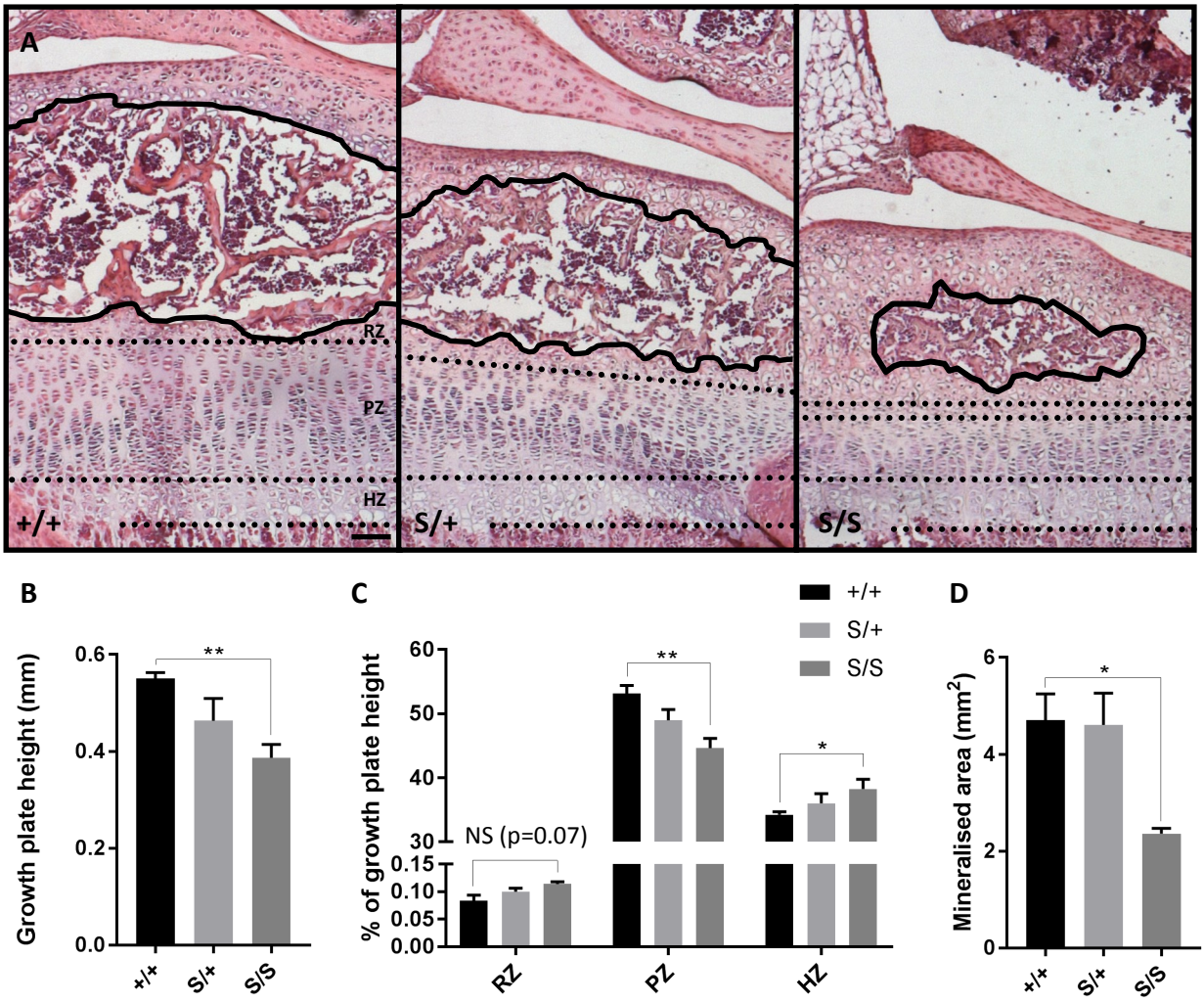

E

		+/+	S/+	S/S	
Growth plate height (mm) ± SEM		0.51±0.01	0.46±0.05	**0.39±0.03****	n≥3
% of total growth plate height ± SEM	RZ	0.08± 0.01	0.10±0.01	0.11±0.004	n≥3
	PZ	53.18± 1.23	48.98±1.69	**44.67±1.49****	n≥3
	HZ	34.25± 0.47	36.05±1.52	**38.30±1.49***	n≥3
Area of secondary centre (mm^2) ± SEM		4.71±0.54	4.61±0.65	**2.36±0.11***	n=3

Figure 42 Tibial growth plate structure in 3 week old SEMD mice.

(A) H&E staining of matching sections from heterozygous and homozygous mutant mice and wild type controls. Homozygous mice had very disorganised growth plates **(B)** with a 23.7% reduction in height. **(C)** All zones were present, but there was a 16% decrease in the proliferative zone, an 11.82% increase in the hypertrophic zone and **(D)** a 49.9% decrease in the mineralised area of the secondary ossification centre (black outline). Heterozygous mice had slightly disorganised growth plates and a well-formed secondary ossification centre. **(E)** Table showing the numeric data used for the generation of graphs B, C and D.

Key: +/+ (wild type) S/+ (heterozygous mutant) S/S (homozygous mutant) RZ (resting zone) PZ (proliferative zone) HZ (hypertrophic zone) NS (not significant) *P≤0.05, **P≤0.01, Two tailed T-test, scale bar = 50µm, n≥3. 3 joint regions analysed from each animal.

Growth plates of mice homozygous for the SEMD mutation also exhibited an altered cellular organisation. The separation between zones was visibly less distinct and chondrocytes were variable in size and arranged in irregular columns which were not always in the direction of growth (Figure 43). In addition to this, the intensity of toluidine staining of the ECM was slightly reduced, indicating a reduction in either proteoglycan abundance or sulfation (n=3) (Figure 43). There was no statistical difference in the parameters measured in the growth plates of mice heterozygous for the SEMD mutation and the secondary ossification centre was well-formed (Figure 42). Cellular organisation in the growth plate was slightly altered, alt-hough chondrocytes were generally arranged in columns parallel to the direction of growth and all zones were present. There was also no difference in toluidine blue staining intensity when compared with wild type controls (Figure 43).

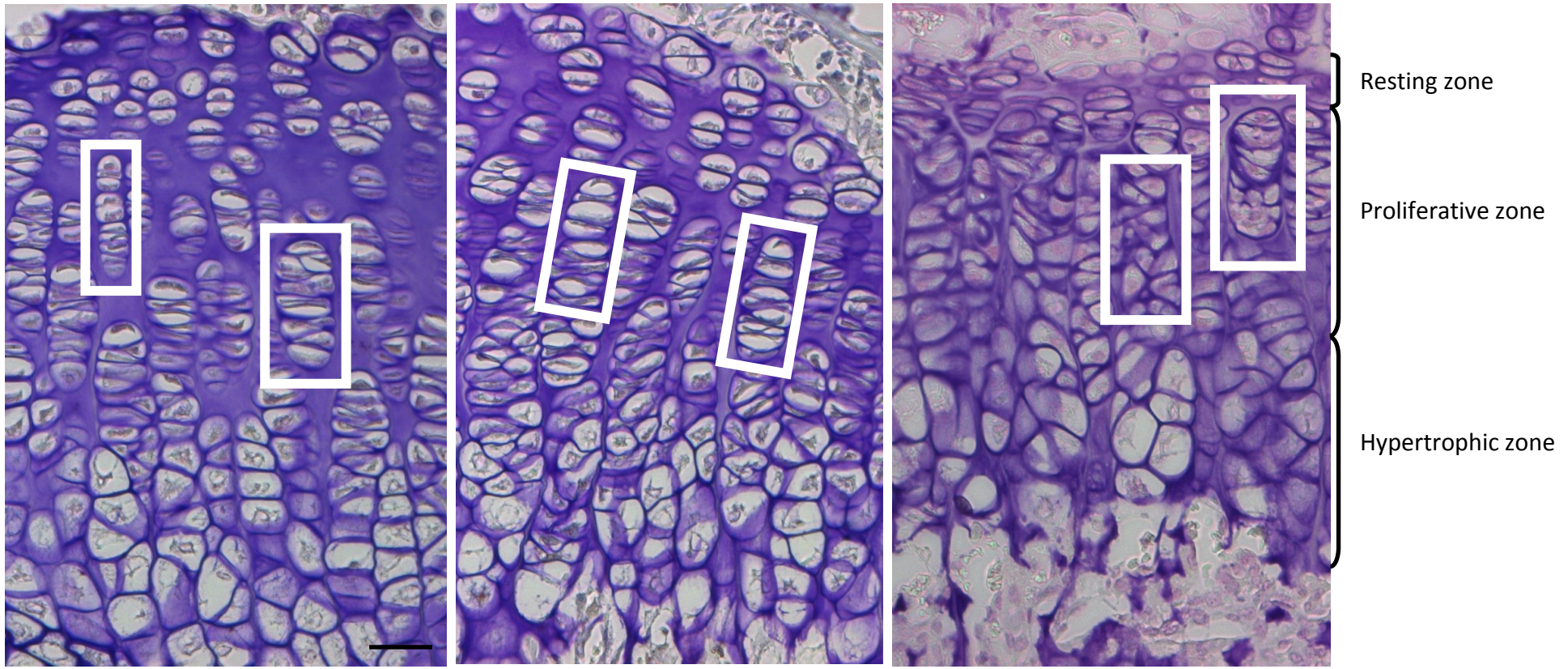

Figure 43 Growth plate structure and proteoglycan abundance in SEMD mice.

Toluidine blue staining of matching tibial growth plate sections from 3 week old male mice heterozygous or homozygous for the mutation and wild type controls. The growth plates of homozygous mice were very disorganised with less distinct zone separation, reduced columnar organisation and a slight reduction in the intensity of toluidine blue staining. The growth plates of heterozygous mice were slightly disorganised with all zones present. There were no visible differences in toluidine blue staining observed.

Key: +/+ (wild type) S/+ (heterozygous for SEMD mutation) S/S (homozygous for SEMD mutation) RZ (resting zone) PZ (proliferative zone) HZ (hypertrophic zone) scale bar = 100µm, 3 joint regions analysed from 3 individual animals.

4.1.2. The OCD mouse model

The tibial growth plates of newborn mice homozygous or heterozygous for the OCD mutation were well organised with normal cell morphology. The chondrocytes were arranged in three distinct zones (resting, proliferative and hypertrophic) with well-formed columns in the proliferative zone (Figure 44A). Furthermore, there was no visible difference in the intensity of toluidine blue staining (Figure 44B). By three weeks of age growth plate height in mice homozygous for the OCD mutation was reduced by 13.7% (Figure 45A-B) although there was no statistical difference in the relative proportion of each zone when compared to that of wild type controls (mutant mice analysed ≥5) (Figure 45C). The mineralized secondary ossification centre appeared visually smaller, suggesting a delay in formation of the secondary ossification (Figure 45A). Quantitative analysis indicated a trend in decreasing size of the mineralised centre in OCD growth plates compared to wild type controls; however, this difference was not statistically significant (mutant mice analysed ≥4, P=0.6) (Figure 45D). The growth plates of mice homozygous for the OCD mutation were disorganised with a slight reduction of toluidine blue staining in the interterritorial ECM (Figure 46). The growth plates of mice heterozygous for the mutation were comparable to those of wild type controls with only a slight reduction in extracellular toluidine blue staining in some areas (Figure 46).

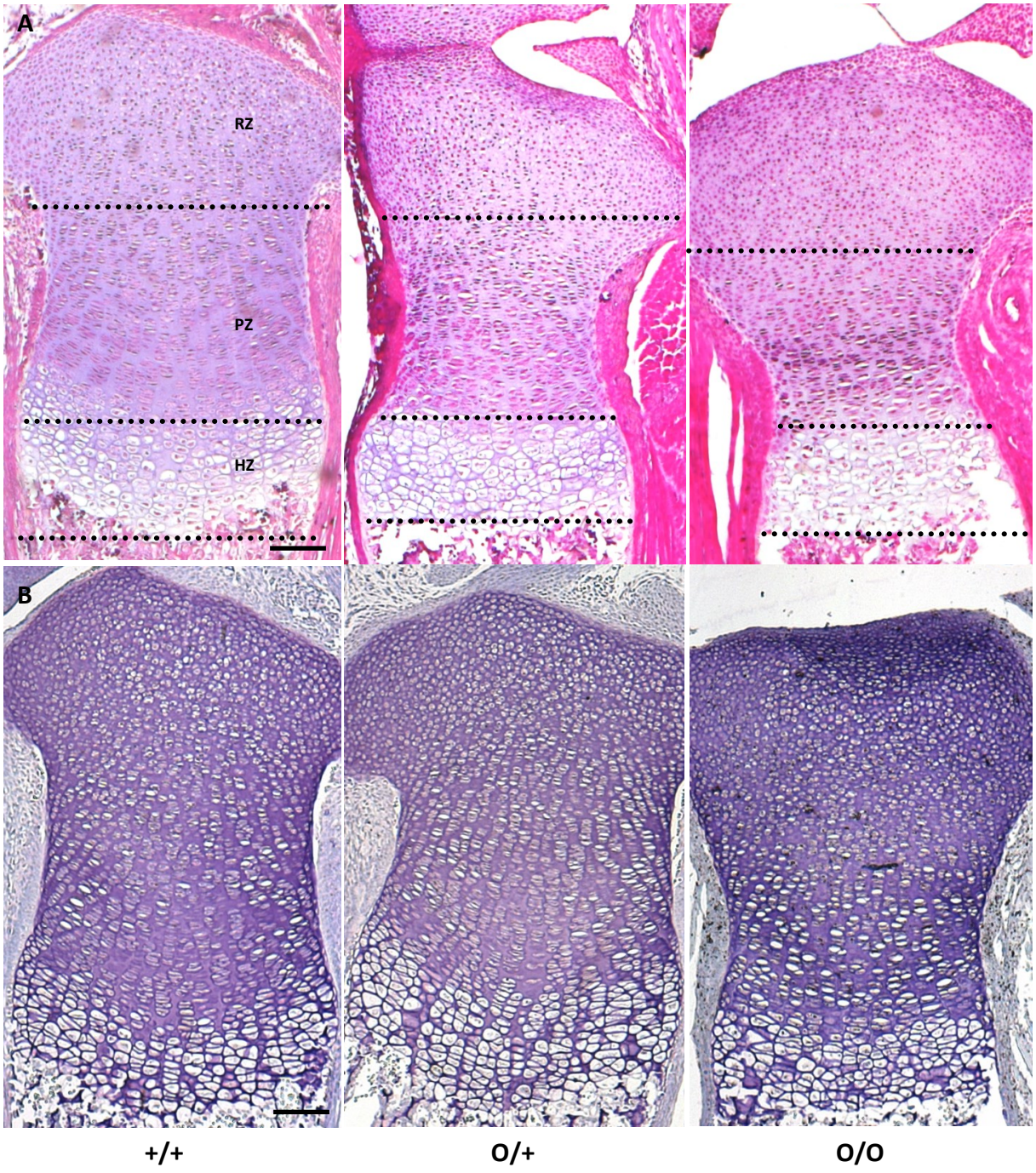

Figure 44 Tibial growth plate structure in newborn OCD mice.

(A) H&E and **(B)** toluidine blue staining of sec ons from heterozygous and homozygous mice and wild type controls. There were no visible differences in growth plate structure and all zones were present. Further to this, there were no visible differences in toluidine blue staining intensity observed.

Key: +/+ (wild type) O/+ (heterozygous mutant) O/O (homozygous mutant) RZ (resting zone) PZ (proliferative zone) HZ (hypertrophic zone) H&E n=3, toluidine blue n≥2, scale bar = 20µm.

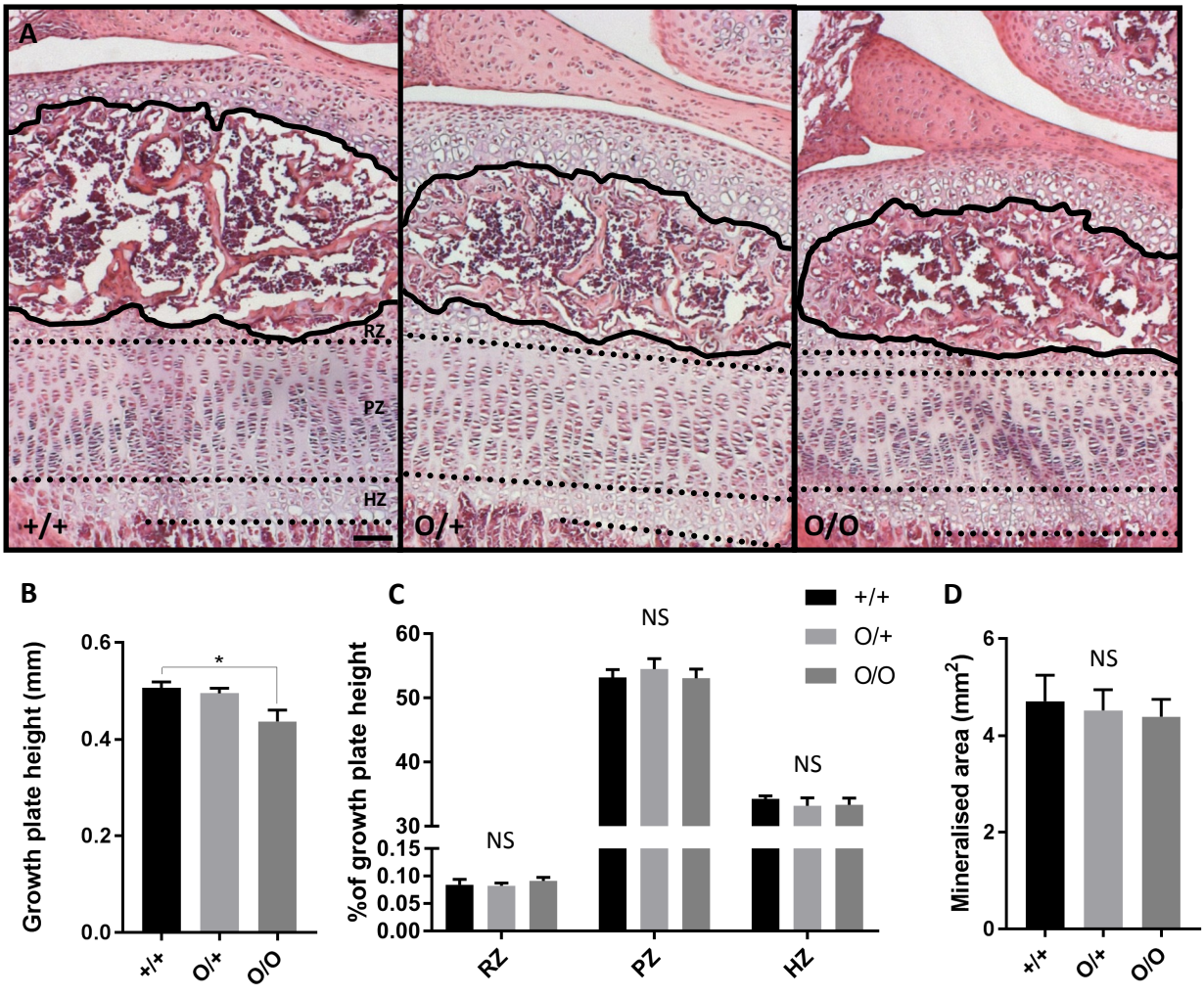

E

		+/+	O/+	O/O	
Growth plate height (mm) ± SEM		0.51±0.01	0.50±0.01	**0.44±0.02***	n≥5
% of total growth plate height ± SEM	RZ	0.08± 0.01	0.08±0.005	0.09±0.007	n≥5
	PZ	53.18± 1.23	54.51±1.59	53.06±1.42	n≥5
	HZ	34.25± 0.47	33.20±1.23	33.35± 1.04	n≥5
Area of secondary centre (mm^2) ± SEM		4.71±0.54	4.52±0.43	4.39±0.36	n≥3

Figure 45 Tibial growth plate structure in 3 week old OCD mice.

(A) H&E staining of matching sections from heterozygous and homozygous mutant mice and wild type controls. Homozygous mice had disorganised growth plates **(B)** with a 13.7% reduc on in height. **(C)** There was no statistical difference in the proportion of the zones in the growth plate **(D)** or the mineralised area of the secondary ossification centre (black outline). Heterozygous mice had slightly disorganised growth plates with a well-formed secondary ossification centre. **(E)** Table showing the numeric data used for the generation of graphs B, C and D.

Key: +/+ (wild type) O/+ (heterozygous mutant) O/O (homozygous mutant) RZ (resting zone) PZ (proliferative zone) HZ (hypertrophic zone) NS (not significant) *P≤0.05, Two tailed T-test, scale bar = 50µm, 3 joint regions analysed from each animal.

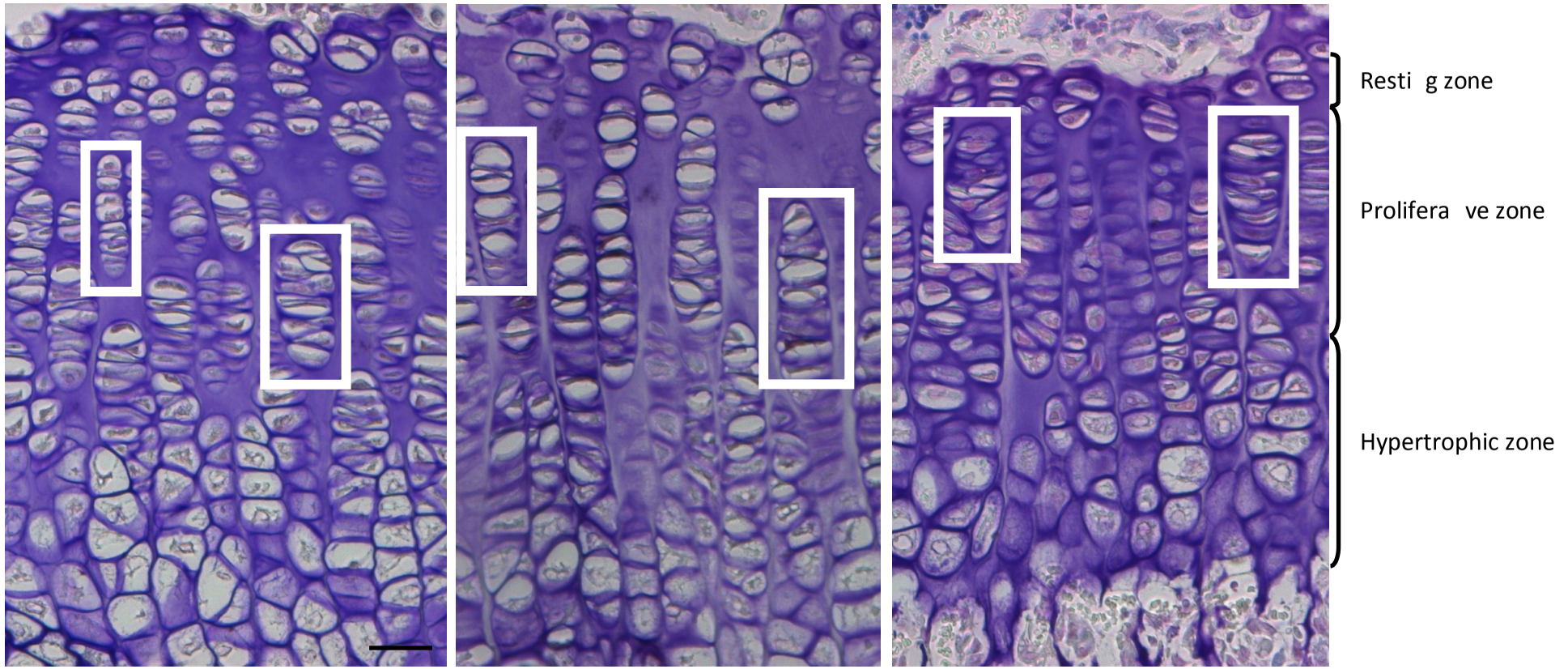

Figure 46 Growth plate structure and proteoglycan abundance in OCD mice.

Toluidine Blue staining of matching tibial growth plate sections from 3 week old mice heterozygous or homozygous for the muta on and their wild type littermates. The growth plates of homozygous mice were quite disorganised and the Toluidine Blue staining was reduced in places, although all zones were present. The growth plates of heterozygote mice were slightly disorganised with all zones present. There was a slight reduction in Toluidine Blue staining observed. (n=3).

Key: +/+ (wild type) O/+ (heterozygous for OCD mutation) O/O (homozygous for OCD mutation) RZ (resting zone) PZ (proliferative zone) HZ (hypertrophic zone) scale bar = 100µm, 3 joint regions analysed from 3 individual animals.

4.2. Histological analysis of collagen fibril orientation

Picrosirius red staining visualised under polarised light was used to visualise the orientation and thickness of collagen fibrils in growth plate and articular surface cartilage of tibias from wild type and mutant male mice at 3 weeks of age. Growth plate cartilage from wild type mice contained thinner green-coloured collagen fibrils with some regions of increased fibril thickness which appeared red under polarized light (Figure 47A).

4.2.1. The SEMD mouse model

Growth plate cartilage from mice heterozygous for the SEMD mutation were visually similar to those of wild type mice. In contrast, collagen fibrils in growth plate cartilage from homozygous mice had an irregular appearance with a greater number of fibrils with increased thickness compare to the control (Figure 47A). Articular cartilage from wild type mice contained thinner green-coloured or yellow-coloured collagen fibrils which were orientated according to zone. Collagen fibrils in the superficial zone were arranged parallel to the articular surface, whereas those in the transitional and deep zones were orientated perpendicular to the joint surface (Figure 47B). Articular cartilage from mice homozygous for the SEMD mutation contained thicker red-coloured collagen fibrils. In addition to this, and although collagen fibril orientation in the superficial zone was maintained, the organisation of fibrils in the transitional and deep zones was completely disrupted (Figure 47B). There was no overt difference in fibril thickness in articular cartilage from heterozygous mice and the orientation of fibrils in the superficial zone was similar to that in the wild type control. The organization of fibrils in the transitional and deep zones was slightly disrupted; however, some fibrils were still per-pendicular to the joint surface (Figure 47B).

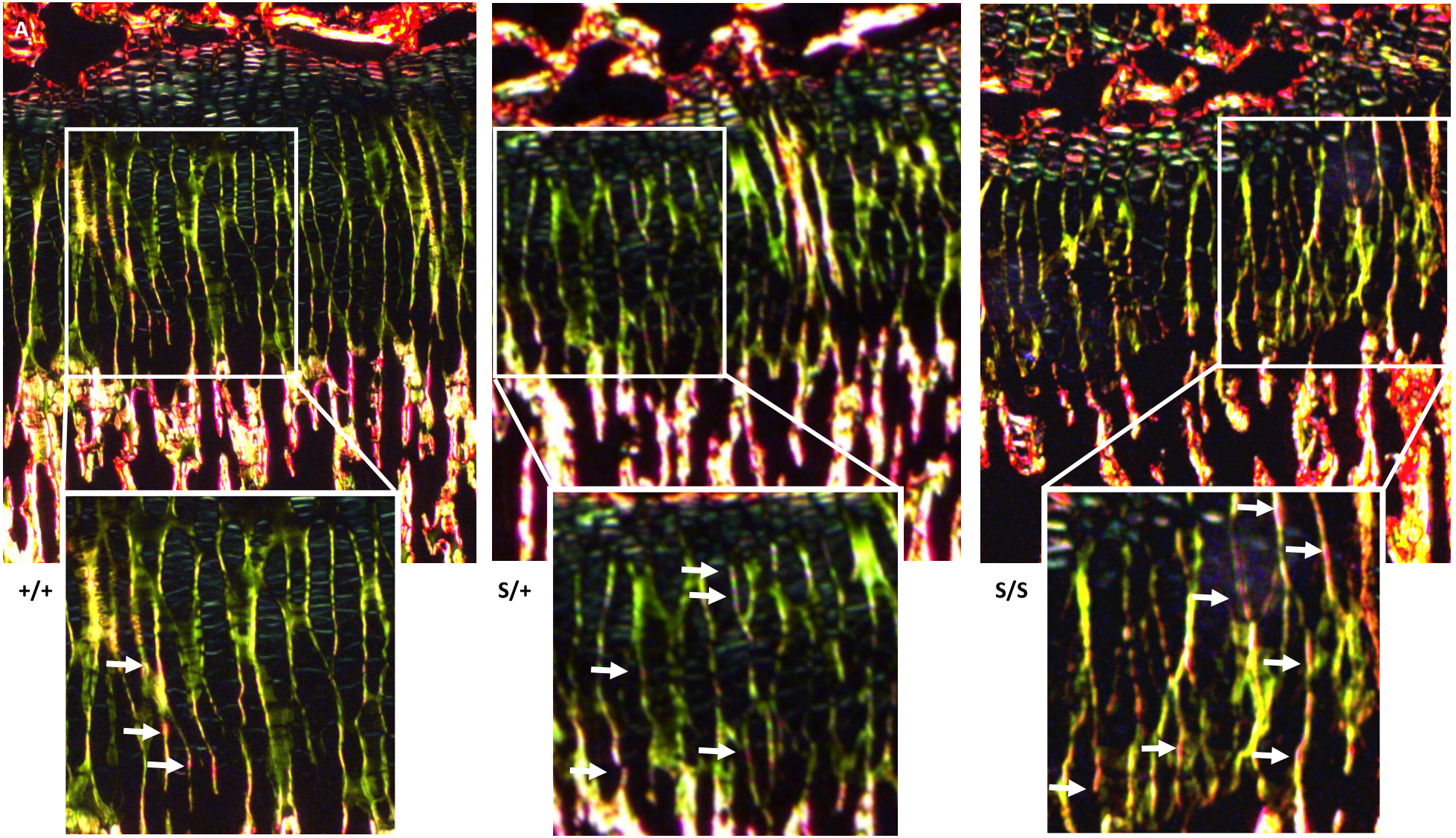

Figure 47 Collagen fibril organisation in SEMD mice (A).

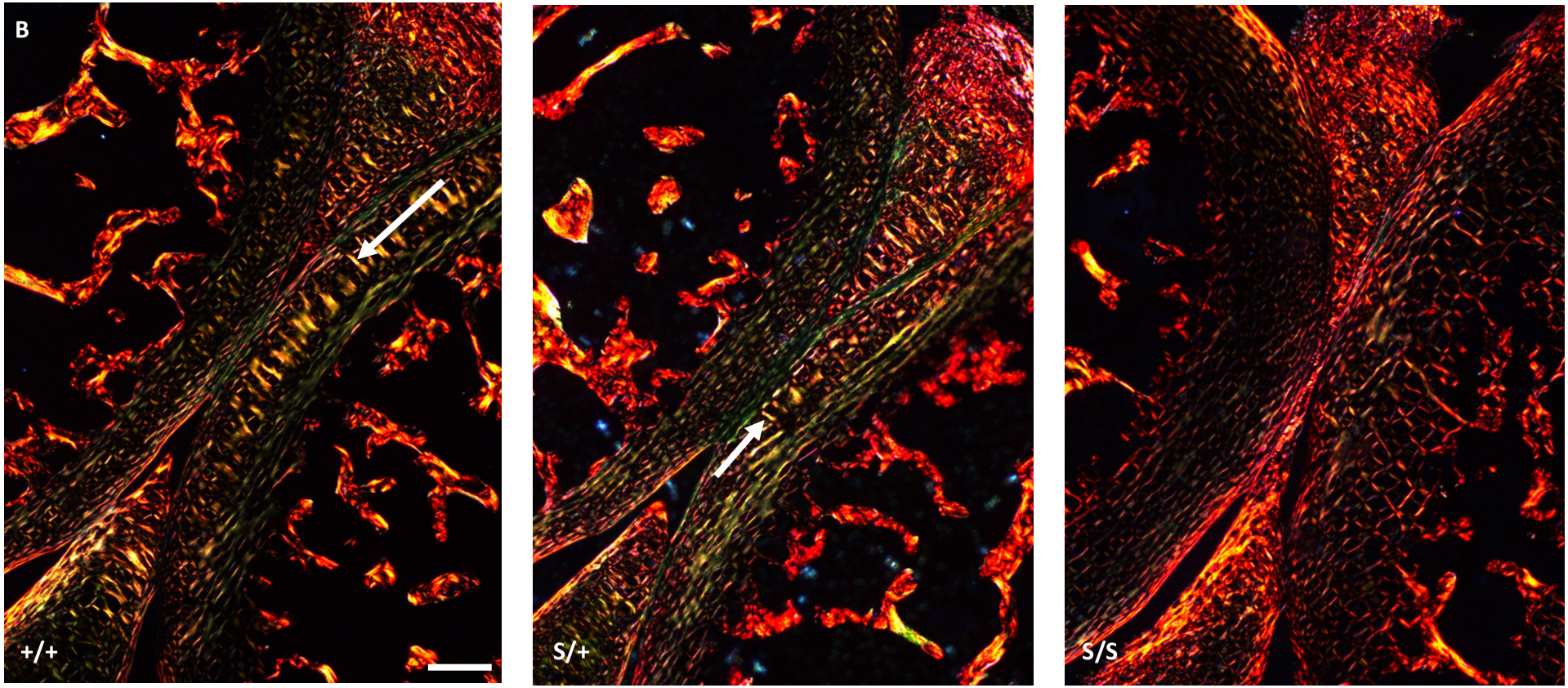

Figure 47 Collagen fibril organisation in SEMD mice (B).

Picrosirius red staining (visualised under polarised light) of matching bial car lage secti ns from 3 week old male mice. **(A)** Growth plates of mice homozygous for the muta on exhibited irregular collagen brils density compared to wild type controls (thicker fi rils appeared red, white arrows). **(B)** The orienta on of brils in the transi onal and deep zones of ar cular car lage from mice heterozygous for the muta on was slightly altered but some brils were s ll perpendicular to the ar cular surface (white arrows). Car lage from homozygous mice contained thicker red collagen fi brils. Fibril organisa on in the transiti nal and deep zones was completely disrupted (n=3).

Key: +/+ (wild type) S/+ (heterozygous for the SEMD muta on) S/S (homozygous for the SEMD muta on) scale bar = 50µm, n=3.

4.2.2. The OCD mouse model

There was no overt difference in fibril orientation or thickness in the cartilage growth plate of mice either heterozygous or homozygous for the OCD mutation and their wild type controls (data not shown). There was also no visual difference between the articular cartilage of mice heterozygous for the OCD mutation and wild type controls (Figure 48). In contrast, articular cartilage from homozygous mice exhibited thicker red-coloured fibrils. The orienta-tion of fibrils in the superficial zone was comparable to that of wild type controls and although the organisation of fibrils in the transitional and deep zones was slightly disrupted, some fibrils were still perpendicular to the joint surface (Figure 48).

Due to the mildness of the skeletal phenotype and lack of overt tissue pathology, mice heterozygous for either the OCD or SEMD causative mutations were not analysed further.

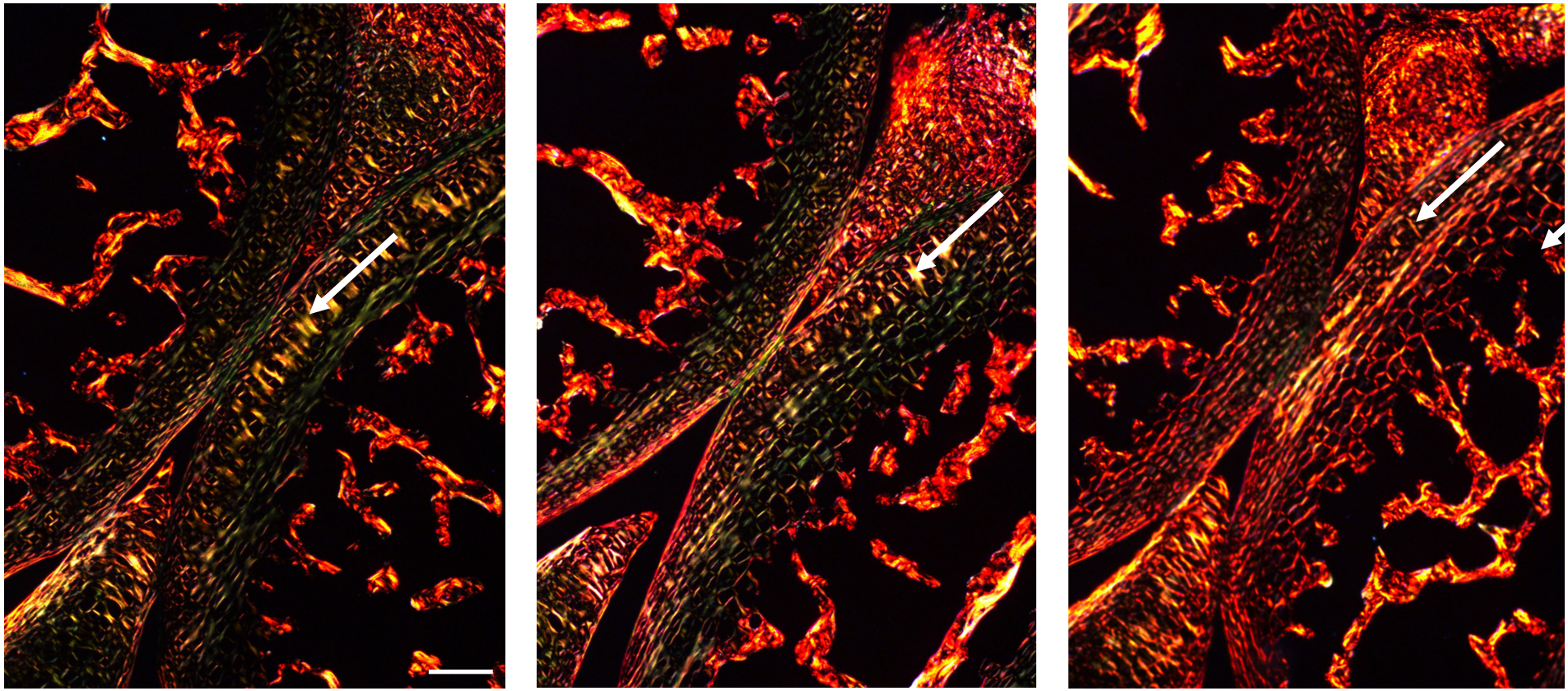

Figure 48 Collagen fibril organisation in OCD mice.

Picrosirius red staining of matching bial ar cular car lage secti ns from 3 week old mice heterozygous or homozygous for the muta on and their wild type li ermates. The orienta on of the collagen fi rils in the deep zone of the ar cular surface of wild type mice was perpendicular to the ar cular surface. The orienta on of brils in mice homozygous for the muta on was very variable but some brils were still perpendicular (white arrows).

Key: +/+ (wild type) O/+ (heterozygous for the OCD muta on) O/O (homozygous for the OCD muta on) scale bar = 50µm, n=3.

4.3. Ultrastructural analysis of the cartilage growth plate

Transmission electron microscopy (TEM) was used to study the ultrastructure of tibial growth plates in seven day old mice. This allowed an in depth assessment of growth plate structure, chondrocyte morphology and composition of the extracellular matrix. Overlapping images were taken at low magnification and used to generate a reconstruction of the entire growth plate (using the Photoshop "photomerge" function).

4.3.1. The SEMD mouse model

The growth plate of the mouse homozygous for the SEMD mutation appeared relatively well organised with all zones present; however, the proportion of the zones within the growth plates appeared altered with an increase in the resting zone and a decrease in the proliferative zone (Figure 49, n=1). Proliferating chondrocytes were arranged in chondrons, but they were more rounded in shape than those in the wild type growth plate and were not always parallel to the direction of growth (Figure 49). At higher magnification chondrocytes exhibited a severely distended endoplasmic reticulum indicative of intracellular protein reten-tion (Figure 50A-B). There was no overt difference in the appearance of the pericellular matrix; however, the inter-territorial matrix had a granular appearance (Figure 50B-C). Pre-hyper-trophic chondrocytes exhibited abnormal morphology with an enlarged endoplasmic reticu-lum (Figure 51A). Cells also displayed single-membraned vesicular bodies containing electron-dense granular material with electron-lucent areas (Figure 51B-C). Chondrocytes in the hy-pertrophic zone contained remnants of a distended ER (Figure 52A-B) but the extracellular matrix appeared normal (Figure 52C).

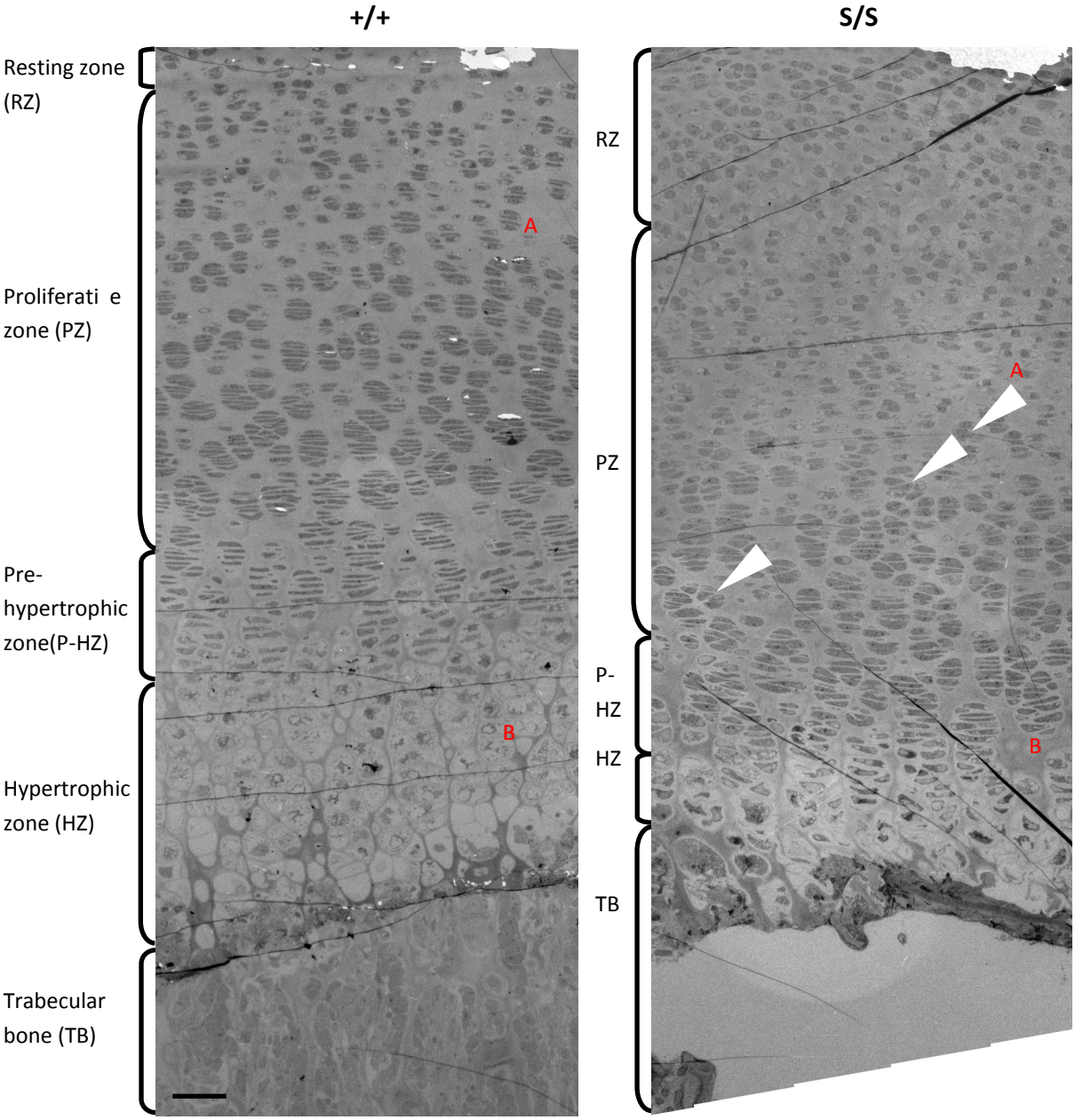

Figure 49 Reconstruction of the SEMD tibial growth plate

Transmission electron microscopy of secti ns from a seven day old homozygous SEMD mouse and a wild type li ermate. The SEMD growth plate exhibited all zones but was dis-propor onate, with an enlarged res ng zone and reduced prolifera ve zone compared to that of the wild type sample. The chondrocytes were arranged in chondrons which were not always parallel to the directi n of growth (arrowheads).

Key: +/+ (wild type) S/S (homozygous for the muta on) n=1, scale bar = 50 µm.

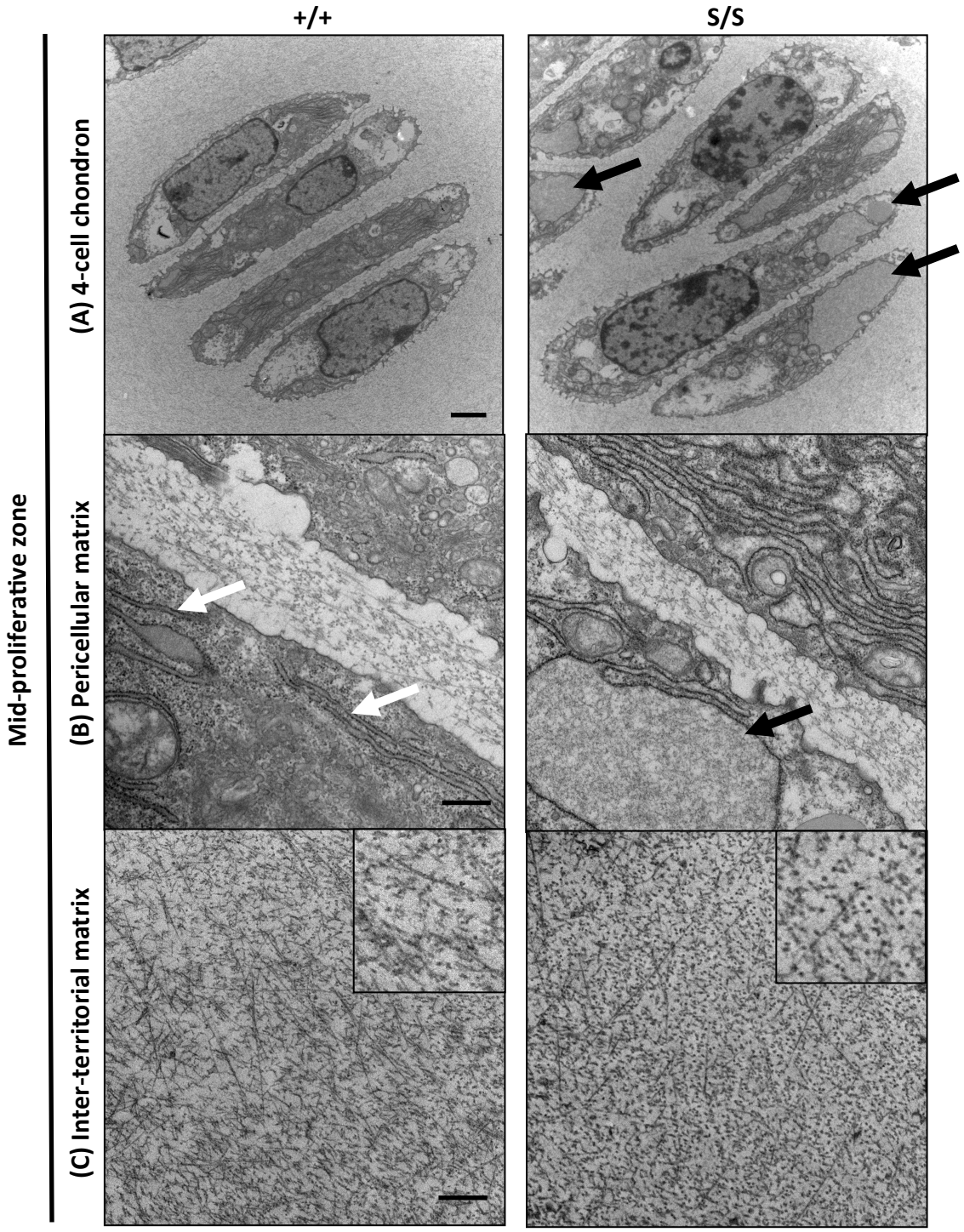

Figure 50 Ultrastructure of the proliferative zone in the SEMD tibial growth plate.

TEM of sectio s from a seven day old SEMD mouse and a wild type control. **(A-B)** Wild type chondrocytes contained an endoplasmic re culum (ER) with a fi e ribboned structure (white arrows) whereas mutant chondrocytes exhibited an enlarged ER (black arrows). There was no di erence in the composi on of the **(B)** pericellular or **(C)** inter-territorial extracellular matrix.

Key: +/+ (wild type) S/S (homozygous for the muta on) (A) scale bar = 2µm, (B,C) scale bars = 500nm, n=1.

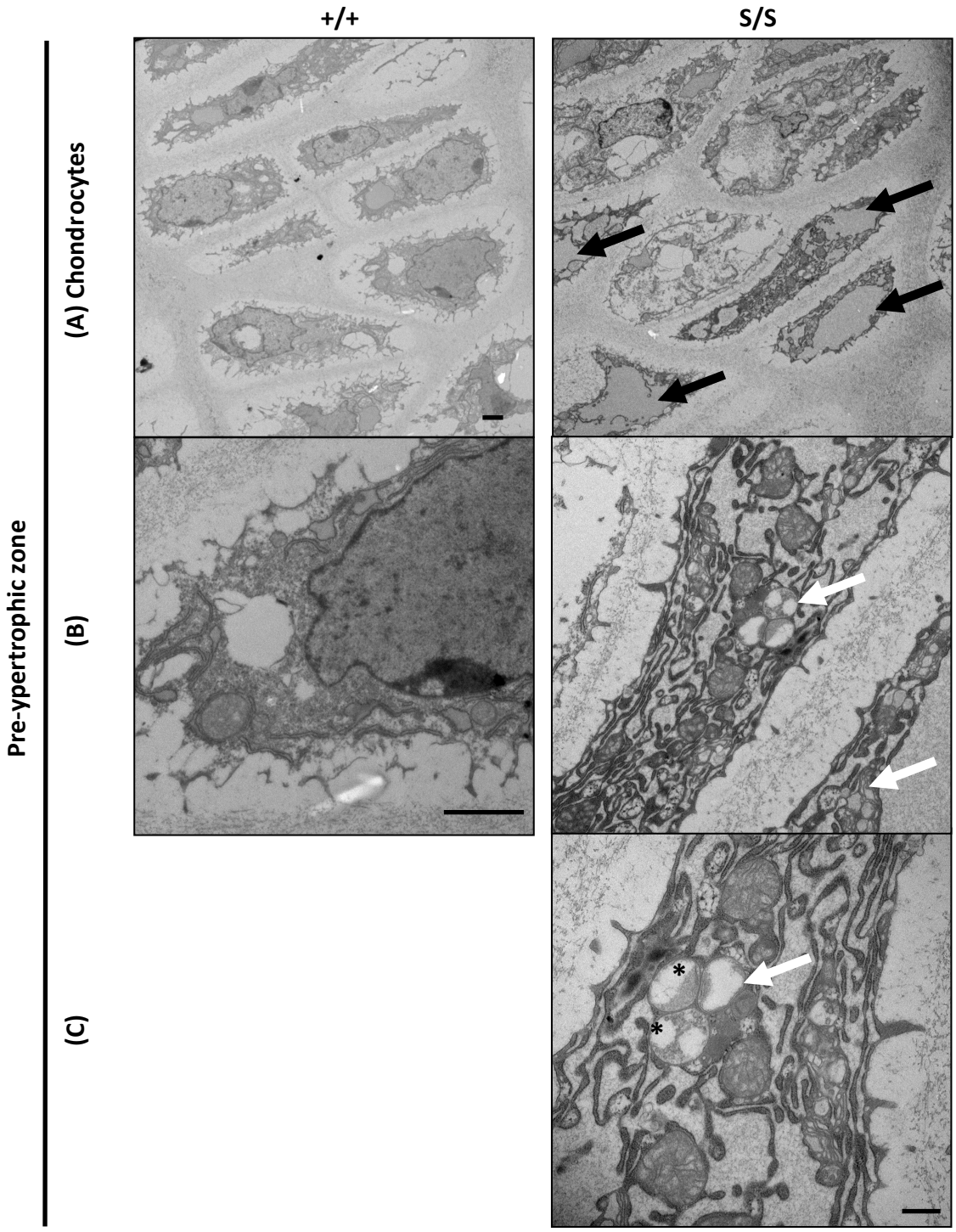

Figure 51 Ultrastructure of the pre-hypertrophic zone in the SEMD growth plate.

TEM of secti ns from a seven day old SEMD mouse and a wild type control. Pre-hypertrophic SEMD chondrocytes exhibited abnormal morphology including **(A)** an enlarged endoplasmic re culum (black arrows) and **(B-C)** electron-dense intracellular vesicles (white arrows) with electro-lucent areas (*).

Key: +/+ (wild type) S/S (homozygous for the muta on) (A,B) scale bars = 2µm (C) scale bar = 500nm, n=1.

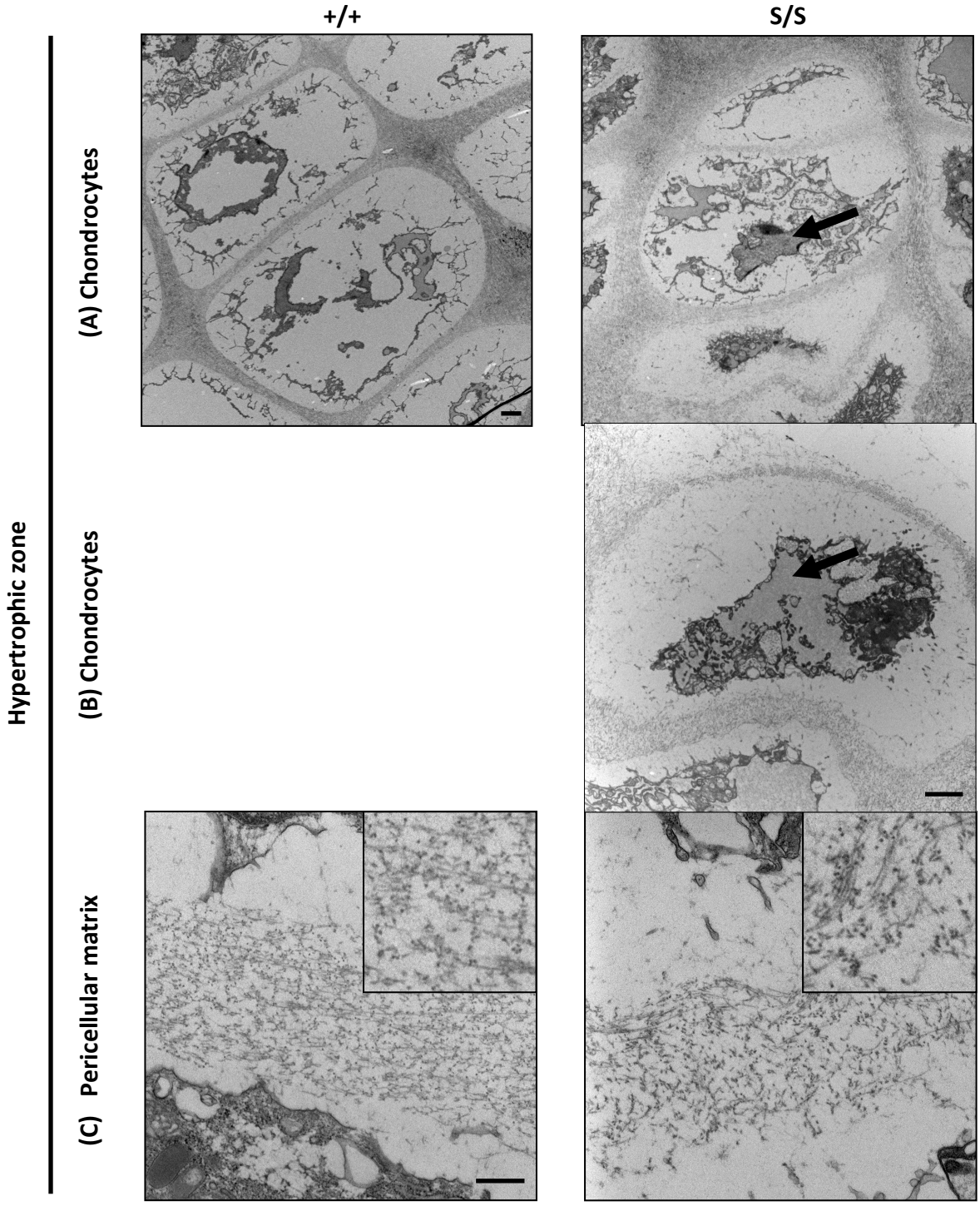

Figure 52 Ultrastructure of the hypertrophic zone in the SEMD growth plate.

TEM of sec ons from a seven day old SEMD mouse and a wild type control. **(A-B)** Hypertrophic SEMD chondrocytes exhibited abnormal morphology with remnants of an enlarged endoplasmic re culum (black arrows). **(C)** There was no overt di erence in the appearance of the extracellular matrix.

Key: +/+ (wild type) S/S (homozygous for the muta on) (A-B) scale bar = 2µm (C) scale bar = 500nm, n=1.

4.3.2. The OCD mouse model

The growth plate obtained from the mouse homozygous for the OCD mutation was well organised with all zones (resting, proliferative and hypertrophic) present (Figure 53). However, the relative proportion of the individual zones was altered with an overall reduction in the hypertrophic zone. Proliferative zone chondrocytes were arranged in chondrons parallel to the direction of growth (Figure 53). Under higher magnification proliferative chondrocytes contained an enlarged endoplasmic reticulum, suggesting intracellular retention of protein, and some cells displayed large electron-lucent vacuoles of undetermined origin (Figure 54A-B). The pericellular and inter-territorial matrix appeared normal (Figure 54D-E). Both proliferative and pre-hypertrophic chondrocytes contained a variety of vesicles 200-500 nm in diameter, which were not present in the wild type cells (Figures 54C and 55B-C). Vesicles containing electron-dense aggregates or microvesicles (50-150 nm in diameter) were surrounded by a double membrane and resembled autophagosomes or multivesicular bodies, which are associated with autophagic pathways (Li, Li et al. 2012). Vesicular structures without electron-dense contents were also observed (Figure 55C). In addition to this, cells in the pre-hypertrophic and hypertrophic zones displayed irregular morphology and contained an enlarged ER (Figures 55A-B and 56A). There was no difference in the appearance of the extracellular and inter-territorial matrix in the pre-hypertrophic and hypertrophic zones (Figures 56B).

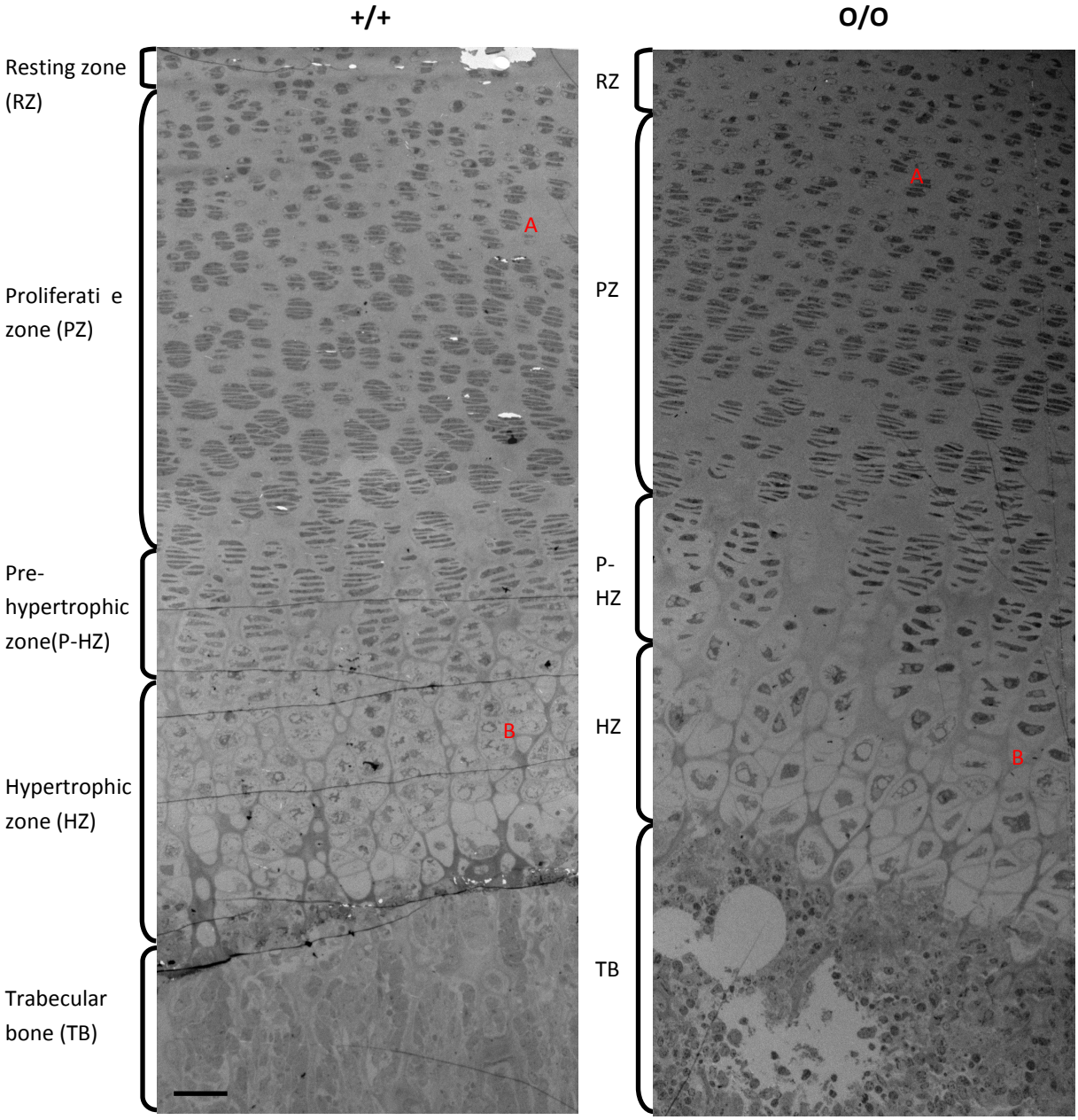

Figure 53 Reconstruction of an OCD tibial growth plate

Transmission electron microscopy of secti ns from a seven day old homozygous OCD mouse and a wild type li ermate. All zones were present in the growth plate of the mouse homozygous for the muta on, although the hypertrophic zone appeared propor onally reduced compared to that of the wild type sample.

Key: +/+ (wild type) O/O (homozygous for the muta on) n=1, scale bar = 50 µm.

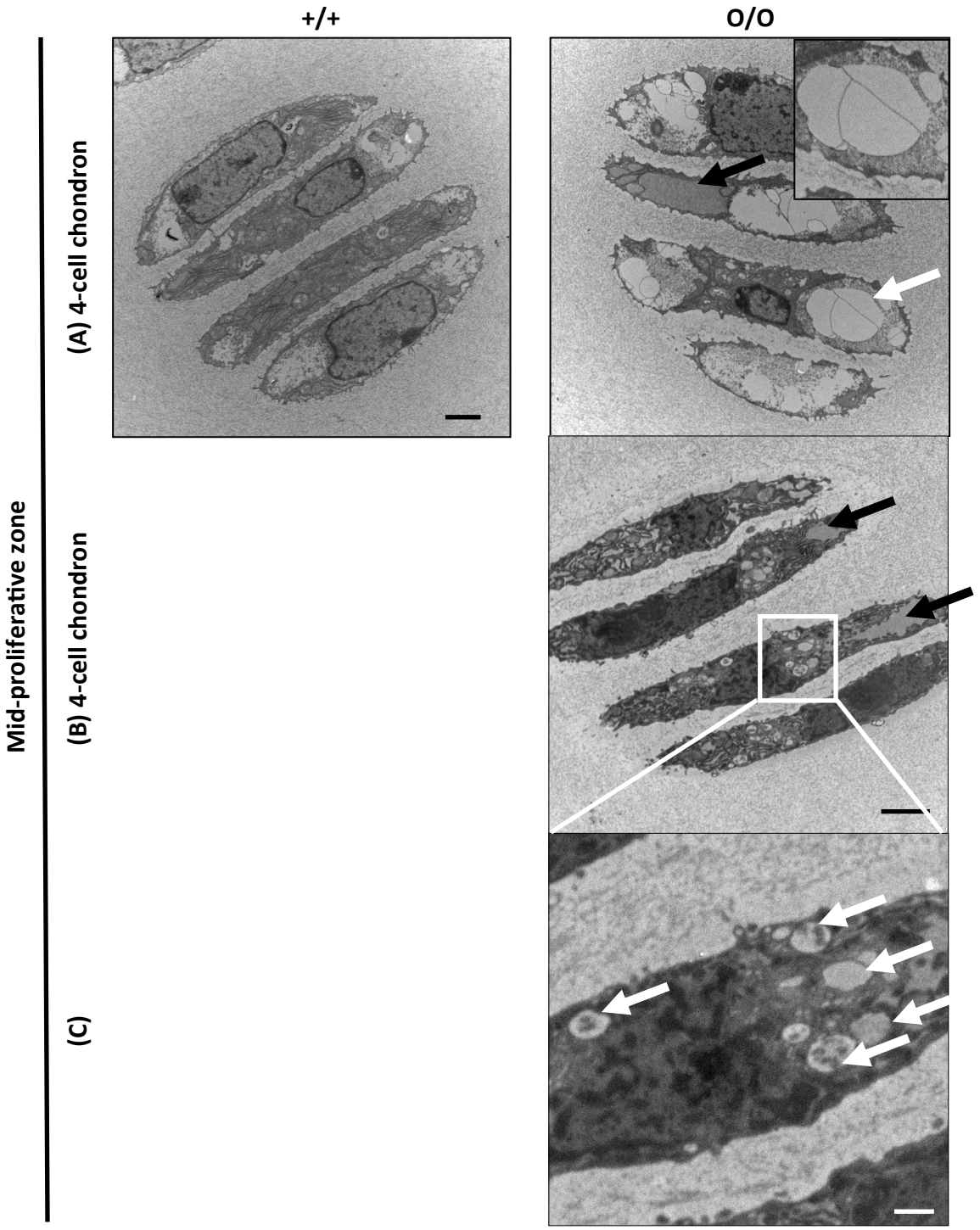

Figure 54 Ultrastructure of the proliferative zone in the OCD growth plate (A-C).

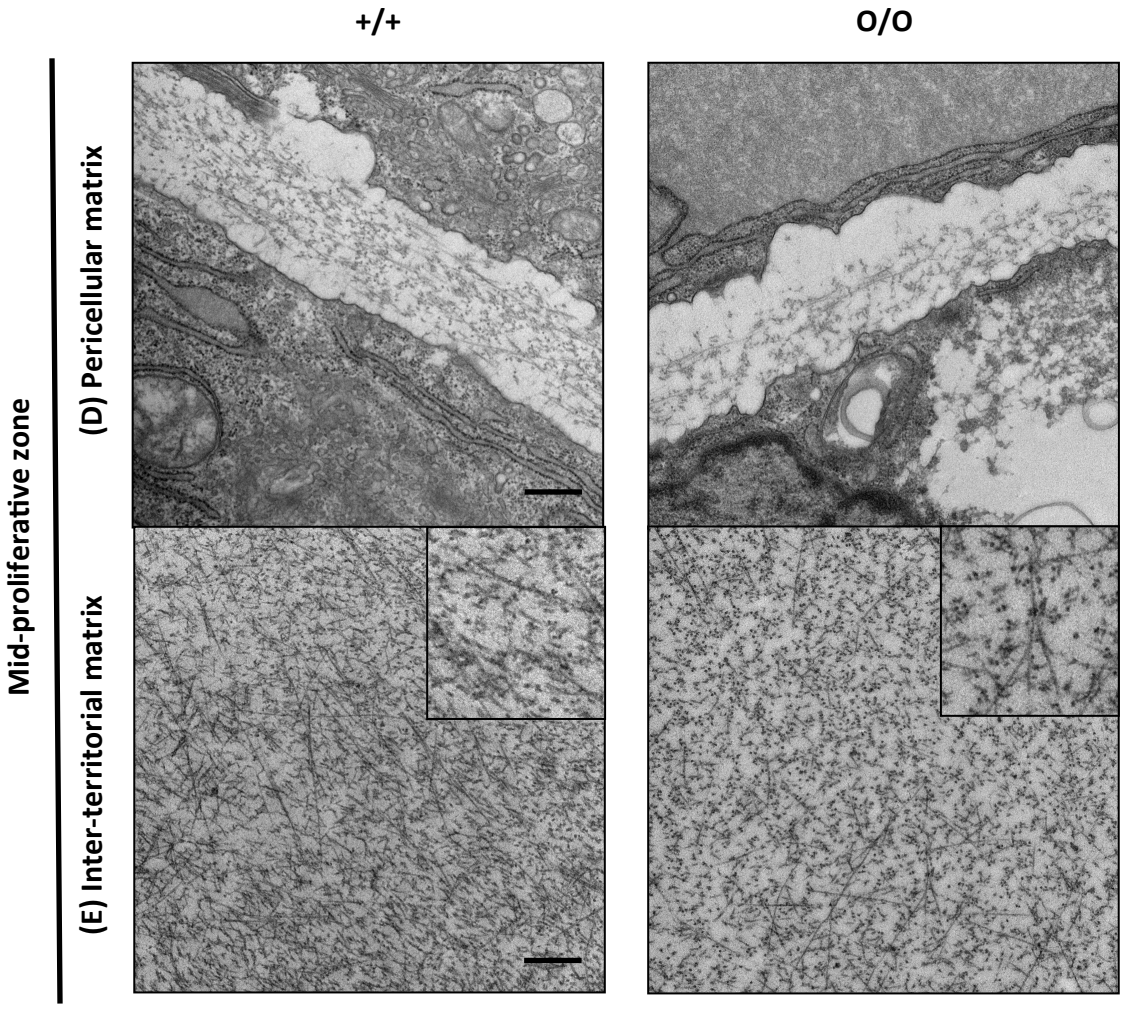

Figure 54 Ultrastructure of the proliferative zone in the OCD growth plate (D-E).

TEM of sectio s from a seven day old OCD mouse and a wild type control. **(A-B)** Mutant chondrocytes have an enlarged endoplasmic re culum (black arrows) and exhibit large electron-lucent vacuoles (white arrows) and **(B-C)** vesicles containing electron-dense material (white arrows). There was no overt di erence in the appearance of the **(D)** pericellular or **(E)** interterritorial extracellular matrix.

Key: +/+ (wild type) O/O (homozygous for the muta on) (A-B) scale bar = 2µm, (C-E) scale bars = 500nm, n=1.

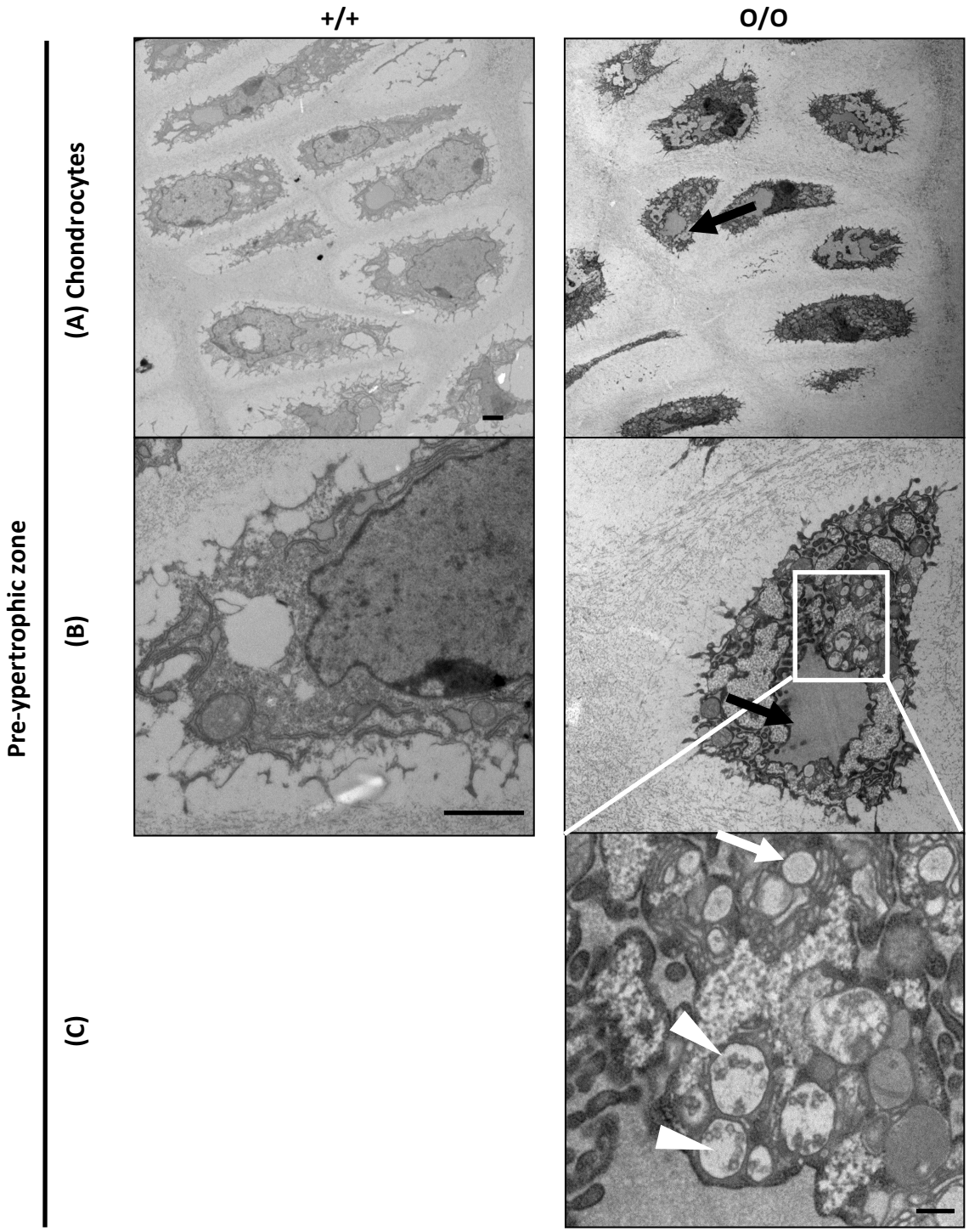

Figure 55 Ultrastructure of the pre-hypertrophic zone in the OCD growth plate.

TEM of secti ns from a seven day old OCD mouse and a wild type control. Pre-hypertrophic OCD chondrocytes exhibited abnormal morphology with **(A)** an enlarged re culum (black arrows) and **(B-C)** intracellular vesicles containing punctate electron-dense material (white arrows) which appeared to have a double-membrane (arrowheads). Vesicles with uniden- fi d electron-lucent contents were also observed (white arrows).

Key: +/+ (wild type) O/O (homozygous for the muta on) (A,B) scale bars = 2µm (C) scale bar = 250nm, n=1.

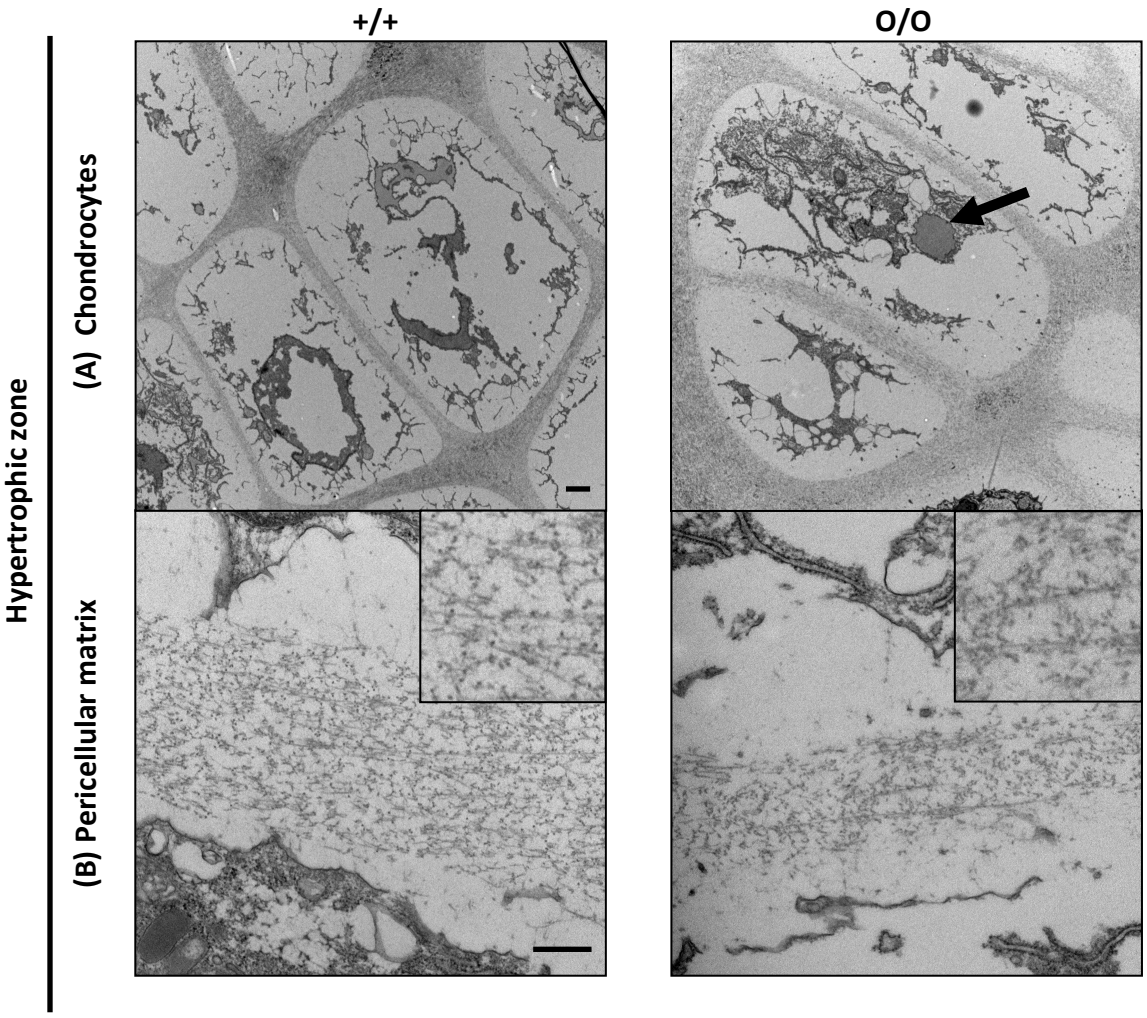

Figure 56 Ultrastructure of the hypertrophic zone in the OCD growth plate.

TEM of sections from a seven day old OCD mouse and a wild type control. Hypertrophic OCD chondrocytes exhibited **(A)** remnants of a distended ER (black arrow). **(B)** There was no overt di erence in the appearance of the extracellular matrix.

Key: +/+ (wild type) O/O (homozygous for the muta on) (A) scale bar = 2µm (B) scale bar = 500nm, n=1.

4.4. Immunohistochemical analysis of the ECM

Immunohistochemistry was used to analyse the localisation and relative abundance of the major extracellular matrix proteins in the tibial growth plate cartilage of male mice at 3 weeks of age. The relative intensity of staining for collagen types II (Figure 57A) IX (Figure 57B) and X (Figure 57C) was decreased overall in growth plates from mice homozygous for the SEMD mutation (n=3). Moreover, the localisation of collagen was altered compared to the wild type controls with staining for collagen type II in the secondary ossification centre (Figure 57A). Reduced staining for collagen type IX was found throughout the growth plate and secondary ossification centre of mutant mice (Figure 57B). Staining for the hypertrophy marker collagen type X was localised to not only the hypertrophic zone but to the secondary ossification centre, suggesting the presence of hypertrophic chondrocytes (n=3, Figure 57C). In contrast, the localisation of these same collagens was only slightly altered in the growth plate cartilage of mice homozygous for the OCD mutation, but with a reduction in staining intensity for collagen types IX (Figure 57B) and X (Figure 57C). There was no statistical difference in the proportion of the growth plate stained for collagen type X in tissue from either the OCD or SEMD mouse (n =3, Figure 57D). The intensity of staining for the adaptor proteins COMP (Figure 56A) and matrilin 3 (Figure 58B) was decreased and localised throughout the growth plate and secondary ossification centre in mice homozygous for the SEMD mutation and was slightly reduced in growth plates from mice homozygous for the OCD mutation (n=3, Figure 58). The abundance of aggrecan in the extracellular matrix was reduced in growth plates from both OCD and SEMD mice with an increase in intracellular staining (Figure 59).

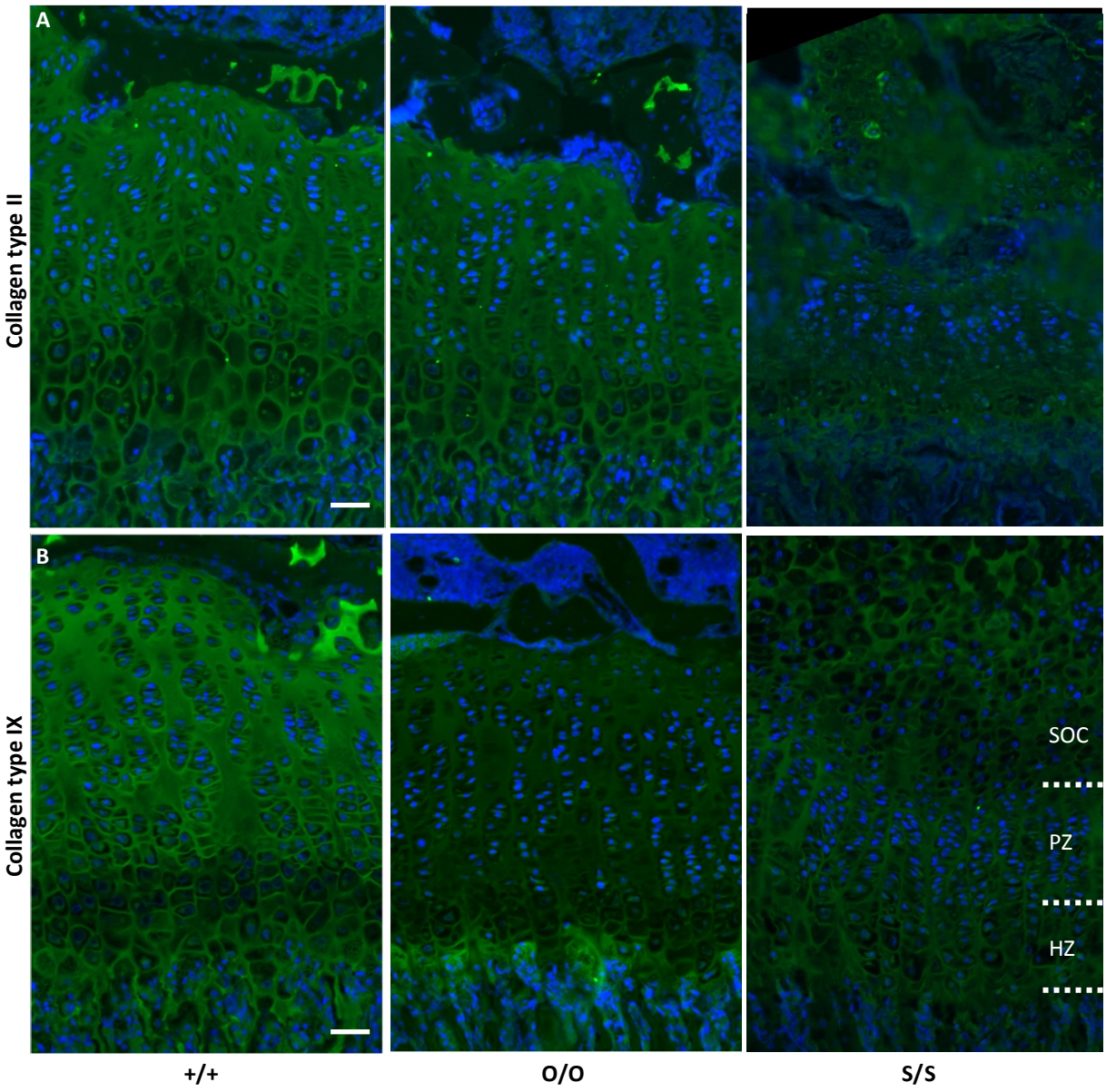

Figure 57 Localisation and abundance of collagen in OCD and SEMD mice (A-B).

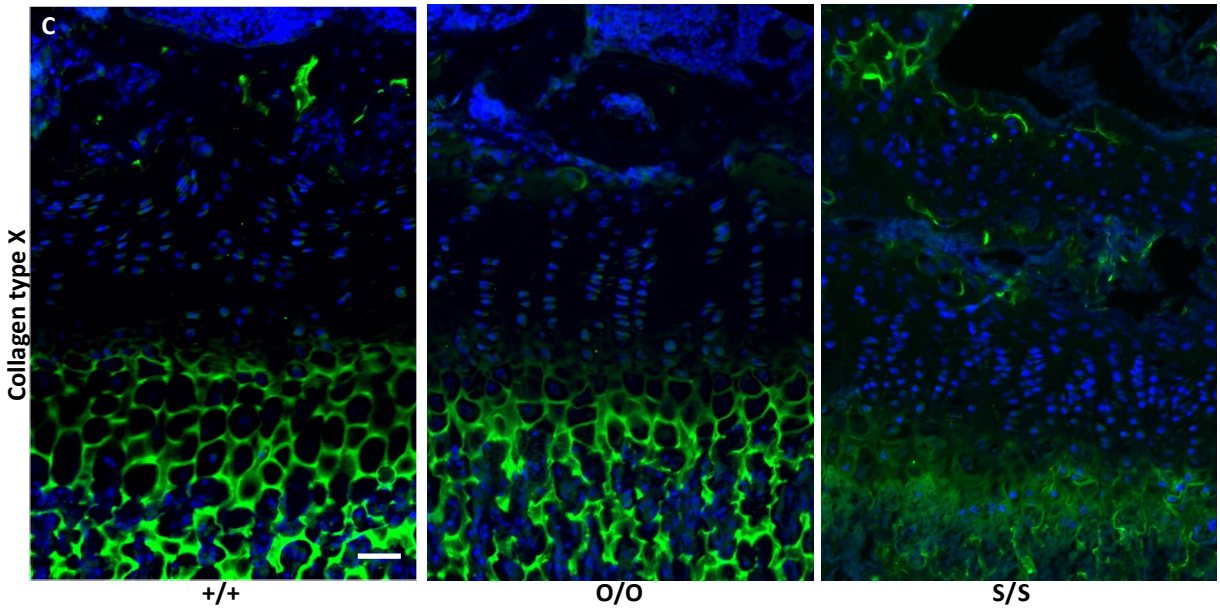

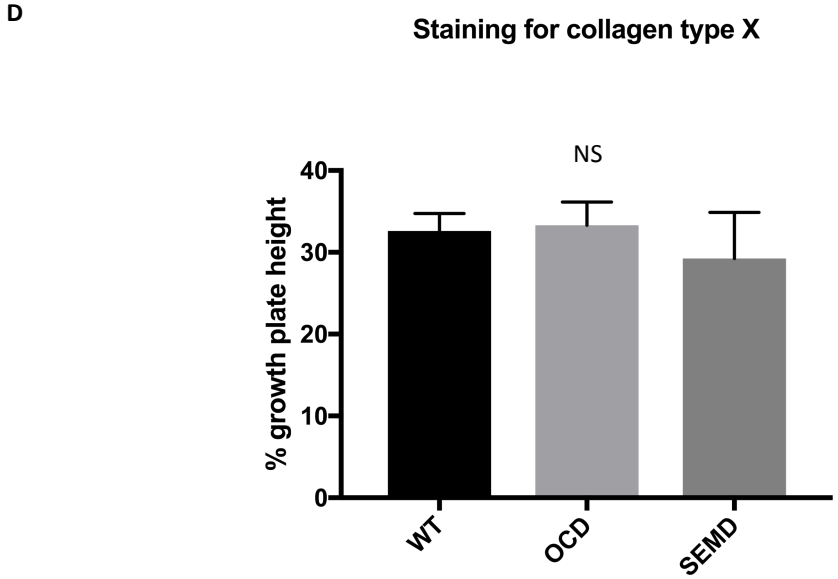

Figure 57 Localisation and abundance of collagen in OCD and SEMD mice (C-D).

Immuno uorescent staining of matching bial growth plate sec ons from male 3 week old wild type, OCD and SEMD mice. The intensity of staining for collagens type IX **(B)** and X **(C)** was reduced in the prolifera ve zone of growth plates from OCD mice. The growth plates of SEMD mice exhibited decreased staining intensity for collagens type II **(A)** IX **(B)** and X **(C)**. Staining for collagens type IX **(B)** was not restricted to the prolifera ve zone and staining for collagen type X **(C)** was localised to both the secondary centre and hypertrophic zone. **(D)** There was no sta stica di erence in the propor on of the growth plate stained for collagen type X.

Key: +/+ (wild type) O/O (homozygous for the OCD muta on) S/S (homozygous for the SEMD muta on) scale bar = 50µm, n=3, NS (not significa t).

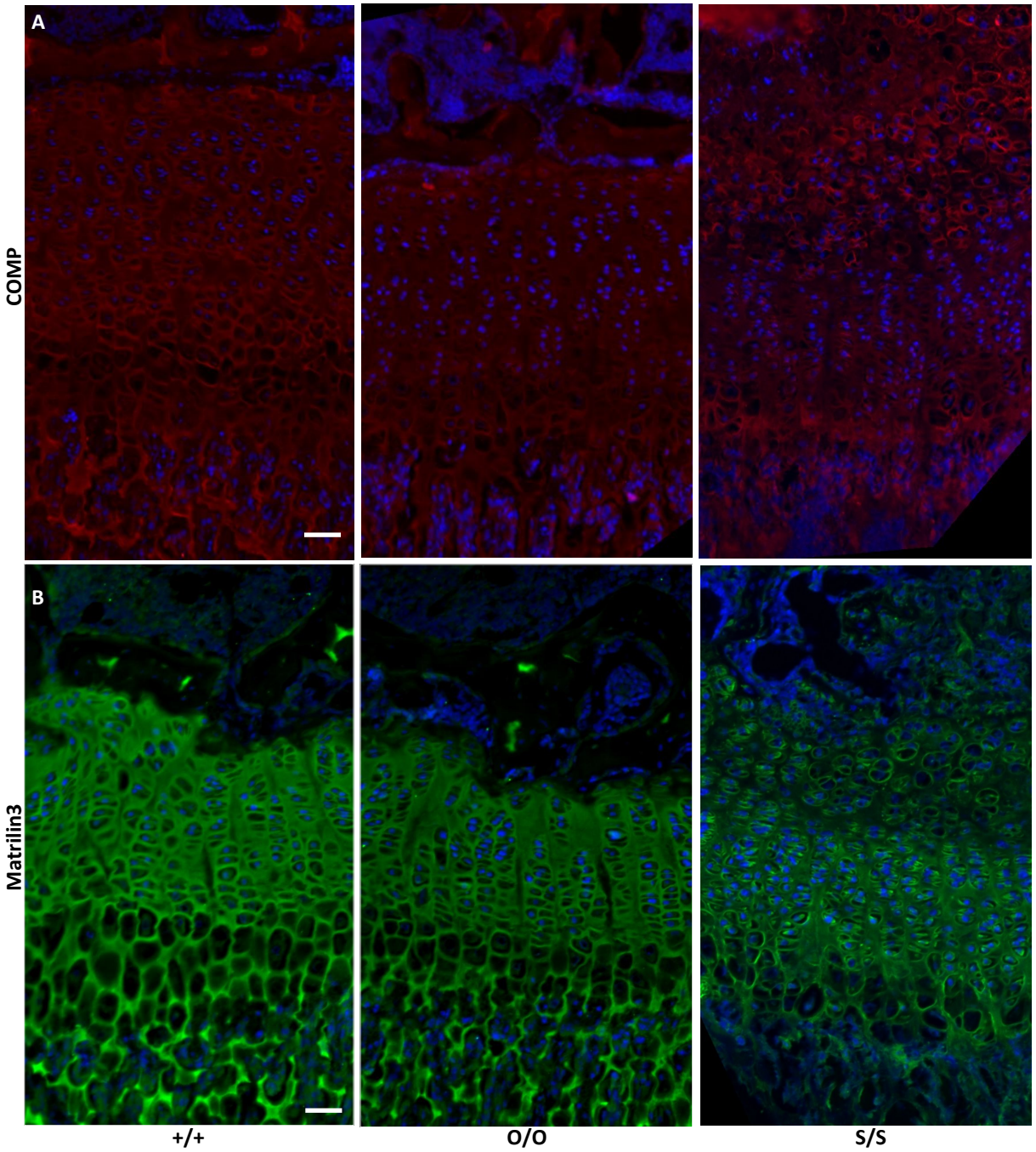

Figure 58 Localisation and abundance of ECM molecules in OCD and SEMD mice.

Immuno uorescent staining of matching bial growth plate secti ns from male 3 week old wild type, OCD and SEMD mice. The intensity of staining for **(A)** COMP and **(B)** matrilin 3 in growth plates from OCD mice was slightly reduced. Staining intensity for **(A)** COMP and **(B)** matrilin 3 was both decreased and also localised to the secondary ossifica n centre in the growth plates of SEMD mice.

Key: +/+ (wild type) O/O (homozygous for the OCD muta on) S/S (homozygous for the SEMD muta on) scale bar = 50µm, n=3.

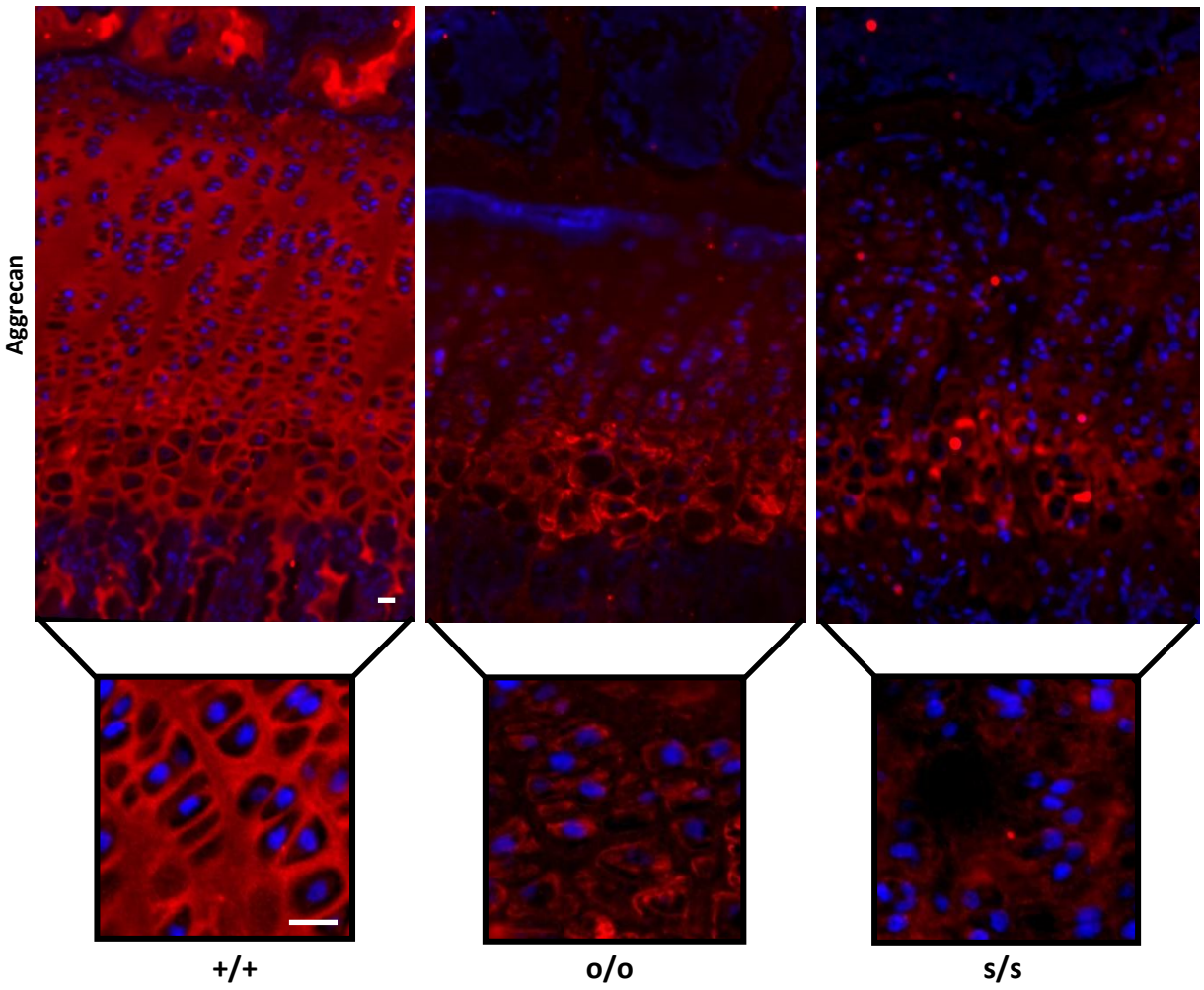

Figure 59 Mutant aggrecan is retained intracellularly in OCD and SEMD mice.

Immuno uorescent staining for aggrecan in matching ti ial growth plate secti ns from male 3 week old wild type, OCD and SEMD mice. The intensity of extracellular staining in the growth plates of OCD and SEMD was visibly reduced, whereas the intracellular staining was increased, sugges ng that mutant aggrecan is retained within the cell (scale bar = 20µm, n=3).

Key: +/+ (wild type) O/O (homozygous for OCD muta on) S/S (homozygous for SEMD muta-on)

4.5. Histological analysis of the articular cartilage of OCD mice

Haematoxylin and Eosin staining was used to assess the morphology of the tibial and femoral articular surface in male mice homozygous for the OCD mutation and their wild type littermates at 3 weeks (n=3), 9 weeks (n = 3), 6 months (n = 2) and 9 months (n = 1) of age. The articular cartilage in wild type controls at all ages studied formed a distinct layer over the subchondral bone and had a smooth surface with no obvious lesions present. The morphology of the articular surface was unaffected in mice homozygous for the mutation up to 6 months of age in both the lateral and medial compartments of the knee joint (Figure 60A-C). Safranin O staining was used to assess proteoglycan abundance in the articular cartilage. The extracellular staining intensity was markedly reduced in the superficial and transitional zones of 9 week (data not shown) and 6-9 month old OCD mice in both the lateral and medial compartments of the knee joint (Figure 60D-E).

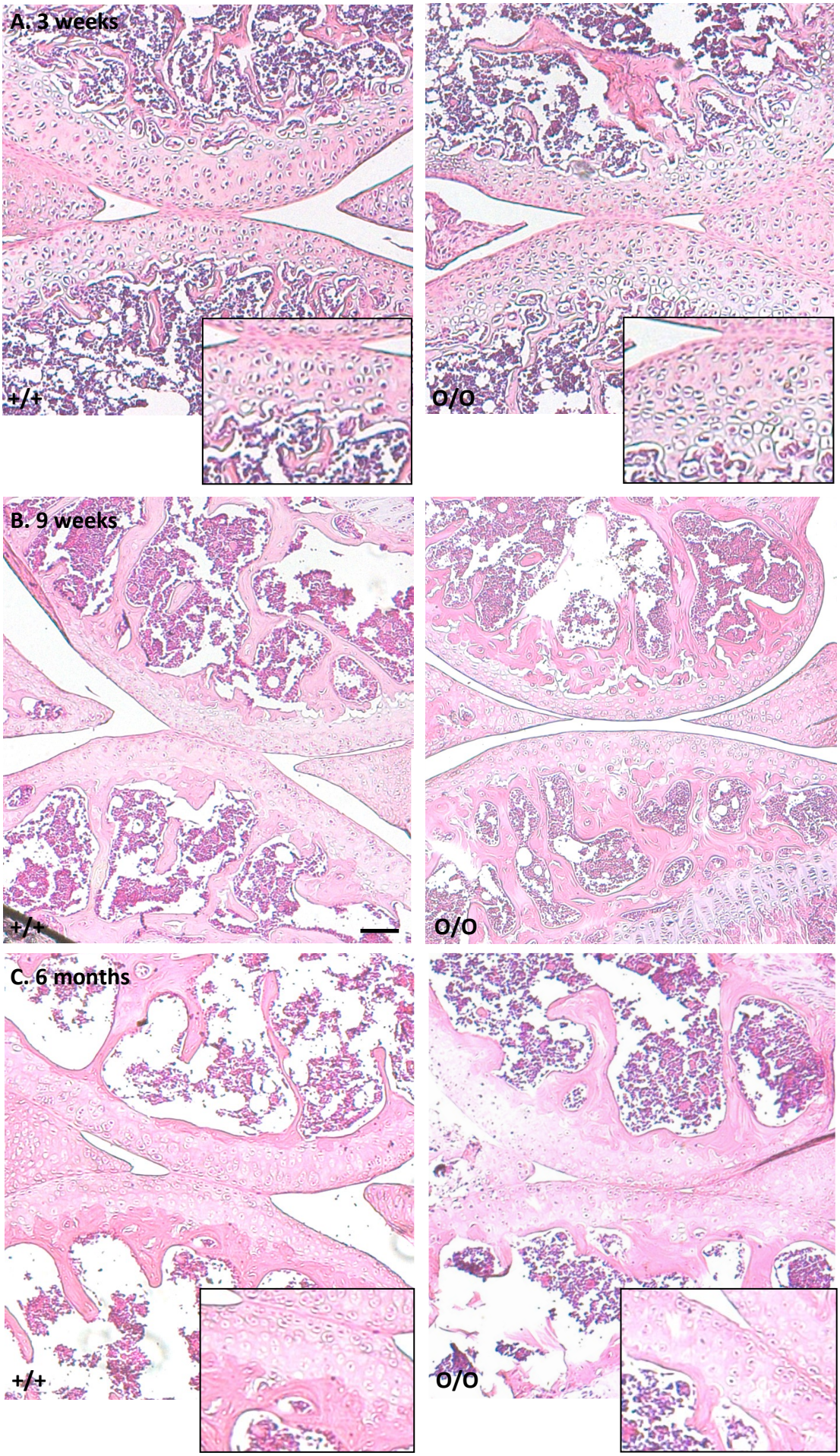

Figure 60 The structure of knee articular cartilage in OCD mice (A-C)

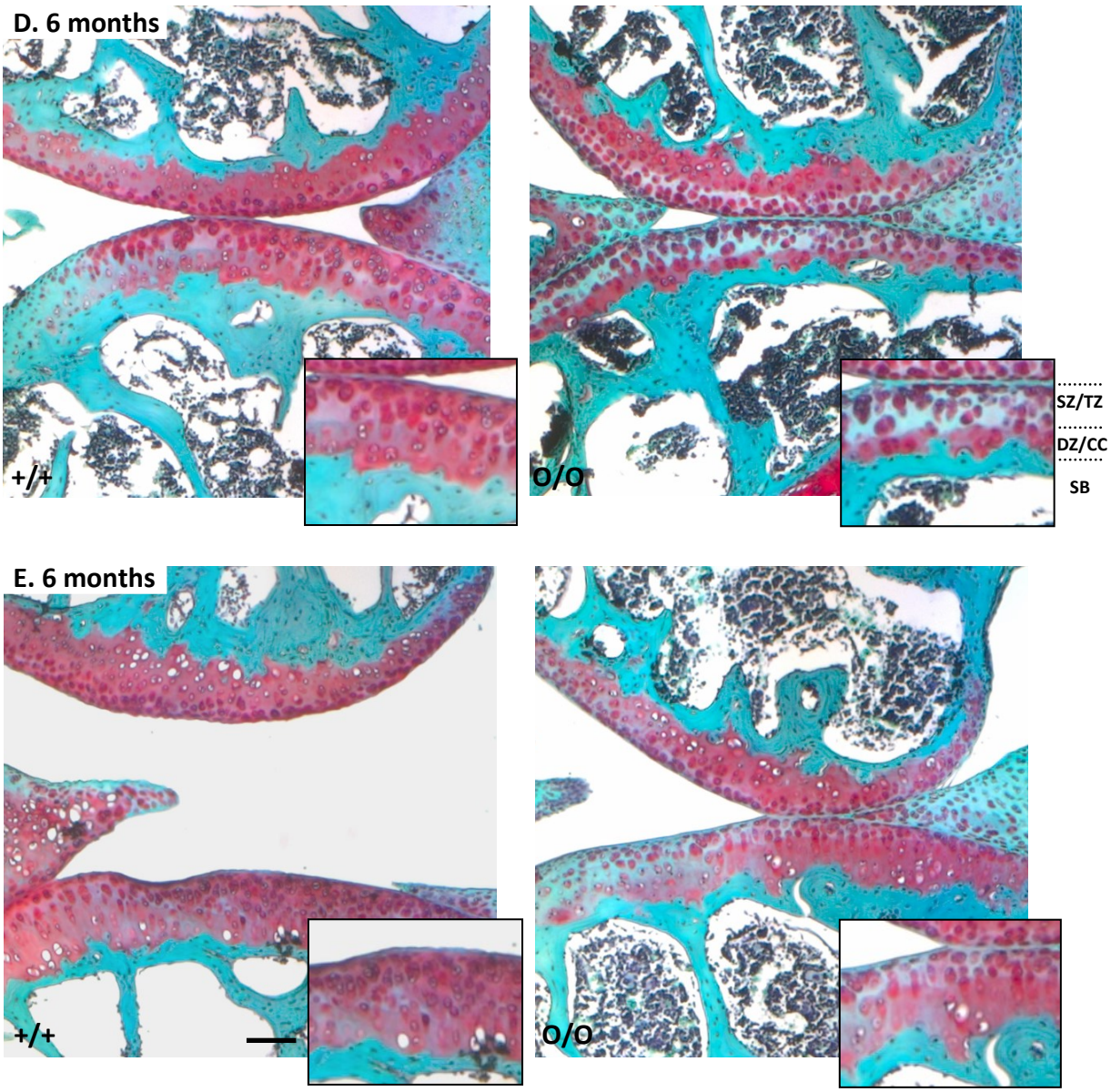

Figure 60 The structure of knee articular cartilage in OCD mice (D-E)

Histological staining of matched secti ns from male mice at 3 weeks, 9 weeks and 6 months of age. Haematoxylin and eosin staining showed no di erence in the integrity of the ar cular car lage surface or underlying sub-chondral bone at **(A)** 3 weeks **(B)** 9 weeks or **(C)** 6 months of age. Safranin O staining was reduced in the superficial and transi onal zones in both the **(D)** lateral and **(E)** medial joint compartments of mice by 6 months of age.

Key: +/+ (wild type) O/O (homozygous for OCD muta on) SZ (superficial zone) TZ (transiti nal zone) DZ (deep zone) CC (calcifie car lage) SB (subchondral bone) scale bar = 20µm, n=3

4.6. Summary

The aim of this chapter was to investigate and compare the tissue pathology of two knock-in mouse models with missense mutations in the C-type lectin domain of aggrecan which result in two distinct conditions, the mild familial OCD and the more severe SEMD aggrecan type. Transmission electron microscopy and a range of histochemical techniques were used to analyse cell morphology and growth plate structure during the growth and maturation of mice either homozygous or heterozygous for the aggrecan mutations compared to wild type controls. Histological analysis of mice homozygous for the SEMD mutation showed that growth plate height appeared reduced at birth. At three weeks of age, the mineralised area of the secondary ossification centre was significantly reduced in size, indicating a delay in the formation of the secondary ossification centre. In addition to this, the SEMD growth plate was reduced in height and disorganised, with rounded chondrocytes arranged into abnormal chondrons which were not always parallel to the direction of bone growth. The individual growth plate zones were disproportionate, with a significant increase in the height of the hypertrophic zone. Interestingly, however, the area of staining for the hypertrophic marker collagen type X was not statistically different in mice homozygous for the SEMD mutation compared with wild type controls, suggesting premature hypertrophy or impaired maturation. In contrast to the SEMD mouse, at birth there were no overt differences in tissue morphology between mice homozygous for the OCD mutation and their wild type littermates. However, by three weeks of age the growth plate was disorganised and significantly reduced in size, although the secondary ossification centre was well-formed and within normal limits. Histological and ultrastructural analysis of the growth plate showed that the murine OCD and SEMD *Acan* mutations delay secretion of the mutant aggrecan protein, causing protein retention within the endoplasmic reticulum and reduced abundance of aggrecan in the ECM. It is important to note that the secretion of mutant aggrecan was not completely impaired in these models, as weak extracellular staining for aggrecan was observed in the OCD and SEMD growth plates of 3 week old mice. Furthermore, aggrecan-null models such as the *Cmd* mouse are known to be embryonic lethal (Rittenhouse, Dunn et al. 1978) and the OCD and SEMD mutations do not impair pup survival (see Chapter 1) confirming that the mutant aggrecan must be secreted into the ECM. Interestingly, ultrastructural analysis indicated a variety of intracellular vesicles in both

OCD and SEMD chondrocytes from growth plate cartilage. Vesicular bodies in the pre-hypertrophic zone of the SEMD growth plate had electron-lucent regions and contained electron-dense granular material, therefore displaying many of the features associated with autolysosomes (Ishikawa, Furuno et al. 1983). In contrast, vesicles in the proliferative and pre-hypertrophic zones of the OCD growth plate were electron-lucent, exhibited a double-membrane and contained electron-dense microvesicles or aggregates. These structures resemble autophagosomes or multivesicular bodies. Autolysosomes, autophagosomes and multivesicular bodies are structures associated with the macro- and micro-autophagy pathways and suggest that autophagy may play a role in the disease mechanisms in the OCD and SEMD mouse models. Ultrastructural analysis did not show any overt differ-ences in the appearance of the pericellular or inter-territorial extracellular matrix in growth plates from seven week old OCD or SEMD mice compared to a wild type control (n=1). In contrast to this, immunohistochemical analysis of 3 week old mice homozygous for the SEMD mutation indicated irregular collagen fibril thickness, mislocalisation and an overall reduction in the abundance of key ECM proteins such as COMP, matrilin 3 and type II collagen (n=3). Collagen fibril thickness in the articular cartilage was also increased and fibril orientation was disrupted in the transitional and deep zones. ECM matrix composition was also altered in the cartilage of OCD mice, with reduced abundance of collagen IX in the growth plate and in-creased collagen fibril thickness in the articular cartilage. Histological analysis of articular car-tilage from mice homozygous for the OCD mutation prior to growth cessation did not show necrosis (a classic hallmark of osteochondritis *latens*) or focal areas of disrupted endochondral ossification (osteochondritis *manifesta*). In addition to this, there was no formation of fissures in the cartilage and subchondral bone (osteochondritis *dissecans*) lesions in OCD animals up to six months of age either in the lateral or medial part of the joint. However, proteoglycan abundance in the superficial and transitional zones of articular cartilage from mice homozy-gous for the OCD mutation appeared reduced at nine weeks of age (upon growth cessation). Staining intensity for proteoglycan in these zones was further reduced by 6 months of age, indicating that proteoglycan loss progressed with age.The growth plates of mice heterozygous for the OCD mutation were not visually different from the wild type mice. Similarly, the growth plates of mice heterozygous for the SEMD mutation were only slightly disorganized. This sug-gested that the presence of one copy of the wild type aggrecan allele was enough to reduce the tissue pathology of both SEMD and OCD. This observation is consistent with published

patient clinical data (on the single family reported) in which SEMD aggrecan type is found to be a recessive disease (Tompson, Merriman et al. 2009).

In conclusion, both the OCD and SEMD mouse models exhibited a disorganised growth plate with impaired trafficking of mutant aggrecan from the endoplasmic reticulum, altered matrix composition and a variety of intracellular vesicles. Histological analysis of the articular cartilage showed that this model of familial OCD does not exhibit the lesion formation observed in classical osteochondrosis. However, mice homozygous for the OCD mutation did exhibit signs of cartilage degradation, displaying progressive proteoglycan loss from the articular cartilage with age. OCD mice exhibited a clear tissue pathology at three weeks of age, but the onset of pathology occurred at an earlier age in SEMD mice with growth plates visibly reduced in height at birth. The growth plate tissue pathology displayed by SEMD mice at 3 weeks of age was also more severe, with irregular collagen fibril thickness, delayed formation of the secondary ossification centre, decreased proliferation zone and an increased hypertrophic zone. In order to further eludicate the downstream effects of these aggrecan mutations, a quantitative analysis of tissue pathology was performed and these data are presented in the following chapter.

Chapter 5. Quantitative Tissue Pathology Analysis of the SEMD and OCD Mouse Models

The qualitative analysis performed in Chapter 4 indicated that growth plates from SEMD and OCD mice are smaller than those of wild type controls and exhibit altered cellular organisation. In addition to this the relative proportion of each zone in growth plates from the SEMD mice was also altered. Further in-depth histological analysis was performed to quantitatively assess a number of parameters including chondrocyte number, chondrocyte proliferation rate and programmed cell death. In order to assess whether the extended hypertrophic zone observed in the SEMD mouse growth plate was due to a defect in cartilage mineralisation or matrix resorption, bone calcification and osteoclast number were determined. Histological analysis in Chapter 4 had demonstrated alterations in matrix composition and so RNA-seq and immunoblotting were used to assess the expression and secretion of key extracellular matrix proteins. Phenotypic analysis performed in Chapter 3 found that SEMD mice exhibited variable scoliosis, whilst intervertebral disc degeneration is often associated with short stature conditions caused by aggrecan mutations (Tatsi, Gkourogianni et al. 2017). Histo-morphometry techniques were therefore used to assess the morphology of the vertebrae and intervertebral discs. Wild type C57/BL6 mice and homozygous mutant mice were included in this quantitative analysis of tissue pathology. Mice were assessed at 5 days, 7 days, 3 weeks and 9 weeks of age to further investigate the tissue pathology of these conditions.

5.1 Chondrocyte number in the OCD and SEMD growth plates

In order to determine whether the altered relative proportion of the individual zones in the growth plates of SEMD mice was due to a change in cell number, rather than volume, individual chondrocytes were counted in each zone. The number of DAPI-positive cells in each zone was then expressed as a percentage of the total cell number. There was a 6.8% decrease in the number of chondrocytes in the resting and proliferative zones of mice homozygous for the mutation compared to wild type controls (n=3, Figure 61). In addition to this, the number of cells in the hypertrophic zone and on the vascular invasion front was increased by 30.6% and 41.2%, respectively. This suggested that the change in the relative proportion of the zones in the SEMD growth plate was most likely to be due to a difference in the number of cells at each stage of maturation. There was no difference in the number of cells per zone in mice homozygous for the OCD mutation compared to wild type controls (n=3, Figure 61).

A

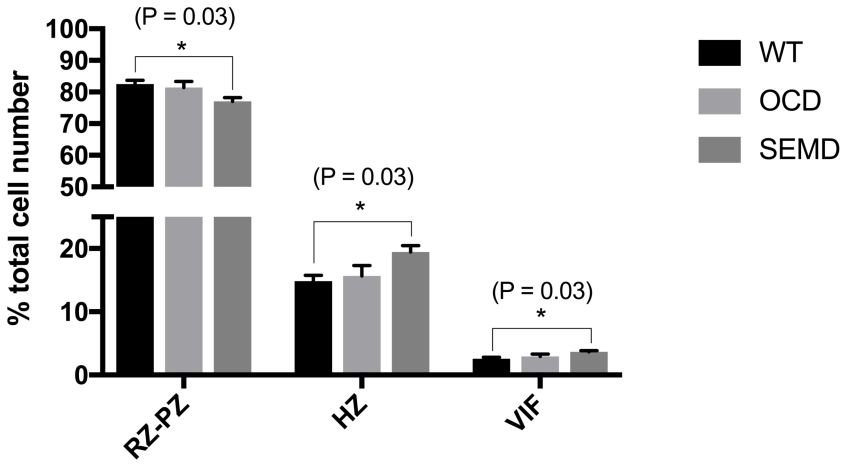

B

Genotype	+/+	O/O	S/S
% cells in the RZ-PZ/total cell number ± SEM	82.56±1.11	81.40±1.97	**76.95±1.19***
% cells in the HZ/total cell number ± SEM	14.87±0.87	15.66±1.64	**19.42±1.01***
% cells on the VIF/total cell number ± SEM	2.57±0.25	2.94±0.34	**3.63±0.18***

Figure 61 Cell number in the tibial growth plates of OCD and SEMD mice.

The number of cells per zone was analysed in the growth plates of 3 week old male OCD, SEMD and wild type mice. **(A)** Graph of the number of cells per zone expressed as a percentage of the total cell number. There was no di erence in the percentage of cells per zone in the growth plates of OCD mice. In contrast, there was a 6.8% decrease in the average cell number in the combined res ng and prolifera ve zones of SEMD mice compared with wild type controls. There was also a 30.6% and a 41.2% increase in the average cell number in the hypertrophic zone and vascular invasion front, respectiv ly. **(B)** Table showing numeric data used for the genera on of graph A.

Key: +/+ (wild type) O/O (homozygous for the OCD muta on) S/S (homozygous for the SEMD muta on) RZ (resti g zone) PZ (prolifera ve zone) HZ (hypertrophic zone) VIF (vascular invasion front) *P≤0.05, Two tailed T-test, n=3.

5.2 Proliferation rate of OCD and SEMD growth plate chondrocytes

The proliferation rate of chondrocytes in the tibial growth plate was analysed using *in vivo* BrdU labelling in mice at 3 weeks of age, followed by immunohistochemistry on nine matched sections per mouse (n=3, Figure 62A). There was a 50% decrease in the number of BrdU-positive labelled cells present in the proliferative zone of mice homozygous for the SEMD mutation when compared to wild type littermates. In contrast, there was no statistical difference in the proportion of BrdU-labelled cells in the growth plates of mice homozygous for the OCD mutation when compared to wild type littermates (Figure 62B-C).

5.3 Apoptosis in OCD and SEMD growth plates

Fluorescent TUNEL (Terminal dUTP Nick End-Labelling) labelling of fragmented DNA was used to analyse chondrocyte apoptosis in tibial growth plates from 3 week old male mice (Figure 63A). Growth plates from wild type mice contained very few apoptotic cells with only 0.2% TUNEL-positive chondrocytes in the resting and proliferative zones. The number of apoptotic cells in the hypertrophic zone and on the vascular invasion front was 2.5% and 14.3%, respectively. In the growth plates of mice homozygous for the SEMD mutation however, there was a 135.3% increase in the proportion of apoptotic cells in the hypertrophic zone compared to wild type littermates (P=0.02, Figure 63). Growth plates from mice homozygous for the OCD mutation exhibited a 77.7% at the vascular invasion front (P=0.05, Figure 63).

A

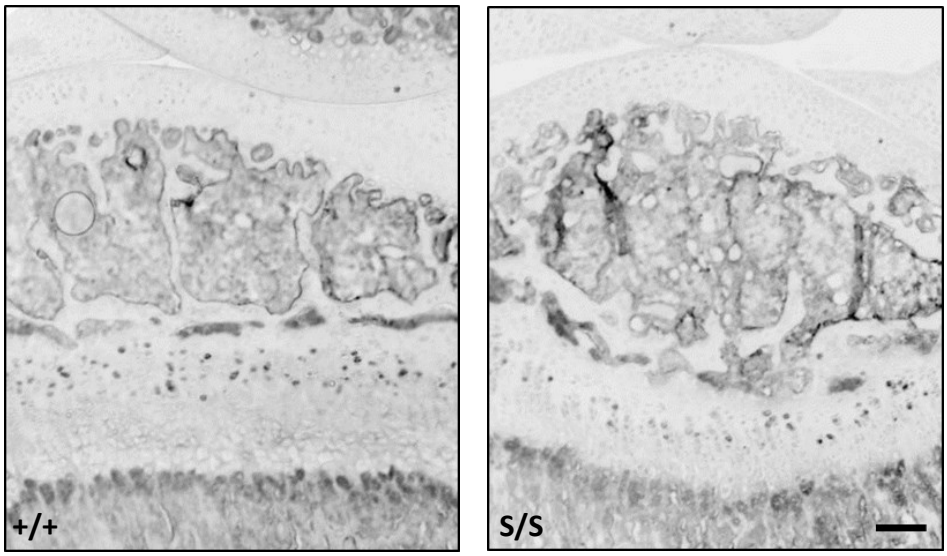

B

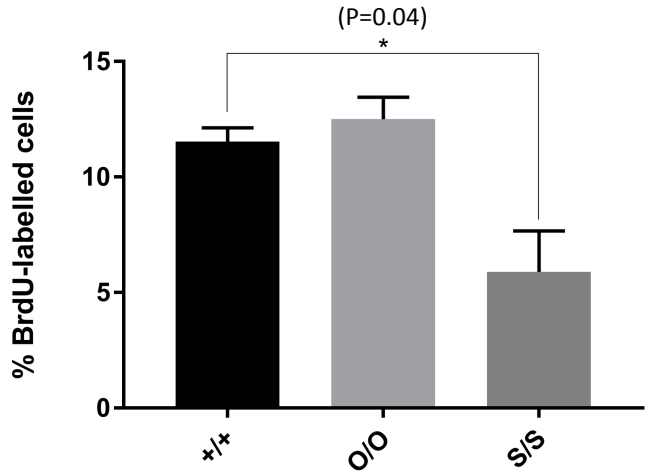

C

Genotype	+/+	O/O	S/S
% of BrdU labelled posi ve cells in the PZ ± SEM	11.53±0.60	12.51±0.95	**5.89±1.77 ***

Figure 62 Chondrocyte proliferation in tibial growth plates of OCD and SEMD mice.

The chondrocyte prolifera on rate was analysed with immunohistochemistry of BrdU-labelled growth plates in 3 week old male OCD and SEMD mice and their wild type li ermates. **(A)** Representative pseudo-coloured images of BrdU-labelled cells in the growth plate. **(B)** Graph of BrdU–labelled cells expressed as a percentage of the total number of cells in the prolifera ve zone. There was a 48.9% decrease in chondrocyte prolifera on in the growth plates of SEMD mice but no sta stical di erence in that of OCD mice when compared with wild type controls. **(C)** Table showing the numeric data used for the genera on of graph B.

Key: +/+ (wild type) O/O (homozygous for OCD mutation) S/S (homozygous for SEMD mutation) PZ (proliferative zone) SEM (standard error of the mean) scale bar = 100µm, *P≤0.05, Two tailed T-test, 3 joint regions analysed from 3 individual animals.

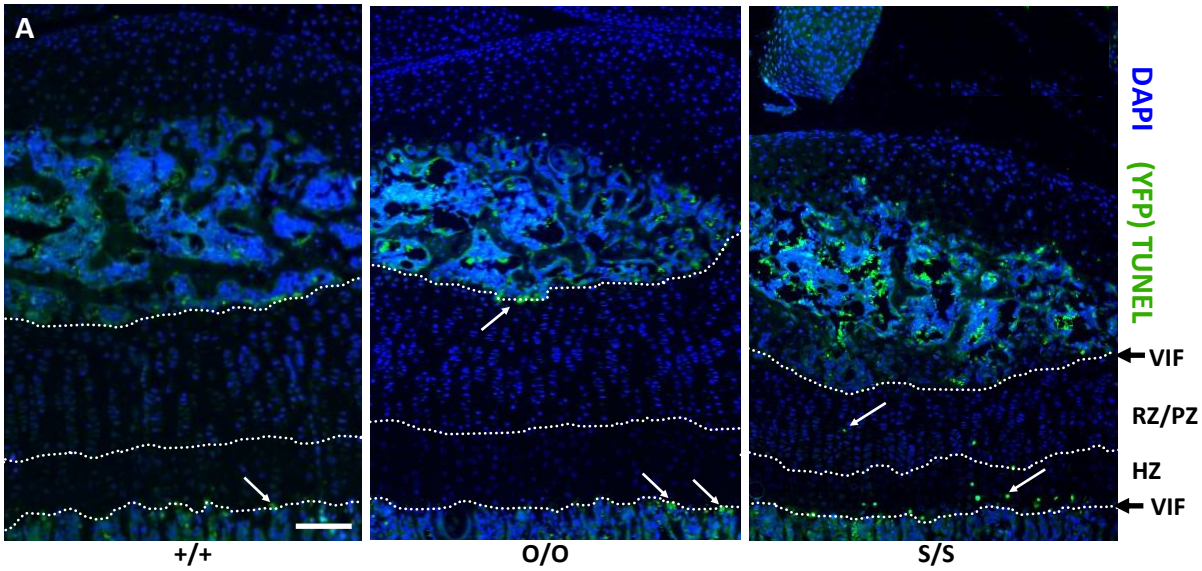

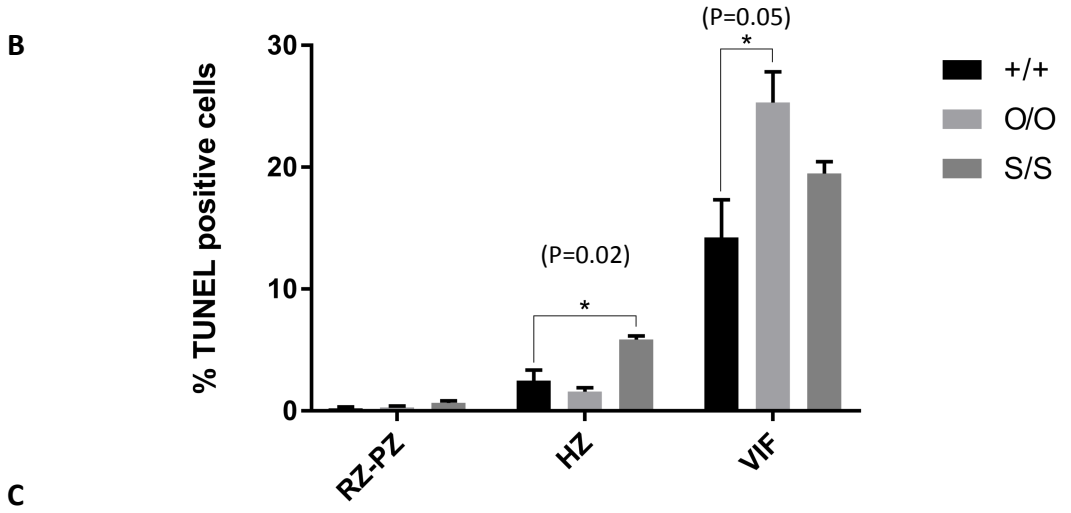

C

Genotype	+/+	O/O	S/S
% of TUNEL posi ve cells in the RZ-PZ ± SEM	0.22±0.12	0.28±0.13	0.66±0.17
% of TUNEL posi ve cells in the HZ ± SEM	2.49±0.87	1.59±0.33	**5.86±0.30 ***
% of TUNEL posi ve cells at the VIF ± SEM	14.25±3.08	**25.32±2.51 ***	19.48±0.98

Figure 63 Chondrocyte apoptosis in tibial growth plates of OCD and SEMD mice.

The number of apoptotic cells was analysed with fluorescent TUNEL of fragmented DNA in 3 week old male OCD, SEMD and wild type mice. **(A)** Representative images of fluorescent TUNEL labelled apoptotic cells (white arrows) in the growth plate. Cell nuclei were detected with DAPI staining **(B)** Graph of TUNEL positive cells expressed as a percentage of the total number of cells in each growth plate zone. There was a 135.3% increase in the number of apoptotic cells in the hypertrophic zone of SEMD mice and a 77.7% increase in apoptotic cells at the vascular invasion front of OCD mice compared with wild type controls. **(C)** Table showing numeric data used for the genera on of graph B.

Key: +/+ (wild type) O/O (homozygous for the OCD muta on) S/S (homozygous for the SEMD mutation) RZ (resting zone) PZ (proliferative zone) HZ (hypertrophic zone) VIF (vascular invasion front) scale bar = 50µm, *P≤0.05, Two tailed T-test, 3 joint regions analysed from 3 individual animals.

5.4 Histological analysis of bone formation in OCD and SEMD mice

Von Kossa staining was used to visualise calcium deposition in the cartilage growth plate and underlying bone of wild type and mutant newborn mice. There was no overt difference in the deposition of calcium in the cartilage matrix or trabecular bone of mice homozygous for either the SEMD (n=2) or OCD (n=3) mutation when compared to wild type controls (Figure 64). Staining for the osteoclast marker tartrate-resistant acid phosphatase (TRAP) was performed on mice at three weeks of age (Figure 65A). There was no statistical difference in the total number of osteoclasts on the chondro-osseous border in either OCD (P=0.31) or SEMD (P=0.23) mice compared to wild type controls (n=3, Figure 65). In addition to this, there was no difference in the number of large mature multinucleate osteoclasts on the chondro-osseous border in OCD (P=0.24) or SEMD (P=0.23) mice (Figure 65).

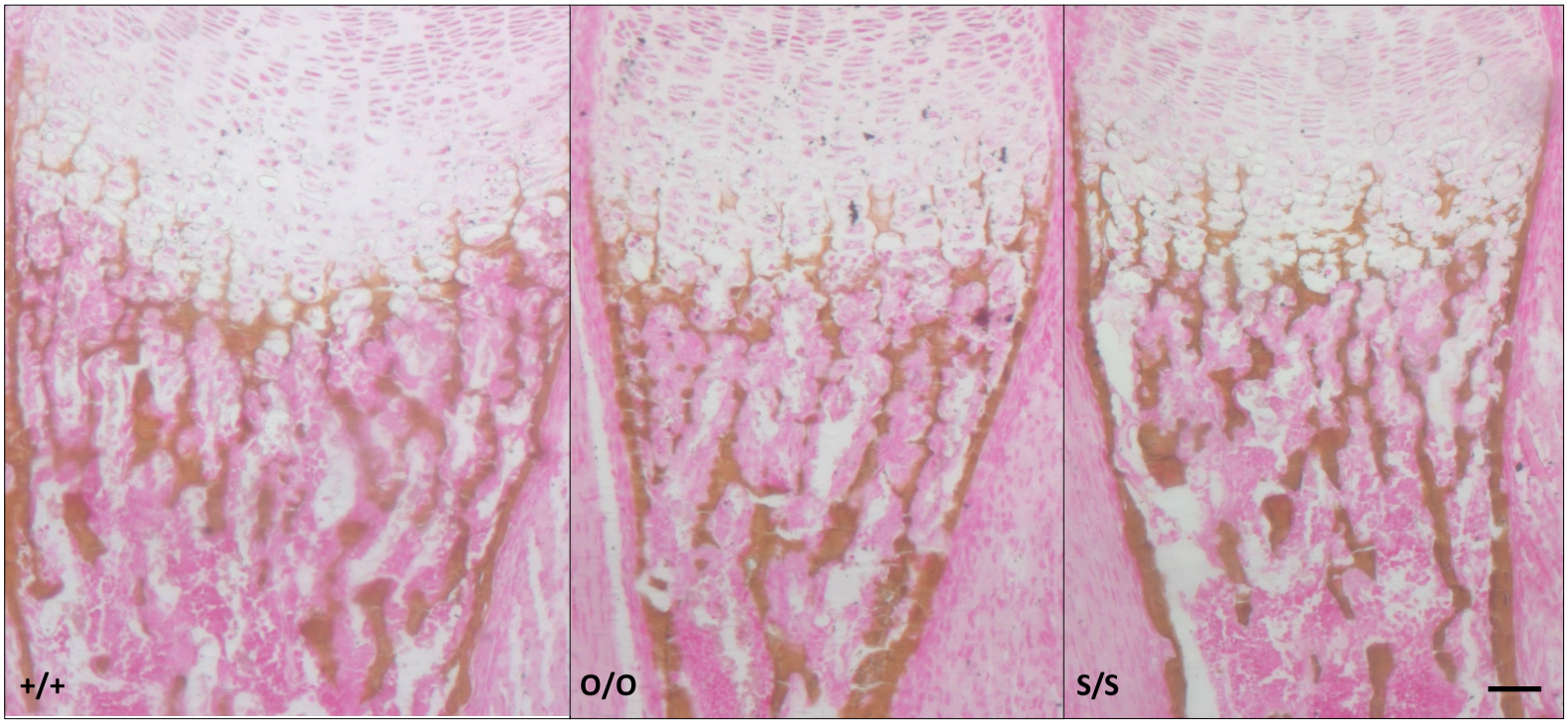

Figure 64 Calcification of the cartilage and bone in OCD and SEMD mice.

Von Kossa staining of growth plates from newborn wild type, OCD and SEMD mice. There was no overt di erence in calcium staining in the hypertrophic car lage or underlying trabecular bone between mice of all three genotypes (OCD n=3, SEMD n=2).

Key: +/+ (wild type) O/O (homozygous for OCD muta on) S/S (homozygous for SEMD muta on) scale bar = 20μm.

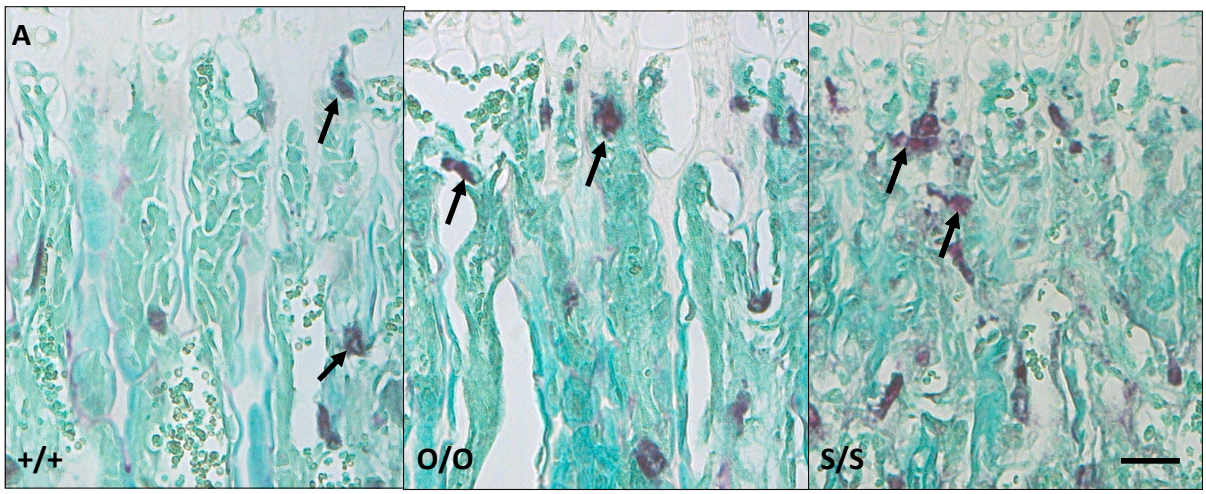

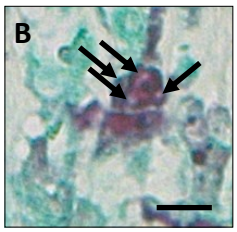

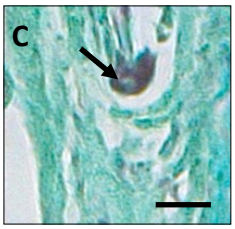

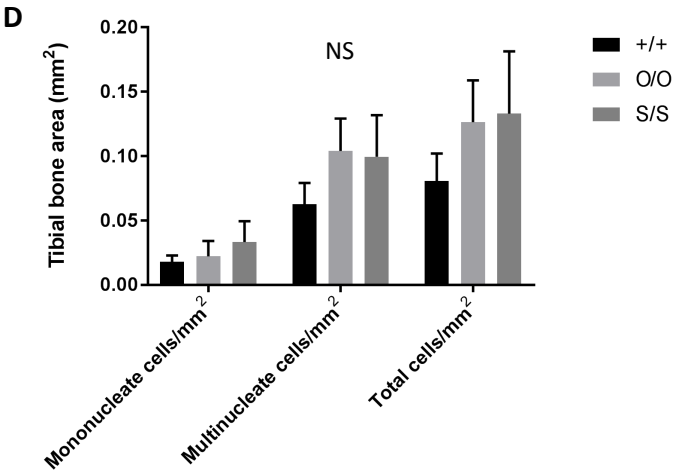

E

	+/+	O/O	S/S
Average mononucleate osteoclast number/mm^2 ± SEM	0.02±0.01	0.02±0.01	0.04±0.01
Average mul nucleate osteoclast number/mm^2 ± SEM	0.06±0.02	0.10±0.03	0.12±0.03
Average total osteoclast number/mm^2 ± SEM	0.08±0.02	0.13±0.03	0.14±0.04

Figure 65 Osteoclast density in OCD and SEMD mice.

(A) TRAP staining for osteoclasts (black arrows) on matched sec ons from male mice at three weeks of age (scale bar = 100µm). Representa ve images of **(B)** mul nucleate and **(C)** mononucleate osteoclasts. Nuclei are indicated with arrows (scale bar = 50µm). **(D)** There was no sta stical di erence in the number of osteoclasts on the chondro-osseous border in OCD or SEMD mice. **(E)** Table showing the numeric data used for the genera on of graph .

Key: +/+ (wild type) O/O (homozygous for OCD muta on) S/S (homozygous for SEMD mutation) NS (not significant) SEM (standard error of the mean) n=3, scale bar = 100µm

5.5 Transcriptional analysis of the ECM

RNA-sequencing was used to compare the transcriptomic profile of chondrocytes from femoral and tibial cartilage extracted from 5 day old mice homozygous for either the SEMD or OCD mutation with that of wild type littermates. There was no statistical difference in the transcript levels of genes encoding the major ECM proteins including collagens (type II, V, VI, IX, X, XI and XXVII) proteoglycans (aggrecan, biglycan, perlecan) and glycoproteins (COMP, matrilin 1 and matrilin 3) in mice homozygous for either the SEMD or OCD mutation compared to wild type controls (Table 4). Gene expression of the SLRPs decorin (fold change = -1.5) and lumican (fold change = -0.46) was statistically decreased in cartilage from mice homozygous for the SEMD mutation compared to the wild type controls. However, gene expression levels were not below the -1.5 log fold change required for a biologically meaningful change. There was increased gene expression of tenascin X (fold change = 1.85) in cartilage from mice homozygous for the OCD mutation (Table 4).

Protein	Gene symbol	OCD		SEMD	
		FC	P value	FC	P value
Aggrecan	*Acan*	-2.01	0.18	-1.40	0.49
Asporin	*Aspn*	1.01	0.94	-1.02	0.92
Biglycan	*Bgn*	-1.13	0.56	-1.35	0.17
Chondroadherin	*Chad*	-1.71	0.24	-1.24	0.63
Collagen type II α1	*Col2a1*	-2.30	0.16	-1.17	0.77
Collagen type V α1	*Col5a1*	-1.13	0.70	-1.37	0.31
Collagen type V α2	*Col5a2*	-1.12	0.67	-1.39	0.23
Collagen type V α3	*Col5a3*	1.48	0.06	1.01	0.94
Collagen type VI α1	*Col6a1*	1.06	0.80	-1.20	0.41
Collagen type VI α2	*Col6a2*	1.05	0.84	-1.26	0.35
Collagen type VI α3	*Col6a3*	1.04	0.86	-1.16	0.55
Collagen type IX α1	*Col9a1*	-2.22	0.24	-1.01	0.98
Collagen type IX α2	*Col9a2*	-2.44	0.12	-1.02	0.97
Collagen type IX α3	*Col9a3*	-2.62	0.08	1.02	0.96
Collagen type X α1	*Col10a1*	-1.67	0.45	-1.28	0.71
Collagen type XI α1	*Col11a1*	-2.00	0.15	-1.65	0.28
Collagen type XI α2	*Col11a2*	-2.07	0.14	-1.24	0.64
Collagen type XXVII α1	*Col27a1*	-1.91	0.09	-1.47	0.14
COMP	*comp*	-1.43	0.28	-1.42	0.28
Decorin	*Dcn*	-1.10	0.56	**-1.51**	**0.04***
Epiphycan	*Epyc*	-2.71	0.25	1.17	0.85
Fibromodulin	*Fmod*	*-0.37*	0.34	-1.59	0.11
Perlecan	*Hspg2*	-1.40	0.19	-1.47	0.14
Lumican	*Lum*	-1.32	0.11	**-1.46**	**0.04***
Matrilin 1	*Matn1*	-2.99	0.13	1.34	0.67
Matrilin 3	*Matn3*	-2.83	0.23	-1.06	0.94
PRELP	*Prelp*	-1.30	0.37	-1.36	0.31
Tenascin X	*Tnxb*	**1.85**	**0.02***	*0.34*	0.32

Table 4 Differential gene expression of extracellular matrix molecules.

Transcriptomics analysis was performed on bial and femoral car lage of ve day old mice homozygous for either the SEMD or OCD muta on and wild type controls. Mice homozygous for the OCD muta on exhibited increased gene expression of tenascin X (n=3, *P ≤ 0.05). Mice homozygous for the SEMD mutation displayed statistically decreased gene expression of decorin and lumican; however, the fold change was not below the standard –1.5 required for a biologically meaningful change.

5.6 Immunoblotting analysis of the ECM

4-12% Bis-Tris SDS-PAGE Western blotting (under reducing conditions) was used to analyse the relative abundance of major extracellular matrix proteins in femoral head cartilage dissected from male mice at 3 weeks of age and rib chondrocytes extracted from mice at 7 days of age. There was a 36% decrease in the total abundance of COMP (P=0.01) in femoral head cartilage extracted from mice homozygous for the SEMD mutation, but no statistical difference in the abundance of collagen type II (n=3, Figure 66A). Mice homozygous for the OCD mutation exhibited a 61% and 47% decrease in the expression of COMP (P=0.03) and collagen type II (P=0.04) respectively (n=3, Figure 66A). Rib chondrocytes were isolated from cartilage of 7 day old mice and cultured in maintenance medium for 48 hours before lysis. 4-12% Bis-Tris SDS-PAGE Western blotting of culture medium (under reducing conditions) showed delayed secretion of mature collagen type II (120kDa) by OCD and SEMD chondrocytes. Immunoblotting of cell lysate from OCD and SEMD mice showed no overt difference in the band intensity for collagen type II but increased abundance of two higher molecular weight bands corresponding to uncleaved (proα1, 200kDa) and partially cleaved (pNα1, 150kDa) procollagen (Figure 66B) (Aubert-Foucher, Mayer et al. 2014, Wieczorek, Rezaei et al. 2015). It was not possible to perform statistical analysis due to the low number of replicates (n=1) but this initial data suggested there may be a delay or impairment in the processing of procollagen II to the mature form.

Sequential protein extraction of femoral head cartilage dissected from male mice at 3 weeks of age did not show any overt difference in the abundance of collagen type II in buffers I and II from mice homozygous for the SEMD mutation. There was however a 44% decrease in the abundance of collagen type II in the final extraction buffer (buffer III) suggesting that the extractability of collagen type II maybe slightly altered in SEMD cartilage compared to wild type controls (n =3) Figure 67).

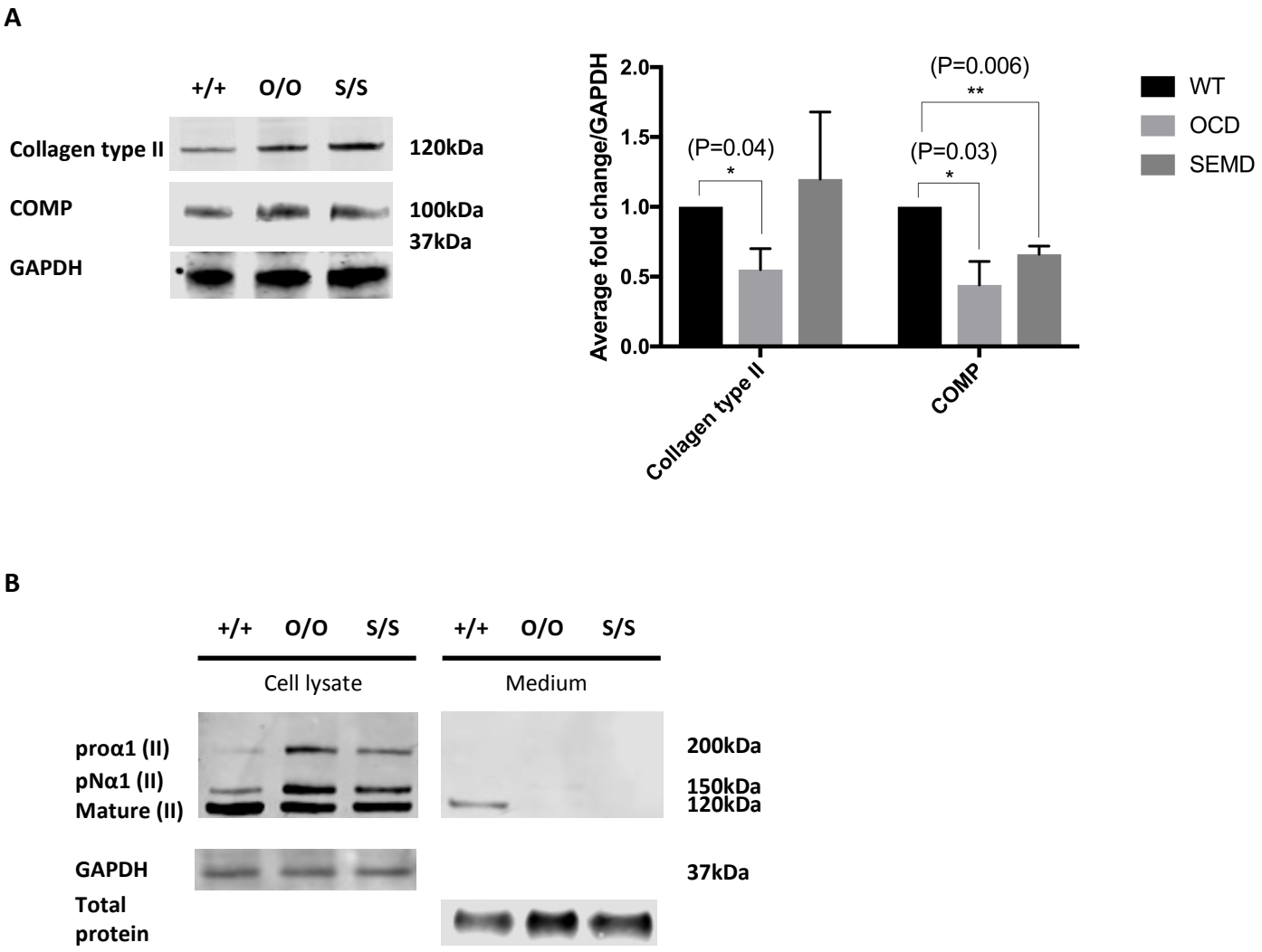

Figure 66 Protein expression of extracellular matrix molecules

(A) Reduced Western blot of femoral head car lage from 3 week old mice homozygous for either the SEMD or OCD muta on and wild type li ermates. Mice homozygous for the OCD or SEMD muta on exhibited a 61% and 36% decrease in COMP abundance rela ve to GAPDH, respectively (n=3). OCD mice also displayed a 47% decrease in COMP expression. **(B)** Reduced Western blot of culture medium and cell lysate indicated that the secre on of collagen type II into the medium was reduced and the ra o of procollagen type II to the mature form was increased in SEMD and OCD chondrocytes compared to wild type controls. This suggested that collagen processing may be impaired in mice homozygous for either the SEMD or OCD muta on (n=1).

Key: +/+ (wild type) O/O (homozygous for OCD muta on) S/S (homozygous for SEMD muta on) *P ≤ 0.05, **P ≤ 0.01, Two tailed T-test.

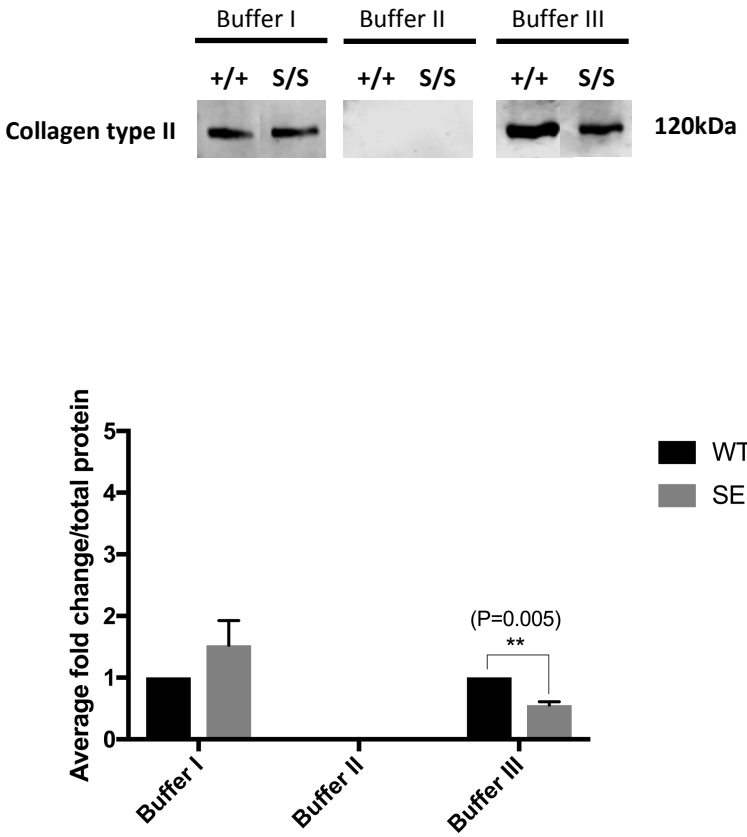

Figure 67 The extractability of collagen type II from the extracellular matrix

Reduced Western blot of sequentially extracted protein from femoral head cartilage in 3 week old mice homozygous for the SEMD mutation and wild type littermates. There was no statistical difference in the extractability of collagen type II from the extracellular matrix of SEMD mice (compared to wild type controls) in buffers I and II. There was a 44% decrease in the average amount of collagen type II (in protein extracted in buffer III) in mice homozygous for the SEMD mutation compared to the wild type controls (n=3).

Key: +/+ (wild type) S/S (homozygous for SEMD mutation) **P ≤ 0.01, Two tailed T-test.

5.7 Histo-morphometric analysis of the thoracic vertebral column

Haematoxylin and eosin staining, safranin O staining and histo-morphometry were used to assess the morphology of the thoracic spine in 9 week old mice homozygous for the OCD and SEMD mutations and their wild type littermates. The vertebral bodies of OCD mice were proportionally smaller compared to wild type mice, with an 8.3% decrease in height (P=0.04) but no statistical difference in the width/height ratio (Figure 68). In contrast, SEMD mice displayed platyspondyly with a 13.2% decrease in vertebral body height (P=0.02) and an increased width/height ratio (P=0.0008, Figure 68). Interestingly, although the majority of SEMD mice analysed (n=3) exhibited flattened vertebrae, the SEMD mouse with the greatest spinal curvature (Diab angle of 30^{o}) also displayed the classical wedge-shaped vertebrae associated with developmental scoliosis (n=1) (Scherrer, Begon et al. 2013). Morphological analysis of the invertebral disc (IVD) indicated that the height of the IVD in OCD mice was unaffected (Figure 69). The nucleus pulposus was flattened, however, with an increase in the width to height ratio (P=0.0003, Figure 69C). There was no statistical difference in the shape of the nucleus pulposus in SEMD mice, although the total height of the IVD was decreased by 18.4% (P=0.04, Figure 69B-D).

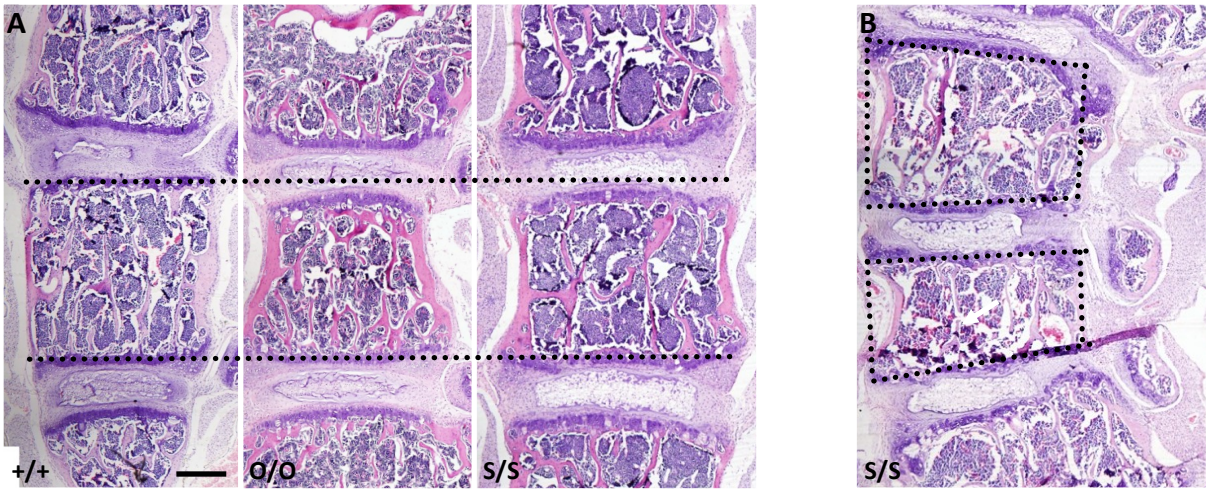

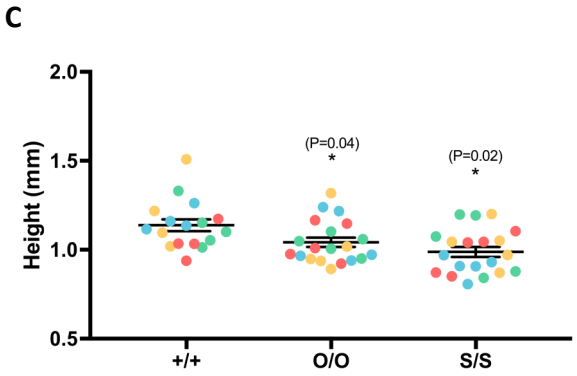

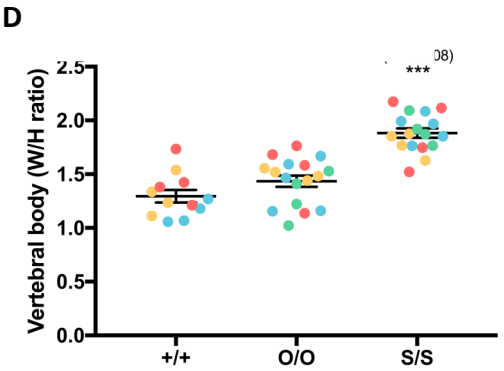

E

Genotype	+/+	O/O	S/S
Average vertebral body height (mm) ± SEM	1.21±0.04	**1.11±0.01***	**1.05±0.03***
Average vertebral body width/height ra o ± SEM	1.30±0.08	1.44±0.05	**1.88±0.03*****

Figure 68 Histological analysis of the thoracic vertebral bodies in OCD and SEMD mice.

The height and weight to height ra o of the vertebral bodies were measured in 9 week old male OCD and SEMD mice and their wild type litter ates. **(A)** Representa ve image of vertebral bodies from wild type, OCD and SEMD mice stained with haematoxylin and eosin. **(B)** Vertebral body wedging at the site of spinal curvature in an SEMD mouse (do ed lines). **(C)** Graph of vertebral body height. Each colour denotes individual measurements from one mouse. The average vertebral body height was decreased by 8.3% and 13.2% in OCD and SEMD mice, respectively, compared to wild type littermates. **(D)** Graph of the width to height (W/H) ra o of the vertebral body. The W/H ra o was not sta sti ally di erent in the vertebral bodies of OCD mice. **(E)** Table showing the average of the numeric data used for the genera on of graphs C and D.

Key: +/+ (wild type) O/O (homozygous for OCD muta on) S/S (homozygous for SEMD muta-on) W (width) H (height) SEM (standard error of the mean) scale bar = 100µm, *P≤0.05, ***P≤0.001 , Two tailed T-test, n≥3.

A

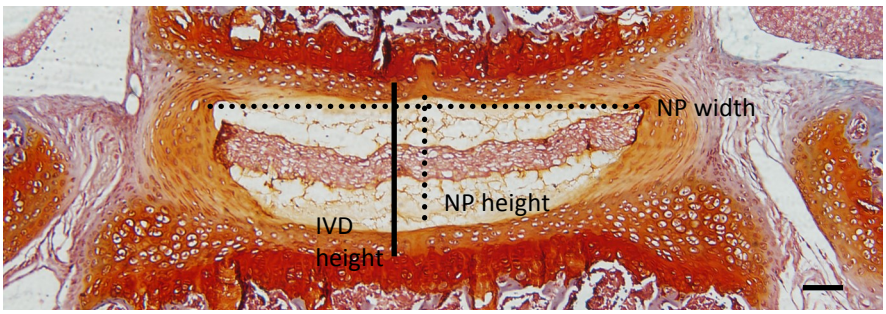

B

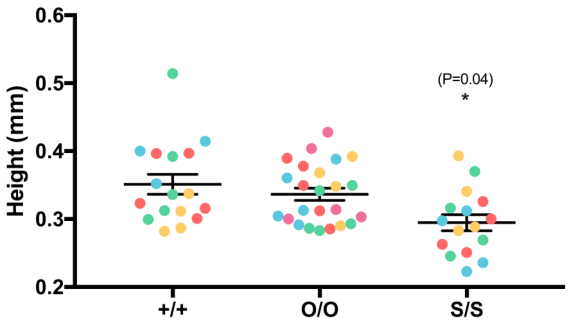

C

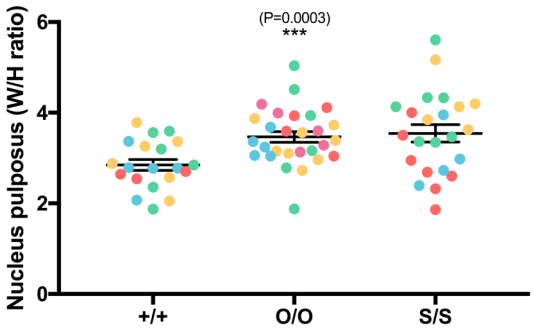

D

Genotype	+/+	O/O	S/S
Average intervertebral disc height (mm) ±	0.38±0.02	0.36±0.01	**0.31±0.01***
Average nucleus pulposus width/height ra o± SEM	2.82±0.08	**3.51±0.07****	3.53±0.35

Figure 69 Morphometric analysis of the thoracic spine in OCD and SEMD mice.

The height and weight to height ra o of the en re intervertebral disc (IVD) and nucleus pulposus were measured in 9 week old male OCD and SEMD mice and their wild type li ermates. **(A)** Representa ve image of a wild type intervertebral disc. **(B)** Graph of intervertebral disc height. Each colour denotes individual measurements from one mouse. The average intervertebral disc height was decreased by 18.4% in SEMD mice compared to wild type li ermates. There was no sta stical di erence in IVD height in OCD mice. **(C)** Graph of the width to height (W/H) ratio of the nucleus pulposus. The W/H ratio was not statistically different in SEMD mice. In OCD mice, however, the height of the nucleus pulposus was reduced compared to its width, indicating that the nucleus pulposus has a flattened morphology. **(D)** Table showing the average of the numeric data used for the generation of graphs B and C.

Key: +/+ (wild type) O/O (homozygous for OCD mutation) S/S (homozygous for SEMD mutation) NP (nucleus pulposus) IVD (intervertebral disc) SEM (standard error of the mean) scale bar = 50µm, *P≤0.05, ***P≤0.001 Two tailed T -test, n≥4.

5.7.1 Degenerative changes in the thoracic intervertebral disc

Histo-morphometric analysis using an established scoring system was performed to assess intervertebral disc (IVD) degeneration (Tam, Chan et al. 2017). IVD were scored for morphological features associated with either normal disc structure or degenerative changes. Normal disc morphology was scored with a value of 0 and degenerative features scored with a value between 1 and 2-4 according to severity. The average score was taken for the boundary between the annulus fibrosis and nucleus pulposus (maximum score of 2) each disc component (maximum score of 6) and as a total IVD score with a maximum potential score of 14. Wild type intervertebral discs consisted of a single cell mass surrounded by extracellular matrix known as the nucleus pulposus (n=3, Figure 70A). This inner structure was distinctly separate from the annulus fibrosis, an outer fibrous ring comprised of concentric lamellae with flattened or slightly rounded cells. Normal discs did not have any clefts or fissures. Intervertebral discs (IVD) from OCD mice (n=5) were either indistinguishable from wild type IVD (Figure 70B) or exhibited a number of morphological changes including reduced cell mass, increased matrix and cell cleft formation in the nucleus pulposus (Figure 70C). The separation between the nucleus pulposus and annulus fibrosis was less defined with some discs exhibiting complete boundary loss. Changes in the annulus fibrosis were more variable with serpentine lamellae and more rounded cells. Quantification of these degenerative changes showed a 1.6 point increase in the average total degeneration score (P=0.002, Figure 70F). Statistically significant changes were observed in scoring for the boundary (P=0.02, Figure 70G) nucleus pulposus (P=0.004, Figure 70H) but not the annulus fibrosis (P=0.06, Figure 70I) indicating that the nucleus pulposus is the primary site of degeneration. SEMD mice displayed moderate to severe intervertebral disc degeneration (IDD). Annulus fibrosis lamellae were undefined and often protruded into the nucleus pulposus (n=4, Figure 70D-E). In severely degenerated discs the boundary between the annulus fibrosis and nucleus pulposus was absent (Figure 70E). The matrix-rich nucleus pulposus exhibited complete cell loss and the formation of small clefts. Quantification of these changes showed a 5.1 point increase in the average total degeneration score (P=0.00005, Figure 70F). Significant changes were observed in both the nucleus pulposus (P=0.004) and annulus fibrosis (P=0.0004, Figure 70H-I).

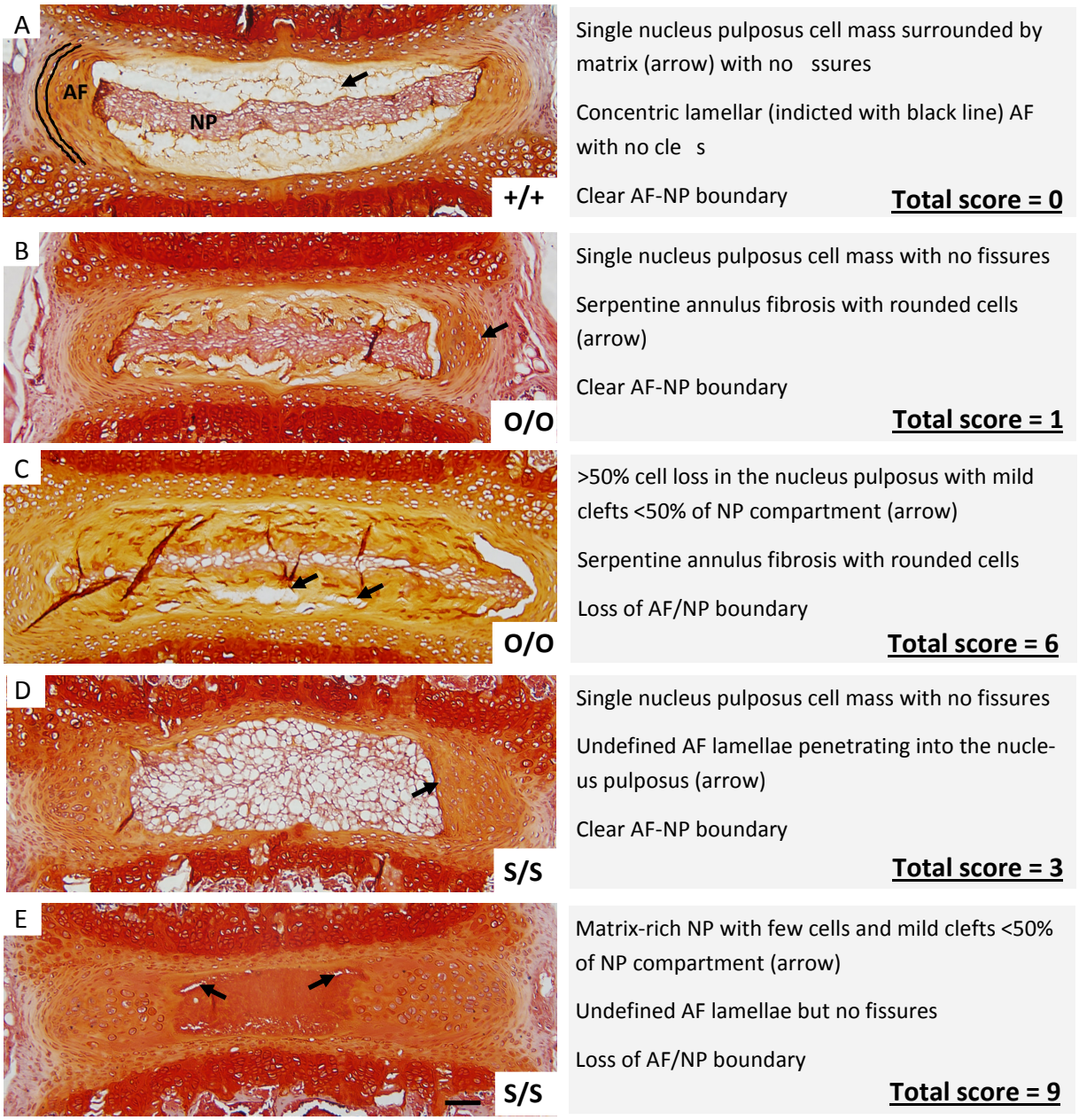

Figure 70 Intervertebral disc degeneration in OCD and SEMD mice (A-E).

The severity of intervertebral disc degeneration (IDD) in the thoracic spine was quantitatively assessed in 9 week old male OCD and SEMD mice and wild type littermates. Intervertebral discs (IVD) were stained with safranin O and images randomly numbered to remove bias. IVD morphology was scored blind for degenerative changes (with a maximum possible score of 14). **(A)** Representative image of wild type IVD with normal morphological features. IVD from OCD mice exhibited both **(B)** relatively normal morphological features and **(C)** degenerative changes such as cell loss and the presence of clefts in the nucleus pulposus. IVD from SEMD displayed **(D)** moderate and **(E)** severe degenerative changes including loss of the AF/NP boundary, fissures and loss of annulus fibrosis structure.

Key: +/+ (wild type) O/O (homozygous for OCD mutation) S/S (homozygous for SEMD mutation) AF (annulus fibrosis) NP (nucleus pulposus) scale bar = 50µm, n≥3.

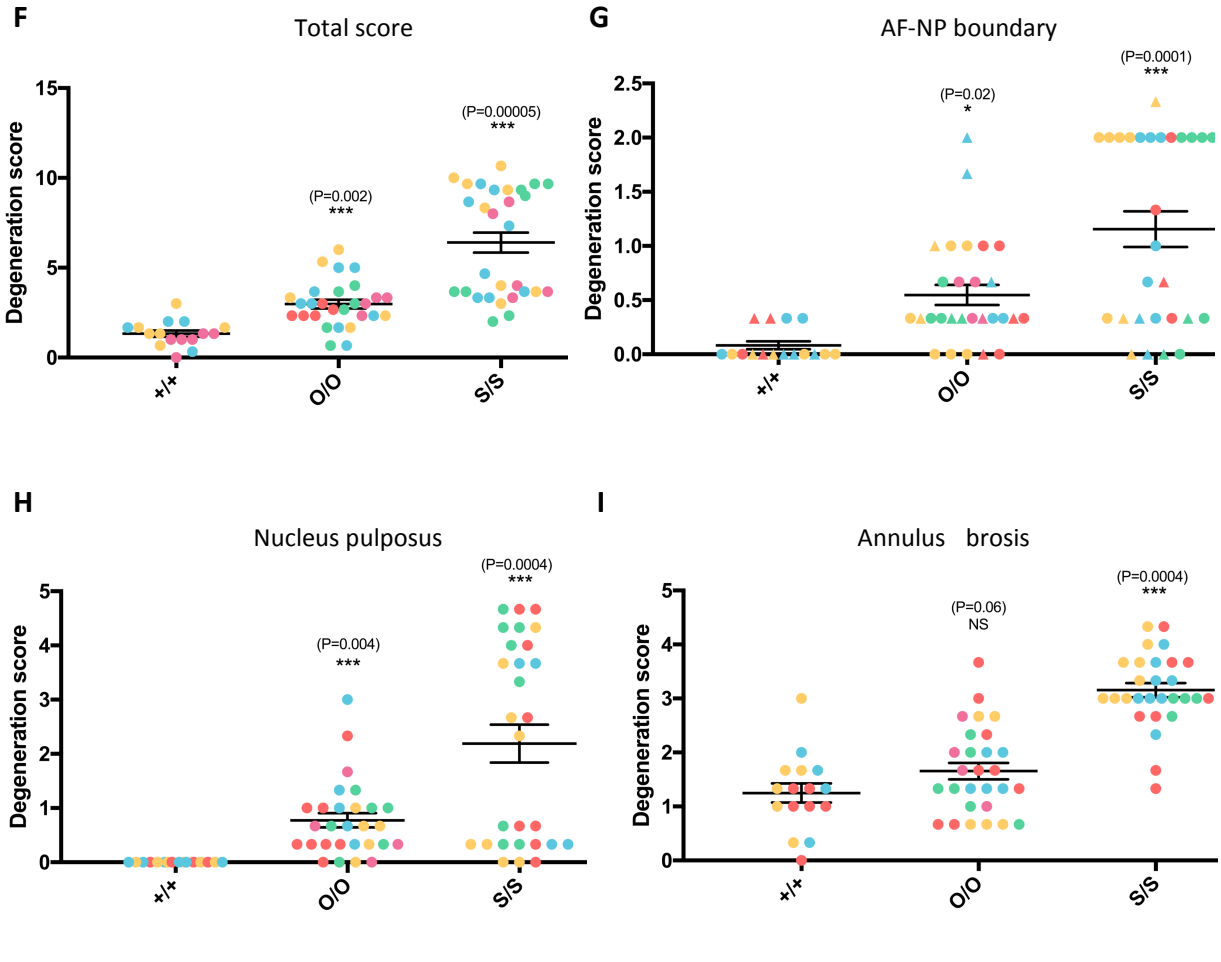

J

Genotype	+/+	O/O	S/S
Average total degenera on score±SEM	1.35±0.21	**2.98±0.21*** **	**6.44±0.30*** **
Average AF-NP boundary score ±SEM	0.09±0.05	**0.56±0.11***	**1.15±0.08*** **
Average AF degenera on score ±SEM	1.26±0.16	1.64±0.09	**3.12±0.15*** **
Average NP degenera on score ±SEM	0.00±0.00	**0.78±0.13*** **	**2.17±0.22*** **

Figure 70 Intervertebral disc degeneration in OCD and SEMD mice (F-J).

The average score of three independent scorers was plotte for each disc. Each colour denotes individual measurements from one mouse. **(F)** The average degenera on score was increased by 1.6 and 5.1 points in the OCD and SEMD mice respectively, compared to wild type controls. Interestingly, discs from OCD mice exhibited degeneration of the **(H)** nucleus pulposus but scoring for the **(I)** annulus fibrosis was not statistically different. In contrast, significantly different degenerative changes were observed in both the **(H)** nucleus pulposus and **(I) a**nnulus fibrosis of SEMD discs. **(J)** Table showing the average of the numeric data used for the generation of graphs F, G, H and I.

Key: +/+ (wild type) O/O (homozygous for OCD muta on) S/S (homozygous for SEMD mutaon) SEM (standard error of the mean) NS (not significa t) *P≤0.05, ***P≤0.001, Two tailed T-test, n≥3.

There was no correlation between the severity of these degenerative changes and the degree of scoliotic curvature, indicating that IDD in the SEMD model is distinct from the scoliotic phenotype (Figure 71). There was however an association with the position of the IVD, with disc degeneration correlating with distance from the head (n=4, Figure 72). A similar trend was not observed in OCD (n=5, Figure 72C) or wild type mice (n=3, data not shown).

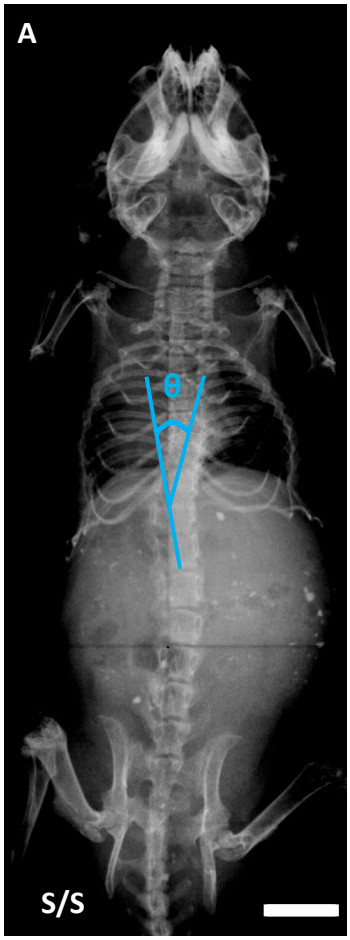

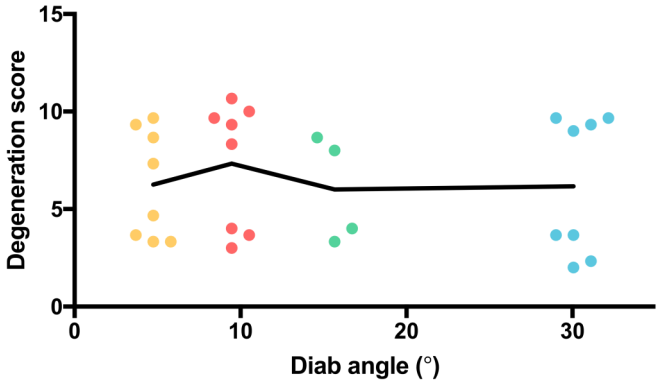

C

Diab angle (°)	4.75	9.47	15.68	30.06
Average degenera on score±SEM	6.25±0.99	7.33±1.13	6.00±1.36	6.17±1.25

Figure 71 Severity of scoliosis does not correlate with IDD in SEMD mice.

The rela onship between the degree of spinal curvature and intervertebral disc degenera- on (IDD) was assessed in 9 week old male SEMD mice. **(A)** Radiographic image of a 9 week old SEMD mouse exhibiting scoliosis. The severity of the spine curvature was quantified by measuring the Diab angle(θ). Mice exhibiting scoliosis had a Diab angle≥12 **(B)** Graph of the degeneration scores of individual intervertebral discs plotted against the Diab angle (the degree of spinal curvature). Each colour denotes individual measurements from one mouse. There was no overt association between the severity of scoliotic curvature and IDD in SEMD mice. **(C)** Table showing the average of the numeric data used for the generation of graph B.

Key: SEM (standard error of the mean) scale bar = 5mm, n=4.

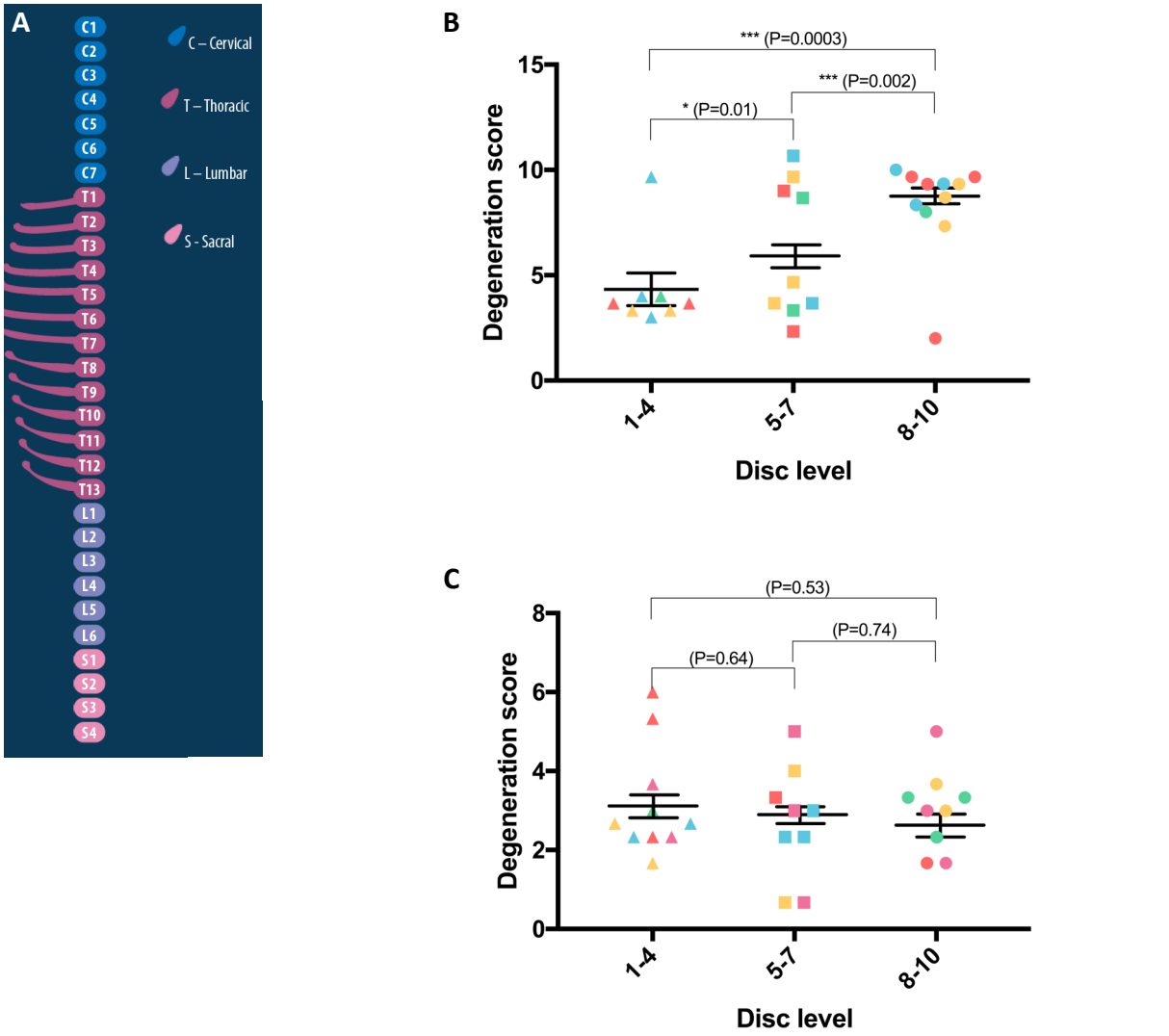

D

Disc level	1-4	5-7	8-10
Average degeneration score (SEMD) ±SEM	**4.14±0.49**	**6.21±0.33**	**8.11±0.18**
Average degeneration score (OCD) ±SEM	3.06±0.53	2.78±0.22	2.62±0.40

Figure 72 Association between disc level and IDD in OCD and SEMD mice.

The associati n between the degree of intervertebral disc degenera on and the level of the disc within the thoracic spine was assessed in 9 week old male SEMD mice. **(A)** Schematic of the numbered intervertebral discs in the murine spine. Diagram adapted from LifeMap Discovery, accessed May 2018 (Edgar et al. 2013). **(B)** Graph of the degeneration scores of intervertebral discs at levels T1-4, T5-7 and T8-10. The average degeneration score increased by 2 points at each stage measured as the distance from the head increased. Each colour denotes individual measure-ments from one mouse. **(C)** There was no correlation between disc level and severity of disc degeneration in OCD mice. **(D)** Table showing the average of the numeric data used for the generation of graphs B and C.

Key: SEM (standard error of the mean) *P≤0.05, ***P≤0.001,Two tailed T -test, n≥4.

5.8 Summary

The aim of this chapter was to further investigate and compare the tissue pathology of the OCD and SEMD mouse models, compared to wild type controls, using quantitative methodology. *In vivo* cell labelling and a range of histochemical techniques were used to analyse cell number, apoptosis and proliferation in the tibial growth plate and osteoclast number and degree of mineralisation of the underlying bone. RNA-seq and immunoblotting were used to assess the expression and composition of the extracellular matrix. The structure and degeneration of the spine was analysed using histo-morphometry. Histochemical analysis of tibial growth plate cartilage from SEMD mice indicated that the proliferative zone contained a reduced number of cells due to a reduction in the chondrocyte proliferation rate. This analysis also indicated that the expansion of the hypertrophic zone was due to increased cell number rather than greater cellular volume. In addition to this, dysregulated apoptosis was observed, with an increase in programmed cell death in the hypertrophic zone. In contrast, the relative proportion of cells in each zone and the chondrocyte proliferation rate were unaffected in growth plates from OCD mice. There was a difference in programmed cell death however, with increased apoptosis observed on the chondro-osseous border between the growth plate cartilage and bone. Analysis of the calcified cartilage and underlying trabecular bone indicated no difference in bone calcification or osteoclast number in tissue from OCD and SEMD mice compared to wild type controls. This suggested that the removal of extracellular matrix and subsequent mineralisation during bone formation were not affected in these mouse models. Transcriptomic and immunoblotting analysis confirmed that the composition of the cartilage extracellular matrix is altered in both the OCD and SEMD mouse models as cartilage from mice homozygous for the OCD mutation showed increased gene expression of tenascin X. There was no change in the transcript level of COMP in mutant cartilage compared to wild type controls; however, SDS-PAGE Western blotting showed decreased abundance of the COMP protein in cartilage from both OCD and SEMD mice. Transcript levels of type II collagen were also unaffected in OCD and SEMD; however, SDS-PAGE Western blotting analysis of femoral head cartilage indicated that collagen type II expression is decreased in OCD cartilage. Furthermore, Western blotting analysis of OCD and SEMD chondrocytes suggested that the processing of procollagen to the mature form may be affected in these models. Histo-morphometric analysis of the vertebral column indicated that both the OCD and SEMD mouse models exhibit reduced vertebral body height and

morphological changes associated with intervertebral disc degeneration. Pathological changes in the SEMD spine were more severe, with platyspondyly and degenerative changes in both the annulus fibrosis and nucleus pulposus.

In conclusion, both the OCD and SEMD mouse models exhibit dysregulated apoptosis, altered matrix composition and intervertebral disc degeneration. Pathological changes in both the tibial growth plate and vertebral column of SEMD mice were noticeably more severe, with decreased proliferation, increased hypertrophy and greater disc degeneration. In order to explain why these two mutations in the G3 globular domain of aggrecan elicit such different tissue pathologies, the potential disease mechanisms of autophagy and cellular stress were investigated in the following chapter.

Chapter 6. Disease Mechanisms of the SEMD and OCD Mouse Models

In order to identify potential disease mechanisms, a biased and non-biased approach was used. RNA-seq was used to generate a transcriptomics profile of both mouse models for a broad spectrum analysis. In parallel to this a more biased approach was used based on the data obtained in the previous two chapters. The analysis of the tissue pathology performed in Chapter 4 indicated that both the SEMD and OCD causative mutations cause delayed secretion of aggrecan and retention of mutant protein within the endoplasmic reticulum. Retention of mutant protein in mouse models of other chondrodysplasias has been shown to cause endoplasmic reticulum stress (Briggs, Bell et al. 2015) as the ER upregulates chaperones to try and re-fold the misfolded protein. The classical ER stress pathway is the unfolded protein response (UPR) and so the genes and proteins involved in this pathway were selected as candidates for investigation of the disease mechanism using transcriptomics analysis and Western Blotting. In addition to this, the UPR has also been shown to interact with a number of pathways involved in protein degradation such as autophagy and the proteasome. Immunofluorescent staining for autophagic markers, chemical autophagy inhibition and Western blotting were therefore used to investigate potential dysregulation of autophagy.

6.1 Transcriptomic analysis of growth plate cartilage

RNA-sequencing was used to investigate and compare the transcriptomics profile of mice homozygous for either the SEMD (D1983N) or OCD (V2019M) *Acan* mutation with those of wild type littermates. Total mRNA was extracted from femoral and tibial cartilage at 5 days of age. Samples were submitted for RNA-sequencing in triplicate. RNA-sequencing and the subsequent initial transcriptomics analysis were performed in house by the Newcastle University Genomics Core Facility and the Bioinformatics Support Unit. Differentially expressed genes which exhibited a biologically meaningful change (fold change ≥1.5 or ≤-1.5) were used for subsequent DAVID analysis (Huang, Sherman et al. 2009) to identify enriched biological themes. REViGO was then used to summarise the resultant gene ontology (GO) terms by clustering functionally redundant terms (Huang, Sherman et al. 2009). Cluster representatives or 'umbrella terms' were selected based on *p*-values supplied by DAVID. A SimRel semantic similarity measure (*C*) of 0.5 was used. This reduced the similarity between the GO terms in each cluster but still indicated a 99% chance of above-background similarity. A lower SimRel semantic similarity measure was not used to avoid the removal of non-redundant GO terms from the analysis (Huang, Sherman et al. 2009, Supek, Bošnjak et al. 2011). A uniqueness score was provided to assess the similarity of each GO term to the overall group. A dispensability score was also given, with a higher value indicating greater redundancy with other GO terms.

2318 genes were significantly differentially expressed in cartilage extracted from mice homozygous for the SEMD mutation compared to wild type controls with 1484 exhibiting a biologically meaningful change (Figure 73). The most significantly enriched terms in REViGO analysis of the SEMD transcriptome were 'flagellated sperm motility' and 'anterior/posterior pattern specification' (Table 5).

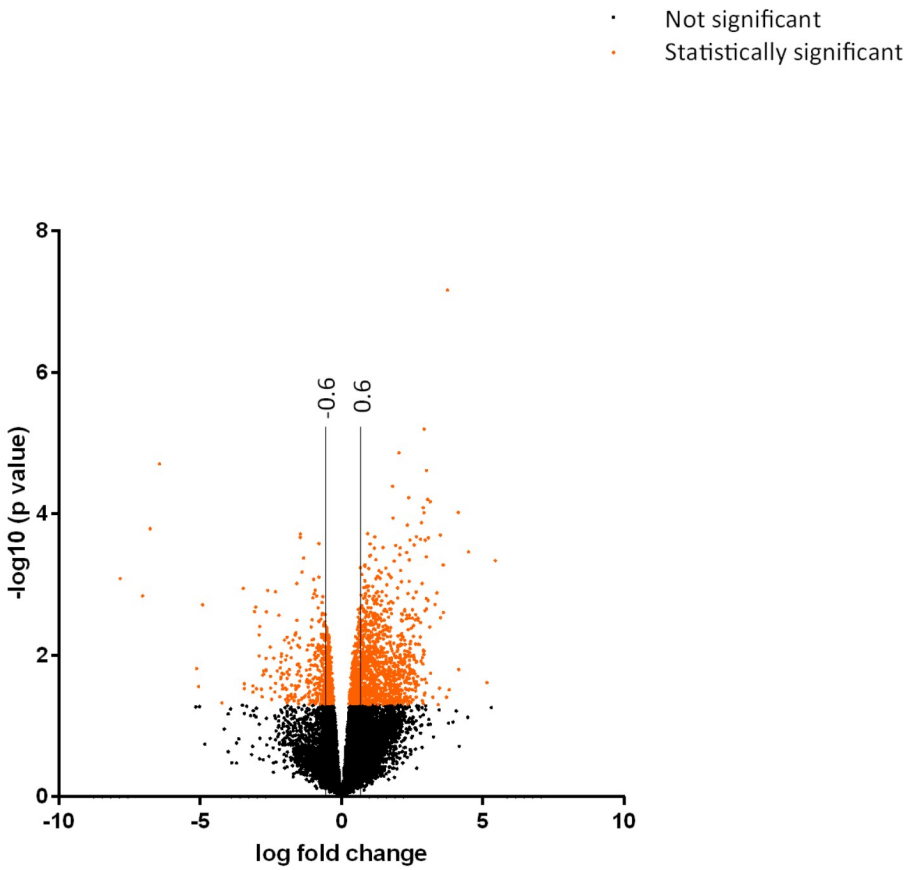

Figure 73 Differential gene expression in SEMD cartilage.

2318 genes were differentially expressed in SEMD tibial and femoral cartilage compared to wild type controls. 1484 genes exhibited a statistically-significant log fold change ≥0.6 (upregulated) or ≤ -0.6 (downregulated) indicating a biologically-significant change.

Term ID	Description	P-value	Uniqueness	Dispensability
GO:0030317	flagellated sperm motility	1.38E-03	0.79	0.00
GO:0032259	methylation	9.12E-02	0.95	0.00
GO:0035456	response to interferon-beta	3.16E-02	0.90	0.00
GO:0061025	membrane fusion	2.45E-02	0.87	0.02
GO:0009952	anterior/posterior pattern specification	3.09E-03	0.69	0.05
GO:0051781	positive regulation of cell division	2.88E-03	0.80	0.11
GO:0051321	meiotic cell cycle	3.20E-02	0.76	0.13
GO:0070050	neuron cellular homeostasis	3.24E-03	0.79	0.14
GO:0000012	single strand break repair	3.85E-02	0.91	0.18
GO:0010807	regulation of synaptic vesicle priming	1.92E-02	0.63	0.30
GO:0003333	amino acid transmembrane transport	3.40E-02	0.74	0.32
GO:0015937	coenzyme A biosynthetic process	4.61E-02	0.76	0.36
GO:0006468	protein phosphorylation	4.82E-02	0.85	0.37
GO:0006355	regulation of transcription, DNA-templated	9.33E-03	0.78	0.38
GO:0042391	regulation of membrane potential	3.53E-02	0.84	0.39
GO:0055085	transmembrane transport	3.16E-03	0.83	0.41
GO:0010459	negative regulation of heart rate	3.85E-02	0.63	0.43
GO:0070286	axonemal dynein complex assembly	3.85E-02	0.77	0.48
GO:0070207	protein homotrimerisation	4.86E-02	0.86	0.48

Table 5 REViGO GO terms in the SEMD transcriptome.

1157 differentially expressed genes were found in cartilage extracted from mice homozygous for the OCD mutation compared to wild type controls, with 990 differentially expressed genes exhibited a biologically meaningful change (Figure 74). The most significantly enriched terms in REViGO analysis of the OCD transcriptome were ‘ion transport' and 'cell adhesion' (Table 6).

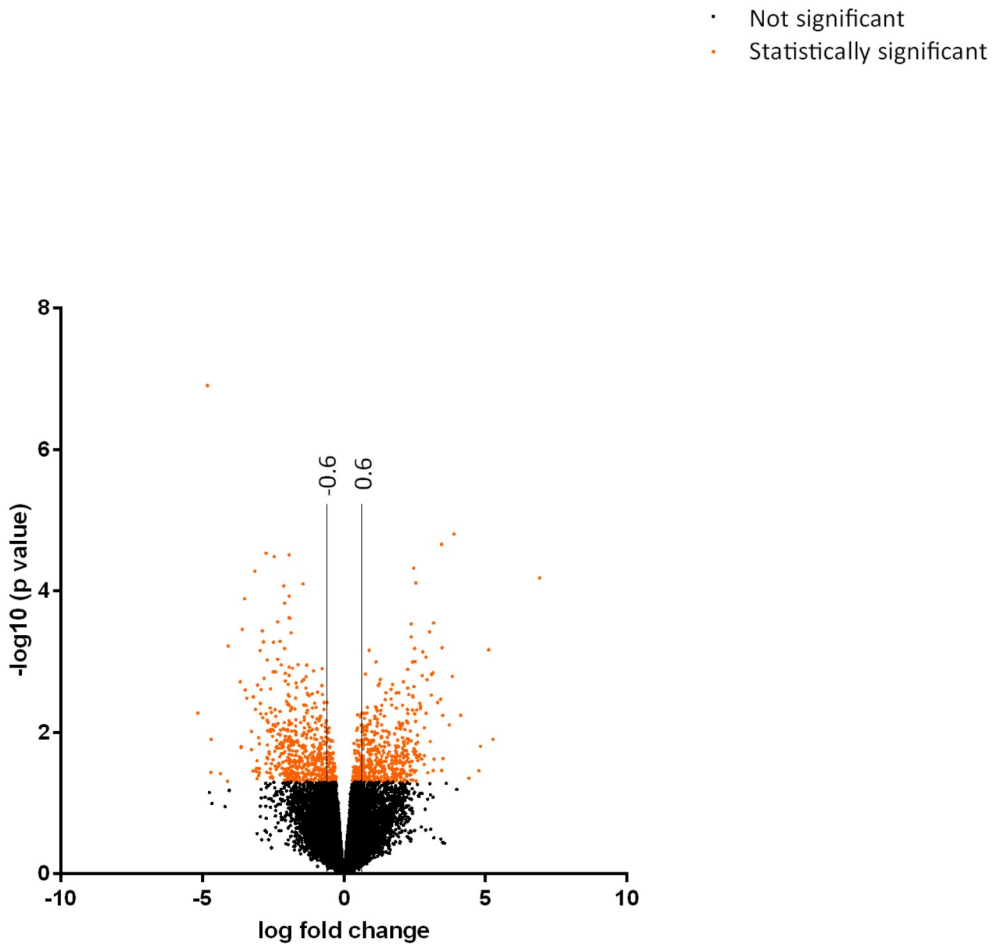

Figure 74 Differential gene expression in OCD cartilage.

1157 genes were differentially expressed in OCD tibial and femoral cartilage compared to wild type controls. 990 genes exhibited a statistically-significant log fold change ≥0.6 (upregulated) or ≤ -0.6 (downregulated) indicating a biologically-significant change.

Term ID	Description	P-value	Uniqueness	Dispensability
GO:0002376	immune system process	2.77E-03	0.97	0.00
GO:0006629	lipid metabolic process	2.06E-03	0.85	0.00
GO:0006816	calcium ion transport	2.21E-02	0.87	0.00
GO:0007155	cell adhesion	3.63E-04	0.87	0.00
GO:0031639	plasminogen activation	2.34E-02	0.95	0.04
GO:0007283	spermatogenesis	2.42E-03	0.64	0.08
GO:0007169	transmembrane receptor protein tyrosine kinase signalling pathway	3.05E-03	0.79	0.08
GO:0005975	carbohydrate metabolic process	1.64E-03	0.95	0.09
GO:0016126	sterol biosynthetic process	3.89E-03	0.73	0.15
GO:0030317	flagellated sperm motility	2.49-E02	0.83	0.18
GO:0006954	inflammatory response	2.17E-02	0.90	0.28
GO:0006811	ion transport	2.39E-04	0.90	0.31
GO:0072166	posterior mesonephric tubule development	4.81E-02	0.71	0.37
GO:0034625	fatty acid elongation, monosaturated fatty acid	3.32E-02	0.75	0.51
GO:0045453	bone resorption	2.22E-02	0.63	0.45
GO:0008202	steroid metabolic process	1.66E-02	0.78	0.47
GO:1901381	positive regulation of potassium ion transmembrane transport	4.43E-02	0.71	0.50

Table 6 REViGO GO terms in the OCD transcriptome.

2414 differentially expressed genes were found in cartilage extracted from mice homozygous for the OCD mutation compared to SEMD cartilage, with 1685 differentially expressed genes exhibited a biologically meaningful change (Figure 75A). Only 2.5% of the differentially expressed genes were downregulated in both OCD and SEMD cartilage and 9.3% upregulated (Figure 75B) indicating that the OCD and SEMD trancriptomes have distinct disease signatures. The most significantly enriched terms in REViGO analysis were ‘cilium movement’ and 'transmembrane transport' (Table 7).

A

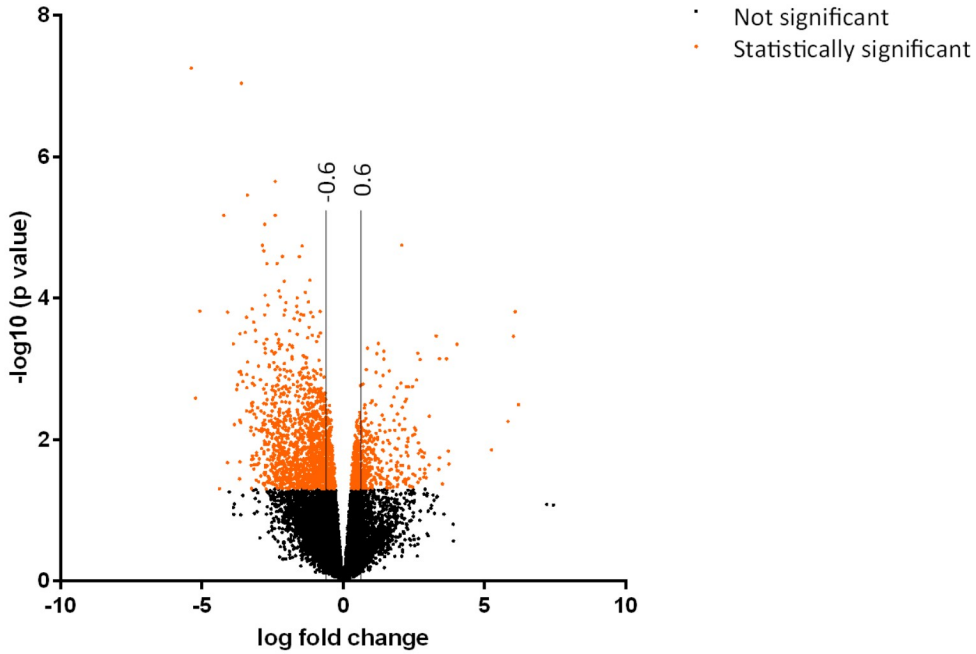

B

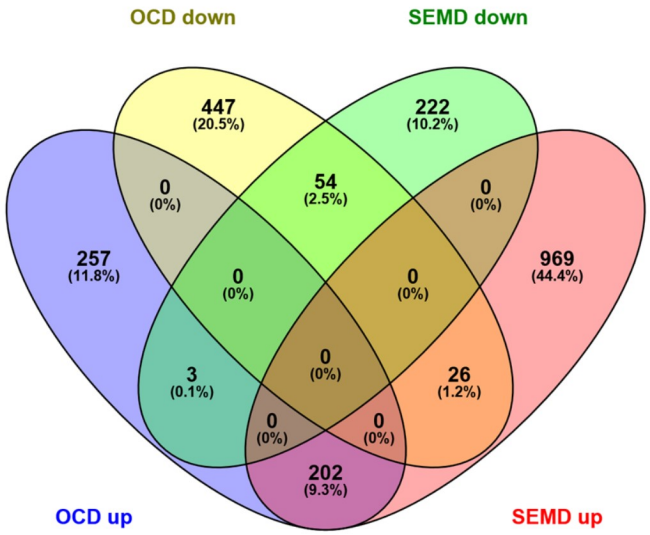

Figure 75 Differential gene expression between OCD and SEMD cartilage.

(A) 2414 genes were differentially expressed between the OCD and SEMD cartilage transcriptomes. 1685 genes exhibited a statistically-significant log fold change ≥0.6 (upregulated) or ≤ -0.6 (downregulated) indicating a biologically-significant change. **(B)** The OCD and SEMD transcriptomes have distinct signatures with only 2.5% (54 genes) of the transcriptome downregulated and 9.3% (202 genes) upregulated in both SEMD and OCD cartilage.

Term ID	Description	P-value	Uniqueness	Dispensability
GO:0002376	immune system process	9.42E-03	0.97	0.00
GO:0003341	cilium movement	4.96E-04	0.80	0.00
GO:0006821	chloride transport	5.74E-03	0.86	0.00
GO:0010923	negative regulation of phosphatase activity	5.37E-03	0.83	0.02
GO:0071773	cellular response to BMP stimulus	1.39E-02	0.88	0.02
GO:0009952	anterior/posterior specification	7.40E-04	0.55	0.05
GO:0045110	intermediate filament bundle assembly	2.30E-02	0.81	0.10
GO:0071502	cellular response to temperature stimulus	1.58E-02	0.92	0.19
GO:0009607	response to biotic stimulus	4.18E-02	0.91	0.28
GO:0055085	transmembrane transport	6.13E-04	0.88	0.31
GO:0035990	tendon cell differentiation	9.72E-03	0.61	0.37
GO:0045662	negative regulation of myoblast differentiation	2.11E-02	0.56	0.42
GO:0046676	negative regulation of insulin secretion	6.46E-03	0.69	0.43
GO:0002024	diet induced thermogenesis	1.48E-02	0.63	0.43
GO:2000543	positive regulation of gastrulation	3.39E-03	0.54	0.45

Table 7 REViGO GO terms between the OCD and SEMD transcriptomes.

6.1.1 The unfolded protein response and apoptosis

Histological analysis in Chapter 4 had shown that mutant aggrecan was intracellularly retained in both OCD and SEMD cartilage. In order to assess whether this protein retention elicited the unfolded protein response a panel of 66 genes was assembled (Appendix J). These genes were known to be associated with the three branches of the UPR (PERK, ATF6 and IRE1) the ER overload response (Kong, Li et al. 2015) and regulated IRE1-dependent decay of mRNA (RIDD) (Maurel, Chevet et al. 2014). There was no statistical difference in the gene expression of either canonical (*Hspa5, Atf6, Ern1, Eif2ak3*) or non-canonical stress sensors (*Creb3*, *Creb3l2*, *Creb3l3*, *Creb3l4*). However, there was a difference in the expression of 11 downstream stress-associated genes in SEMD cartilage, including a 3-fold increase in the ERAD component *Derl3* and a 2-fold increase in the chaperone *Hspa12a*. This transcriptomic data suggested that SEMD chondrocytes may exhibit mild ER stress but that the classical UPR is not upregulated in either OCD or SEMD cartilage. Histological analysis in Chapter 5 had indicated that apoptosis is upregulated in both OCD and SEMD cartilage. This was also suggested by transcriptomic analysis, with increased gene expression of *Bcl2l15* and decreased expression of the anti-apoptotic Bcl2a1d in OCD cartilage and both a 7-fold decrease in *Bcl2a1d* and 2-fold increase in the pro-apoptotic *Trib3* in SEMD cartilage.

6.1.2 Autophagic flux

Transmission electron microscopy in Chapter 4 had suggested that autophagy may be either increased or dysregulated in OCD and SEMD cartilage. Transcriptional analysis indicated that the aggresome-autophagy pathway may be upregulated in SEMD cartilage, with increased expression of *Park2,* a known mediator of aggresome formation, and *Ulk3*, an ULK1-independant autophagy inducer (Chin, Olzmann et al. 2010, Braden and Neufeld 2016). In contrast, there was decreased gene expression of the alternative autophagy markers *Eva1a* and *Rab9b* (which is involved in autophagosome-lysosome fusion) in OCD cartilage, suggesting that autophagy may be dysregulated (Hirota, Yamashita et al. 2015, Hu, Li et al. 2016) (Appendix J). This indicates that the regulation of alternative autophagy pathways (which selectively degrade protein aggregates or organelles) may be altered between OCD and SEMD cartilage.

6.1.3 Vesicle trafficking and cilia formation

Upregulated genes in SEMD cartilage (including those annotated with the GO term 'membrane fusion') encoded for SNARE complex components and vesicle transport regulators (Appendix J). These included motor proteins (*Kif5a, Kifc2, Kif17*) syntaxins (*Stx1a, Stx1b, Stx16*) SNAPs (*Napb*) and synaptobrevin (*Vamp1*) (Fukuda 2007). In contrast, genes associated with vesicular transport were downregulated in OCD cartilage, such as synaptotagmins (*Syt8, Syt14, Sytl2*) syntaphilin (*Snph*) and Rab GTPases (*Rab3c, Rab9b, Rab25*). Vesicle trafficking also regulates the assembly and organisation of primary cilia (Hsiao, Tuz et al. 2012) REViGO analysis indicated that cilia organisation (under the umbrella term 'axonemal dynain complex assembly') is an enriched biological theme in SEMD cartilage with increased gene expression of Kif motor proteins, *Fam161a* and *Msn1*.

6.1.4 Regulatory signalling and differentiation

The GO term 'anterior/posterior pattern specification' was enriched in SEMD cartilage compared to both OCD and wild type cartilage. Further analysis of the 65 genes under this umbrella term revealed that many upregulated genes belonged to the HOX transcription factor family with the *Hoxa* (*Hoxa5, Hoxa9, Hoxa13*) *Hoxc* (*Hoxc4, Hoxc5, Hoxc6, Hoxc8*) and *Hoxd* (*Hoxd3, Hoxd4*) gene clusters represented (Appendix J). The role of Hox genes in developmental patterning is well-characterised; however, they have also been shown to have a regulatory role in postnatal chondrocyte maturation (González-Martín, Mallo et al. 2014). The highest upregulated gene *Hoxd3* (12-fold increase) may be a marker of terminal chondrocyte differentiation and promote angiogenesis (Charboneau, East et al. 2005, Okuma, Hirata et al. 2015). WNT signalling also appeared to be perturbed in SEMD cartilage with decreased gene expression of WNT signalling components (*Wnt4*, *Wnt5b, Fzd1*) and increased expression of the WNT signalling inhibitor *Wt1* (Kim, McGarry et al. 2009).

In contrast, *Wt1* and another WNT signalling inhibitor *Dkk1* were downregulated in OCD cartilage, with a 17-fold decrease in OCD cartilage compared to SEMD samples. *Bmp8a, Gdf1, Runx2*, *Runx3*, and the IHH/PTHRP signalling receptors *Ptch1* and *Pth1r* were also significantly downregulated in OCD cartilage compared to wild type controls, suggesting that

regulatory signalling may be altered. Gene expression changes in OCD cartilage were also associated with osteoblast differentiation and bone formation, with decreased expression of *Satb2* and mineralisation regulators such as the SIBLING phosphoproteins osteopontin (*Spp1*) bone sialoprotein (*Ibsp*) and *Dmp1*. Osteoclasts/chondroclasts markers such as tartrate-resistant phosphatase (*Acp5*) and the osteoclast fusion mediator *Ocstamp* were also downregulated, suggesting that cartilage remodelling and bone formation may be perturbed in OCD cartilage.

6.2 Immunoblotting analysis of the unfolded protein response

Transcriptomics profiling had indicated that gene expression of BIP, the master regulator of the classical UPR, was not upregulated in either SEMD or OCD chondrocytes at five days of age. In order to validate this finding at protein level Western blotting was performed on protein extracted from OCD, SEMD and wildtype femoral head cartilage at 3 weeks of age. There was no statistical difference in the protein levels of BiP in cartilage extracted from either SEMD or OCD mice when compared with wild type littermates (Figure 76).

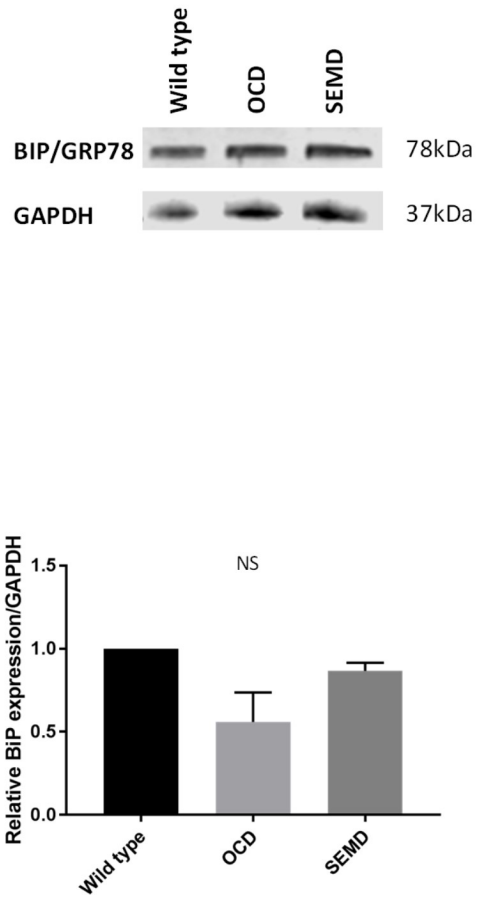

Figure 76 Immunoblotting analysis of BIP expression in OCD and SEMD cartilage

Western blotting of femoral head cartilage from 3 week old mice homozygous for either the SEMD or OCD mutation and wild type littermates. There was no significant difference in the abundance of BIP (relative to GAPDH) in either OCD or SEMD mice compared to wild type controls (n=3).

Key: +/+ (wild type) O/O (homozygous for OCD mutation) S/S (homozygous for SEMD mutation) NS (not significant) Two tailed T-test.

6.3 Immunofluorescent analysis of indian hedgehog signalling

Transcriptional analysis had indicated that regulatory signalling pathways such as the IHH/PTHRP feedback loop may be altered in OCD cartilage. Furthermore, the hedgehog signalling pathway is known to involve the primary cilium and gene expression associated with cilium organisation was unregulated in SEMD cartilage. Immunofluorescence was therefore used to assess the relative abundance and localisation of the secreted mature form of IHH in the growth plates of mice at three weeks of age. IHH is known to be highly expressed by pre-hypertrophic chondrocytes (Gualeni, Facchini et al. 2010) and staining for secreted IHH was greatest in the pre-hypertrophic and hypertrophic zones of wild type cartilage (Figure 77). There was no overt difference in staining intensity for indian hedgehog in OCD cartilage. Staining for indian hedgehog was reduced in SEMD cartilage, with the greatest staining intensity observed on the chondro-osseous border and in the forming secondary ossification centre, indicating that the distribution or anchoring of secreted indian hedgehog may be altered in the SEMD growth plate.

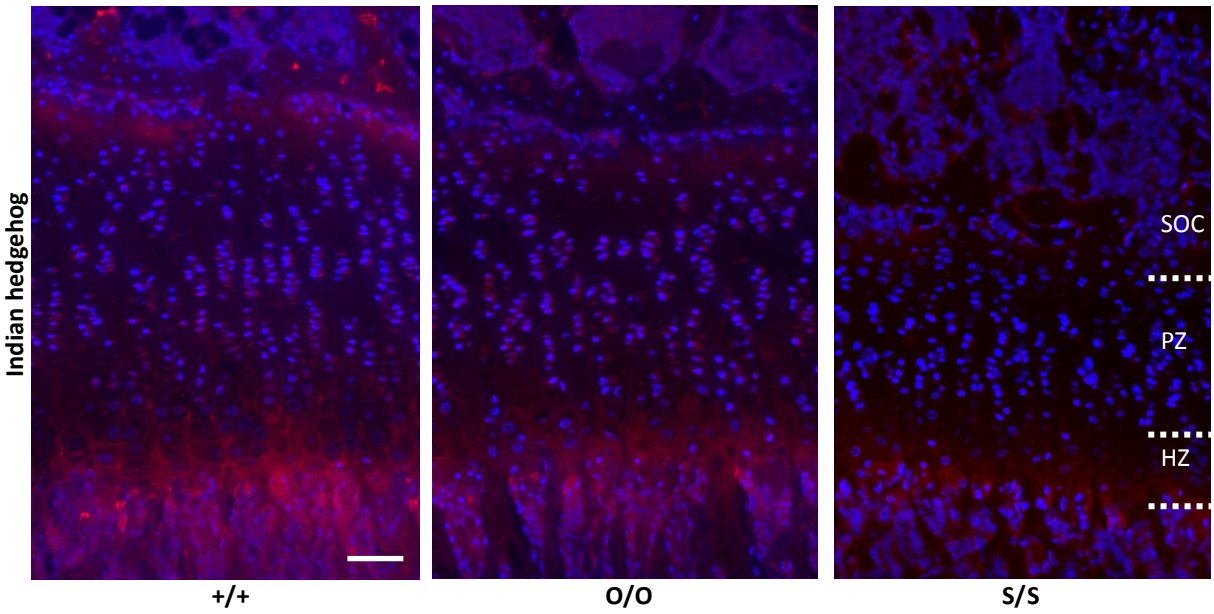

Figure 77 Localisation and abundance of indian hedgehog in OCD and SEMD mice.

Immuno uorescent staining of matching bial growth plate secti ns from male 3 week old wild type, OCD and SEMD mice. The intensity of staining for indian hedgehog was reduced in growth plates from SEMD mice. There was no di erence in staining intensity in growth plates from OCD mice compared to wild type controls.

Key: +/+ (wild type) O/O (homozygous for the OCD muta on) S/S (homozygous for the SEMD muta on) scale bar = 50µm, n=3

6.4 Analysis of autophagic flux

The relative abundance of autophagic vesicles in the growth plates of mice at three weeks of age was assessed with immunofluorescence. LC3B is a well-characterised marker of autophagy, which undergoes lipidation for recruitment to the autophagosome. Immunofluorescent staining for LC3B in wild type controls was mainly cytosolic, with some punctate staining observed, particularly in the early hypertrophic zone (Figure 78) (Srinivas, Bohensky et al. 2008). Resting, proliferative and early hypertrophic chondrocytes in SEMD cartilage exhibited increased punctate staining for LC3B (n=3) compared to wild type controls. In contrast, only proliferative OCD chondrocytes displayed the increased punctate LC3B staining associated with autophagosomes (n=3).

Western blotting and autophagy inhibition was used to assess autophagic vesicle accumulation. Femoral and tibial cartilage was extracted from seven day old mice homozygous for either the OCD mutation and wild type controls. Cartilage explants were treated with the end-stage autophagy inhibitor chloroquine for 0, 1, 3, and 6 hours and analysed by Western blotting and densitometry. The scaffold protein p62 acts as a cargo receptor for ubiquitylated substrates and so is degraded by autophagy (Navone, Genevini et al. 2015). It can therefore be used as a marker of autophagic flux. Western blotting of wild type protein extracts showed significantly increased accumulation of P62 at 3 and 6 hours of chloroquine treatment, consistent with inhibition of basal macroautophagy (Figure 79). The expression level of P62 (relative to GAPDH) was increased in OCD cartilage compared to the wild type control in untreated samples, but P62 abundance did not statistically increase with chloroquine-treatment. This indicated that the increase in autophagosomes in OCD chondrocytes may be due to defective rather than upregulated autophagy or that P62 is not involved in the OCD autophagic pathway.

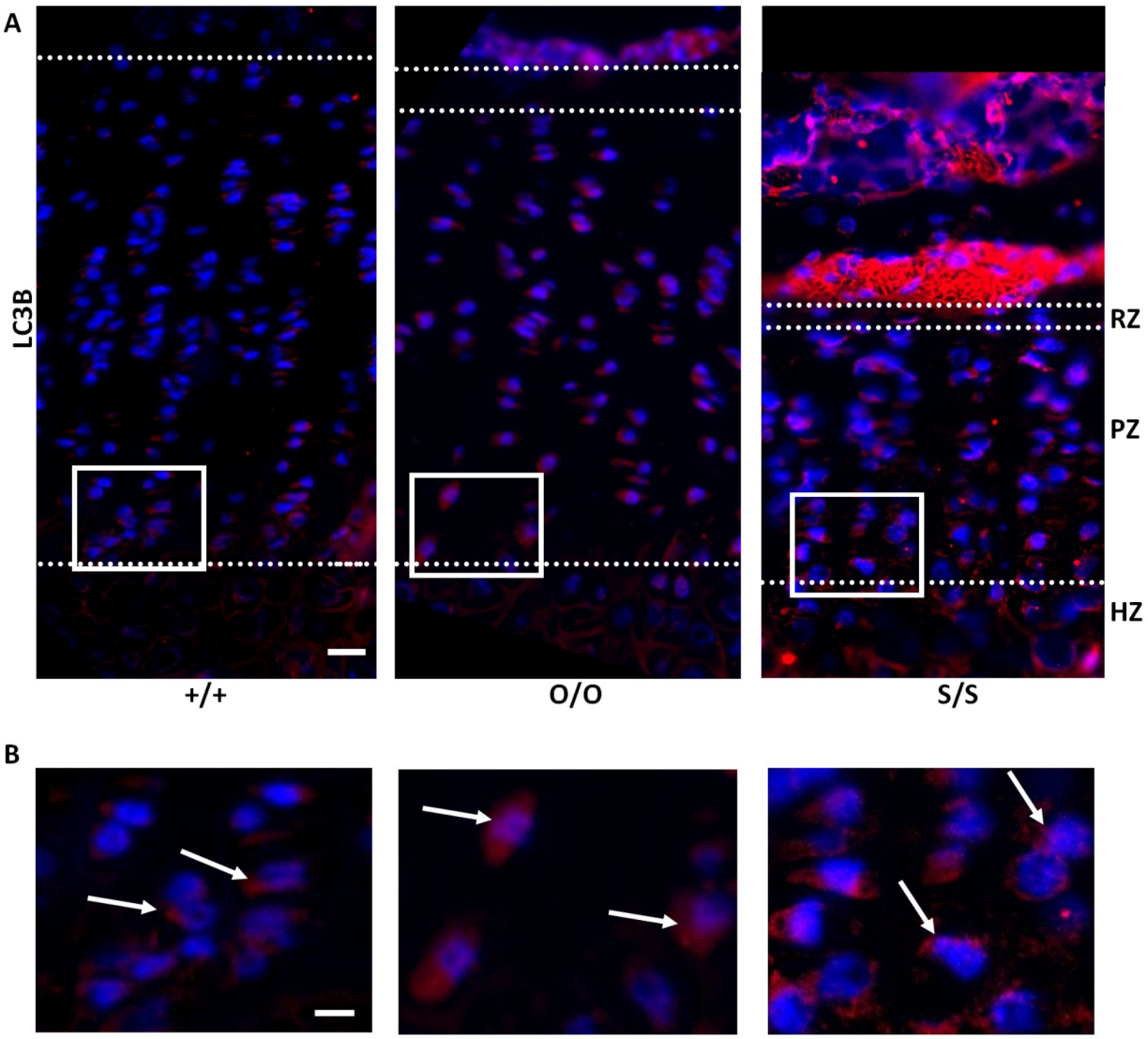

Figure 78 Autophagosome formation in OCD and SEMD cartilage

(A) Immunofluorescent staining for the autophagosome marker LC3B in matching tibial growth plate sections from male 3 week old wild type, OCD and SEMD mice. Increased punctate staining was observed in proliferative OCD chondrocytes and SEMD chondrocytes in the resting, proliferative and early hypertrophic zones (arrows, n=3, scale bar=50µm). **(B)** Magnification of proliferative chondrocytes (white box, scale bar=20µm).

Key: +/+ (wild type) O/O (homozygous for the OCD mutation) S/S (homozygous for the SEMD mutation) RZ (resting zone) PZ (proliferative zone) HZ (hypertrophic zone)

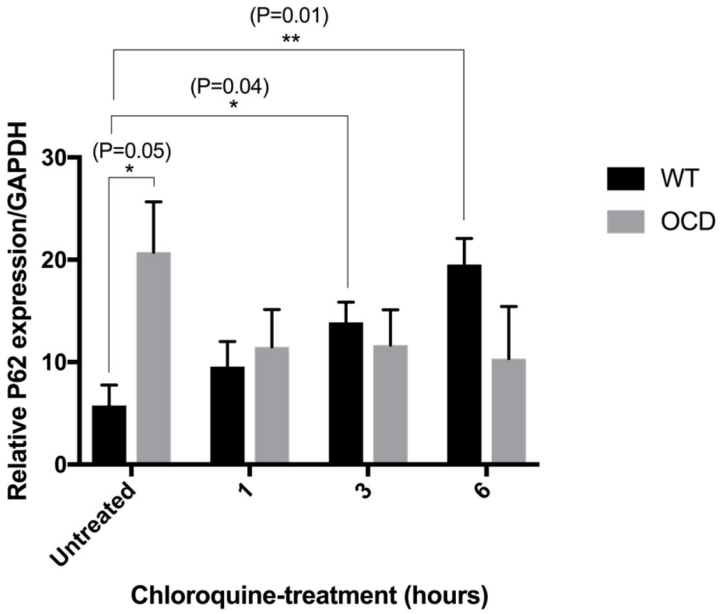

Figure 79 Autophagic flux in OCD cartilage

Densitometry analysis of Western blotting was used to assess P62 accumulation in cartilage explants from wild type and OCD mice at seven days of age. Explants were treated with chloroquine for 0, 1, 3 and 6 hours to inhibit autophagosome-lysosome fusion. P62 accumulation did not occur in OCD chondrocytes, suggesting that autophagy may be impaired (n=3).

6.5 Summary

The aim of this chapter was to identify and compare potential disease mechanisms of the OCD and SEMD disorders. Transcriptomic analysis of RNA at 5 days of age and immunoblotting of protein at 3 weeks of age indicated that the classical UPR is not upregulated in OCD or SEMD cartilage but that SEMD chondrocytes exhibit gene changes associated with mild cellular stress. Comparison of the OCD and SEMD transcriptomes suggested that genes associated with vesicular transport, cilia organisation and regulatory pathways such as WNT signalling are differentially expressed between OCD and SEMD cartilage. Immunofluorescent staining for the secreted indian hedgehog also suggested that the distribution of this signalling molecule is altered in SEMD cartilage. OCD cartilage exhibited decreased expression of genes associated with osteoblast differentiation and cartilage mineralisation suggesting that cartilage calcification may be affected. Furthermore, immunoblotting and immunofluorescence suggested that autophagy may be impaired in OCD cartilage.

Chapter 7. Discussion

The aim of this thesis was to characterise and compare two knock-in mouse models with mutations in the C-type lectin domain of aggrecan. These two mutations are only 36 base pairs apart but result in two very different phenotypes; one with severe short stature and a range of skeletal abnormalities (spondyloepimetaphyseal dysplasia) and one with mild short stature and osteochondritis dissecans (familial osteochondritis dissecans). There are a number of well-studied aggrecan models in the literature, however all (except the A1946V *Acan* mouse) are known to be caused by either reduced aggrecan abundance or defective proteoglycan sulfation in the growth plate. Therefore, although they provide an invaluable insight into aggrecan's roles in growth plate organization, regulatory signalling, chondrocyte survival and differentiation (Wai, Ng et al. 1998, Lauing, Cortes et al. 2014) they cannot be used to assess the effect of human aggrecan mutations. The work presented in this thesis is therefore the first in-depth *in vivo* study of aggrecan mutations known to cause human genetic disorders.

7.1. The homozygous D1983N *Acan* mouse recapitulates the SEMD phenotype

Mice homozygous for the D1983N *Acan* mutation exhibited extreme short stature from birth indicating that the onset of SEMD occurs during foetal development, although interestingly there was no overt effect on skeletal patterning at birth and no statistical effect on pup viability. SEMD is recessive in the human population, consistent with the mouse SEMD model in which homozygosity for the D1983N *Acan* allele was required to recapitulate the SEMD phenotype (Tompson, Merriman et al. 2009). The SEMD mouse replicated the human SEMD disproportionate short stature phenotype with characteristic skeletal abnormalities such as a bell-shaped rib cage, brachydactyly, irregular epiphyses, hip dysplasia, mid-face hypoplasia and relative mandibular prognathism (Tompson, Merriman et al. 2009). The reduction in size of both the long bones and craniofacial bones indicated that the SEMD mutation affects both endochondral and intramembranous ossification. The mouse phenotype did differ from the human phenotype in the degree of spinal involvement. All three of the human patients exhibited mild thoracic scoliosis and a range of other spinal malformations including cervical-vertebral clefts. Radiographs and skeletal preps of the SEMD mouse did not display any visible cervical-vertebral clefts. However, a third of the mice

displayed mild thoracic scoliosis at three weeks of age, with the incidence of spine curvature increasing to 3 in 5 by 9 weeks of age. The degree of spine curvature was very variable and although vertebral wedging was observed in the most severely curved spine, it was not possible to assess a greater number of mice. A more in-depth analysis using *in vivo* micro CT imaging would therefore be necessary to assess the progression of scoliosis in individual mice throughout post-natal development. However, it was not within the scope of this initial study to investigate spinal abnormality during the aging process and so no further research was conducted after this point. The incomplete penetrance of the spinal phenotype may be due to the difference in posture and gait between bipedal upright humans and quadrupedal mice, which will alter the physical force and pressure placed on the spine during development. As examples, severe kyphoscoliosis is not observed in 100% of FGFR3 null mice and there is great debate as to whether rodent tail models accurately model the human lumbar spine in intervertebral disc degeneration (Gao, Chen et al. 2015, Daly, Ghosh et al. 2016).

It was not possible to use homozygous mutant breeding crosses during this study due to a high level of infanticide. The increased pup survival which occurred in crosses which had an additional heterozygote mutant female suggested that homozygous breeding pairs struggled to care for their offspring. Furthermore, the jaw misalignment caused by the mandibular prognathism resulted in a very high incidence of malocclusion. Mouse incisors (unlike humans) have an open root and grow continuously throughout the animal's lifetime. Rodents must therefore gnaw in order to grind these teeth down, which is impaired when the jaw is not aligned correctly. Malocclusion impairs the animal's ability to eat, impacting survival and growth unless the teeth are clipped upon weaning and softer food provided. This provides an important example of the need to be aware of species-specific downstream effects of a mutation.

7.2. The homozygous V2019M *Acan* mouse recapitulates the short-stature OCD phenotype

Homozygosity for the OCD mutation (V2019M *Acan*) also had no effect on pre-natal lethality, consistent with clinical observations of human fOCD patients who do not report higher incidence of miscarriage (Stattin personal communication 2017). However, in contrast

to SEMD mice, mice homozygous for the OCD mutation were not statistically smaller at birth and did not exhibit altered cranial vault morphology, indicating that this missense aggrecan mutation does not grossly affect skeletal development or intramembranous ossification. Furthermore, although this disorder is dominantly-inherited in the human population (Stattin, Wiklund et al. 2010) homozygosity for the OCD mutation was necessary to replicate the short stature fOCD phenotype in mice. This has previously been reported in other mouse models of skeletal dysplasia such as the homozygous D469del COMP mouse model of dominantly-inherited human pseudoachondroplasia (Suleman, Gualeni et al. 2012). In contrast to the human fOCD phenotype, the homozygous V2019M *Acan* mouse did not display any other skeletal abnormalities, such as hip dysplasia, scoliosis or loose bodies in the joint spaces, although radiographic assessment was limited by the resolution of the X-ray machine available. Histological analysis also did not indicate the development of characteristic OCD lesions in mice homozygous for the mutation. However, proteoglycan content in the articular cartilage progressively declined up to 6 months of age, suggesting that these mice may be susceptible to joint degeneration due impaired resistance to mechanical loading. It is therefore possible that OCD or early-onset osteoarthritis may occur in aged OCD mice as observed with genetically-susceptible OA models such as the STR/ort mouse (Staines, Poulet et al. 2017). It may also be necessary to mechanically-challenge the mice by providing treadmills (Kotwal, Li et al. 2012) in order to cause the formation of lesions in the articular surface.

7.3. OCD and SEMD mice exhibit intervertebral disc degeneration

Interestingly, both the OCD and SEMD mouse models exhibited early-onset intervertebral disc degeneration, which has not previously been reported in human patients but has been shown in other conditions in the aggrecanopathy phenotypic spectrum (Nilsson, Guo et al. 2014, Gkourogianni, Andrew et al. 2017, Tatsi, Gkourogianni et al. 2017). Scoring for changes in IVD structure indicated that the nucleus pulposus was the primary source of degeneration, consistent with current literature in this area (Inoue and Espinoza Orías 2011). Initial degeneration of the aggrecan-rich nucleus pulposus is characterised by proteoglycan loss, which causes decreased resistance to mechanical loading in the spine (Inoue and

Espinoza Orías 2011). It is therefore unsurprising that mice homozygous for mutations which cause delayed secretion of aggrecan would be susceptible to IVD degeneration.

7.4. Aggrecan trafficking is impaired in OCD and SEMD cartilage

Histological and ultrastructural analysis indicated that both the OCD and SEMD mutations cause retention of mutant aggrecan within the endoplasmic reticulum, delaying trafficking of the core aggrecan protein to the Golgi. This is not surprising as the G3 domain is known to facilitate the secretion and folding of aggrecan and mutations in this domain have previously been shown to cause abnormal trafficking of the aggrecan polypeptide to the nucleus (Chen, Wang et al. 2001). This is however not consistent with previous *in vitro* analysis which suggested that the SEMD mutation does not affect aggrecan secretion (Tompson, Merriman et al. 2009). However, this analysis was performed using recombinant G3 domains rather than full length aggrecan and so the data presented in this thesis is likely to have greater biological relevance. Studies of the human V2303M *ACAN* OCD mutation have provided conflicting evidence on its effect on protein secretion. This appeared to vary depending on whether the study investigated early stage development *in vitro* (MSC or iPSC pellet culture, impaired secretion) or late-stage cartilage (arthroplasty cartilage, no effect on secretion) possibly reflecting that while aggrecan secretion is delayed by the OCD mutation it is not completely impaired. Transcriptomic analysis suggested that vesicle-mediated transport through exocytosis is altered in both OCD and SEMD cartilage. Aggrecan is known to be trafficked through the exocytotic pathway (Chen, Wang et al. 2001) and so this may reflect impaired constitutive or calcium-mediated regulated exocytosis trafficking (Kreutzberger, Kiessling et al. 2017).

7.5. Intracellular retention of mutant aggrecan does not elicit the UPR in OCD or SEMD cartilage

Studies of other skeletal dysplasia mouse models has shown that the intracellular retention of mutant protein often elicits the unfolded protein response (UPR) (Pirog-Garcia, Meadows et al. 2007, Nundlall, Rajpar et al. 2010). Transcriptional changes in SEMD cartilage suggested mild cellular stress and the rate of chondrocyte proliferation was decreased, a known downstream effect of ER stress (Gualeni, Rajpar et al. 2013). Furthermore, increased/spatially dysregulated cell apoptosis was observed in both OCD and SEMD cartilage. However, the classical UPR was not upregulated in either mouse model. This was confirmed by not only transcriptional and western blotting data but by ultrastructural analysis, which did not show any ER fragmentation or free ribosomes characteristic of endoplasmic reticulum stress (Kudelko, Chan et al. 2016). The master UPR regulator and chaperone BIP is known to preferentially bind hydrophobic residues, which may become exposed in misfolded proteins (Blond-Elguindi, Cwirla et al. 1993, Knarr, Gething et al. 1995). It is therefore possible that the OCD and SEMD mutations do not cause the exposure of hydrophobic residues and so do not cause the dissociation of BIP from ATF6, IRE1 or PERK. Mouse models of skeletal dysplasia without UPR have been reported (Suleman, Gualeni et al. 2012) and it is possible to hypothesise that cells may also be able to adapt to constant ER stress without eliciting the UPR.

7.6. The macroautophagy pathway is altered in OCD and SEMD cartilage

Histological and immunoblotting analysis suggested that autophagy may be dysregulated in OCD cartilage. Unfortunately due to difficulties in breeding mice homozygous for the SEMD mutation it was not possible to assess whether the increase in autophagosomes observed in SEMD cartilage was due to an upregulation or impairment of autophagy. Further work will therefore be required to determine whether autophagy is differentially regulated between OCD and SEMD chondrocytes. In order to assess whether increased mutant protein degradation might ease the metabolic burden of the cell and allow improved secretion of ECM

molecules, a brief pilot drug treatment study on limb explants was conducted. Carbamazepine (CBZ) treatment was previously shown to ameliorate the phenotype of metaphysical chondrodysplasia, Schmid type (MCDS) by acting through both autophagic and proteosomal pathways to degrade misfolded protein (Mullan, Mularczyk et al. 2017). CBZ treatment had no statistical difference on bone growth in either the OCD (n≥5) or SEMD (n=2) model (Appendix K). This suggested that drug amelioration of the autophagic and proteasomal pathways does not ameliorate the phenotype of these disorders. However, due to a lack of samples and a flawed experimental design, a larger more rigorous study would be required to make a scientific conclusion about the efficacy of this drug in these models. It was not possible to use commercial CBZ pellets for *in vivo* subcutaneous implantation due to restrictions on the minimum weight required for animals to undergo the procedure. However, it may be possible to utilise a gavaging technique to apply the drug in order to radiographically and histologically analyse post-natal bone growth *in vivo.*

7.7. Altered matrix composition in OCD and SEMD cartilage may impair chondrocyte differentiation

In addition to the intracellular stress caused by the delayed secretion of mutant aggrecan it was also important to consider the extracellular effect of the mutant aggrecan once it was secreted into the matrix. Immunofluorescent and Western Blotting analysis had indicated that the expression of some key ECM structural proteins such as COMP was abnormal in both OCD and SEMD cartilage. This is consistent with current literature as the G3 domain is known to mediate matrix organisation by the binding of aggrecan with other extracellular matrix molecules such as COMP and matrilin 3 (Olin, Morgelin et al. 2001, Lundell, Olin et al. 2004). A reduction in aggrecan abundance within the matrix and altered G3 interactions are therefore likely to affect matrix composition. In addition to this, the SEMD mutation is situated in the CLD calcium coordinating loops, which facilitate calcium-dependent binding (Tompson, Merriman et al. 2009) and the OCD mutation is found in the CLD ligand-interaction site (Tompson, Merriman et al. 2009, Stattin, Wiklund et al. 2010). *In vitro* studies have also shown that both the OCD and SEMD mutations disrupt binding with ECM molecules such as fibulin 1 and tenescin R (Tompson, Merriman et al. 2009, Stattin,

Wiklund et al. 2010). This altered matrix composition is likely to affect not only the structural integrity of the ECM but important regulatory signalling pathways necessary for correct differentiation within the growth plate. Aggrecan is particularly important for proper signalling as it binds to indian hedgehog through its GAG chains. The efficacy of this binding is affected by the degree of sulfation and so altered aggrecan abundance in the ECM would alter the distribution of secreted IHH within the growth plate. This is illustrated by mouse models with defects in proteoglycan sulfation such as the *dtd* mouse which exhibits altered IHH signalling and abnormal chondrocyte differentiation (Gualeni, Facchini et al. 2010). Furthermore, the aggrecan-null nanomelic chicken, which expresses a truncated aggrecan precursor, is characterised by altered IHH, BMP and FGF signalling causing reduced proliferation and premature hypertrophic maturation (Domowicz, Cortes et al. 2009). Interestingly, transcriptomic and immunofluorescent analysis of OCD and SEMD cartilage suggested that a number of signalling pathways including WNT and IHH/PTHRP may be altered between these two disorders. In addition to this, the formation of cilia (a fundamental structure in regulatory signalling such as hedgehog) was enriched in the SEMD transcriptome. Cell signalling and signal transduction can attenuate many downstream pathways including transcription, cell cycle and chondrocyte differentiation. Histological analysis indicated that both OCD and SEMD mice have a shortened growth plate compared to wild type controls. In addition to this, SEMD cartilage exhibited defective chondrocyte proliferation and a proportionally expanded growth plate, indicating that SEMD chondrocytes may exit the cell cycle early and enter hypertrophy prematurely. Histological analysis of OCD and SEMD cartilage at birth had indicated that mineralisation was not grossly affected. However, transcriptomic changes in 5 day old cartilage suggested that processes associated with cartilage ECM remodelling and bone formation such as osteoblast differentiation, chondroclast maturation and mineralisation may be disrupted in OCD cartilage. It is possible however that histological techniques may not be sufficiently sensitive to accurately assess calcium calcification. Future work could therefore be conducted using microCT to assess trabecular and cortical bone formation in mice after growth cessation. It would also be essential to assess the gene expression of key markers such as collagen type II, collagen type X and osteopontin using *in situ* hybridisation in order to confirm whether chondrocyte differentiation is disrupted in OCD and SEMD cartilage.

In summary, this thesis characterises the first *in vivo* models of skeletal dysplasia caused by aggrecan mutations. Patho-molecular analysis thus far suggests that the disease

mechanisms of these two disorders are distinct, however, both are characterised by altered matrix organisation, disrupted signalling and impaired differentiation.

Appendices

c.DNA	Variant	Exon	Domain	Bone age	Other phenotypic features	
t(10;15)(q22;q24)	n/a	n/a	n/a	No data	Propor onate short stature	Crippa et al 2018
c.-7-2A>C	n/a	int1	n/a	No data	SEDK	Sentchordi-Montane et al 2018
c.6_13delCACTTTAC	p.T3Lfs*21	2	-	No data	Pectus excavatum	Hu et al 2017
c.61G>T	p.E21*	2	-	Advanced	Frontal bossing	Gkourogianni et al 2017
c.223T>C	p.W75R	3	G1	Advanced	IDD, early-onset OA	
c.272delA	p.R93Afs*	3	G1	Advanced, premature growth cessa on	Brachydactyly, midface hypoplasia, progna-thism, IDD	Gkourogianni et al 2017, Nilsson et al 2014
c.371G>A	p.R124H	3	G1	Delayed	Brachydactyly, coxa valga, hyperlordosis	Sentchordi-Montane et al 2018
c.492C>G	p.Y164*	4	G1	Advanced	IDD, early-onset OA	Gkourogianni et al 2017
c.532A>T	p.N178Y	4	G1	Normal/slightly advanced	No data	
c.661delT	p.Y221Mfs*10	5	G1	No data	No data	Hu et al 2017
c.742G>A	p.A248T			Normal	Brachydactyly, coxa valga	Sentchordi-Montane et al 2018
c.903G>C	p.W301C	6	G1	Normal/slightly advanced	Midface hypoplasia, frontal bossing, IDD, ear-ly-onset OA	
c.916A>T	p.S306C	6	G1	Advanced	IDD	Gkourogianni et al 2017
c.1047_1048delinsAC	p.Y349*	6	G1	Normal/slightly advanced	Brachydactyly, frontal bossing, midface hypo-plasia, anteverted ears	
c.1117_1120delCAGA	p.T374*	7	IGD	No data	No data	Hu et al 2017
c.1443G>T	p.E415*	7		Normal/slightly advanced	Midface hypoplasia, IDD, early-onset OA	Gkourogianni et al 2017

Appendix A (i) Variants and phenotypic features of the aggrecanopathies

c. DNA	Variant	Exon	Domain	Bone age	Other phenotypic features	
c.1425delA	p.V478Sfs*	8	G2	Normal/slightly advanced	Early-onset OA	Gkourogianni et al 2017
c.1526C>A	p.S509*	8	G2	Normal/slightly advanced	Early-onset OA	Gkourogianni et al 2017
c.1598C>T	p.T533I	9	G2	No data	SEDK	Sentchordi-Montane et al 2018
c.1608C>A	p.Y536*	9	G2	Normal/slightly advanced	Broad toes, short thumbs, midface hypoplasia, posteriorly rotated ears, lumbar lordosis, early-onset OA	Van der Steen 2017
c.1744delT	p.F582fs*69	10	G2	Advanced	IDD	Dateki et al 2017
c.1930G>A	p.G644S	10	G2	Normal	Brachydactyly, short femoral necks	Sentchordi-Montane et al 2018
c.1948G>A	p.V650M	10	G2	Delayed	Brachydactyly	Sentchordi-Montane et al 2018
c.2026+1G>A	n/a	int10	G2	Advanced, premature growth cessa on	Brachydactyly, midface hypoplasia	Gkourogianni et al 2017, Nilsson et al 2014
c.2218A>T	p.T740S	12	KS	Normal	Brachydactyly	Sentchordi-Montane et al 2018
c.2369C>G	p.S790*	12	KS	Advanced	Brachydactyly, hyperlordosis	Sentchordi-Montane et al 2018
c.4657G>T	p.E1553*	12	CS	Normal/slightly advanced	Midface hypoplasia, IDD,,early-onset OA	Gkourogianni et al 2017
c.4762_4765del	p.G1588fs*	12	CS	Advanced	Broad toes, midface hypoplasia, posteriorly rotated ears, joint pain	Van der Steen et al 2017
c.4852C>T	p.Q1618X	12	CS	Slightly delayed	Midface hypoplasia, retrognathia, scoliosis, IDD, early-onset OA	Tatsi et al 2017
c.5391delG	p.G1797Gfs*	12	CS	Advanced, premature growth cessa on	Midface hypoplasia, possible early-onset OA	Gkourogianni et al 2017, Quintos et al 2015

Appendix A (ii) Variants and phenotypic features of the aggrecanopathies

c. DNA	Variant	Exon	Domain	Bone age	Other phenotypic features	
c.6404delC	p.A2135Dfs	12	CS	Advanced	Midface hypoplasia	Tatsi et al 2017
c.6142C>G	p.P2048A	12	CS	Normal	Brachydactyly	Sentchordi-Montane et al 2018
c.7153G>A	p.E2385K	15	G3	Normal/slightly advanced	IDD, early-onset OA	Gkourogianni et al 2017
c.7203G	p.W2401*	15	G3	Normal/slightly advanced	IDD, early-onset OA	Gkourogianni et al 2017
c.7269delG	p.E2424fs*5	15	G3	Advanced	Brachydactyly	Sentchordi-Montane et al 2018
c.7276G>A	p.E2426K	16	G3	Normal	Brachydactyly, cone-shaped epiphysis	Sentchordi-Montane et al 2018
c.7276G>T	p.E2426*	16	G3	Normal/slightly advanced	Short femoral neck	Gkourogianni et al 2017
c.7342G>T	p.G2448R	16	G3	No data	Brachydactyly	Sentchordi-Montane et al 2018

Appendix A (iii) Variants and phenotypic features of the aggrecanopathies

Appendix B (i) Antibodies and dilutions

Primary antibody	Dilution for IHC	Dilution for Western Blot	Supplier
Monoclonal rabbit against aggrecan	1:400	n/a	Professor Tim Hardingham, University of Manchester
Polyclonal goat against BIP	n/a	1:500	Santa Cruz (SC105)
Monoclonal rat against BrdU	1:100	n/a	Abcam (AB6326)
Polyclonal rabbit against collagen type II	1:500	n/a	Abcam (AB34712)
Monoclonal mouse against collagen type II	n/a	1:200	Abcam (AB185430)
Polyclonal guinea pig against collagen type IX	1:500	n/a	Professor Frank Zaucke, Orthopedic University Hospital Friedrichsheim
Polyclonal rabbit against collagen type X	1:500	n/a	Professor Karl Kadler, University of Manchester
Polyclonal rabbit against COMP	1:100	1:1000	Genetex (GTX14515)
Monoclonal mouse against GAPDH	n/a	1:40 000	Millipore (MAB374)
Polyclonal rabbit against indian hedgehog	1:100	n/a	Abcam (AB39634)
Polyclonal rabbit against LC3B	1:100	n/a	Cell signaling (2775S)
Polyclonal goat against matrilin 3	1:500	n/a	R&D (AF3357)
Monoclonal mouse against P62	n/a	1:10	Abnova (H00008878-M01)

Secondary antibody	Dilution for IHC	Dilution for Western Blot	Supplier
Polyclonal goat anti-rabbit IgG (H+L) Alexafluor 594	1:200	n/a	ThermoFisher Scientific (A11012)
Polyclonal donkey anti-goat IgG (H+L) Alexafluor 488	1:200	n/a	ThermoFisher Scientific (A11055)
Polyclonal goat anti-guinea pig IgG (H+L) Alexafluor 488	1:200	n/a	ThermoFisher Scientific (A11073)
Polyclonal donkey polyclonal anti-rat IgG (H+L) Alexafluor 488	1:200	n/a	ThermoFisher Scientific (A21208)
IRDye 800CW goat anti-rabbit IgG (H + L)	n/a	1:5000	Licor (P/N 925-32211)
IRDye 680RD goat anti-mouse IgG (H + L)	n/a	1:5000	Licor (P/N 925-68070)
IRDye 800CW donkey anti-goat IgG (H + L)	n/a	1:5000	Licor (P/N 925-32214)

Appendix B (ii) Immunofluoresence secondary antibody controls (no primary antibody)

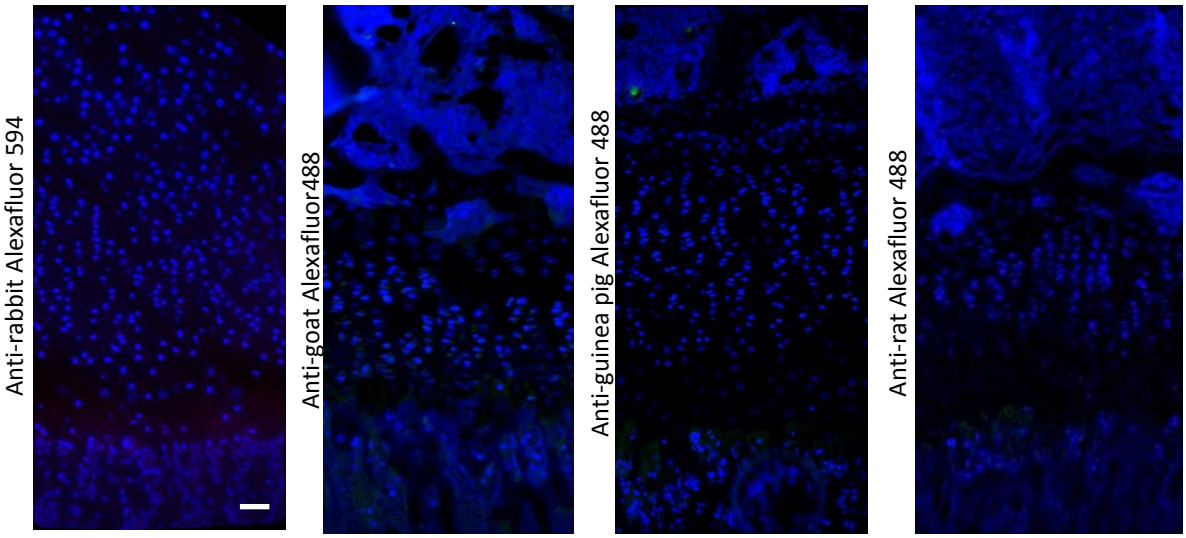

scale bar = 50µm

Appendix C Solutions

Blocking buffer	5% bovine serum albumin in PBS-T
Borate buffer (0.1M)	30.9g boric acid 13.5ml 10M NaOH dH_2O to 1L pH adjusted to 8.5
Buffer I (Sequential extraction)	0.15M NaCl 50mM Tris pH adjusted to 7.4 protein inhibitors added before use
Buffer II (Sequential extraction)	1M NaCl 50mM Tris 10mM EDTA pH adjusted to 7.4 protein inhibitors added before use
Buffer III (Sequential extraction)	4M GuHCl 50mM Tris 10mM EDTA ph adjusted to 7.4 protein inhibitors added before use
Acid alcohol (1%)	990ml 70% ethanol 10ml hydrochloric acid

Alcian Blue	15mg Alcian Blue 8GX 80ml 95% EtOH 20ml glacial acetic acid pH adjusted to 0.75
Alizarin Red S	50mg/L Alizarin Red S 2% (w/v) KOH)
Citric buffer	10mM citric acid 0.05% Tween 20 pH adjusted to 6.0
Lysis buffer (hotshot)	25 mM NaOH 0.2 mM EDTA pH8.0
Neutralising buffer (hotshot)	40 mM Trizma Hydrochloride pH 5.0
Maintenance media	500ml DMEM F-12 10% fetal bovine serum 50U/ml penicillin 50µg/ml streptomycin 50µg/ml non-essential amino acids 2µl/ml L-ascorbic acid 2-phosphate sesquimagnesium salt
PBS	1 PBS tablet/200ml
PBS-T	1 PBS tablet/200ml 0.1% (v/v) Tween-20

RIPA buffer	10mM Tris pH7.4
	1% sodium deoxycholate
	150mM NaCl
	0.1% SDS
SDS-PAGE loading buffer	4ml 1.5M Tris-Hcl (pH7 6.8)
	50% glycerol
	2g sodium dodecyl sulfate
	1ml 1% bromophenol blue
	dH_2O to 20ml
TAE buffer	242 g Tris-base
	57.1 mL glacial acetic Acid 100 mL 0.5 M EDTA pH 8.0 dH_2O to 1L
Toluidine Blue	0.04g Toluidine Blue
	100ml 0.1M sodium acetate buffer (pH3.75-4.25)
Transfer buffer (20x)	1M Tris
	0.77M glycine
	25mM SDS
Transfer running buffer	5% transfer buffer (20x)
	20% methanol

Trap staining	0.5ml Fast Garnet GBC base solution
solution	0.5ml sodium nitrite solution
	45ml pre-warmed (37^{o}C) distilled water
	0.5ml Naphthol AS-BI phosphate solution
	2ml acetate solution
	1ml tartrate solution
Wash solution (sequential extraction)	96% EtOH:PBS 9:1 ratio

Appendix D(i) Primer sequences

Primer	Sequence (5’ to 3’)
D115.2	GTGCATAGGGCTTCTGTAGTAAGG
5182LRPCR2	GTTGTGCCCAGTCATAGCCGAATAG
D115.3	AAATGAATCCTTGAGGTTTATG
D115.4	GCCCATGACTTTCATCTCC
SD24	CTAATGTTGTGGGAAATTGGAGC
SD25	CTCGAGGATAACTTGTTTATTGC
P12	GGCTGGATAGACTTTACC
P13	GGTATGACTTGGCTAGAC
SY01.14	GAAGGCTCCTCTTGGGCTTAG
LRPCRneo1	AATGGGCTGACCGCTTCCTCGTGCTTT
SY01.15	ACAGGGAGCTAGAGGAAG
SY01.16	GCTGTCACACCTTCATTTCC

Appendix D(ii) PCR thermocycler programme

Step	Temperature (°C)		Time (minutes)	Number of cycles
Initial denaturation	95		5	1
Denaturation	95		1	30
Primer annealing	D115.3/D115.4	53	1	
	P12/P13	53		
	SD24/SD25	58		
	SY01.15/SY01.16	56		
Elongation	72		1	
Elongation	72		5	1

Appendix E Embedding programme

70% ethanol	1 hour
90% ethanol	45 minutes
95% ethanol	45 minutes
100% ethanol	45 minutes
100% ethanol	45 minutes
100% ethanol	45 minutes
xylene	30 minutes
xylene	30 minutes
xylene	30 minutes
paraffin wax	1 hour
paraffin wax	1 hour

Appendix F(i) Linistat linear stainer programme: haematoxylin and eosin

100% ethanol	single bucket
90% ethanol	single bucket
70% ethanol	single bucket
50% ethanol	single bucket
Running tap water	single bucket
Harris' modified haematoxylin	single bucket
Running tap water	single bucket
1% acid alcohol	single bucket
Running tap water	single bucket
Eosin Y	single bucket
Running tap water	single bucket
50% ethanol	single bucket
70% ethanol	single bucket
90% ethanol	single bucket
100% ethanol	single bucket

Appendix F(ii) Linistat linear stainer programme: toluidine blue

100% ethanol	single bucket
90% ethanol	single bucket
70% ethanol	single bucket
50% ethanol	single bucket
Running tap water	single bucket
Toluidine blue	double bucket
Running tap water	single bucket
Nuclear fast red	double bucket
Running tap water	single bucket
50% ethanol	single bucket
70% ethanol	single bucket
90% ethanol	single bucket
100% ethanol	single bucket

Appendix G (i) BCA assay protein standards

Vial	Diluent volume (µl)	source and volume of BSA (µl)	final BSA concentration (µg/ml)
A	0	300 (stock)	2000
B	125	375 (stock)	1500
C	325	325 (stock)	1000
D	175	175 (vial B)	750
E	325	325 (vial C)	500
F	325	325 (vial E)	250
G	325	325 (vial F)	125
H	400	100 (vial G)	25
I	400	0	0

(ii) REVERT total protein stain

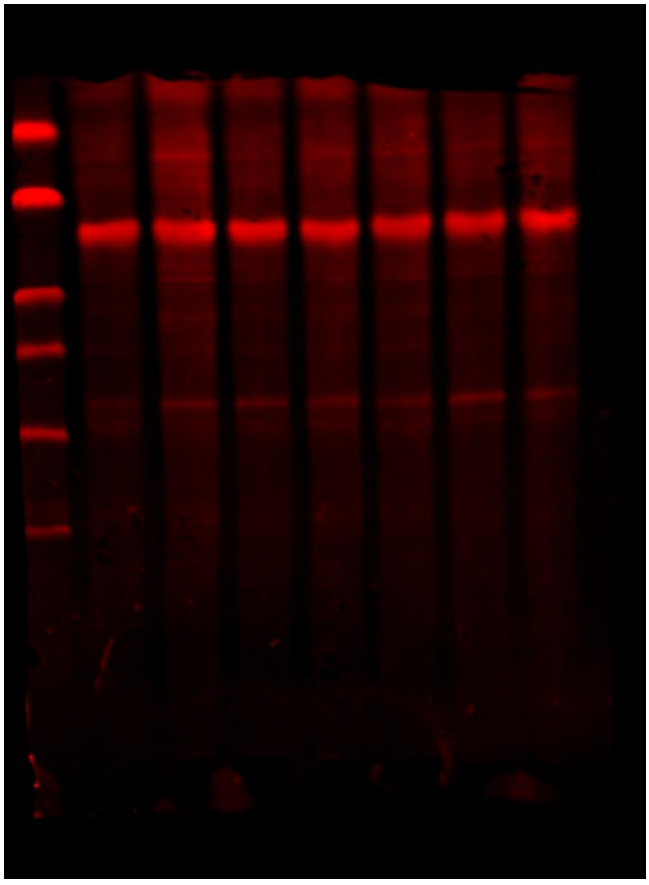

Appendix H(i) Representative Agilent 2100 Bioanalyser results

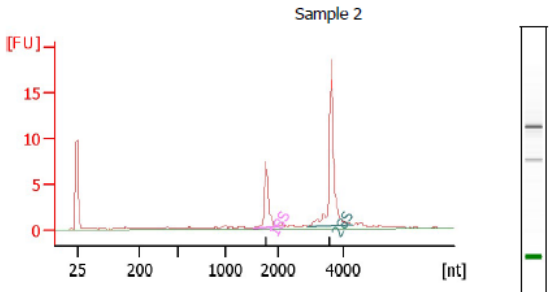

Overall Results for sample 2 : **Sample 2**

RNA Area:	44.3
RNA Concentration:	45 ng/µl
rRNA Ratio [28s / 18s]:	2.7
RNA Integrity Number (RIN):	9.2 (B.02.02)

Fragment table for sample 2 : **Sample 2**

Name	Start Size [nt]	End Size [nt]	Area	% of total Area
18S	1,546	2,045	7.3	16.6
28S	2,937	4,283	19.8	44.7

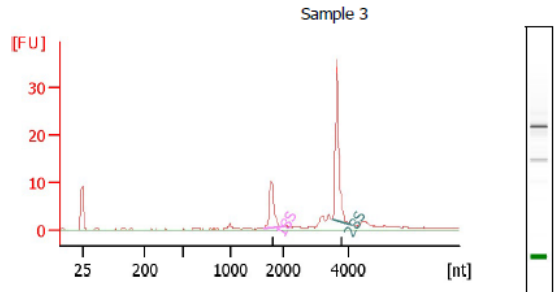

Overall Results for sample 3 : **Sample 3**

RNA Area:	73.1
RNA Concentration:	74 ng/µl
rRNA Ratio [28s / 18s]:	2.3
RNA Integrity Number (RIN):	9.1 (B.02.02)

Fragment table for sample 3 : **Sample 3**

Name	Start Size [nt]	End Size [nt]	Area	% of total Area
18S	1,628	2,021	12.3	16.8
28S	3,508	4,139	28.0	38.3

Appendix H(ii) Principal component analysis (PCA)

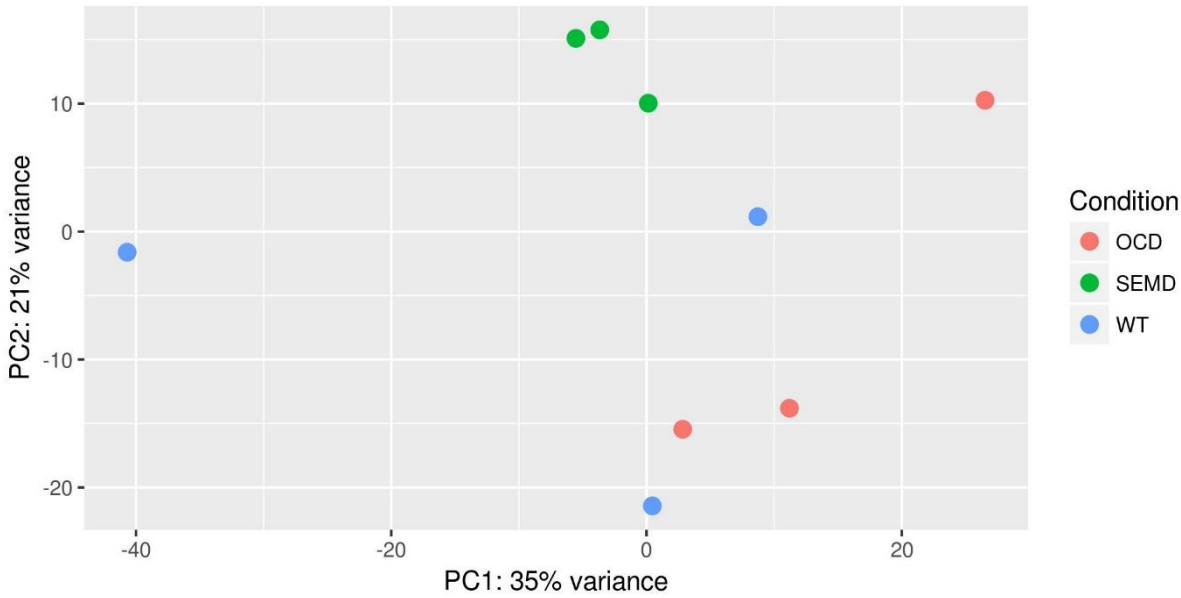

A

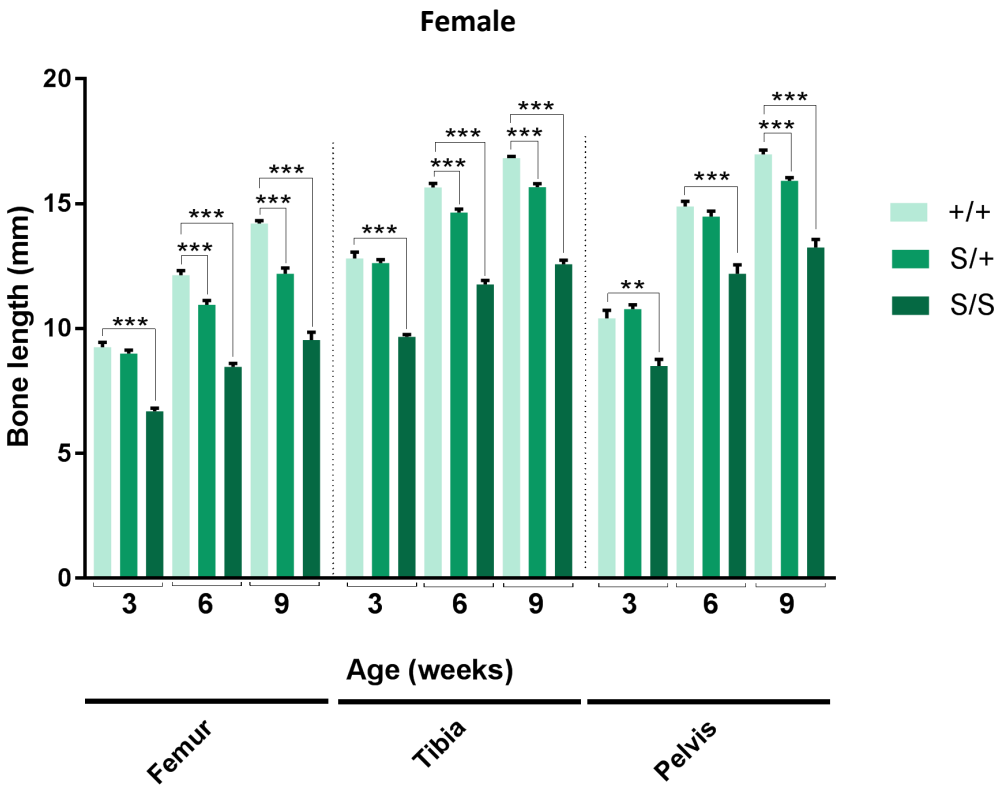

B

Age (weeks)		+/+	S/+	S/S
Femur (mm) ± SEM	3	9.25±0.20	9.00±0.14	**6.69±0.13** ***
	6	12.14±0.18	**10.95±0.18** ***	**8.47±0.14** ***
	9	14.21±0.11	**12.19±0.23** ***	**9.54±0.31** ***
Tibia (mm) ± SEM	3	12.81±0.25	12.63±0.14	**9.67±0.09** ***
	6	15.66±0.16	**14.64±0.15** ***	**11.77±0.16** ***
	9	16.83±0.06	**15.67±0.13** ***	**12.59±0.15** ***
Pelvis (mm) ± SEM	3	10.41±0.33	10.78±0.18	**8.51±0.26** **
	6	14.89±0.21	14.49±0.22	**12.20±0.36** ***
	9	16.98±0.18	**15.92±0.13** ***	**13.26±0.32** ***

Appendix I (i) Morphometric analysis of female SEMD mice.

Tibia, femur and pelvic (illium and ischium) bone lengths were measured at 3, 6 and 9 weeks of age in female mice of all 3 genotypes. **(A)** The average femur, bia and pelvis lengths of mice homozygous for the muta on was reduced, reaching 67.1%, 74.8% and 78.1% of wild type bone lengths respectively by 9 weeks. The average femur, bia and pelvis lengths of mice heterozygous for the muta on was reduced to 85.8%, 93.1% and 93.8% of wild type bone lengths respectivel by 9 weeks. **(B)** Numeric data used for the generaon of graph A.

Key: +/+ (wild type) S/+ (heterozygous for the muta on) S/S (homozygous for the muta on) **p>0.01, ***p>0.001, Two tailed T-test, SEM (standard error of the mean) n≥4.

A

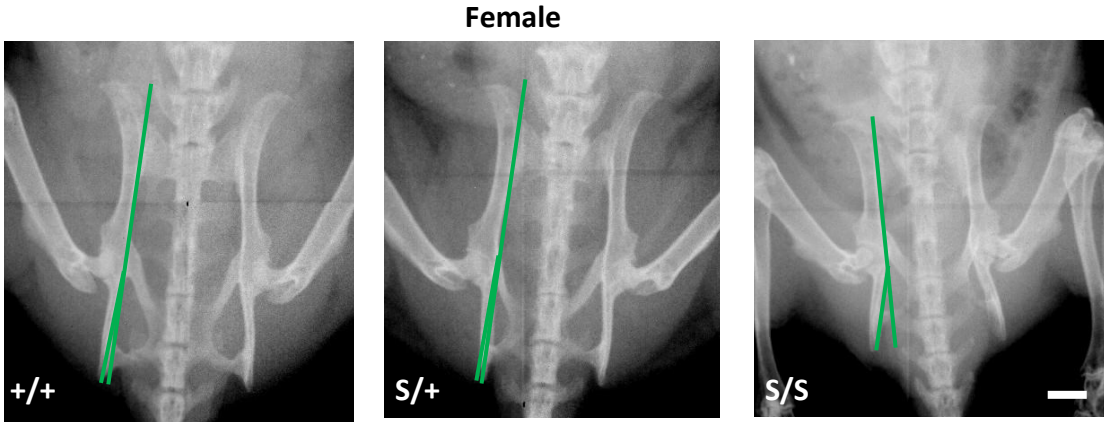

B

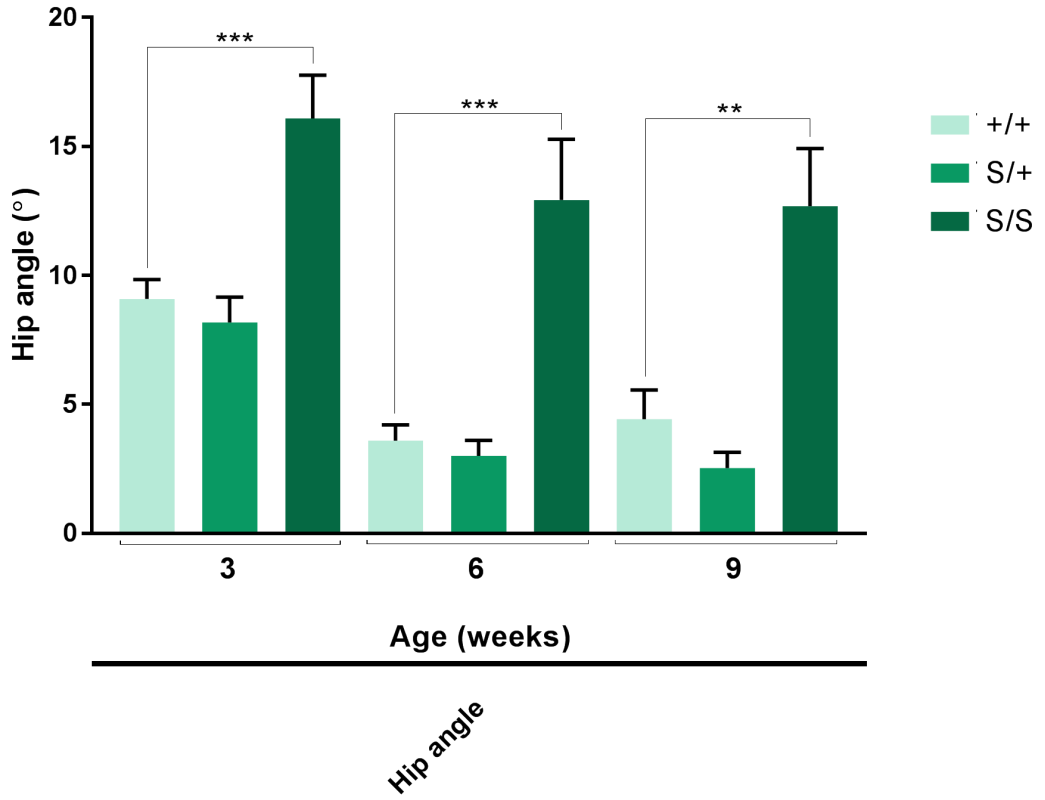

C

Age (weeks)		+/+	S/+	S/S
Hip angle (°) ± SEM	3	9.09± 0.75	8.18± 0.99	**16.09± 1.68 *** **
	6	3.60± 0.60	3.01± 0.60	**12.93± 2.36 *** **
	9	4.43± 1.13	2.53± 0.61	**12.68± 2.25 ** **

Appendix I (ii) Hip dysplasia in female SEMD mice.

The angle of the hip was measured at 3, 6 and 9 weeks of age in female mice of all 3 genotypes . **(A)** Representative X-ray imaging of 9 week old female mice (dorsal view). **(B)** There was a 3-fold increase in the average hip angle of homozygous mice compared with that of wild type li ermates. **(C)** Numeric data used for the genera on of graph B.

Key: +/+ (wild type) S/+ (heterozygous for the muta on) S/S (homozygous for the muta on) **p>0.01, ***p>0.001, Two tailed T-test, SEM (standard error of the mean) scale bar = 2mm, n≥4.

A

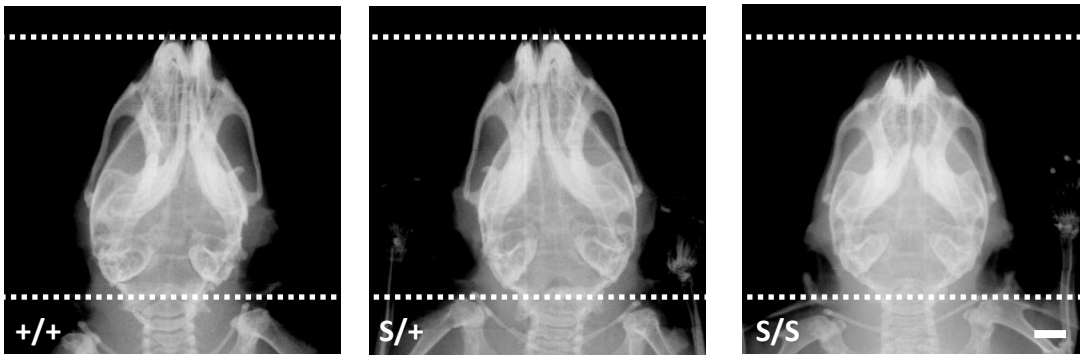

B

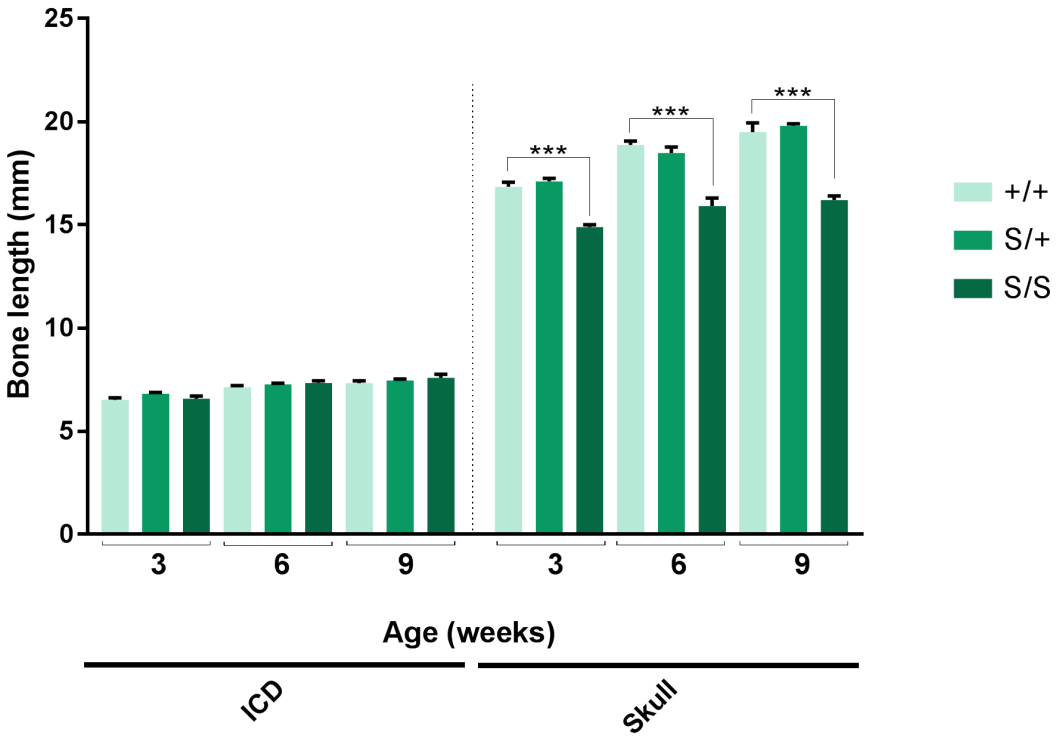

C

Age (weeks)		+/+	S/+	S/S
ICD (mm) ± SEM	3	6.52±0.10	6.83±0.05	6.58±0.13
	6	7.13±0.08	7.26±0.06	7.34±0.11
	9	7.33±0.11	7.46±0.06	7.58±0.17
Skull (mm) ± SEM	3	16.85±0.22	17.11±0.15	**14.89±0.12** ***
	6	18.88±0.18	18.48±0.29	**15.91±0.39** ***
	9	19.50±0.45	19.79±0.10	**16.20±0.21** ***

Appendix I (iii) Morphometric analysis of the skull in female SEMD mice.

ICD (inner canthal distance) and skull length were measured at 3, 6 and 9 weeks of age in female mice of all 3 genotypes. **(A)** Representa ve X-ray imaging of 9 week old female mice (dorsal view). **(B)** There was no di erence in ICD but the average skull length of mice homozygous for the muta on was reduced, reaching 83.1% of wild type bone length by 9 weeks. **(C)** Numeric data used for the genera on of graph B.

Key: +/+ (wild type) S/+ (heterozygous for the muta on) S/S (homozygous for the muta on) ***p>0.001, Two tailed T-test, SEM (standard error of the mean) scale bar = 2mm, n≥4.

A

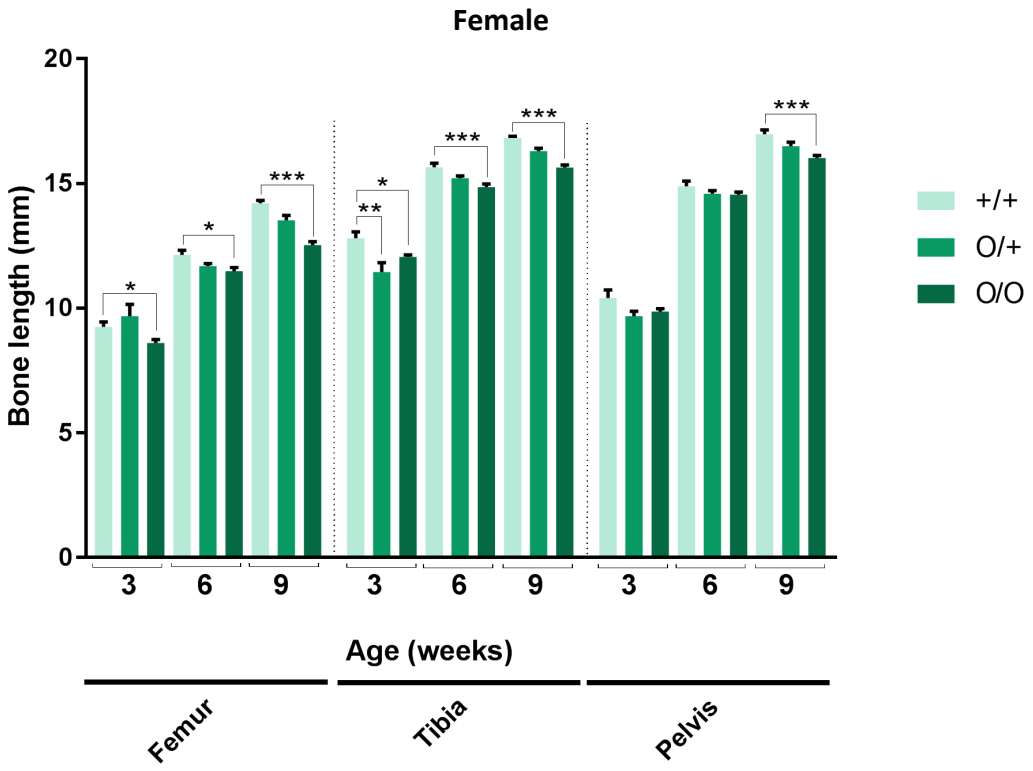

B

Age (weeks)		+/+	O/+	O/O
Femur (mm) ± SEM	3	9.25 ± 0.20	9.68 ± 0.48	**8.61 ± 0.14 ***
	6	12.14 ± 0.18	11.69 ± 0.10	**11.48 ± 0.16 ***
	9	14.21 ± 0.11	13.52 ± 0.20	**12.54 ± 0.14 *****
Tibia (mm) ± SEM	3	12.81 ± 0.25	**11.44 ± 0.39 ****	**12.06 ± 0.09 ***
	6	15.66 ± 0.16	15.21 ± 0.09	**14.85 ± 0.13 *****
	9	16.83 ± 0.06	16.30 ± 0.11	**15.64 ± 0.11 *****
Pelvis (mm) ± SEM	3	10.41 ± 0.33	9.68 ± 0.20	9.86 ± 0.11
	6	14.89 ± 0.21	14.59 ± 0.13	14.55 ± 0.10
	9	16.98 ± 0.18	16.50 ± 0.16	**16.03 ± 0.10 *****

Appendix I (iv) Morphometric analysis of female OCD mice.

Tibia, femur and pelvic (illium and ischium) bone length were measured at 3, 6 and 9 weeks of age in female mice of all 3 genotypes. **(A)** The average femur, bia and pelvis lengths for mice homozygous for the muta on were reduced, reaching 88.2%, 92.9% and 94.4% of wild type bone length respectively at 9 weeks. The average pelvic bone length of mice homozygous for the muta on was reduced, reaching 94.4% of wild type bone length by 9 weeks. The average bia length of mice heterozygous for the muta on was reduced to 89.3% of wild type bia length at 3 weeks but there was no sta stical di erence at 9 weeks. **(B)** Numeric data used for the genera on of graph A.

Key: +/+ (wild type) O/+ (heterozygous for the muta on) O/O (homozygous for the muta-on) *p>0.05, **p>0.01, ***p>0.001, Two tailed T-test, SEM (standard error of the mean) n≥8.

A

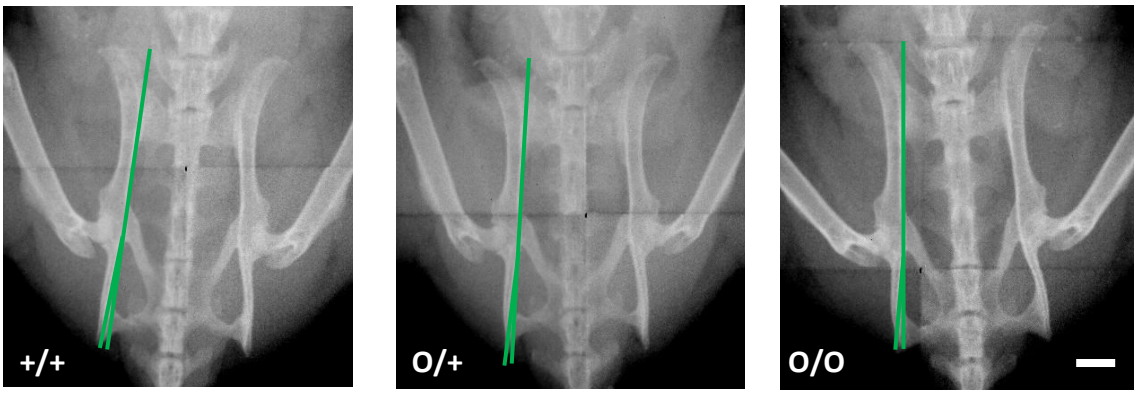

B

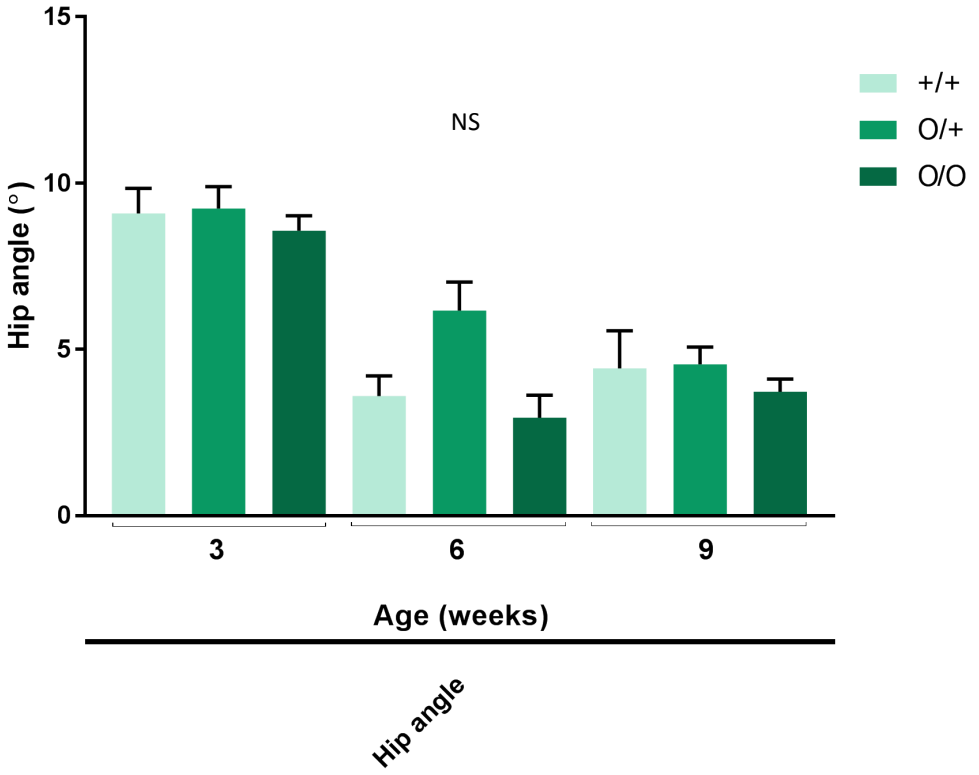

C

Age (weeks)		+/+	O/+	O/O
Hip angle (°) ± SEM	3	9.09 ± 0.75	9.24 ± 0.66	8.57 ± 0.45
	6	3.60 ± 0.60	6.17 ± 0.86	2.95 ± 0.68
	9	4.43 ± 1.13	4.55 ± 0.52	3.73 ± 0.38

Appendix I (v) Hip dysplasia in female OCD mice.

The angle of the hip was measured at 3, 6 and 9 weeks of age in female mice of all 3 genotypes . **(A)** Representa ve X-ray imaging of 9 week old female mice (dorsal view). **(B)** There was no sta s cal di erence in the average hip angle of heterozygous or homozygous mice compared with that of wild type li ermates. **(C)** Numeric data used for the genera on of graph B.

Key: +/+ (wild type) O/+ (heterozygous for the muta on) O/O (homozygous for the muta-on) NS (non-significa t) Two tailed T-test, SEM (standard error of the mean) scale bar = 2mm, n≥8.

A

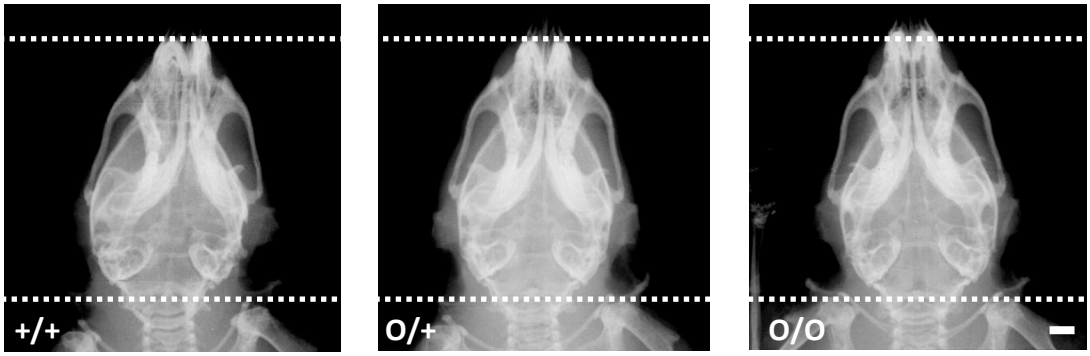

B

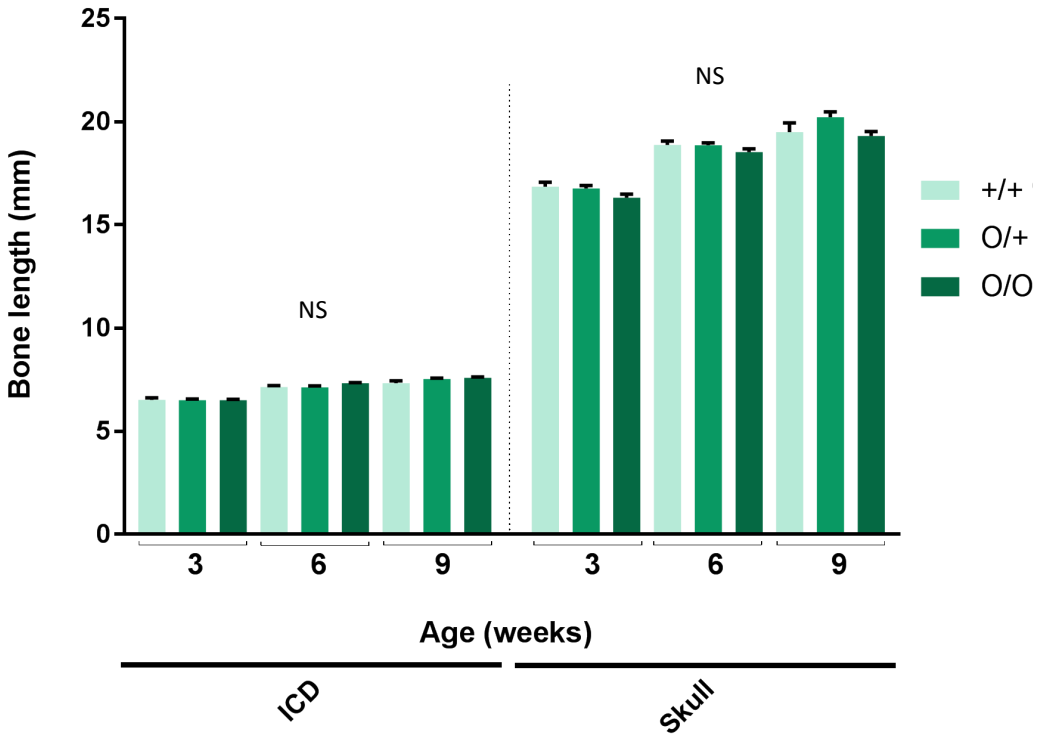

C

Age (weeks)		+/+	O/+	O/O
ICD (mm) ± SEM	3	6.52±0.10	6.50±0.06	6.50±0.05
	6	7.13±0.08	7.13±0.07	7.32±0.03
	9	7.33±0.11	7.53±0.04	7.59±0.04
Skull (mm) ± SEM	3	16.85±0.22	16.76±0.14	16.32±0.17
	6	18.88±0.18	18.85±0.12	18.53±0.16
	9	19.50±0.45	20.21±0.26	19.31±0.21

Appendix I(vi) Morphometric analysis of the skull in female OCD mice.

ICD (inner canthal distance) and skull length were measured at 3, 6 and 9 weeks of age in female mice of all 3 genotypes. **(A)** Representa ve X-ray imaging of 9 week old female mice (dorsal view). **(B)** There was no di erence in ICD or skull length between female li ermates of all 3 genotypes. **(C)** Numeric data used for the genera on of graph B.

Key: +/+ (wild type) O/+ (heterozygous for the muta on) O/O (homozygous for the muta-on) NS (not signific nt) Two tailed T-test, SEM (standard error of the mean) scale bar = 2mm, n≥10.

Appendix J Differential gene expression (i) The unfolded protein response and apoptosis

Protein	Gene symbol	OCD		SEMD	
		FC	P value	FC	P value
UPR stress sensors					
BIP	*Hspa5*	1.07	7.63E-01	-1.21	4.20E-01
ATF6	*Atf6*	-1.14	4.42E-01	-1.19	3.30E-01
ATF6B/CREBL1	*Atf6b*	1.01	9.50E-01	-1.32	4.95E-02
IRE1	*Ern1*	-1.03	8.06E-01	1.04	7.76E-01
PERK	*Eif2ak3*	-1.21	2.43E-01	-1.24	1.91E-01
LUMAN	*Creb3*	-1.03	7.52E-01	-1.19	3.71E-02
BBF2H7	*Creb3l2*	-1.31	2.15E-01	-1.08	7.08E-01
CREBH	*Creb3l3*	1.22	3.85E-01	1.05	8.40E-01
AIBZIP	*Creb3l4*	-1.41	7.12E-02	1.10	5.65E-01
OASIS	*Creb3l1*	-1.07	7.31E-01	**-1.61**	**3.71E-02**
UPR-associated genes					
ATF3	*Atf3*	1.14	8.22E-01	-1.13	8.44E-01
ATF4	*Atf4*	-1.08	6.95E-01	-1.27	2.27E-01
BCL2-related protein A1	*Bcl2a1d*	**-5.25**	**3.34E-02**	**-6.74**	**1.86E-02**
BCL2 like 15	*Bcl2l15*	**7.16**	**2.85E-02**	4.32	1.32E-01
calre culin	*Calr*	-1.08	5.39E-01	1.13	3.28E-01
calre culin 4	*Calr4*	**-4.08**	**3.73E-02**	1.55	4.54E-01
calnexin	*Canx*	-1.17	2.81E-01	1.25	1.40E-01
CD74	*Cd74*	-1.38	4.00E-01	**-2.79**	**2.31E-02**
CHOP	*Ddit*	1.40	4.26E-01	1.18	6.96E-01
derlin 3	*Derl3*	1.09	7.28E-01	**2.84**	**3.17E-03**
HSP40 member A2	*Dnaja2*	1.04	6.36E-01	-1.13	1.79E-01
HSP40 member B12	*Dnajb12*	-1.20	1.47E-01	-1.31	4.35E-02
HSP40 member C1	*Dnajc1*	-1.13	2.86E-01	-1.07	5.31E-01
dolichol-phosphate mannosyltransferase	*Dpm1*	1.11	5.59E-01	**1.56**	**2.97E-02**
EDEM1	*Edem1*	-1.14	3.35E-01	1.07	6.22E-01
eukaryotic transla on initi tion fac or 2A	*Eif2a*	-1.05	4.26E-01	-1.06	5.46E-01
ERp72	*Pdia4*	-1.32	1.95E-01	-1.34	1.70E-01
predicted gene 5160	*Gm5160*	**-6.04**	**3.27e-02**	-1.68	4.75E-01
HERPUD1	*Herpud1*	-1.22	3.39E-01	-1.30	2.18E-01
HSP90 alpha member B1	*Hsp90ab1*	-1.09	4.70E-01	-1.28	4.84E-02
GRP94	*Hsp90b1*	-1.16	3.69E-01	1.21	2.60E-01
HSP9	*Hspa9*	-1.22	1.04E-01	-1.19	1.50E-01
heat shock 70kDa protein 12A	*Hspa12a*	1.20	2.87E-01	**1.53**	**2.84E-02**
HSP25	*Hspb1*	1.63	1.60E-01	1.09	7.84E-01
insulin-like growth factor 1	*Igf1*	1.35	1.64E-01	1.06	7.71E-01
lecti , mannose-binding 1	*Lman1*	-1.28	1.70E-01	-1.35	2.60E-01
ARMET	*Manf*	1.02	8.08E-01	-1.20	8.24E-01
mitogen-activa ed protein kinase 14	*Mapk14*	-1.04	6.34E-01	1.02	8.18E-01
transmembrane protein 180	*Mfsd13b*	**-4.80**	**1.45E-02**	-1.29	6.19E-01
natriuretic pe ti e type A	*Nppa*	2.11	3.22E-01	1.91	7.00E-01
parkin	*Park2*	1.15	4.49E-01	**2.24**	**1.85E-03**
pep dylprolyl isomerase F	*Ppif*	**-1.89**	**3.34E-02**	1.18	5.25E-01
sec61 alpha subunit	*Sec61a1*	-1.23	1.60E-01	-1.36	5.32E-02

Protein	Gene symbol	OCD		SEMD	
		FC	P value	FC	P value
SLC7A11	*Slc7a11*	**1.66**	**5.39E-03**	**1.66**	**5.38E-03**
SLC22A29	*Slc22a29*	-1.31	4.42E-01	**5.13**	**1.34E-03**
SLC23A1	*Slc23a1*	2.34	7.93E-02	**4.21**	**9.87E-03**
SLC29A4	*Slc29a4*	1.57	2.70E-01	**2.84**	**2.59E-02**
STEAP1	*Steap1*	**-2.65**	**2.85E-02**	-1.06	8.70E-01
STT3	*Stt3a*	-1.27	2.26E-01	-1.39	1.07E-01
Tribbles homolog 3	*Trib3*	-1.23	3.20E-01	**1.60**	**4.28E-02**
regulator of nonsense transcripts 3B	*Upf3b*	1.16	2.38E-01	**1.58**	**4.55E-03**
VCP	*Vcp*	-1.09	3.72E-01	-1.30	2.62E-02
VLDLR	*Vldlr*	**-2.07**	**1.87E-02**	1.28	3.34E-01
WFS1	*Wfs1*	-1.19	1.65E-01	-1.30	4.75E-02
XBP1	*Xbp1*	1.03	7.76E-01	-1.09	4.55E-01
ER overload response					
Caspase 12	*Casp12*	1.29	1.47E-01	1.06	9.25E-01
Cyclin D1	*Ccnd1*	1.09	6.37E-01	-1.14	4.48E-01
Myelocytomatosis oncogene	*Myc*	-1.45	3.64E-01	-1.85	1.51E-01
Myeloid cell leukemia sequence 1	*Mcl1*	1.09	6.13E-01	-1.10	5.52E-01
Matrix metallopep dase 9	*Mmp9*	-3.16	8.40E-02	-2.25	2.00E-01
NF-kB	*Nfkb1*	1.00	9.68E-01	-1.05	6.27E-01
IRE1-dependant decay (RIDD)					
BLOC1S1	*Bloc1s1*	1.09	7.33E-01	-1.05	8.37E-01
HGSNAT	*Hgsnat*	-1.13	3.40E-01	-1.10	4.86E-01
Platelet derived growth factor receptor	*Pdgfrb*	-1.07	7.52E-01	-1.06	7.90E-01
Scavenger receptor A3	*Scara3*	-1.12	6.08E-01	-1.17	4.72E-01

Appendix J Differential gene expression (ii) Autophagic flux

Protein	Gene symbol	OCD		SEMD	
		FC	P value	FC	P value
EVA1A	*Eva1a*	**-1.63**	**4.74E-03**	1.09	5.16E-01
Parkin	*Park2*	1.15	4.49E-01	**2.24**	**1.85E-03**
RAB9B	*Rab9b*	**-7.62**	**2.50E-03**	2.11	1.41E-01
Unc-51 like kinase 3	*Ulk3*	1.04	8.74E-01	**1.80**	**2.85E-02**

Appendix J Differential gene expression (iii) Vesicle trafficking and cilia formation

Protein	Gene symbol	OCD		SEMD	
		FC	P value	FC	P value
FAM161A	*Fam161a*	1.06	7.51E-01	**1.60**	**3.34E-02**
Kinesin family member 5A	*Kif5a*	-1.02	9.29E-01	**1.61**	**3.98E-02**
Kinesin family member C2	*Kifc2*	1.26	2.07E-01	**1.90**	**1.09E-03**
Kinesin family member 17	*Kif17*	1.52	2.25E-01	**2.48**	**2.26E-02**
MNS1	*Mns1*	1.51	1.14E-01	**1.94**	**3.08E-02**
SNAB	*Napb*	1.05	7.06E-01	**1.57**	**5.16E-03**
RAB3C	*Rab3c*	**-3.64**	**1.52E-02**	-1.08	8.61E-01
RAB9B	*Rab9b*	**-7.62**	**2.50E-03**	2.11	1.41E-01
RAB25	*Rab25*	**-2.18**	**4.65E-02**	1.89	8.91E-02
Syntaphilin	*Snph*	**-1.68**	**5.00E-02**	1.30	2.76E-01
Spectrin beta	*Sptbn2*	-1.17	5.38E-01	**1.81**	**4.05E-02**
Syntaxin 1A	*Stx1a*	-1.05	7.64E-01	**1.53**	**3.23E-02**
Syntaxin 1B	*Stx1b*	1.10	6.24E-01	**2.00**	**5.51E-03**
Syntaxin 16	*Stx16*	1.05	6.80E-01	**1.56**	**3.15E-03**
Synapsin 3	*Syn3*	-1.71	1.03E-01	**2.21**	**2.70E-02**
Synaptotagmin 8	*Syt8*	**-2.44**	**2.68E-02**	1.16	6.68E-01
Synaptotagmin 14	*Syt14*	**-3.28**	**1.34E-02**	1.29	5.10E-01
Synaptotagmin-like 2	*Sytl2*	**-1.75**	**1.69E-02**	1.42	9.32E-01
Synaptobrevin	*Vamp1*	1.24	2.29E-01	**1.72**	**3.70E-02**

Appendix J Differential gene expression (iv) regulatory signalling and differentiation

Protein	Gene symbol	OCD		SEMD	
		FC	P value	FC	P value
TRAP	*Acp5*	**-2.50**	**3.32E-02**	**-2.43**	**3.76E-02**
Bone morphogenetic p otein 8a	*Bmp8a*	**-6.06**	**9.74E-03**	-1.34	5.89E-01
Chordin-like 2	*Chrdl2*	**-2.15**	**4.75E-02**	1.49	2.53E-01
C-type lectin omain family 3	*Clec3b*	**1.83**	**3.05E-02**	1.02	9.20E-01
Dickkopf WNT signalling inhibitor 1	*Dkk1*	**-3.91**	**7.92E-03**	-1.38	4.18E-01
Den n matrix protein 1	*Dmp1*	**-3.32**	**2.66E-02**	1.13	7.90E-01
Frizzled class receptor 1	*Fzd1*	-1.27	1.22E-01	**-1.54**	**1.52E-02**
Growth diff ren a on factor 1	*Gdf1*	**-8.42**	**4.42E-02**	**-10.81**	**2.96E-02**
Homeobox A5	*Hoxa5*	-1.12	4.35E-01	**1.67**	**5.65E-03**
Homeobox A9	*Hoxa9*	-1.00E+00	9.97E-01	**1.52**	**3.82E-02**
Homeobox A13	*Hoxa13*	1.08	7.47E-01	**-1.86**	**2.50E-02**
Homeobox C4	*Hoxc4*	1.12	3.75E-01	**1.71**	**2.40E-03**
Homeobox C5	*Hoxc5*	1.19	3.56E-01	**1.67**	**2.06E-02**
Homeobox C6	*Hoxc6*	-1.22	1.02E-01	**1.57**	**3.63E-03**
Homeobox C8	*Hoxc8*	-1.01	9.45E-01	**2.23**	**1.44E-03**
Homeobox D3	*Hoxd3*	**10.70**	**3.40E-03**	**12.25**	**2.50E-03**
Homeobox D4	*Hoxd4*	1.99	8.81E-01	**2.46**	**3.59E-02**
IBSP	*Ibsp*	**-2.87**	**2.46E-02**	1.03	9.48E-01
OC-STAMP	*Ocstamp*	**-2.67**	**4.29E-02**	-2.30	7.51E-02
PHEX	*Phex*	**-1.74**	**4.07E-02**	-1.29	3.00E-01
Patched	*Ptch1*	**-2.14**	**2.23E-02**	1.29	3.62E-01
Parathyroid hormone 1 receptor	*Pth1r*	**-2.04**	**1.08E-02**	1.34	2.02E-01
SATB2	*Satb2*	**-2.32**	**8.40E-03**	1.53	1.12E-01
Osteoponti	*Spp1*	**-2.06**	**3.83E-02**	1.00	9.88E-01
RUNX2	*Runx2*	**-1.73**	**1.18E-02**	1.28	1.84E-01
RUNX3	*Runx3*	**-1.72**	**4.47E-02**	1.36	2.13E-01
VEGF-D	*Vegfd*	**1.95**	**2.86E-02**	**2.41**	**8.22E-03**
WNT4	*Wnt4*	-1.43	1.04E-01	**-1.68**	**3.05E-02**
WNT5B	*Wnt5b*	-1.57	5.96E-02	**-1.76**	**2.51E-02**
Wilms tumor 1 homolog	*Wt1*	**-3.85**	**1.16E-02**	**4.44**	**7.10E-03**

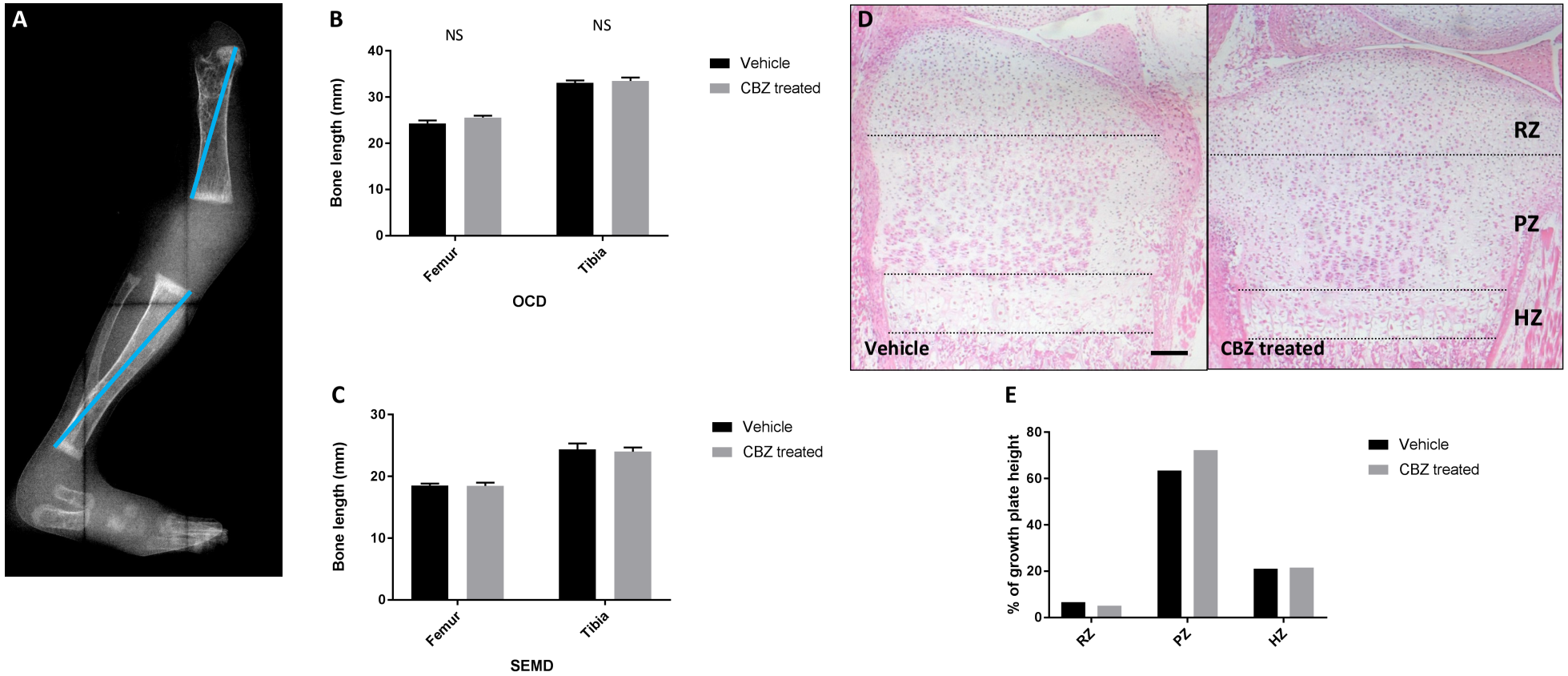

Appendix K Drug treatment of skeletal dysplasia phenotypes

(A) Radiographic image showing the parameters measured. Carbamazepine (CBZ) treatment of explants extracted from **(B)** OCD (n≥5) and **(C)** SEMD (n=2) mice at 7 days of age had no effect on tibial or femoral bone growth. **(D)** Haematoxylin and eosin staining of an SEMD explant did not show any overt visual difference in growth plate organisation following CBZ treatment although **(E)** there was an 8.8% increase in the proportional height of the proliferation zone (n=1, scale bar=20μm).

Key: RZ (resting zone) PZ (proliferative zone) HZ (hypertrophic zone)

References

Acharya, C., J. Yik, A. Kishore, V. Van Dinh, P. Dicesare and D. Haudenschild (2014). Cartilage Oligomeric Matrix Protein and its binding partners in the cartilage extracellular matrix: Interaction, regulation and role in chondrogenesis.
Akiyama, H., M.-C. Chaboissier, J. F Martin, A. Schedl and B. de Crombrugghe (2002). Akiyama, H. , Chaboissier, M.C. , Martin, J.F. , Schedl, A. & de Crombrugghe, B. The transcription factor Sox9 has essential roles in successive steps of the chondrocyte differentiation pathway and is required for expression of Sox5 and Sox6. Genes Dev. 16, 2813-2828.
Alexopoulos Leonidas, G., I. Youn, P. Bonaldo and F. Guilak (2009). "Developmental and osteoarthritic changes in Col6a1-knockout mice: Biomechanics of type VI collagen in the cartilage pericellular matrix." Arthritis & Rheumatism **60**(3): 771-779.
Anderson, S. M., W. H. McLean and R. J. Elliott (1991). "The effects of ascorbic acid on collagen synthesis by cultured human skin fibroblasts." Biochem Soc Trans **19**(1): 48s.
Aoyama, E., T. Hattori, M. Hoshijima, D. Araki, T. Nishida, S. Kubota and M. Takigawa (2009). "N-terminal domains of CCN family 2/connective tissue growth factor bind to aggrecan." Biochemical Journal **420**(3): 413-420.
Arikawa-Hirasawa, E., A. H. Le, I. Nishino, I. Nonaka, N. C. Ho, C. A. Francomano, P. Govindraj, J. R. Hassell, J. M. Devaney and J. Spranger (2002). "Structural and functional mutations of the perlecan gene cause Schwartz-Jampel syndrome, with myotonic myopathy and chondrodysplasia." The American Journal of Human Genetics **70**(5): 1368-1375.
Arikawa-Hirasawa, E., R. Wilcox William and Y. Yamada (2001). "Dyssegmental dysplasia, Silverman-Handmaker type: Unexpected role of perlecan in cartilage development#." American Journal of Medical Genetics **106**(4): 254-257.
Arnold, M. A., Y. Kim, M. Czubryt, D. Phan, J. McAnally, X. Qi, J. M Shelton, J. A Richardson, R. Bassel-Duby and E. Olson (2007). MEF2C Transcription Factor Controls Chondrocyte Hypertrophy and Bone Development.
Ashley, J. W., M. Enomoto-Iwamoto, L. J. Smith, R. L. Mauck, D. Chan, J. Lee, M. F. Heyworth, H. An and Y. Zhang (2016). "Intervertebral disc development and disease-related genetic polymorphisms." Genes & Diseases **3**(3): 171-177.
Aspberg, A. (2012). "The different roles of aggrecan interaction domains." J Histochem Cytochem **60**(12): 987-996.
Aspberg, A. (2016). Cartilage proteoglycans. Cartilage, Springer**:** 1-22.
Aspberg, A., S. Adam, G. Kostka, R. Timpl and D. Heinegård (1999). "Fibulin-1 is a ligand for the C-type lectin domains of aggrecan and versican." Journal of Biological Chemistry **274**(29): 20444-20449.
Aspberg, A., R. Miura, S. Bourdoulous, M. Shimonaka, D. Heinegård, M. Schachner, E. Ruoslahti and Y. Yamaguchi (1997). "The C-type lectin domains of lecticans, a family of aggregating chondroitin sulfate proteoglycans, bind tenascin-R by protein–protein interactions independent of carbohydrate moiety." Proceedings of the National Academy of Sciences **94**(19): 10116-10121.
Aszódi, A., D. Chan, E. Hunziker, J. F. Bateman and R. Fässler (1998). "Collagen II Is Essential for the Removal of the Notochord and the Formation of Intervertebral Discs." The Journal of Cell Biology **143**(5): 1399-1412.
Aubert-Foucher, E., N. Mayer, M. Pasdeloup, A. Pagnon, D. Hartmann and F. Mallein-Gerin (2014). "A unique tool to selectively detect the chondrogenic IIB form of human type II procollagen protein." Matrix Biology **34**: 80-88.
Baffi, M. O., M. A. Moran and R. Serra (2006). "Tgfbr2 regulates the maintenance of boundaries in the axial skeleton." Developmental Biology **296**(2): 363-374.
Baldwin, C. T., A. M. Reginato, C. Smith, S. A. Jimenez and D. J. Prockop (1989). "Structure of cDNA clones coding for human type II procollagen. The α1(II) chain is more similar to the α1(I) chain than two other α chains of fibrillar collagens." Biochemical Journal **262**(2): 521-528.
Bandyopadhyay, A., K. Tsuji, K. Cox, B. D Harfe, V. Rosen and C. Tabin (2007). Genetic Analysis of the Roles of BMP2, BMP4, and BMP7 in Limb Patterning and Skeletogenesis.
Bates, J. T., J. Jacobs, K. Shea and J. Oxford (2014). Emerging Genetic Basis of Osteochondritis Dissecans.
Beederman, M., E. M. Farina and R. R. Reid (2014). "Molecular basis of cranial suture biology and disease: Osteoblastic and osteoclastic perspectives." Genes & diseases **1**(1): 120-125.

Bella, J. and D. J. S. Hulmes (2017). Fibrillar Collagens. Fibrous Proteins: Structures and Mechanisms. D. A. D. Parry and J. M. Squire. Cham, Springer International Publishing**:** 457-490.
Blancher, C. and A. Jones (2001). "SDS -PAGE and Western Blotting Techniques." Methods Mol Med **57**: 145-162.
Blaschke, U. K., E. F. Eikenberry, D. J. S. Hulmes, H. J. Galla and P. Bruckner (2000). "Collagen XI nucleates self-assembly and limits lateral growth of cartilage fibrils." Journal of Biological Chemistry **275**(14): 10370-10378.
Blond-Elguindi, S., S. E. Cwirla, W. J. Dower, R. J. Lipshutz, S. R. Sprang, J. F. Sambrook and M.-J. H. Gething (1993). "Affinity panning of a library of peptides displayed on bacteriophages reveals the binding specificity of BiP." Cell **75**(4): 717-728.
Boeuf, S., F. Graf, J. Fischer and B. Moradi (2012). "Regulation of aggrecanases from the ADAMTS family and aggrecan neoepitope formation during in vitro chondrogenesis of human mesenchymal stem cells." European Cells and Materials (ECM).
Bonaventure, J., N. Kadhom, L. Cohen-Solal, K. H. Ng, J. Bourguignon, C. Lasselin and P. Freisinger (1994). "Reexpression of cartilage-specific genes by dedifferentiated human articular chondrocytes cultured in alginate beads." Exp Cell Res **212**(1): 97-104.
Borochowitz, Z. U., D. Scheffer, V. Adir, N. Dagoneau, A. Munnich and V. Cormier-Daire (2004). "Spondylo-epi-metaphyseal dysplasia (SEMD) matrilin 3 type: homozygote matrilin 3 mutation in a novel form of SEMD." J Med Genet **41**(5): 366-372.
Brachvogel, B., F. Zaucke, K. Dave, E. L. Norris, J. Stermann, M. Dayakli, M. Koch, J. J. Gorman, J. F. Bateman and R. Wilson (2013). "Comparative proteomic analysis of normal and collagen IX null mouse cartilage reveals altered extracellular matrix composition and novel components of the collagen IX interactome." Journal of Biological Chemistry **288**(19): 13481-13492.
Braden, C. R. and T. P. Neufeld (2016). "Atg1-independent induction of autophagy by the Drosophila Ulk3 homolog, ADUK." Febs j **283**(21): 3889-3897.
Briggs, M., J. Brock, S. C Ramsden and P. A Bell (2014). Genotype to phenotype correlations in cartilage oligomeric matrix protein associated chondrodysplasias.
Briggs, M. D., P. A. Bell and K. A. Pirog (2015). "The utility of mouse models to provide information regarding the pathomolecular mechanisms in human genetic skeletal diseases: The emerging role of endoplasmic reticulum stress (Review)." International journal of molecular medicine **35**(6): 1483-1492.
Briggs, M. D., S. M. Hoffman, L. M. King, A. S. Olsen, H. Mohrenweiser, J. G. Leroy, G. R. Mortier, D. L. Rimoin, R. S. Lachman, E. S. Gaines and et al. (1995). "Pseudoachondroplasia and multiple epiphyseal dysplasia due to mutations in the cartilage oligomeric matrix protein gene." Nat Genet **10**(3): 330-336.
Bruckner, P. (2010). "Suprastructures of extracellular matrices: paradigms of functions controlled by aggregates rather than molecules." Cell Tissue Res **339**(1): 7-18.
Buckwalter, J. A. and H. J. Mankin (1998). "Articular cartilage repair and transplantation." Arthritis & Rheumatism **41**(8): 1331-1342.
Budde, B., K. Blumbach, J. Ylostalo, F. Zaucke, H. W. Ehlen, R. Wagener, L. Ala-Kokko, M. Paulsson, P. Bruckner and S. Grassel (2005). "Altered integration of matrilin-3 into cartilage extracellular matrix in the absence of collagen IX." Mol Cell Biol **25**(23): 10465-10478.
Calfon, M., H. Zeng, F. Urano, J. H. Till, S. R. Hubbard, H. P. Harding, S. G. Clark and D. Ron (2002). "IRE1 couples endoplasmic reticulum load to secretory capacity by processing the XBP-1 mRNA." Nature **415**(6867): 92-96.
Cao, L., Y. Zhang and B. B. Yang (1998). Expression of the G1 domain of aggrecan interferes with chondrocyte attachment.
Catalina Cabrera, L., B. R. McNabb, S. E. Woods, A. N. Cartoceti and R. C. Busch (2016). "Hydrops associated with chondrodysplasia of the fetus in a miniature Scottish Highland cow." Journal of the American Veterinary Medical Association **248**(5): 552-556.
Cavanagh, J. A., I. Tammen, P. A. Windsor, J. F. Bateman, R. Savarirayan, F. W. Nicholas and H. W. Raadsma (2007). "Bulldog dwarfism in Dexter cattle is caused by mutations in ACAN." Mamm Genome **18**(11): 808-814.

Cescon, M., F. Gattazzo, P. Chen and P. Bonaldo (2015). "Collagen VI at a glance." Journal of Cell Science **128**(19): 3525-3531.
Chan, D., Y. M. Weng, H. K Graham, D. O Sillence and J. F Bateman (1998). A nonsense mutation in the carboxyl-terminal domain of type X collagen causes haploinsufficiency in Schmid metaphyseal chondrodysplasia.
Chan, W., T. Y. K. Au, V. Tam, K. S. E. Cheah and D. Chan (2014). Coming together is a beginning: The making of an intervertebral disc.
Chang, Y.-T., C.-N. Tseng, P. Tannenberg, L. Eriksson, K. Yuan, V. A. de Jesus Perez, J. Lundberg, M. Lengquist, I. R. Botusan, S.-B. Catrina, P.-K. Tran, U. Hedin and K. Tran-Lundmark (2015). "Perlecan heparan sulfate deficiency impairs pulmonary vascular development and attenuates hypoxic pulmonary hypertension." Cardiovascular Research **107**(1): 20-31.
Chapman, K. L., G. R. Mortier, K. Chapman, J. Loughlin, M. E. Grant and M. D. Briggs (2001). "Mutations in the region encoding the von Willebrand factor A domain of matrilin-3 are associated with multiple epiphyseal dysplasia." Nat Genet **28**(4): 393-396.
Charboneau, A., L. East, N. Mulholland, M. Rohde and N. Boudreau (2005). "Pbx1 is required for Hox D3-mediated angiogenesis." Angiogenesis **8**(4): 289-296.
Chen, C., Y. Jiang, C. Xu, X. Liu, L. Hu, Y. Xiang, Q. Chen, D. Chen, H. Li, X. Xu and S. Tang (2016). "Skeleton Genetics: a comprehensive database for genes and mutations related to genetic skeletal disorders." Database **2016**: baw127-baw127.
Chen, F. H., M. E. Herndon, N. Patel, J. T. Hecht, R. S. Tuan and J. Lawler (2007). "Interaction of cartilage oligomeric matrix protein/thrombospondin 5 with aggrecan." J Biol Chem **282**(34): 24591-24598.
Chen, F. H., A. O. Thomas, J. T. Hecht, M. B. Goldring and J. Lawler (2005). "Cartilage oligomeric matrix protein/thrombospondin 5 supports chondrocyte attachment through interaction with integrins." J Biol Chem **280**(38): 32655-32661.
Chen, S., J. Feng, H. Zhang, M. Jia, Y. Shen and Z. Zong (2014). "Key role for the transcriptional factor, osterix, in spine development." The Spine Journal **14**(4): 683-694.
Chen, T. L., P. Y. Wang, W. Luo, S. S. Gwon, N. Flay, J. Zheng, C. X. Guo, M. L. Tanzer and B. Vertel (2001). Aggrecan Domains Expected to Traffic through the Exocytic Pathway Are Misdirected to the Nucleus.
Chen, Y., J. Cossman, C. T. Jayasuriya, X. Li, Y. Guan, V. Fonseca, K. Yang, C. Charbonneau, H. Yu, K. Kanbe, P. Ma, E. Darling and Q. Chen (2016). "Deficient Mechanical Activation of Anabolic Transcripts and Post-Traumatic Cartilage Degeneration in Matrilin-1 Knockout Mice." PLOS ONE **11**(6): e0156676.
Chin, L.-S., James A. Olzmann and L. Li (2010). "Parkin-mediated ubiquitin signalling in aggresome formation and autophagy." Biochemical Society Transactions **38**(1): 144-149.
Christensen, S. E., J. M. Coles, N. A. Zelenski, B. D. Furman, H. A. Leddy, S. Zauscher, P. Bonaldo and F. Guilak (2012). "Altered Trabecular Bone Structure and Delayed Cartilage Degeneration in the Knees of Collagen VI Null Mice." PLOS ONE **7**(3): e33397.
Cinque, L., A. Forrester, R. Bartolomeo, M. Svelto, R. Venditti, S. Montefusco, E. Polishchuk, E. Nusco, A. Rossi, D. Medina, R. Polishchuk, M. De Matteis and C. Settembre (2015). FGF signalling regulates bone growth through autophagy.
Clements Kristen, M., S. Price Joanne, G. Chambers Mark, M. Visco Denise, A. R. Poole and M. Mason Roger (2003). "Gene deletion of either interleukin-1β, interleukin-1β–converting enzyme, inducible nitric oxide synthase, or stromelysin 1 accelerates the development of knee osteoarthritis in mice after surgical transection of the medial collateral ligament and partial medial meniscectomy." Arthritis & Rheumatism **48**(12): 3452-3463.
Cook, M. J. (1965, February 2008). "The anatomy of the laboratory mouse." 2018, from http://www.informatics.jax.org/cookbook/.
Costell, M., E. Gustafsson, A. Aszódi, M. Mörgelin, W. Bloch, E. Hunziker, K. Addicks, R. Timpl and R. Fässler (1999). "Perlecan maintains the integrity of cartilage and some basement membranes." The Journal of cell biology **147**(5): 1109-1122.
Cox, M. K. and R. Serra (2014). Development of the Intervertebral Disc. The Intervertebral Disc: Molecular and Structural Studies of the Disc in Health and Disease. I. M. Shapiro and M. V. Risbud. Vienna, Springer Vienna**:** 33-51.

Crippa, M., S. Giangiobbe, R. Villa, I. Bestetti, T. De Filippis, L. Fatti, J. Taurino, L. Larizza, L. Persani, F. Bellini, P. Finelli and M. T. Bonati (2018). "A balanced reciprocal translocation t(10;15)(q22.3;q26.1) interrupting ACAN gene in a family with proportionate short stature." Journal of Endocrinological Investigation.
Czarny-Ratajczak, M., J. Lohiniva, P. Rogala, K. Kozlowski, M. Perälä, L. Carter, T. D. Spector, L. Kolodziej, U. Seppänen, R. Glazar, J. Królewski, A. Latos-Bielenska and L. Ala-Kokko (2001). "A Mutation in COL9A1 Causes Multiple Epiphyseal Dysplasia: Further Evidence for Locus Heterogeneity." The American Journal of Human Genetics **69**(5): 969-980.
Daly, C., P. Ghosh, G. Jenkin, D. Oehme and T. Goldschlager (2016). "A Review of Animal Models of Intervertebral Disc Degeneration: Pathophysiology, Regeneration, and Translation to the Clinic." BioMed Research International **2016**: 14.
Danielson, K. G., H. Baribault, D. F. Holmes, H. Graham, K. E. Kadler and R. V. Iozzo (1997). "Targeted disruption of decorin leads to abnormal collagen fibril morphology and skin fragility." Journal of Cell Biology **136**(3): 729-743.
Dateki, S. (2017). ACAN mutations as a cause of familial short stature.
Day, J. M., A. I. Olin, A. D. Murdoch, A. Canfield, T. Sasaki, R. Timpl, T. E. Hardingham and A. Aspberg (2004). "Alternative splicing in the aggrecan G3 domain influences binding interactions with tenascin-C and other extracellular matrix proteins." Journal of Biological Chemistry **279**(13): 12511-12518.
Deere, M., T. Sanford, H. L. Ferguson, K. Daniels and J. T. Hecht (1998). "Identification of twelve mutations in cartilage oligomeric matrix protein (COMP) in patients with pseudoachondroplasia." Am J Med Genet **80**(5): 510-513.
Del Santo, M., F. Marches, M. Ng and R. Hinton (2000). Age-associated changes in decorin in rat mandibular condylar cartilage.
Di Cesare, P. E., C. S. Carlson, E. S. Stollerman, F. S. Chen, M. Leslie and R. Perris (1997). "Expression of cartilage oligomeric matrix protein by human synovium." FEBS Lett **412**(1): 249-252.
Di Cesare, P. E., F. S. Chen, M. Moergelin, C. S. Carlson, M. P. Leslie, R. Perris and C. Fang (2002). "Matrix-matrix interaction of cartilage oligomeric matrix protein and fibronectin." Matrix Biol **21**(5): 461-470.
Diab, K. M., J. A. Sevastik, R. Hedlund and I. A. Suliman (1995). "Accuracy and applicability of measurement of the scoliotic angle at the frontal plane by Cobb's method, by Ferguson's method and by a new method." European Spine Journal **4**(5): 291-295.
DiCesare, P., N. Hauser, D. Lehman, S. Pasumarti and M. Paulsson (1994). "Cartilage oligomeric matrix protein (COMP) is an abundant component of tendon." FEBS Letters **354**(2): 237-240.
DiCesare, P. E., M. Morgelin, K. Mann and M. Paulsson (1994). "Cartilage oligomeric matrix protein and thrombospondin 1. Purification from articular cartilage, electron microscopic structure, and chondrocyte binding." Eur J Biochem **223**(3): 927-937.
Doege, K., M. Sasaki, E. Horigan, J. R. Hassell and Y. Yamada (1987). "Complete primary structure of the rat cartilage proteoglycan core protein deduced from cDNA clones." J Biol Chem **262**(36): 17757-17767.
Doege, K. J., S. N. Coulter, L. M. Meek, K. Maslen and J. G. Wood (1997). "A human-specific polymorphism in the coding region of the aggrecan gene: Variable number of tandem repeats produce a range of core protein sizes in the general population." Journal of Biological Chemistry **272**(21): 13974-13979.
Doege, K. J., M. Sasaki, T. Kimura and Y. Yamada (1991). "Complete coding sequence and deduced primary structure of the human cartilage large aggregating proteoglycan, aggrecan. Human-specific repeats, and additional alternatively spliced forms." J Biol Chem **266**(2): 894-902.
Domowicz, M. S., M. Cortes, J. G. Henry and N. B. Schwartz (2009). "Aggrecan modulation of growth plate morphogenesis." Developmental Biology **329**(2): 242-257.
Dontas, I. A., A. I. Tsolakis, L. Khaldi, E. Patra and G. P. Lyritis (2010). "Malocclusion in aging Wistar rats." Journal of the American Association for Laboratory Animal Science **49**(1): 22-26.
Douglas, T., S. Heinemann, S. Bierbaum, D. Scharnweber and H. Worch (2006). "Fibrillogenesis of collagen types I, II, and III with small leucine-rich proteoglycans decorin and biglycan." Biomacromolecules **7**(8): 2388-2393.

Dressler, S., P. Meyer-Marcotty, N. Weisschuh, A. Jablonski-Momeni, K. Pieper, G. Gramer and E. Gramer (2010). "Dental and Craniofacial Anomalies Associated with Axenfeld-Rieger Syndrome with PITX2 Mutation." Case reports in medicine **2010**: 621984.
Dudhia, J., M. Davidson Catherine, M. Wells Terri, E. Hardingham Timothy and T. Baylis Michael (1996). "Studies on the G3 Domain of Aggrecan from Human Cartilagea." Annals of the New York Academy of Sciences **785**(1): 245-247.
Edgar, R., Y. Mazor, A. Rinon, J. Blumenthal, Y. Golan, E. Buzhor, I. Livnat, S. Ben-Ari, I. Lieder, A. Shitrit, Y. Gilboa, A. Ben-Yehudah, O. Edri, N. Shraga, Y. Bogoch, L. Leshansky, S. Aharoni, M. D. West, D. Warshawsky and R. Shtrichman (2013). "LifeMap Discovery™: The Embryonic Development, Stem Cells, and Regenerative Medicine Research Portal." PLoS ONE **8**(7): e66629.
Egging, D., F. Van Den Berkmortel, G. Taylor, J. Bristow and J. Schalkwijk (2007). "Interactions of human tenascin-X domains with dermal extracellular matrix molecules." Archives of Dermatological Research **298**(8): 389-396.
Ekeowa, U. I., J. Freeke, E. Miranda, B. Gooptu, M. F. Bush, J. Pérez, J. Teckman, C. V. Robinson and D. A. Lomas (2010). "Defining the mechanism of polymerization in the serpinopathies." Proceedings of the National Academy of Sciences **107**(40): 17146-17151.
Erwin, W. M., D. Islam, R. D. Inman, M. G. Fehlings and F. W. L. Tsui (2011). "Notochordal cells protect nucleus pulposus cells from degradation and apoptosis: implications for the mechanisms of intervertebral disc degeneration." Arthritis Research & Therapy **13**(6): R215.
Estrada, K. D., W. Wang, K. N. Retting, C. T. Chien, F. F. Elkhoury, R. Heuchel and K. M. Lyons (2013). "Smad7 regulates terminal maturation of chondrocytes in the growth plate." Developmental Biology **382**(2): 375-384.
Eyre, D. R. (2004). "Collagens and cartilage matrix homeostasis." Clinical orthopaedics and related research **427**: S118-S122.
Eyre, D. R., T. Pietka, M. A. Weis and J. J. Wu (2004). "Covalent Cross-linking of the NC1 Domain of Collagen Type IX to Collagen Type II in Cartilage." Journal of Biological Chemistry **279**(4): 2568-2574.
Faiyaz-Ul-Haque, M., L. M. King, D. Krakow, R. M. Cantor, M. E. Rusiniak, R. T. Swank, A. Superti-Furga, S. Haque, H. Abbas, W. Ahmad, M. Ahmad and D. H. Cohn (1998). Mutations in orthologous genes in human spondyloepimetaphyseal dysplasia and the brachymorphic mouse.
Ferguson, S. (2008). Biomechanics of the Spine. Spinal Disorders: Fundamentals of Diagnosis and Treatment. N. Boos and M. Aebi. Berlin, Heidelberg, Springer Berlin Heidelberg**:** 41-66.
Filmus, J. and M. Capurro (2014). "The role of glypicans in Hedgehog signaling." Matrix Biology **35**: 248-252.
Flecknell, P. (2002). "Replacement, reduction and refinement." Altex **19**(2): 73-78.
Fosang, A. J. and T. E. Hardingham (1989). "Isolation of the N-terminal globular protein domains from cartilage proteoglycans. Identification of G2 domain and its lack of interaction with hyaluronate and link protein." Biochemical Journal **261**(3): 801-809.
Fosang, A. J., P. J. Neame, K. Last, T. E. Hardingham, G. Murphy and J. A. Hamilton (1992). "The interglobular domain of cartilage aggrecan is cleaved by PUMP, gelatinases, and cathepsin B." Journal of Biological Chemistry **267**(27): 19470-19474.
Frantz, C., K. M. Stewart and V. M. Weaver (2010). "The extracellular matrix at a glance." Journal of Cell Science **123**(24): 4195-4200.
Freemont, A. and J. Hoyland (2006). Lineage plasticity and cell biology of fibrocartilage and hyaline cartilage: Its significance in cartilage repair and replacement.
Fukuda, M. (2007). The Role of Synaptotagmin and Synaptotagmin-Like Protein (Slp) in Regulated Exocytosis. Molecular Mechanisms of Exocytosis. New York, NY, Springer New York**:** 42-61.
Fulop, C., C. S. S. Gabriella and T. T. Glant (1996). "Species-specific alternative splicing of the epidermal growth factor-like domain 1 of cartilage aggrecan." Biochemical Journal **319**(3): 935-940.
Fülöp, C., E. Walcz, M. Valyon and T. T. Glant (1993). "Expression of alternatively spliced epidermal growth factor-like domains in aggrecans of different species: Evidence for a novel module." Journal of Biological Chemistry **268**(23): 17377-17383.
Gao, C., B. Chen, M. B Sullivan, J. Hui, J. Ouellet, J. E Henderson and N. Saran (2015). Micro CT Analysis of Spine Architecture in a Mouse Model of Scoliosis.

Gao, Y., S. Liu, J. Huang, W. Guo, J. Chen, L. Zhang, B. Zhao, J. Peng, A. Wang, Y. Wang, W. Xu, S. Lu, M. Yuan and Q. Guo (2014). "The ECM-Cell Interaction of Cartilage Extracellular Matrix on Chondrocytes." BioMed Research International **2014**: 8.
Garrison, P., S. Yue, J. Hanson, J. Baron and J. C. Lui (2017). "Spatial regulation of bone morphogenetic proteins (BMPs) in postnatal articular and growth plate cartilage." PLOS ONE **12**(5): e0176752.
Geister, K. A. and S. A. Camper (2015). Advances in Skeletal Dysplasia Genetics. Annual Review of Genomics and Human Genetics. **16:** 199-227.
Gibson-Brown, J. J., S. I. Agulnik, D. L. Chapman, M. Alexiou, N. Garvey, S. M. Lee and V. E. Papaioannou (1996). "Evidence of a role for T-☐ genes in the evolution of limb morphogenesis and the specification of forelimb/hindlimb identity." Mechanisms of Development **56**(1): 93-101.
Gkourogianni, A., M. Andrew, L. Tyzinski, M. Crocker, J. Douglas, N. Dunbar, J. Fairchild, M. F. A. Funari, K. E. Heath, A. A. L. Jorge, T. Kurtzman, S. LaFranchi, S. Lalani, J. Lebl, Y. Lin, E. Los, D. Newbern, C. Nowak, M. Olson, J. Popovic, S. Pruhova, L. Elblova, J. B. Quintos, E. Segerlund, L. Sentchordi, M. Shinawi, E. L. Stattin, J. Swartz, A. G. Del Angel, S. D. Cuellar, H. Hosono, P. A. Sanchez-Lara, V. Hwa, J. Baron, O. Nilsson and A. Dauber (2017). "Clinical characterization of patients with autosomal dominant short stature due to aggrecan mutations." Journal of Clinical Endocrinology and Metabolism **102**(2): 460-469.
Gleghorn, L., R. Ramesar, P. Beighton and G. Wallis (2005). "A mutation in the variable repeat region of the aggrecan gene (AGC1) causes a form of spondyloepiphyseal dysplasia associated with severe, premature osteoarthritis." Am J Hum Genet **77**(3): 484-490.
González-Martín, M. C., M. Mallo and M. A. Ros (2014). "Long bone development requires a threshold of Hox function." Developmental Biology **392**(2): 454-465.
Grafe, I., T. Yang, S. Alexander, E. P. Homan, C. Lietman, M. M. Jiang, T. Bertin, E. Munivez, Y. Chen, B. Dawson, Y. Ishikawa, M. A. Weis, T. K. Sampath, C. Ambrose, D. Eyre, H. P. Bachinger and B. Lee (2014). "Excessive transforming growth factor-beta signaling is a common mechanism in osteogenesis imperfecta." Nat Med **20**(6): 670-675.
Graff Ronald, D., S. Kelley Scott and M. Lee Greta (2003). "Role of pericellular matrix in development of a mechanically functional neocartilage." Biotechnology and Bioengineering **82**(4): 457-464.
Grimsrud, C. D., P. R. Romano, M. D'Souza, J. Edward Puzas, E. M. Schwarz, P. R. Reynolds, R. N. Roiser and R. J. O'Keefe (2001). "BMP signaling stimulates chondrocyte maturation and the expression of Indian hedgehog." Journal of Orthopaedic Research **19**(1): 18-25.
Grosch, M., B. Grüner, S. Spranger, A. M. Stütz, T. Rausch, J. O. Korbel, D. Seelow, P. Nürnberg, H. Sticht and E. Lausch (2013). "Identification of a Ninein (NIN) mutation in a family with spondyloepimetaphyseal dysplasia with joint laxity (leptodactylic type)-like phenotype." Matrix Biology **32**(7-8): 387-392.
Grover, J. and P. J. Roughley (1993). "Versican gene expression in human articular cartilage and comparison of mRNA splicing variation with aggrecan." Biochemical Journal **291**(2): 361-367.
Gualeni, B., M. Facchini, F. De Leonardis, R. Tenni, G. Cetta, M. Viola, A. Passi, A. Superti-Furga, A. Forlino and A. Rossi (2010). "Defective proteoglycan sulfation of the growth plate zones causes reduced chondrocyte proliferation via an altered Indian hedgehog signalling." Matrix Biology **29**(6): 453-460.
Gualeni, B., M. H. Rajpar, A. Kellogg, P. A. Bell, P. Arvan, R. P. Boot-Handford and M. D. Briggs (2013). "A novel transgenic mouse model of growth plate dysplasia reveals that decreased chondrocyte proliferation due to chronic ER stress is a key factor in reduced bone growth." Dis Model Mech **6**(6): 1414-1425.
Gubbiotti, M. A., S. D. Vallet, S. Ricard-Blum and R. V. Iozzo (2016). "Decorin interacting network: A comprehensive analysis of decorin-binding partners and their versatile functions." Matrix Biol **55**: 7-21.
Guerassimov, A., Y. Zhang, A. Cartman, L. C. Rosenberg, J. Esdaile, M.-A. Fitzcharles and R. Poole (1999). Immune responses to cartilage link protein and the G1 domain of proteoglycan aggrecan in patients with osteoarthritis.
Halasz, K., A. Kassner, M. Morgelin and D. Heinegard (2007). "COMP acts as a catalyst in collagen fibrillogenesis." J Biol Chem **282**(43): 31166-31173.

Hall Brian, K. and T. Miyake (2000). "All for one and one for all: condensations and the initiation of skeletal development." BioEssays **22**(2): 138-147.
Hansen, U., J. M. Allen, R. White, C. Moscibrocki, P. Bruckner, J. F. Bateman and J. Fitzgerald (2012). "WARP Interacts with Collagen VI-Containing Microfibrils in the Pericellular Matrix of Human Chondrocytes." PLOS ONE **7**(12): e52793.
Harding, H. P., Y. Zhang and D. Ron (1999). "Protein translation and folding are coupled by an endoplasmic-reticulum-resident kinase." Nature **397**(6716): 271-274.
Hardingham, T. E. and A. J. Fosang (1992). "Proteoglycans: many forms and many functions." The FASEB Journal **6**(3): 861-870.
Harper, P. A., M. R. Latter, F. W. Nicholas, R. W. Cook and P. A. Gill (1998). "Chondrodysplasia in Australian Dexter cattle." Aust Vet J **76**(3): 199-202.
Hasnain, S., R. Lourie, I. Das, A. C-H Chen and M. McGuckin (2012). The interplay between endoplasmic reticulum stress and inflammation.
Hassan, M., D. Selimovic, M. Hannig, Y. Haikel, R. T. Brodell and M. Megahed (2015). "Endoplasmic reticulum stress-mediated pathways to both apoptosis and autophagy: Significance for melanoma treatment." World J Exp Med **5**(4): 206-217.
Haudenschild, D. R., E. Hong, J. H. N. Yik, B. Chromy, M. Mörgelin, K. D. Snow, C. Acharya, Y. Takada and P. E. Di Cesare (2011). "Enhanced activity of transforming growth factor β1 (TGF-β1) bound to cartilage oligomeric matrix protein." Journal of Biological Chemistry **286**(50): 43250-43258.
Hedlund, H., E. Hedbom, D. Heinegård, S. Mengarelli-Widholm, F. P. Reinholt and O. Svensson (1999). "Association of the Aggrecan Keratan Sulfate-rich Region with Collagen in Bovine Articular Cartilage." Journal of Biological Chemistry **274**(9): 5777-5781.
Heinegård, D. (2009). "Fell-Muir Lecture: Proteoglycans and more – from molecules to biology." International Journal of Experimental Pathology **90**(6): 575-586.
Heinegard, D. and T. Saxne (2011). "The role of the cartilage matrix in osteoarthritis." Nat Rev Rheumatol **7**(1): 50-56.
Hessle, L., G. A. Stordalen, C. Wenglén, C. Petzold, E. K. Tanner, S.-H. Brorson, E. S. Baekkevold, P. Önnerfjord, F. P. Reinholt and D. Heinegård (2013). "Correction: The Skeletal Phenotype of Chondroadherin Deficient Mice." PLOS ONE **8**(7): 10.1371/annotation/cb1377d1377b1374c-1624f-1346e1376-1957e-1313b1355ca1378e1302.
Hiramatsu, N., C. Messah, J. Han, M. M. LaVail, R. J. Kaufman and J. H. Lin (2014). "Translational and posttranslational regulation of XIAP by eIF2alpha and ATF4 promotes ER stress-induced cell death during the unfolded protein response." Mol Biol Cell **25**(9): 1411-1420.
Hirata, M., F. Kugimiya, A. Fukai, T. Saito, F. Yano, T. Ikeda, A. Mabuchi, B. R. Sapkota, T. Akune, N. Nishida, N. Yoshimura, T. Nakagawa, K. Tokunaga, K. Nakamura, U. Chung and H. Kawaguchi (2012). "C/EBPβ and RUNX2 cooperate to degrade cartilage with MMP-13 as the target and HIF-2α as the inducer in chondrocytes." Human Molecular Genetics **21**(5): 1111-1123.
Hirota, Y., S. Yamashita, Y. Kurihara, X. Jin, M. Aihara, T. Saigusa, D. Kang and T. Kanki (2015). "Mitophagy is primarily due to alternative autophagy and requires the MAPK1 and MAPK14 signaling pathways." Autophagy **11**(2): 332-343.
Hjorten, R., U. Hansen, R. A. Underwood, H. E. Telfer, R. J. Fernandes, D. Krakow, E. Sebald, S. Wachsmann-Hogiu, P. Bruckner, R. Jacquet, W. J. Landis, P. H. Byers and J. M. Pace (2007). "Type XXVII collagen at the transition of cartilage to bone during skeletogenesis." Bone **41**(4): 535-542.
Howard, C. A., P. Norred William and L. Roth Ivan (1969). "Antimicrobial activity of dimethyl sulfoxide against Escherichia coli, Pseudomonas aeruginosa, and Bacillus megaterium." Journal of Pharmaceutical Sciences **58**(7): 836-839.
Hsiao, Y.-C., K. Tuz and R. J. Ferland (2012). "Trafficking in and to the primary cilium." Cilia **1**(1): 4.
Hu, X., B. Gui, J. Su, H. Li, N. Li, T. Yu, Q. Zhang, Y. Xu, G. Li and Y. Chen (2017). "Novel pathogenic ACAN variants in non-syndromic short stature patients." Clinica Chimica Acta **469**: 126-129.
Hu, Y., X. Li, W. Xue, J. Pang, Y. Meng, Y. Shen and Q. Xu (2017). "TP53INP2-related basal autophagy is involved in the growth and malignant progression in human liposarcoma cells." Biomedicine & Pharmacotherapy **88**: 562-568.
Huang da, W., B. T. Sherman and R. A. Lempicki (2009). "Systematic and integrative analysis of large gene lists using DAVID bioinformatics resources." Nat Protoc **4**(1): 44-57.

Hung, I. H., G. C. Schoenwolf, M. Lewandoski and D. M. Ornitz (2016). "A combined series of Fgf9 and Fgf18 mutant alleles identifies unique and redundant roles in skeletal development." Dev Biol **411**(1): 72-84.
Hunziker, E. B., K. Lippuner, M. J. Keel and N. Shintani (2015). "An educational review of cartilage repair: precepts & practice--myths & misconceptions--progress & prospects." Osteoarthritis Cartilage **23**(3): 334-350.
Ikegawa, S., G. Nishimura, T. Nagai, T. Hasegawa, H. Ohashi and Y. Nakamura (1998). "Mutation of the Type X Collagen Gene (COL10A1) Causes Spondylometaphyseal Dysplasia." The American Journal of Human Genetics **63**(6): 1659-1662.
Inoue, N. and A. A. Espinoza Orías (2011). "Biomechanics of Intervertebral Disc Degeneration." The Orthopedic clinics of North America **42**(4): 487-499.
Iozzo, R. V. and L. Schaefer (2015). "Proteoglycan form and function: A comprehensive nomenclature of proteoglycans." Matrix Biology **42**: 11-55.
Ishikawa, T., K. Furuno and K. Kato (1983). "Ultrastructural studies on autolysosomes in rat hepatocytes after leupeptin treatment." Exp Cell Res **144**(1): 15-24.
Isogai, Z., A. Aspberg, D. R. Keene, R. N. Ono, D. P. Reinhardt and L. Y. Sakai (2002). "Versican interacts with fibrillin-1 and links extracellular microfibrils to other connective tissue networks." Journal of Biological Chemistry **277**(6): 4565-4572.
Izu, Y., Y. Ezura, F. Mizoguchi, A. Kawamata, T. Nakamoto, K. Nakashima, T. Hayata, H. Hemmi, P. Bonaldo and M. Noda (2012). "Type VI collagen deficiency induces osteopenia with distortion of osteoblastic cell morphology." Tissue and Cell **44**(1): 1-6.
Jackson Gail, C., D. Marcus-Soekarman, I. Stolte-Dijkstra, A. Verrips, A. Taylor Jacqueline and D. Briggs Michael (2010). "Type IX collagen gene mutations can result in multiple epiphyseal dysplasia that is associated with osteochondritis dissecans and a mild myopathy." American Journal of Medical Genetics Part A **152A**(4): 863-869.
Jackson, G. C., L. Mittaz-Crettol, J. A. Taylor, G. R. Mortier, J. Spranger, B. Zabel, M. Le Merrer, V. Cormier-Daire, C. M. Hall, A. Offiah, M. J. Wright, R. Savarirayan, G. Nishimura, S. C. Ramsden, R. Elles, L. Bonafe, A. Superti-Furga, S. Unger, A. Zankl and M. D. Briggs (2012). "Pseudoachondroplasia and multiple epiphyseal dysplasia: a 7-year comprehensive analysis of the known disease genes identify novel and recurrent mutations and provides an accurate assessment of their relative contribution." Hum Mutat **33**(1): 144-157.
Jang, J. Y., E. K Park, H.-M. Ryoo, H. I Shin, T. H Kim, J. S Jang, H. Park, J.-Y. Choi and T.-G. Kwon (2010). Polymorphisms in the Matrilin-1 Gene and Risk of Mandibular Prognathism in Koreans.
Jay, G. D. and K. A. Waller (2014). "The biology of Lubricin: Near frictionless joint motion." Matrix Biology **39**: 17-24.
Jiang, X., S. Iseki, R. E. Maxson, H. M. Sucov and G. M. Morriss-Kay (2002). "Tissue origins and interactions in the mammalian skull vault." Developmental Biology **241**(1): 106-116.
Jin, S.-W., K.-B. Sim and S.-D. Kim (2016). Development and Growth of the Normal Cranial Vault : An Embryologic Review.
Kadler, K., A. Hill and E. Canty-Laird (2008). Collagen fibrillogenesis: fibronectin, integrins, and minor collagens as organizers and nucleators.
Kanbe, K., X. Yang, L. Wei, C. Sun and Q. Chen (2007). "Pericellular Matrilins Regulate Activation of Chondrocytes by Cyclic Load-Induced Matrix Deformation." Journal of Bone and Mineral Research **22**(2): 318-328.
Karaplis, A. C. (2008). Chapter 3 - Embryonic Development of Bone and Regulation of Intramembranous and Endochondral Bone Formation. Principles of Bone Biology (Third Edition). J. P. Bilezikian, L. G. Raisz and T. J. Martin. San Diego, Academic Press**:** 53-84.
Karp, S. J., E. Schipani, B. St-Jacques, J. Hunzelman, H. Kronenberg and A. P. McMahon (2000). "Indian hedgehog coordinates endochondral bone growth and morphogenesis via parathyroid hormone related-protein-dependent and -independent pathways." Development **127**(3): 543-548.
Karuppaiah, K., K. Yu, J. Lim, J. Chen, C. Smith, F. Long and D. M. Ornitz (2016). "FGF signaling in the osteoprogenitor lineage non-autonomously regulates postnatal chondrocyte proliferation and skeletal growth." Development **143**(10): 1811-1822.

Katsianou, M. A., C. Adamopoulos, H. Vastardis and E. K. Basdra (2016). "Signaling mechanisms implicated in cranial sutures pathophysiology: Craniosynostosis." BBA Clinical **6**: 165-176.
Kavanagh, E. and D. E. Ashhurst (1999). "Development and aging of the articular cartilage of the rabbit knee joint: Distribution of biglycan, decorin, and matrilin-1." Journal of Histochemistry and Cytochemistry **47**(12): 1603-1615.
Kawakami, M. and K.-i. Yamamura (2008). "Cranial bone morphometric study among mouse strains." BMC Evolutionary Biology **8**: 73-73.
Kennedy, A. M., M. Inada, S. M. Krane, P. T. Christie, B. Harding, C. Lopez-Otin, L. M. Sanchez, A. A. Pannett, A. Dearlove, C. Hartley, M. H. Byrne, A. A. Reed, M. A. Nesbit, M. P. Whyte and R. V. Thakker (2005). "MMP13 mutation causes spondyloepimetaphyseal dysplasia, Missouri type (SEMD(MO)." J Clin Invest **115**(10): 2832-2842.
Khoshnoodi, J., J.-P. Cartailler, K. Alvares, A. Veis and B. G. Hudson (2006). "Molecular Recognition in the Assembly of Collagens: Terminal Noncollagenous Domains Are Key Recognition Modules in the Formation of Triple Helical Protomers." Journal of Biological Chemistry **281**(50): 38117-38121.
Kiani, C., L. Chen, Y. J. Wu, A. J. Yee and B. B. Yang (2002). "Structure and function of aggrecan." Cell Research **12**(1): 19-32.
Kiani, C., L. E. E. Vivian, C. A. O. Liu, C. Liwen, W. U. Yaojiong, Y. Zhang and M. E. Adams (2001). "Roles of aggrecan domains in biosynthesis, modification by glycosaminoglycans and product secretion." Biochemical Journal **354**(1): 199-207.
Kim, H. J., D. Rice, P. J Kettunen and I. Thesleff (1998). FGF-, BMP-and Shh-mediated signalling pathways in the regulation of cranial suture morphogenesis and calvarial bone development.
Kim, M. K. H., T. J. McGarry, P. Ó Broin, J. M. Flatow, A. A. J. Golden and J. D. Licht (2009). "An integrated genome screen identifies the Wnt signaling pathway as a major target of WT1." Proceedings of the National Academy of Sciences **106**(27): 11154-11159.
Kirsch, T. and M. Pfäffle (1992). Selective binding of anchorin CII (annexin V) to type II and X collagen and to chondrocalcin (C-propeptide of type II collagen).
Klatt, A. R., A. K. A. Becker, C. D. Neacsu, M. Paulsson and R. Wagener (2011). "The matrilins: Modulators of extracellular matrix assembly." International Journal of Biochemistry and Cell Biology **43**(3): 320-330.
Klatt, A. R., B. Paul-Klausch, C. Klinger, C. Kühn, J. H. Renno, M. Banerjee, G. Malchau and K. Wielckens (2009). "A critical role for collagen II in cartilage matrix degradation: Collagen II induces pro-inflammatory cytokines and MMPS in primary human chondrocytes." Journal of Orthopaedic Research **27**(1): 65-70.
Klatt, A. R., M. Paulsson and R. Wagener (2002). "Expression of matrilins during maturation of mouse skeletal tissues." Matrix Biology **21**(3): 289-296.
Kleemann-Fischer, D., G. R. Kleemann, D. Engel, J. R. Yates, J.-J. Wu and D. R. Eyre (2001). "Molecular Properties of Matrilin-3 Isolated from Human Growth Cartilage." Archives of Biochemistry and Biophysics **387**(2): 209-215.
Klüppel, M., T. N. Wight, C. Chan, A. Hinek and J. L. Wrana (2005). "Maintenance of chondroitin sulfation balance by chondroitin-4-sulfotransferase 1 is required for chondrocyte development and growth factor signaling during cartilage morphogenesis." Development **132**(17): 3989-4003.
Knarr, G., M. J. Gething, S. Modrow and J. Buchner (1995). "BiP binding sequences in antibodies." J Biol Chem **270**(46): 27589-27594.
Knudson, C. (1993). Hyaluronan receptor-directed assembly of chondrocyte pericellular matrix.
Knudson, C. and W. Knudson (2001). Cartilage proteoglycans.
Kobayakawa, M. (1985). "[Morphological study of the epiphyseal cartilage in cartilage matrix deficiency (CMD) mouse--a consideration on the roles and functions of cartilage-specific proteoglycan]." Nihon Seikeigeka Gakkai Zasshi **59**(2): 203-214.
Koch, M., F. Laub, P. Zhou, R. A. Hahn, S. Tanaka, R. E. Burgeson, D. R. Gerecke, F. Ramirez and M. K. Gordon (2003). "Collagen XXIV, a Vertebrate Fibrillar Collagen with Structural Features of Invertebrate Collagens: Selective expression in developing cornea and bone." Journal of Biological Chemistry **278**(44): 43236-43244.

Kong, L., S. Li, M. Huang, Y. Xiong, Q. Zhang, L. Ye, J. Liu, X. Zhu, R. Sun and Y. Guo (2015). "The Roles of Endoplasmic Reticulum Overload Response Induced by HCV and NS4B Protein in Human Hepatocyte Viability and Virus Replication." PLOS ONE **10**(4): e0123190.
Kotwal, N., J. Li, J. Sandy, A. Plaas and D. R. Sumner (2012). "Initial Application of EPIC – μCT to Assess Mouse Articular Cartilage Morphology and Composition: Effects of Aging and Treadmill Running." Osteoarthritis and cartilage / OARS, Osteoarthritis Research Society **20**(8): 10.1016/j.joca.2012.1004.1012.
Kozhemyakina, E., M. Zhang, A. Ionescu, M. Ayturk Ugur, N. Ono, A. Kobayashi, H. Kronenberg, L. Warman Matthew and B. Lassar Andrew (2015). "Identification of a Prg4-Expressing Articular Cartilage Progenitor Cell Population in Mice." Arthritis & Rheumatology **67**(5): 1261-1273.
Kreutzberger, A. J. B., V. Kiessling, B. Liang, P. Seelheim, S. Jakhanwal, R. Jahn, J. D. Castle and L. K. Tamm (2017). "Reconstitution of calcium-mediated exocytosis of dense-core vesicles." Science Advances **3**(7).
Kronenberg, H. (2003). Kronenberg, H.M.: Developmental regulation of the growth plate. Nature 423, 332-336.
Krueger, R. C., Jr., K. Kurima and N. B. Schwartz (1999). "Completion of the mouse aggrecan gene structure and identification of the defect in the cmd-Bc mouse as a near complete deletion of the murine aggrecan gene." Mamm Genome **10**(12): 1119-1125.
Kudelko, M., C. W. L. Chan, R. Sharma, Q. Yao, E. Lau, I. K. Chu, K. S. E. Cheah, J. A. Tanner and D. Chan (2016). "Label-Free Quantitative Proteomics Reveals Survival Mechanisms Developed by Hypertrophic Chondrocytes under ER Stress." Journal of Proteome Research **15**(1): 86-99.
Kvist, A. J., A. E. Johnson, M. Mörgelin, E. Gustafsson, E. Bengtsson, K. Lindblom, A. Aszódi, R. Fässler, T. Sasaki, R. Timpl and A. Aspberg (2006). "Chondroitin Sulfate Perlecan Enhances Collagen Fibril Formation: IMPLICATIONS FOR PERLECAN CHONDRODYSPLASIAS." Journal of Biological Chemistry **281**(44): 33127-33139.
Kwan, A. P. L., C. E. Cummings, J. A. Chapman and M. E. Grant (1991). "Macromolecular organization of chicken type X collagen in vitro." Journal of Cell Biology **114**(3): 597-604.
Kwok, J. C. F., G. Dick, D. Wang and J. W. Fawcett (2011). "Extracellular matrix and perineuronal nets in CNS repair." Developmental neurobiology **71**(11): 1073-1089.
Landauer, W. (1965). "NANOMELIA, A LETHAL NUTATION OF THE FOWL." J Hered **56**: 131-138.
Lauing, K. L., M. Cortes, M. S. Domowicz, J. G. Henry, A. T. Baria and N. B. Schwartz (2014). "Aggrecan is required for growth plate cytoarchitecture and differentiation." Dev Biol **396**(2): 224-236.
Lawson, L. and B. D. Harfe (2015). "Notochord to Nucleus Pulposus Transition." Current Osteoporosis Reports **13**(5): 336-341.
Li, H., N. B. Schwartz and B. M. Vertel (1993). "cDNA cloning of chick cartilage chondroitin sulfate (aggrecan) core protein and identification of a stop codon in the aggrecan gene associated with the chondrodystrophy, nanomelia." J Biol Chem **268**(31): 23504-23511.
Li, W. W., J. Li and J. K. Bao (2012). "Microautophagy: lesser-known self-eating." Cell Mol Life Sci **69**(7): 1125-1136.
Little, C. B., C. T. Meeker, R. M. Hembry, N. A. Sims, K. E. Lawlor, S. B. Golub, K. Last and A. J. Fosang (2005). "Matrix metalloproteinases are not essential for aggrecan turnover during normal skeletal growth and development." Molecular and Cellular Biology **25**(8): 3388-3399.
Liu, C., E. Nakamura, V. Knezevic, S. Hunter, K. Thompson and S. Mackem (2003). "A role for the mesenchymal T-box gene Brachyury in AER formation during limb development." Development **130**(7): 1327-1337.
Liu, Z., K. Lavine, I. H Hung and D. Ornitz (2007). FGF18 is required for early chondrocyte proliferation, hypertrophy and vascular invasion of the growth plate.
Liu, Z., J. Xu, J. S. Colvin and D. M. Ornitz (2002). "Coordination of chondrogenesis and osteogenesis by fibroblast growth factor 18." Genes & development **16**(7): 859-869.
Lohmander, L. S., Y. Yoshihara, H. Roos, T. Kobayashi, H. Yamada and M. Shinmei (1996). "Procollagen II C-propeptide in joint fluid: changes in concentration with age, time after knee injury, and osteoarthritis." J Rheumatol **23**(10): 1765-1769.

Lohmander, S. L., H. Roos, L. Dahlberg, L. A. Hoerrner and M. Lark (1994). Temporal patterns of stromelysin-1, tissue inhibitor, and proteoglycan fragments in human knee joint fluid after injury to the cruciate ligament or meniscus.
Low, K. J., M. Ansari, R. Abou Jamra, A. Clarke, S. El Chehadeh, D. Fitzpatrick, M. Greenslade, A. Henderson, J. Hurst, K. Keller, P. Kuentz, T. Prescott, F. Roessler, K. Selmer, M. C Schneider, F. Stewart, K. Tatton-Brown, J. Thevenon, M. Vigeland and S. Slaney (2017). PUF60 variants cause a syndrome of ID, short stature, microcephaly, coloboma, craniofacial, cardiac, renal and spinal features.
Lundell, A., A. I. Olin, M. Mörgelin, S. Al-Karadaghi, A. Aspberg and D. T. Logan (2004). "Structural basis for interactions between tenascins and lectican C-type lectin domains: evidence for a crosslinking role for tenascins." Structure **12**(8): 1495-1506.
Luo, W., C. Guo, J. Zheng, T. L. Chen, P. Y. Wang, B. M. Vertel and M. L. Tanzer (2000). "Aggrecan from start to finish." Journal of Bone and Mineral Metabolism **18**(2): 51-56.
Luo, Y., D. Sinkeviciute, Y. He, M. Karsdal, Y. Henrotin, A. Mobasheri, P. Onnerfjord and A. Bay-Jensen (2017). "The minor collagens in articular cartilage." Protein Cell **8**(8): 560-572.
Mackie, E. J., Y. A. Ahmed, L. Tatarczuch, K. S. Chen and M. Mirams (2008). "Endochondral ossification: How cartilage is converted into bone in the developing skeleton." The International Journal of Biochemistry & Cell Biology **40**(1): 46-62.
Mackie, E. J., L. Tatarczuch and M. Mirams (2011). "The skeleton: a multi-functional complex organ: the growth plate chondrocyte and endochondral ossification." J Endocrinol **211**(2): 109-121.
Maier, J. A., Y. Lo and B. D. Harfe (2013). "Foxa1 and Foxa2 Are Required for Formation of the Intervertebral Discs." PLOS ONE **8**(1): e55528.
Mak, K. K., H. M. Kronenberg, P. T. Chuang, S. Mackem and Y. Yang (2008). "Indian hedgehog signals independently of PTHrP to promote chondrocyte hypertrophy." Development **135**(11): 1947-1956.
Mann, H. H., S. Ozbek, J. Engel, M. Paulsson and R. Wagener (2004). "Interactions between the cartilage oligomeric matrix protein and matrilins. Implications for matrix assembly and the pathogenesis of chondrodysplasias." J Biol Chem **279**(24): 25294-25298.
Mao, J. R., G. Taylor, W. B. Dean, D. R. Wagner, V. Afzal, J. C. Lotz, E. M. Rubin and J. Bristow (2002). "Tenascin-X deficiency mimics Ehlers-Danlos syndrome in mice through alteration of collagen deposition." Nature Genetics **30**(4): 421-425.
Marcelino, J. and C. A. McDevitt (1995). Attachment of articular cartilage chondrocytes to the tissue form of type VI collagen.
Mariani, F. V., M. Fernandez-Teran and M. A. Ros (2017). "Ectoderm-mesoderm crosstalk in the embryonic limb: The role of fibroblast growth factor signaling." Dev Dyn **246**(4): 208-216.
Mariani, F. V. and G. R. Martin (2003). "Deciphering skeletal patterning: clues from the limb." Nature **423**: 319.
Marieb, E. and K. Hoehn (2006). Human Anatomy And Physiology, Benjamin-Cummings Pub Co.
Maroudas, A., M. T. Bayliss, N. Uchitel-Kaushansky, R. Schneiderman and E. Gilav (1998). "Aggrecan turnover in human articular cartilage: use of aspartic acid racemization as a marker of molecular age." Arch Biochem Biophys **350**(1): 61-71.
Massey Christopher, J., C. van Donkelaar Corrinus, E. Vresilovic, A. Zavaliangos and M. Marcolongo (2012). "Effects of aging and degeneration on the human intervertebral disc during the diurnal cycle: A finite element study." Journal of Orthopaedic Research **30**(1): 122-128.
Matsumoto, K., M. Shionyu, M. Go, K. Shimizu, T. Shinomura, K. Kimata and H. Watanabe (2003). "Distinct interaction of versican/PG-M with hyaluronan and link protein." Journal of Biological Chemistry **278**(42): 41205-41212.
Matthew, D. S. and T. R. Ronald (2009). "Collagen Structure and Stability." Annual Review of Biochemistry **78**(1): 929-958.
Maurel, M., E. Chevet, J. Tavernier and S. Gerlo (2014). "Getting RIDD of RNA: IRE1 in cell fate regulation." Trends Biochem Sci **39**(5): 245-254.
McCann, M. R., O. J. Tamplin, J. Rossant and C. A. Seguin (2012). "Tracing notochord-derived cells using a Noto-cre mouse: implications for intervertebral disc development." Dis Model Mech **5**(1): 73-82.

McCoy, A. M., F. Toth, N. I. Dolvik, S. Ekman, J. Ellermann, K. Olstad, B. Ytrehus and C. S. Carlson (2013). "Articular osteochondrosis: a comparison of naturally-occurring human and animal disease." Osteoarthritis and Cartilage **21**(11): 1638-1647.
McKee, M. D. and W. G. Cole (2012). Chapter 2 - Bone Matrix and Mineralization. Pediatric Bone (Second Edition). F. H. Glorieux, J. M. Pettifor and H. Jüppner. San Diego, Academic Press**:** 9-37.
McNulty, A. L., T. P. Vail and V. B. Kraus (2005). "Chondrocyte transport and concentration of ascorbic acid is mediated by SVCT2." Biochim Biophys Acta **1712**(2): 212-221.
Melin Fürst, C., M. Mörgelin, K. Vadstrup, D. Heinegård, A. Aspberg and A. M. Blom (2013). "The C-Type Lectin of the Aggrecan G3 Domain Activates Complement." PLOS ONE **8**(4): e61407.
Melrose, J., P. Roughley, S. Knox, S. Smith, M. Lord and J. Whitelock (2007). The Structure, Location, and Function of Perlecan, a Prominent Pericellular Proteoglycan of Fetal, Postnatal, and Mature Hyaline Cartilages.
Merline, R., K. Moreth, J. Beckmann, M. V. Nastase, J. Zeng-Brouwers, J. G. Tralhao, P. Lemarchand, J. Pfeilschifter, R. M. Schaefer, R. V. Iozzo and L. Schaefer (2011). "Signaling by the matrix proteoglycan decorin controls inflammation and cancer through PDCD4 and MicroRNA-21." Sci Signal **4**(199): ra75.
Meulenbelt, I., C. Bijkerk, S. C. M. De Wildt, H. S. Miedema, H. A. Valkenburg, F. C. Breedveld, H. A. P. Pols, J. M. Te Koppele, V. F. G. Sloos, A. Hofman, P. E. Slagboom and C. M. Van Duijn (1997). "Investigation of the association of the CRTM and CRTL1 genes with radiographically evident osteoarthritis in subjects from the Rotterdam study." Arthritis and Rheumatism **40**(10): 1760-1765.
Min, J. L., I. Meulenbelt, N. Riyazi, M. Kloppenburg, J. J. Houwing-Duistermaat, A. B. Seymour, C. M. van Duijn and P. E. Slagboom (2006). "Association of matrilin-3 polymorphisms with spinal disc degeneration and osteoarthritis of the first carpometacarpal joint of the hand." Annals of the rheumatic diseases **65**(8): 1060-1066.
Misra, S., P. Heldin, V. C. Hascall, N. K. Karamanos, S. S. Skandalis, R. R. Markwald and S. Ghatak (2011). "Hyaluronan-CD44 interactions as potential targets for cancer therapy." FEBS Journal **278**(9): 1429-1443.
Miura, R., A. Aspberg, I. M. Ethell, K. Hagihara, R. L. Schnaar, E. Ruoslahti and Y. Yamaguchi (1999). "The proteoglycan lectin domain binds sulfated cell surface glycolipids and promotes cell adhesion." Journal of Biological Chemistry **274**(16): 11431-11438.
Mok, S. S., K. Masuda, H. J. Häuselmann, M. B. Aydelotte and E. J. Thonar (1994). "Aggrecan synthesized by mature bovine chondrocytes suspended in alginate. Identification of two distinct metabolic matrix pools." Journal of Biological Chemistry **269**(52): 33021-33027.
Morawski, M., G. Bruckner, T. Arendt and R. T. Matthews (2012). "Aggrecan: Beyond cartilage and into the brain." Int J Biochem Cell Biol **44**(5): 690-693.
Morgelin, M., D. Heinegard, J. Engel and M. Paulsson (1992). "Electron microscopy of native cartilage oligomeric matrix protein purified from the Swarm rat chondrosarcoma reveals a five-armed structure." J Biol Chem **267**(9): 6137-6141.
Mullan, L. A., E. J. Mularczyk, L. H. Kung, M. Forouhan, J. M. A. Wragg, R. Goodacre, J. F. Bateman, E. Swanton, M. D. Briggs and R. P. Boot-Handford (2017). "Increased intracellular proteolysis reduces disease severity in an ER stress–associated dwarfism." The Journal of Clinical Investigation **127**(10): 3861-3865.
Muttigi, M., I. Han, H.-K. Park, H. Park and S.-H. Lee (2016). "Matrilin-3 Role in Cartilage Development and Osteoarthritis." International Journal of Molecular Sciences **17**(4): 590.
Nascimbeni Anna, C., F. Giordano, N. Dupont, D. Grasso, I. Vaccaro Maria, P. Codogno and E. Morel (2017). "ER–plasma membrane contact sites contribute to autophagosome biogenesis by regulation of local PI3P synthesis." The EMBO Journal **36**(14): 2018-2033.
Navone, F., P. Genevini and N. Borgese (2015). "Autophagy and Neurodegeneration: Insights from a Cultured Cell Model of ALS." Cells **4**(3): 354.
Nicolae, C., Y. P. Ko, N. Miosge, A. Niehoff, D. Studer, L. Enggist, E. B. Hunziker, M. Paulsson, R. Wagener and A. Aszodi (2007). "Abnormal collagen fibrils in cartilage of matrilin-1/matrilin-3-deficient mice." Journal of Biological Chemistry **282**(30): 22163-22175.
Nilsson, O., E. A Parker, A. Hegde, M. Chau, K. M Barnes and J. Baron (2007). Gradients in bone morphogenetic protein-related gene expression across the growth plate.

Nilsson, O., M. H. Guo, N. Dunbar, J. Popovic, D. Flynn, C. Jacobsen, J. C. Lui, J. N. Hirschhorn, J. Baron and A. Dauber (2014). "Short stature, accelerated bone maturation, and early growth cessation due to heterozygous aggrecan mutations." J Clin Endocrinol Metab **99**(8): E1510-1518.
Noden Drew, M. (1983). "The embryonic origins of avian cephalic and cervical muscles and associated connective tissues." American Journal of Anatomy **168**(3): 257-276.
Nundlall, S., M. H. Rajpar, P. A. Bell, C. Clowes, L. A. H. Zeeff, B. Gardner, D. J. Thornton, R. P. Boot-Handford and M. D. Briggs (2010). "An unfolded protein response is the initial cellular response to the expression of mutant matrilin-3 in a mouse model of multiple epiphyseal dysplasia." Cell Stress and Chaperones **15**(6): 835-849.
Okuma, T., M. Hirata, F. Yano, D. Mori, H. Kawaguchi, U. I. Chung, S. Tanaka and T. Saito (2015). "Regulation of mouse chondrocyte differentiation by CCAAT/enhancer-binding proteins." Biomed Res **36**(1): 21-29.
Oldberg, A., P. Antonsson, K. Lindblom and D. Heinegard (1992). "COMP (cartilage oligomeric matrix protein) is structurally related to the thrombospondins." J Biol Chem **267**(31): 22346-22350.
Olin, A. I., M. Mörgelin, T. Sasaki, R. Timpl, D. Heinegård and A. Aspberg (2000). "The proteoglycans aggrecan and Versican form networks with fibulin-2 through their lectin domain binding." Journal of Biological Chemistry.
Önnerfjord, P., A. Khabut, F. P Reinholt, O. Svensson and D. Heinegård (2012). Quantitative Proteomic Analysis of Eight Cartilaginous Tissues Reveals Characteristic Differences as well as Similarities between Subgroups.
Ono, N., W. Ono, T. Nagasawa and H. M. Kronenberg (2014). "A subset of chondrogenic cells provides early mesenchymal progenitors in growing bones." Nat Cell Biol **16**(12): 1157-1167.
Opperman Lynne, A. (2000). "Cranial sutures as intramembranous bone growth sites." Developmental Dynamics **219**(4): 472-485.
Orlowsky, E. W. and V. Kraus (2015). The Role of Innate Immunity in Osteoarthritis: When Our First Line of Defense Goes On the Offensive.
Otten, C., U. Hansen, A. Talke, R. Wagener, M. Paulsson and F. Zaucke (2010). A Matrilin-3 Mutation Associated With Osteoarthritis Does Not Affect Collagen Affinity But Promotes the Formation of Wider Cartilage Collagen Fibrils.
Paassilta, P., J. Lohiniva, S. Annunen, J. Bonaventure, M. Le Merrer, L. Pai and L. Ala-Kokko (1999). "COL9A3: A third locus for multiple epiphyseal dysplasia." American Journal of Human Genetics **64**(4): 1036-1044.
Page-McCaw, A., A. J. Ewald and Z. Werb (2007). "Matrix metalloproteinases and the regulation of tissue remodelling." Nat Rev Mol Cell Biol **8**(3): 221-233.
Pahl, H. L. and P. Baeuerle (1997). The ER overload response: Activation of NF-κB.
Pahl, H. L. and P. A. Baeuerle (1995). "A novel signal transduction pathway from the endoplasmic reticulum to the nucleus is mediated by transcription factor NF-kappa B." Embo j **14**(11): 2580-2588.
Parr, B. A. and A. P. McMahon (1995). "Dorsalizing signal Wnt-7a required for normal polarity of D-V and A-P axes of mouse limb." Nature **374**(6520): 350-353.
Parsons, P., S. J. Gilbert, A. Vaughan-Thomas, D. A. Sorrell, R. Notman, M. Bishop, A. J. Hayes, D. J. Mason and V. C. Duance (2011). "Type IX Collagen Interacts with Fibronectin Providing an Important Molecular Bridge in Articular Cartilage." Journal of Biological Chemistry **286**(40): 34986-34997.
Pearson, J. C., D. Lemons and W. McGinnis (2005). "Modulating Hox gene functions during animal body patterning." Nature Reviews Genetics **6**: 893.
Pennypacker, J. P., K. Kimata and K. S. Brown (1981). "Brachymorphic mice (bm/bm): A generalized biochemical defect expressed primarily in cartilage." Developmental Biology **81**(2): 280-287.
Percival Christopher, J. and T. Richtsmeier Joan (2013). "Angiogenesis and intramembranous osteogenesis." Developmental Dynamics **242**(8): 909-922.
Perera, R., P. Harsha Dissanayake, U. Senarath, L. Sirimevan Wijayaratne, A. Karunanayake and V. Harshadeva Weerabaddana Dissanayake (2017). Single Nucleotide Variants of Candidate Genes in Aggrecan Metabolic Pathway Are Associated with Lumbar Disc Degeneration and Modic Changes.
Peters, H., B. Wilm, N. Sakai, K. Imai, R. Maas and R. Balling (1999). "Pax1 and Pax9 synergistically regulate vertebral column development." Development **126**(23): 5399-5408.
Petit, F., K. E. Sears and N. Ahituv (2017). Limb development: a paradigm of gene regulation.

Pirog-Garcia, K. A., R. S. Meadows, L. Knowles, D. Heinegard, D. J. Thornton, K. E. Kadler, R. P. Boot-Handford and M. D. Briggs (2007). "Reduced cell proliferation and increased apoptosis are significant pathological mechanisms in a murine model of mild pseudoachondroplasia resulting from a mutation in the C-terminal domain of COMP." Hum Mol Genet **16**(17): 2072-2088.
Plaas, A. H. K., S. Wong-Palms, P. J. Roughley, R. J. Midura and V. C. Hascall (1997). "Chemical and immunological assay of the nonreducing terminal residues of chondroitin sulfate from human aggrecan." Journal of Biological Chemistry **272**(33): 20603-20610.
Plumb, D. A., V. Dhir, A. Mironov, L. Ferrara, R. Poulsom, K. E. Kadler, D. J. Thornton, M. D. Briggs and R. P. Boot-Handford (2007). "Collagen XXVII is developmentally regulated and forms thin fibrillar structures distinct from those of classical vertebrate fibrillar collagens." J Biol Chem **282**(17): 12791-12795.
Plumb, D. A., L. Ferrara, T. Torbica, L. Knowles, A. Mironov, Jr., K. E. Kadler, M. D. Briggs and R. P. Boot-Handford (2011). "Collagen XXVII Organises the Pericellular Matrix in the Growth Plate." PLOS ONE **6**(12): e29422.
Poole, R. and I. Pidoux (1989). Immunoelectron microscopy of type X collagen in endochondral ossification.
Posey, K. L., F. Coustry, A. C. Veerisetty, M. Hossain, D. Gattis, S. Booten, J. L. Alcorn, P. P. Seth and J. T. Hecht (2017). "Antisense Reduction of Mutant COMP Reduces Growth Plate Chondrocyte Pathology." Molecular Therapy **25**(3): 705-714.
Potter, P., M. Bowl, P. Jeyarajan, L. Wisby, A. Blease, M. Goldsworthy, M. Simon, S. Greenaway, V. Michel, A. Barnard, C. Aguilar, T. Agnew, G. Banks, A. Blake, L. Chessum, J. Dorning, S. Falcone, L. Goosey, S. Harris and S. Brown (2016). Novel gene function revealed by mouse mutagenesis screens for models of age-related disease.
Prein, C., N. Warmbold, Z. Farkas, M. Schieker, A. Aszodi and H. Clausen-Schaumann (2016). "Structural and mechanical properties of the proliferative zone of the developing murine growth plate cartilage assessed by atomic force microscopy." Matrix Biology **50**: 1-15.
Primorac, D., C. V. Johnson, J. B. Lawrence, M. B. McKinstry, M. L. Stover, M. S. Schanfield, S. Andjelinovic, T. Tadic and D. W. Rowe (1999). "Premature termination codon in the aggrecan gene of nanomelia and its influence on mRNA transport and stability." Croat Med J **40**(4): 528-532.
Primorac, D., M. L. Stover, S. H. Clark and D. W. Rowe (1994). "Molecular basis of nanomelia, a heritable chondrodystrophy of chicken." Matrix Biol **14**(4): 297-305.
Pulai Judit, I., M. Del Carlo and F. Loeser Richard (2002). "The α5β1 integrin provides matrix survival signals for normal and osteoarthritic human articular chondrocytes in vitro." Arthritis & Rheumatism **46**(6): 1528-1535.
Purmessur, D., C. C. Guterl, S. K. Cho, M. C. Cornejo, Y. W. Lam, B. A. Ballif, J. C. Laudier and J. C. Iatridis (2013). "Dynamic pressurization induces transition of notochordal cells to a mature phenotype while retaining production of important patterning ligands from development." Arthritis Res Ther **15**(5): R122.
Quintos, J. B., M. Guo and A. Dauber (2016). ISS due to Aggrecan Mutation.
Rauch, F. (2004). Bone Growth in Length and Width: The Yin and Yang of Bone Stability.
Rauch, U., A. Clement, C. Retzler, L. Fröhlich, R. Fässler, W. Göhring and A. Faissner (1997). "Mapping of a defined neurocan binding site to distinct domains of tenascin-C." Journal of Biological Chemistry **272**(43): 26905-26912.
Ricard-Blum, S. (2011). The Collagen Family.
Risbud, M. V. and I. M. Shapiro (2011). "Notochordal cells in the adult intervertebral disc: new perspective on an old question." Critical reviews in eukaryotic gene expression **21**(1): 29-41.
Rittenhouse, E., L. C. Dunn, J. Cookingham, C. Calo, M. Spiegelman, G. B. Dooher and D. Bennett (1978). "Cartilage matrix deficiency (cmd): a new autosomal recessive lethal mutation in the mouse." J Embryol Exp Morphol **43**: 71-84.
Robinson, K. A., M. Sun, C. E. Barnum, S. N. Weiss, J. Huegel, S. S. Shetye, L. Lin, D. Saez, S. M. Adams, R. V. Iozzo, L. J. Soslowsky and D. E. Birk (2017). "Decorin and biglycan are necessary for maintaining collagen fibril structure, fiber realignment, and mechanical properties of mature tendons." Matrix Biology **64**: 81-93.

Rodrigues-Pinto, R., S. M. Richardson and J. A. Hoyland (2014). "An understanding of intervertebral disc development, maturation and cell phenotype provides clues to direct cell-based tissue regeneration therapies for disc degeneration." Eur Spine J **23**(9): 1803-1814.
Roughley, P. J. and J. S. Mort (2014). "The role of aggrecan in normal and osteoarthritic cartilage." Journal of Experimental Orthopaedics **1**(1): 8.
Sahni, M., D.-C. Ambrosetti, A. Mansukhani, R. Gertner, D. Levy and C. Basilico (1999). "FGF signaling inhibits chondrocyte proliferation and regulates bone development through the STAT-1 pathway." Genes & Development **13**(11): 1361-1366.
Sakoh-Nakatogawa, M., H. Kirisako, H. Nakatogawa and Y. Ohsumi (2015). "Localization of Atg3 to autophagy-related membranes and its enhancement by the Atg8-family interacting motif to promote expansion of the membranes." FEBS Lett **589**(6): 744-749.
Salazar, V. S., L. W. Gamer and V. Rosen (2016). "BMP signalling in skeletal development, disease and repair." Nat Rev Endocrinol **12**(4): 203-221.
Sandy, J. D. (2006). "A contentious issue finds some clarity: On the independent and complementary roles of aggrecanase activity and MMP activity in human joint aggrecanolysis." Osteoarthritis and Cartilage **14**(2): 95-100.
Sandy, J. D. and C. Verscharen (2001). "Analysis of aggrecan in human knee cartilage and synovial fluid indicates that aggrecanase (ADAMTS) activity is responsible for the catabolic turnover and loss of whole aggrecan whereas other protease activity is required for C-terminal processing in vivo." Biochemical Journal **358**(3): 615-626.
Santer, V., R. J. White and P. Roughley (1982). O-Linked oligosaccharides of human articular cartilage proteoglycan.
Scherrer, S.-A., M. Begon, A. Leardini, C. Coillard, C.-H. Rivard and P. Allard (2013). "Three-Dimensional Vertebral Wedging in Mild and Moderate Adolescent Idiopathic Scoliosis." PLOS ONE **8**(8): e71504.
Schmidt, S. and P. Friedl (2010). "Interstitial cell migration: Integrin-dependent and alternative adhesion mechanisms." Cell and Tissue Research **339**(1): 83-92.
Schneider, C. A., W. S. Rasband and K. W. Eliceiri (2012). "NIH Image to ImageJ: 25 years of image analysis." Nat Methods **9**(7): 671-675.
Schwartz, N. B. and M. Domowicz (2002). "Chondrodysplasias due to proteoglycan defects." Glycobiology **12**(4): 57r-68r.
Seki, K. and A. Hata (2004). "Indian Hedgehog Gene Is a Target of the Bone Morphogenetic Protein Signaling Pathway." Journal of Biological Chemistry **279**(18): 18544-18549.
Sentchordi-Montané, L., M. Aza-Carmona, S. Benito-Sanz, C. Barreda- Bonis Ana, C. Sánchez-Garre, P. Prieto-Matos, P. Ruiz-Ocaña, A. Lechuga-Sancho, A. Carcavilla-Urquí, I. Mulero-Collantes, A. Martos-Moreno Gabriel, A. del Pozo, E. Vallespín, A. Offiah, M. Parrón-Pajares, I. Dinis, B. Sousa Sergio, P. Ros-Pérez, I. González-Casado and E. Heath Karen (2018). "Heterozygous aggrecan variants are associated with short stature and brachydactyly: Description of 16 probands and a review of the literature." Clinical Endocrinology **88**(6): 820-829.
Settembre, C., E. Arteaga-Solis, M. D. McKee, R. de Pablo, Q. Al Awqati, A. Ballabio and G. Karsenty (2008). "Proteoglycan desulfation determines the efficiency of chondrocyte autophagy and the extent of FGF signaling during endochondral ossification." Genes & Development **22**(19): 2645-2650.
Shen, G. (2005). "The role of type X collagen in facilitating and regulating endochondral ossification of articular cartilage." Orthodontics & Craniofacial Research **8**(1): 11-17.
Shoulders, M. D. and R. T. Raines (2009). "Collagen structure and stability." Annual review of biochemistry **78**: 929-958.
Skagen, P., T. Horn, H. A. Kruse, B. Staergaard, M. M Rapport and T. Nicolaisen (2011). Osteochondritis dissecans (OCD), an endoplasmic reticulum storage disease?: A morphological and molecular study of OCD fragments.
Snow Holly, E., M. Riccio Lin, H. Mjaatvedt Corey, S. Hoffman and A. Capehart Anthony (2005). "Versican expression during skeletal/joint morphogenesis and patterning of muscle and nerve in the embryonic mouse limb." The Anatomical Record Part A: Discoveries in Molecular, Cellular, and Evolutionary Biology **282A**(2): 95-105.

Soille, P. and L. M. Vincent (1990). Determining watersheds in digital pictures via flooding simulations. Visual Communications and Image Processing '90, SPIE.
Sophia Fox, A. J., A. Bedi and S. A. Rodeo (2009). "The basic science of articular cartilage: structure, composition, and function." Sports Health **1**(6): 461-468.
Srinivas, V., J. Bohensky and I. M. Shapiro (2008). "Autophagy: A New Phase in the Maturation of Growth Plate Chondrocytes Is Regulated by HIF, mTOR and AMP Kinase." Cells, Tissues, Organs **189**(1-4): 88-92.
Staines, K. A., B. Poulet, D. N. Wentworth and A. A. Pitsillides (2017). "The STR/ort mouse model of spontaneous osteoarthritis – an update." Osteoarthritis and Cartilage **25**(6): 802-808.
Stattin, E.-L., Y. Tegner, M. Domellöf and N. Dahl (2008). Familial osteochondritis dissecans associated with early osteoarthritis and disproportionate short stature.
Stattin, E. L., F. Wiklund, K. Lindblom, P. Onnerfjord, B. A. Jonsson, Y. Tegner, T. Sasaki, A. Struglics, S. Lohmander, N. Dahl, D. Heinegard and A. Aspberg (2010). "A missense mutation in the aggrecan C-type lectin domain disrupts extracellular matrix interactions and causes dominant familial osteochondritis dissecans." Am J Hum Genet **86**(2): 126-137.
Stemple, D. L. (2005). "Structure and function of the notochord: an essential organ for chordate development." Development **132**(11): 2503-2512.
Strusberg, I., A. Sembaj, S. Tabares, A. M. Strusberg, I. del Castillo, M. Villamar and J. Moreno Barral (2002). "Association analysis of genotypic frequencies of matrilin-1 gene in patients with osteoarthritis." Clinical and Experimental Rheumatology **20**(4): 543-545.
Suleman, F., B. Gualeni, H. J. Gregson, M. P. Leighton, K. A. Pirog, S. Edwards, P. Holden, R. P. Boot-Handford and M. D. Briggs (2012). "A novel form of chondrocyte stress is triggered by a COMP mutation causing pseudoachondroplasia." Hum Mutat **33**(1): 218-231.
SundarRaj, N., D. Fite, S. Ledbetter, S. Chakravarti and J. R. Hassell (1995). Perlecan is a component of cartilage matrix and promotes chondrocyte attachment.
Supek, F., M. Bošnjak, N. Škunca and T. Šmuc (2011). "REVIGO Summarizes and Visualizes Long Lists of Gene Ontology Terms." PLOS ONE **6**(7): e21800.
Svensson, L., A. Aszódi, D. Heinegård, E. B. Hunziker, F. P. Reinholt, R. Fässler and Å. Oldberg (2002). "Cartilage Oligomeric Matrix Protein-Deficient Mice Have Normal Skeletal Development." Molecular and Cellular Biology **22**(12): 4366-4371.
Takahara, M., T. Ogino, S. Fukushima, H. Tsuchida and K. Kaneda (1999). "Nonoperative Treatment of Osteochondritis Dissecans of the Humeral Capitellum." The American Journal of Sports Medicine **27**(6): 728-732.
Takeuchi, A., M. Nagayama, M. Ehara, J.-i. Tanuma and N. Kitai (2015). Abnormal Cranial Base Synchondrosis Development and Growth in Cartilage Calcification in Sufficient Rat.
Tam, V., W. Chan, V. Leung, K. S.E. Cheah, K. Cheung, D. Sakai, M. McCann, J. Bedore, C. A. S eguin and D. Chan (2017). Histological and reference system for the analysis of mouse intervertebral disc.
Tan, K., M. Duquette, A. Joachimiak and J. Lawler (2009). "The crystal structure of the signature domain of cartilage oligomeric matrix protein: implications for collagen, glycosaminoglycan and integrin binding." Faseb j **23**(8): 2490-2501.
Tan, K. and J. Lawler (2009). The interaction of Thrombospondins with extracellular matrix proteins.
Tanaka, M., D. Sakai, A. Hiyama, F. Arai, D. Nakajima, K. Yokoyama and J. Mochida (2012). "Evidence of Nonnotochordal Origin in Chondrocyte-like Cells of the Nucleus Pulposus Appearing in Early Stage Disk Degeneration in the Mouse Model." Global Spine Journal **2**(1_suppl): s-0032-1319861-s-1310032-1319861.
Tanaka, M., M. Watanabe, I. Yokomi, N. Matsumoto, K. Sudo, H. Satoh, T. Igarashi, A. Seki, H. Amano, K. Ohura, K. Ryu, S. Shibata, M. Nagayama and J.-i. Tanuma (2014). Establishment of a novel dwarf rat strain: Cartilage calcification insufficient (CCI) rats.
Tatsi, C., A. Gkourogianni, K. Mohnike, D. DeArment, S. Witchel, A. C. Andrade, T. C. Markello, J. Baron, O. Nilsson and Y. H. Jee (2017). "Aggrecan Mutations in Nonfamilial Short Stature and Short Stature Without Accelerated Skeletal Maturation." Journal of the Endocrine Society **1**(8): 1006-1011.
Tavakoli, J., M. Elliott Dawn and J. Costi John (2016). "Structure and mechanical function of the inter-lamellar matrix of the annulus fibrosus in the disc." Journal of Orthopaedic Research **34**(8): 1307-1315.

Thur, J., K. Rosenberg, D. P. Nitsche, T. Pihlajamaa, L. Ala-Kokko, D. Heinegård, M. Paulsson and P. Maurer (2001). "Mutations in Cartilage Oligomeric Matrix Protein Causing Pseudoachondroplasia and Multiple Epiphyseal Dysplasia Affect Binding of Calcium and Collagen I, II, and IX." Journal of Biological Chemistry **276**(9): 6083-6092.
Tompson, S. W., B. Merriman, V. A. Funari, M. Fresquet, R. S. Lachman, D. L. Rimoin, S. F. Nelson, M. D. Briggs, D. H. Cohn and D. Krakow (2009). "A recessive skeletal dysplasia, SEMD aggrecan type, results from a missense mutation affecting the C-type lectin domain of aggrecan." Am J Hum Genet **84**(1): 72-79.
Toole, B. P. (2001). "Hyaluronan in morphogenesis." Seminars in Cell and Developmental Biology **12**(2): 79-87.
Topol, L., W. Chen, H. Song, T. F Day and Y. Yang (2009). Sox9 Inhibits Wnt Signaling by Promoting -Catenin Phosphorylation in the Nucleus.
Toth, F., M. Nissi, L. Wang, J. Ellermann and C. S. Carlson (2014). Surgical induction, histological evaluation, and MRI identification of cartilage necrosis in the distal femur in goats to model early lesions of osteochondrosis.
Troeberg, L. and H. Nagase (2012). "Proteases involved in cartilage matrix degradation in osteoarthritis." Biochimica et Biophysica Acta (BBA)-Proteins and Proteomics **1824**(1): 133-145.
Tysoe, C., J. Saunders, L. White, N. Hills, M. Nicol, G. Evans, T. Cole, S. Chapman and F. M. Pope (2003). "A glycine to aspartic acid substitution of COL2A1 in a family with the Strudwick variant of spondyloepimetaphyseal dysplasia." Qjm **96**(9): 663-671.
Valhmu, W. B., G. D. Palmer, P. A. Rivers, S. Ebara, J. F. Cheng, S. Fischer and A. Ratcliffe (1995). "Structure of the human aggrecan gene: Exon-intron organization and association with the protein domains." Biochemical Journal **309**(2): 535-542.
van der Steen, M., R. Pfundt, S. J. W. H. Maas, W. M. Bakker-van Waarde, R. J. Odink and A. C. S. Hokken-Koelega (2016). "ACAN gene mutations in short children born SGA and response to growth hormone treatment." The Journal of Clinical Endocrinology & Metabolism **102**(5): 1458-1467.
Vertel, B. M. (1995). "The ins and outs of aggrecan." Trends in Cell Biology **5**(12): 458-464.
Verzijl, N., J. DeGroot, R. A. Bank, M. T. Bayliss, J. W. Bijlsma, F. P. Lafeber, A. Maroudas and J. M. TeKoppele (2001). "Age-related accumulation of the advanced glycation endproduct pentosidine in human articular cartilage aggrecan: the use of pentosidine levels as a quantitative measure of protein turnover." Matrix Biol **20**(7): 409-417.
Vincent, T. (2000). "The effect of age on proteoglycan aggregation in human cartilage." Arthritis Research & Therapy **3**(1): 66797.
Vincourt, J. B., S. Etienne, L. Grossin, J. Cottet, C. Bantsimba-Malanda, P. Netter, D. Mainard, V. Libante, P. Gillet and J. Magdalou (2012). "Matrilin-3 switches from anti- to pro-anabolic upon integration to the extracellular matrix." Matrix Biology **31**(5): 290-298.
Vlodavsky, I., R. Bar-Shavit, R. Ishai-Michaeli, P. Bashkin and Z. Fuks (1991). Vlodavsky, I., Bar-Shavit, R., Ishai-Michaeli, R., Bashkin, P. & Fuks, Z. Extracellular sequestration and release of fibroblast growth factor: a regulatory mechanism? Trends Biochem. Sci. 16, 268-271.
Wai, A. W., L. J. Ng, H. Watanabe, Y. Yamada, P. P. Tam and K. S. Cheah (1998). "Disrupted expression of matrix genes in the growth plate of the mouse cartilage matrix deficiency (cmd) mutant." Dev Genet **22**(4): 349-358.
Wang, M. and R. J. Kaufman (2014). "The impact of the endoplasmic reticulum protein-folding environment on cancer development." Nature Reviews Cancer **14**: 581.
Warman, M. L., V. Cormier-Daire, C. Hall, D. Krakow, R. Lachman, M. LeMerrer, G. Mortier, S. Mundlos, G. Nishimura, D. L. Rimoin, S. Robertson, R. Savarirayan, D. Sillence, J. Spranger, S. Unger, B. Zabel and A. Superti-Furga (2011). "Nosology and classification of genetic skeletal disorders: 2010 revision." Am J Med Genet A **155a**(5): 943-968.
Warren, S. M., L. J Brunet, R. Harland, A. N Economides and M. T Longaker (2003). The BMP antagonist Noggin regulates cranial suture fusion.
Watanabe, H., S. C. Cheung, N. Itano, K. Kimata and Y. Yamada (1997). "Identification of hyaluronan-binding domains of aggrecan." J Biol Chem **272**(44): 28057-28065.

Watanabe, H., K. Kimata, S. Line, D. Strong, L. Y. Gao, C. A. Kozak and Y. Yamada (1994). "Mouse cartilage matrix deficiency (cmd) caused by a 7 bp deletion in the aggrecan gene." Nat Genet **7**(2): 154-157.
Watanabe, H., K. Nakata, K. Kimata, I. Nakanishi and Y. Yamada (1997). "Dwarfism and age-associated spinal degeneration of heterozygote cmd mice defective in aggrecan." Proceedings of the National Academy of Sciences **94**(13): 6943-6947.
Weedon, M. N., H. Lango, C. M. Lindgren, C. Wallace, D. M. Evans, M. Mangino, R. M. Freathy, J. R. B. Perry, S. Stevens, A. S. Hall, N. J. Samani, B. Shields, I. Prokopenko, M. Farrall, A. Dominiczak, T. Johnson, S. Bergmann, J. S. Beckmann, P. Vollenweider, D. M. Waterworth, V. Mooser, C. N. A. Palmer, A. D. Morris, W. H. Ouwehand, J. H. Zhao, S. Li, R. J. F. Loos, I. Barroso, P. Deloukas, M. S. Sandhu, E. Wheeler, N. Soranzo, M. Inouye, N. J. Wareham, M. Caulfield, P. B. Munroe, A. T. Hattersley, M. I. McCarthy and T. M. Frayling (2008). "Genome-wide association analysis identifies 20 loci that influence adult height." Nature Genetics **40**(5): 575-583.
Wiberg, C., A. R. Klatt, R. Wagener, M. Paulsson, J. F. Bateman, D. Heinegård and M. Mörgelin (2003). "Complexes of matrilin-1 and biglycan or decorin connect collagen VI microfibrils to both collagen II and aggrecan." Journal of Biological Chemistry **278**(39): 37698-37704.
Wieczorek, A., N. Rezaei, C. K. Chan, C. Xu, P. Panwar, D. Brömme, E. F. Merschrod S and N. R. Forde (2015). "Development and characterization of a eukaryotic expression system for human type II procollagen." BMC Biotechnology **15**(1): 112.
Wight, T., I. Kang and M. Merrilees (2014). Versican and the Control of Inflammation.
Wight, T. N., M. G. Kinsella, S. P. Evanko, S. Potter-Perigo and M. J. Merrilees (2014). "Versican and the regulation of cell phenotype in disease." Biochimica et Biophysica Acta - General Subjects **1840**(8): 2441-2451.
Wilusz, R. E., J. Sanchez-Adams and F. Guilak (2014). "The structure and function of the pericellular matrix of articular cartilage." Matrix Biology **39**: 25-32.
Wong, M., T. Lawton, P. F. Goetinck, J. L. Kuhn, S. A. Goldstein and J. Bonadio (1992). "Aggrecan core protein is expressed in membranous bone of the chick embryo. Molecular and biomechanical studies of normal and nanomelia embryos." Journal of Biological Chemistry **267**(8): 5592-5598.
Wu, J.-J., M. Ann Weis, L. S Kim, B. G Carter and D. R Eyre (2009). Differences in Chain Usage and Cross-linking Specificities of Cartilage Type V/XI Collagen Isoforms with Age and Tissue.
Wu, J.-J., M. Ann Weis, L. S Kim and D. R Eyre (2010). Type III Collagen, a Fibril Network Modifier in Articular Cartilage.
Wu, Y. J., D. P. La Pierre, J. Wu, A. J. Yee and B. B. Yang (2005). "The interaction of versican with its binding partners." Cell Res **15**(7): 483-494.
Xu, M., E.-l. Stattin, M. Murphy and F. Barry (2017). "Generation of induced pluripotent stem cells (ARO-iPSC1-11) from a patient with autosomal recessive osteopetrosis harboring the c.212+1G>T mutation in SNX10 gene." Stem Cell Research **24**: 51-54.
Yamaguchi, Y. and E. Ruoslahti (1988). "Expression of human proteoglycan in Chinese hamster ovary cells inhibits cell proliferation." Nature **336**(6196): 244-246.
Yang, L., K. Y. Tsang, H. C. Tang, D. Chan and K. S. E. Cheah (2014). "Hypertrophic chondrocytes can become osteoblasts and osteocytes in endochondral bone formation." Proceedings of the National Academy of Sciences **111**(33): 12097-12102.
Yang, X., S. K. Trehan, Y. Guan, C. Sun, D. C. Moore, C. T. Jayasuriya and Q. Chen (2014). "Matrilin-3 inhibits chondrocyte hypertrophy as a bone morphogenetic protein-2 antagonist." Journal of Biological Chemistry **289**(50): 34768-34779.
Yoon, B. S., D. A. Ovchinnikov, I. Yoshii, Y. Mishina, R. R. Behringer and K. M. Lyons (2005). "Bmpr1a and Bmpr1b have overlapping functions and are essential for chondrogenesis in vivo." Proceedings of the National Academy of Sciences of the United States of America **102**(14): 5062-5067.
Yoshida, C. A., H. Yamamoto, T. Fujita, T. Furuichi, K. Ito, K. Inoue, K. Yamana, A. Zanma, K. Takada, Y. Ito and T. Komori (2004). "Runx2 and Runx3 are essential for chondrocyte maturation, and Runx2 regulates limb growth through induction of Indian hedgehog." Genes Dev **18**(8): 952-963.

Yoshida, M., K. Hata, R. Takashima, K. Ono, E. Nakamura, Y. Takahata, T. Murakami, S. Iseki, T. Takano-Yamamoto, R. Nishimura and T. Yoneda (2015). The transcription factor Foxc1 is necessary for Ihh–Gli2-regulated endochondral ossification.
Ytrehus, B., S. Ekman, C. S. Carlson, J. Teige and F. P. Reinholt (2004). "Focal changes in blood supply during normal epiphyseal growth are central in the pathogenesis of osteochondrosis in pigs." Bone **35**(6): 1294-1306.
Zaucke, F. (2016). Cartilage Glycoproteins.
Zelenski Nicole, A., A. Leddy Holly, J. Sanchez-Adams, J. Zhang, P. Bonaldo, W. Liedtke and F. Guilak (2015). "Type VI Collagen Regulates Pericellular Matrix Properties, Chondrocyte Swelling, and Mechanotransduction in Mouse Articular Cartilage." Arthritis & Rheumatology **67**(5): 1286-1294.
Zeller, R., J. Lopez-Rios and A. Zuniga (2009). "Vertebrate limb bud development: moving towards integrative analysis of organogenesis." Nat Rev Genet **10**(12): 845-858.
Zhang, H., H. Wang, C. Zeng, B. Yan, J. Ouyang, X. Liu, Q. Sun, C. Zhao, H. Fang, J. Pan, D. Xie, J. Yang, T. Zhang, X. Bai and D. Cai (2017). "mTORC1 activation downregulates FGFR3 and PTH/PTHrP receptor in articular chondrocytes to initiate osteoarthritis." Osteoarthritis and Cartilage **25**(6): 952-963.
Zhang, H., S. Zhao, Z. Zhao, L. Tang, Q. Guo, S. Liu and L. Chen (2014). "The association of rs1149048 polymorphism in Matrilin-1(MATN1) gene with adolescent idiopathic scoliosis susceptibility: a meta-analysis." Molecular Biology Reports **41**(4): 2543-2549.
Zhang, Q., Q. Ji, X. Wang, L. Kang, Y. Fu, Y. Yin, Z. Li, Y. Liu, X. Xu and Y. Wang (2015). "SOX9 is a regulator of ADAMTSs-induced cartilage degeneration at the early stage of human osteoarthritis." Osteoarthritis Cartilage **23**(12): 2259-2268.
Zhang, Y., L. Cao, B. L. Yang and B. B. Yang (1998). "The G3 domain of versican enhances cell proliferation via epidermial growth factor-like motifs." J Biol Chem **273**(33): 21342-21351.
Zhang, Y., Y. Wu, L. Cao, V. Lee, L. Chen, Z. Lin, C. Kiani, M. E. Adams and B. B. Yang (2001). "Versican modulates embryonic chondrocyte morphology via the epidermal growth factor-like motifs in G3." Experimental cell research **263**(1): 33-42.
Zheng, J., W. Luo and M. L. Tanzer (1998). "Aggrecan Synthesis and Secretion: A PARADIGM FOR MOLECULAR AND CELLULAR COORDINATION OF MULTIGLOBULAR PROTEIN FOLDING AND INTRACELLULAR TRAFFICKING." Journal of Biological Chemistry **273**(21): 12999-13006.
Zhou, G., Q. Zheng, F. Engin, E. Munivez, Y. Chen, E. Sebald, D. Krakow and B. Lee (2007). Dominance of SOX9 function over RUNX2 during skeletogenesis.
Zhou, X., K. von der Mark, S. Henry, W. Norton, H. Adams and B. de Crombrugghe (2014). "Chondrocytes Transdifferentiate into Osteoblasts in Endochondral Bone during Development, Postnatal Growth and Fracture Healing in Mice." PLOS Genetics **10**(12): e1004820.
Zuniga, A., F. Laurent, J. Lopez-Rios, C. Klasen, N. Matt and R. Zeller (2012). "Conserved cis-regulatory regions in a large genomic landscape control SHH and BMP-regulated Gremlin1 expression in mouse limb buds." BMC Dev Biol **12**: 23.